THE UNIVERSITY
of ADELAIDE

FACULTY OF SCIENCES

SCHOOL OF PHYSICAL SCIENCES

Wavefront modelling and sensing for advanced gravitational wave detectors

Alexei Ciobanu

Supervisors:

Prof. David OTTAWAY

Dr. Daniel BROWN

Prof. Peter VEITCH

A thesis submitted towards the degree of

Doctor of Philosophy

at

The Faculty of Sciences

The University of Adelaide

June 2021

Abstract

The Advanced Laser Interferometer Gravitational-wave Observatory (aLIGO) directly detected gravitational waves for the first time on the 14th of September 2015. In 2017 the detection of gravitational waves from a binary neutron star merger was subsequently followed up by observations by optical and radio astronomers — the first time an astrophysical event was observed by two completely separate astrophysical signals. This marked the beginning of multi-messenger astronomy. Since then 90 astrophysical events have been observed using gravitational waves. To increase the rate of event detection the sensitivity of gravitational wave detectors must be improved.

Current state of the art gravitational wave detectors are optical interferometers in the dual recycled Fabry-Perot Michelson (DRFPMI) configuration with quantum squeezed light injected to reduce vacuum noise. Future plans to improve the sensitivity further rely on increasing the circulating laser power and improving the efficiency of quantum squeezing. Squeezing efficiency is drastically reduced by optical losses in the interferometer of which mode mismatch is a large component. Higher laser power introduces larger thermal distortions in the interferometer, which increase mode mismatch.

This thesis covers topics relevant to optical modelling of coupled cavity interferometers such as the DRFPMI with a focus on mode mismatch. Novel applications in aLIGO commissioning based on existing mode mismatch sensing techniques using the output mode cleaner (OMC) are presented. A new mode mismatch sensing technique based on transverse higher order mode sidebands is demonstrated on an optical tabletop and its applications to mode mismatch sensing in aLIGO is discussed. A new optical modelling framework based on linear canonical transformations and signal flow graph theory is also presented.

Declaration

I certify that this work contains no material which has been accepted for the award of any other degree or diploma in my name, in any university or other tertiary institution and, to the best of my knowledge and belief, contains no material previously published or written by another person, except where due reference has been made in the text. In addition, I certify that no part of this work will, in the future, be used in a submission in my name, for any other degree or diploma in any university or other tertiary institution without the prior approval of the University of Adelaide and where applicable, any partner institution responsible for the joint award of this degree.

I give permission for the digital version of my thesis to be made available on the web, via the University's digital research repository, the Library Search and also through web search engines, unless permission has been granted by the University to restrict access for a period of time.

I acknowledge the support I have received for my research through the provision of an Australian Government Research Training Program Scholarship.

Acknowledgements

This thesis has been the largest project in my life and I would like to thank a number of people. I would like to thank my parents for giving me the opportunity to study and work on this project, supporting me every step of the way.

To Dave, thank you for agreeing to be my supervisor. You gave me a lot of freedom to pursue what I was interested in and I greatly appreciate it. To Dan, you are one of the main reasons this PhD went as smooth as it did. I can't imagine how any of this would have gone without you. Thanks for your efforts and your patience with me. To Peter and Jesper, thank you for your continued insights and wisdom.

I would like to thank the people I met at the LIGO Hanford observatory. I would like to thank Daniel, Sheila, Jenne, TVo, Georgia, Craig, and Nutsinee. I enjoyed our time together and thanks to you I have fond memories of the site.

I would like to thank the people at OzGrav. I enjoyed meeting all of you at the annual retreats and discussing each others work. It helped to put my work into perspective and make it feel like a part of a larger whole.

The University of Adelaide felt like a second home to me and I would like to thank everyone that has shared it with me in making it such a friendly place. To Sarah, Jonathan, Jarrah, Jamie, Rhona, Jed, Kyle, and Joshua thanks for the great company.

To Alex and Baden, it has been fun. I enjoyed our time together. I hope we will have more fun in the future.

I would like to thank everyone who shared the office with me. I would like to thank Seb, Cao, Craig, Mitchell, Tom, Sophie, Georgia, Kendall, Muskan, Deeksha, Zac, and Madi. You're all lovely people.

Contents

Chapter 1

Introduction

A fundamental fact about the nature of our reality that is all but confirmed is that the relationship between space, time, and energy is described by the Einstein field equation from general relativity (GR), first published in 1915 [2]. It is the most well tested and one of the most complete descriptions of all gravitational phenomena. A simple interpretation of the Einstein field equation is given by the phrase: "space tells matter how to move and matter tells space how to curve." [29]. The consequences of such a theory are far-reaching, some of which are still being researched.

Einstein initially developed the theory of general relativity to extend his theory of special relativity to accelerating reference frames, which he found to be equivalent to inertial reference frames in a gravitational potential. The first major success of general relativity was to accurately predict the precession of the perihelion of Mercury's orbit. The precession of the perihelion of Mercury's orbit was first published in 1859 [1] and could not be explained with Newtonian gravity without introducing a hypothetical planet "Vulcan" that orbited between Mercury and the Sun [7]. In 1915 Einstein accurately modelled the perihelion's precession using only general relativity without needing to introduce any hypothetical planets [3]. The precession of Mercury's orbit was shown to be due to the curvature of spacetime caused by the mass of the Sun — exacerbated by the high eccentricity of Mercury's orbit. Corrections to the orbits of all other planets in the solar system were also made but the deviation from Newtonian gravity are greatly diminished the further the orbit is from the Sun.

The ability of general relativity to accurately predict celestial phenomena of the day led to its adoption as the prevailing theory of gravity. However, in addition to explaining past results the theory of general relativity was used to make predictions about physical phenomena that were yet to be observed. One of these phenomena is a motivation for this thesis: gravitational waves.

1.1 Gravitational waves

The prediction of the existence of gravitational waves was first published by Einstein in 1916 [4, 5] where he found that the linearized weak-field equations had wave solutions generated by time variations of the mass quadrupole of the source [146]. Einstein found that the amplitude of these gravitational waves would be too small to be measured by anything available at the time. He also did not know about the existence of compact stellar objects such as black holes, and neutron stars, which are the only sources of gravitational waves observed to date.

The first experimental observation of the effects of gravitational waves was published in 1982 by Taylor and Weisberg [39], where the orbital period of a binary pulsar [30] was found to decay in agreement with the energy dissipation predicted by the emission of gravitational waves [94, 149]. The measured orbital period decay from 1975 to 2013 and the decay predicted from general relativity is shown in figure 1.1. It would not be until 2015 before a direct measurement of gravitational waves was made.

Direct measurements of gravitational waves are challenging due to the fact that gravitational waves have an extremely small measurable impact, even if the waves themselves have a significant energy density when they reach Earth. Gravitational waves modulate a length L proportional to the gravitational wave strain h such that the change in length ΔL is given by

$$\Delta L = hL, \tag{1.1}$$

where the strain h given by the lowest order correction to Newtonian gravity by general

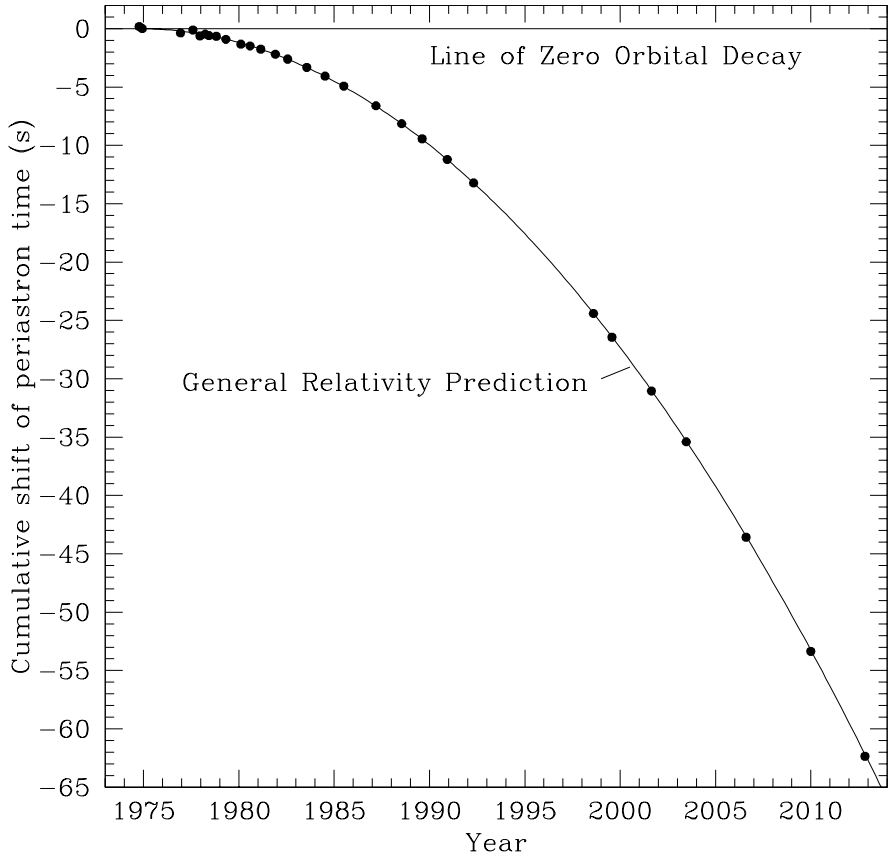

Figure 1.1: Cumulative orbital decay measurements of the B1913+16 pulsar from 1975 to 2013. The measurements closely follow to the predicted orbital decay from general relativity via gravitational wave emission. Source: [149].

relativity, ie the post-Newtonian expansion [108] is

$$h_{jk} = \frac{2G}{c^4 r} \frac{d^2 Q_{jk}}{dt^2}, \tag{1.2}$$

where G is the gravitational constant, c is the speed of light, r is the distance to the source, d^2Q_{jk}/dt^2 is the second time derivative of the quadrupole moment tensor Q. The lowest order gravitational waves are quadrupole waves. They can be decomposed into two orthogonal polarizations: h_+ and $h_\times$, which are shown in figure 1.2.

The constant out the front of equation (1.2) is $2G/c^4 = 10^{-44}$ $\mathrm{s^2 kg^{-1} m^{-1}}$. A tiny quantity that has to be offset by a massive second time derivative of the quadrupole in order to produce a measurable strain. Fortunately, the universe provides us with such massive changing quadrupoles: binary black holes — a pair of black holes that orbit their common center of mass. The strain amplitude of any random binary black hole unfortunately is not enough; their orbiting speeds are not large enough. But as

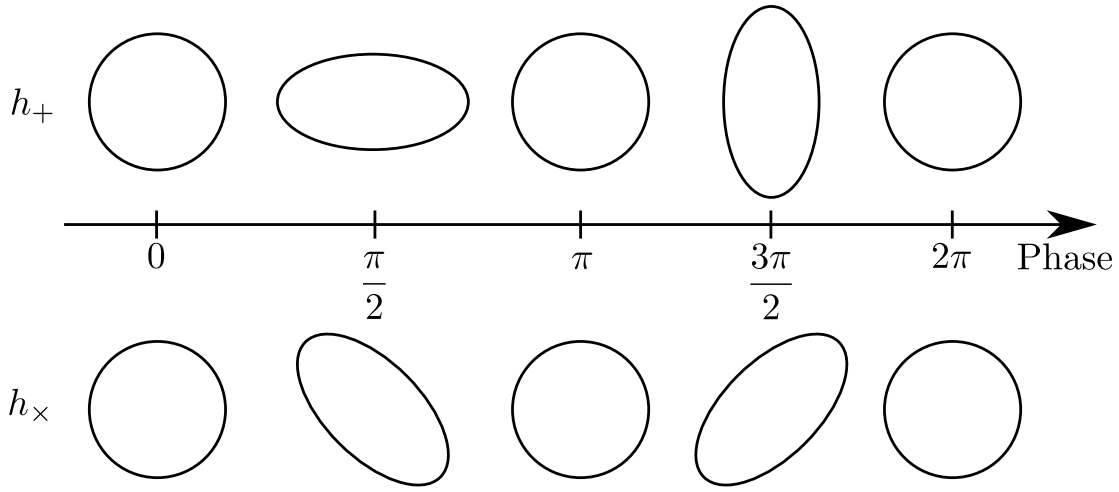

Figure 1.2: A ring of space being deformed under a full period of a gravitational wave. The two orthogonal gravitational wave polarizations h_+ and $h_\times$ are shown in the top and bottom row respectively.

we saw with the binary pulsar earlier gravitational waves function as a loss mechanism in a binary system — dissipating energy and bringing the black holes in the binary closer together. Conservation of angular momentum means the binaries' orbiting speed must increase, in the process leading to greater emission of gravitational waves. This forms a loop of ever increasing gravitational wave emission until the two black holes collide and merge forming a larger black hole. In the final moments of this process the black holes orbit each other at relativistic speeds, emitting more energy in gravitational waves than any other known process in physics. This energy, which is on the order of a solar mass radiates away from the merger as gravitational waves at the speed of light in all directions. It will be precisely this moment that the first gravitational wave detectors observed roughly 1.4 billion years after it happened [146].

The first direct measurement of gravitational waves from the merger of a binary black hole system occurred at the twin LIGO observatories on the 14th of September 2015 [146]. The measured gravitational wave strain in both detectors is shown in figure 1.3.

Fits to these waveforms by numerical relativity predictions of various binary black hole mergers allows the physical properties of the binary system to be determined [138, 139]. The masses of the two black holes were found to be 36^{+5}_{-4} and 29^{+4}_{-4} solar masses, with the final merged black hole mass of 62^{+4}_{-4} solar masses. This means that $3.0^{+0.5}_{-0.5}$ solar

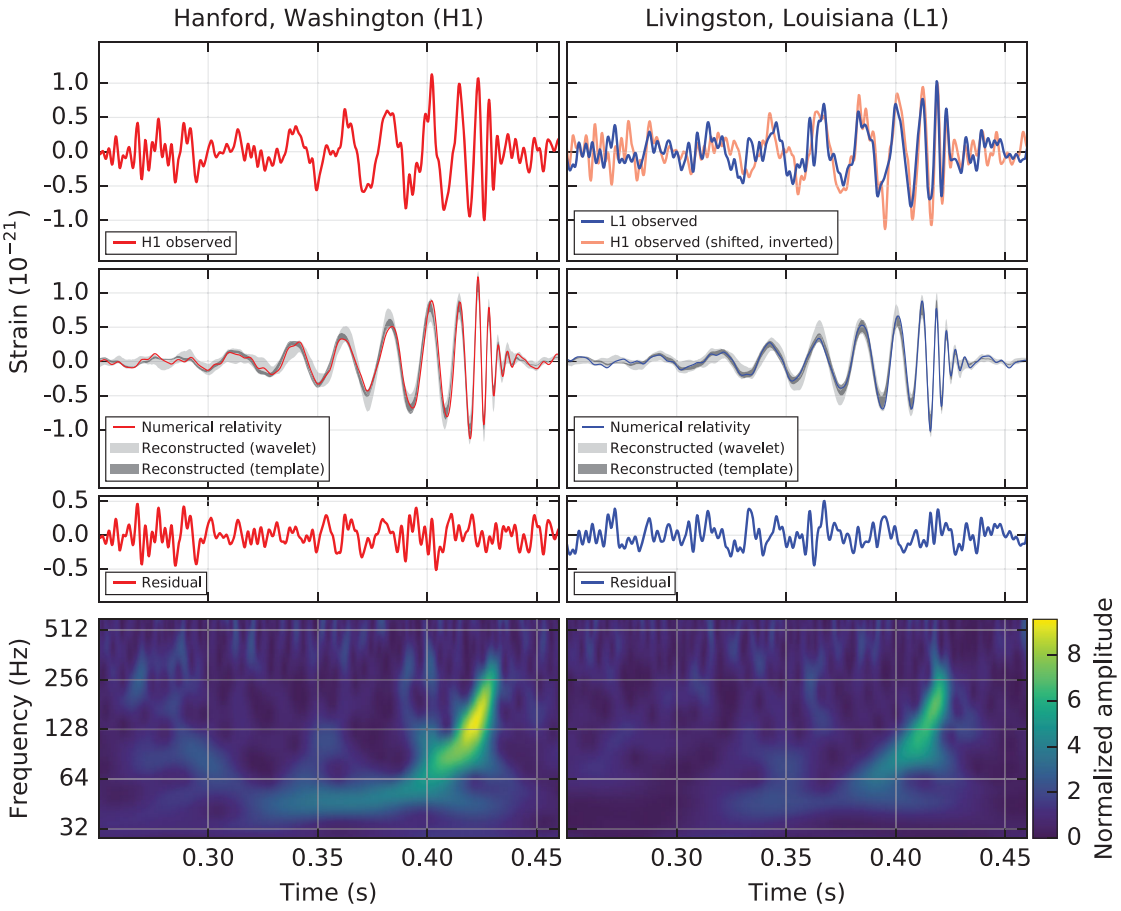

Figure 1.3: Gravitational wave strain data as observed by the LIGO Hanford (left) and LIGO Livingston (right) detectors for the GW150914 event. Figure reproduced from [146]. Top row: measured strain data in the H1 and L1 detectors. Note that the top right also has the H1 signal shifted and inverted to demonstrate the similarity of the waveform. Second row: Best fit strain prediction of a binary black hole merger calculated using numerical relativity. Third row: subtraction of the best fit numerical relativity model from the measured data. The residual structure is consistent with interferometer noise giving confidence to the predictions of extreme general relativity. Bottom row: time-frequency representation of the strain data showing the amplitude of strain frequency as a function of time at H1 (left) and L1 (right).

masses was radiated as gravitational waves, making it the most energetic astrophysical event recorded to date. Despite all that energy the peak gravitational wave strain measured on Earth was only 1×10^{-21}, meaning that the induced length change in the 4 km detector arms was only 4×10^{-18} m — 250 times less than the diameter of a proton. Measuring this was an unprecedented feat of precision measurement that was achieved using state of the art laser based interferometry, which we will discuss later in section 1.2.

Nearly two years later the LIGO and Virgo gravitational wave detectors observed gravitational waves from a binary neutron star merger in the GW170817 event [160]. This event is significant because it was the first time an astrophysical event was detected with both gravitational waves and electromagnetic waves — the first event to be observed with two different kinds of astronomical "messengers" in what is called multi-messenger astronomy. The gravitational wave strain data of the merger, and the subsequent optical spectra over several days are both shown in figure 1.4.

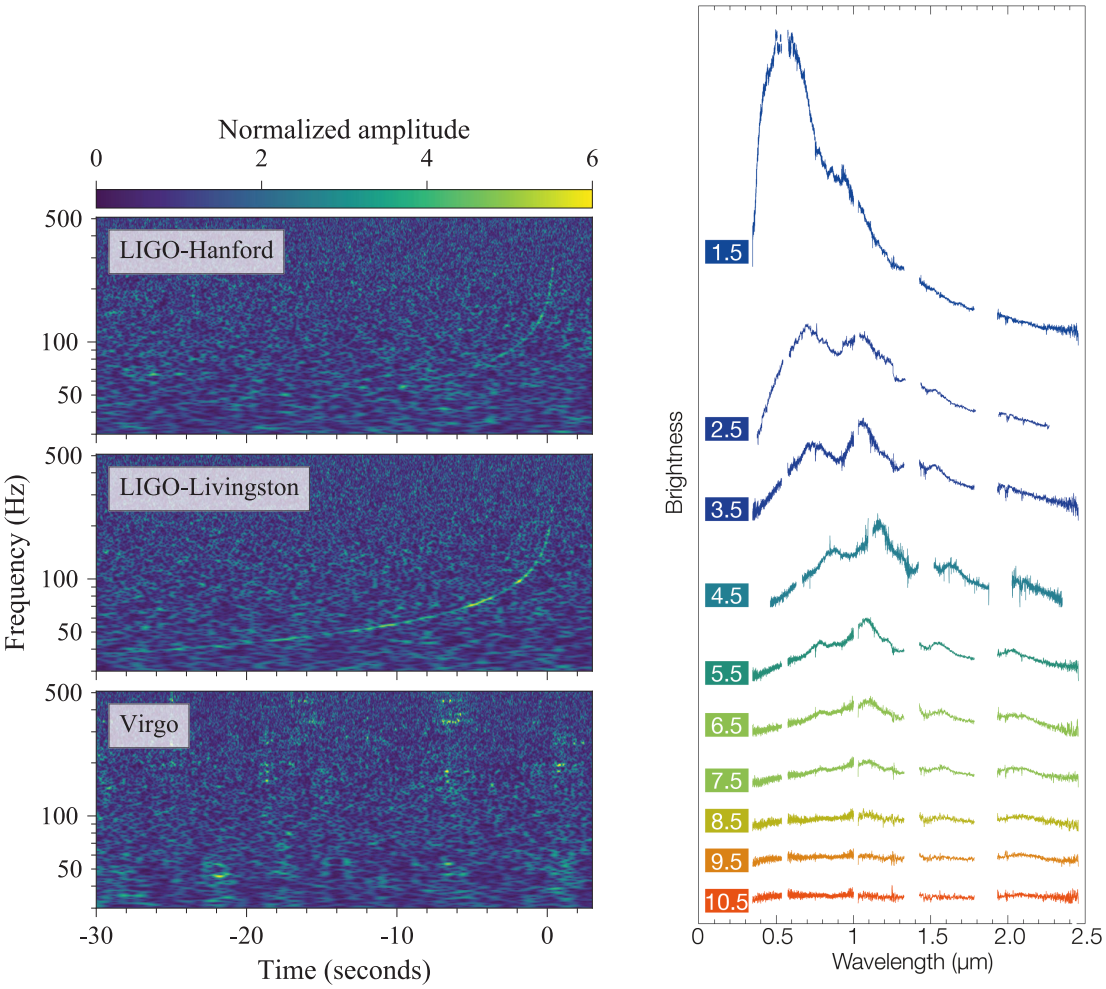

Figure 1.4: Gravitational wave strain time-frequency spectrum as observed by the LIGO Hanford, LIGO Livingston, and Virgo detectors for the GW170817 event (left). Source: [160]. Optical emission spectra evolution over the course of 10.5 days (right). Source: [156].

The sky localization of GW170817 was possible due to a simultaneous measurement by three separate gravitational wave detectors triangulating the signal based on the arrival time and measured amplitude. The Virgo detector contributed to this despite

not measuring any signal during the event because the sky localization was narrowed down by requiring that the signal came from one of the blind spots in Virgo's antenna pattern. This significantly decreased the area of the sky that had to be searched by the optical astronomers and within 11 hours they were able to locate the precise patch of sky to point their telescopes to. The subsequent spectral analysis of the optical observations allowed the elemental composition of the event to be analyzed [164]. Large quantities of elements heavier than iron were detected. This confirmed that neutron star mergers play an important role in producing the heavy elements of the universe [158].

The measured gravitational wave strain from GW170817 played an important role in validating general relativity, placing further constraints and excluding some alternative theories to general relativity. An estimate of the Hubble constant, which quantifies the expansion of the universe was also obtained. For neutron stars tidal effects are expected to have significant contributions to gravitational wave emission. The estimated tidal deformability from GW170817 provided constraints on the neutron star equation of state, which has ruled out some models of dense matter physics [179, 203].

Sources of gravitational waves

We've discussed compact binary inspirals as a source of gravitational wave emission with their characteristic chirp signal as seen in the BH-BH merger in GW150914 and NS-NS merger in GW170817. Signals of that magnitude are infrequent, happening once every couple of years. As GW detectors become more sensitive they will be more sensitive to more distant events. As of time of writing a total of 90 GW events have been detected by the LIGO and Virgo detectors [221]. At some point the event rate will become so high that at any particular moment there will be so many GW events happening simultaneously that it would be difficult if not impossible to separate them out from the sea of signals. That point is referred to as the astrophysical stochastic background of gravitational waves. Anisotropies in the stochastic background could be used to study populations of stellar objects in different regions of the universe [187]. Additionally there is also a cosmological stochastic background of gravitational waves, which is expected to contain information about the early universe much in the same way that the cosmic microwave background (CMB) does for electromagnetic waves [57]. This is interesting because in principle the early universe was not opaque to gravita-

tional waves and so the cosmological GW background could contain information about the universe much closer to inflation than the CMB [173].

Continuous wave (CW) GW signals are continuous single frequency gravitational waves that are emitted by binary systems long before they merge. These signals are generally at frequencies below 10 Hz, outside the LIGO band. A possible source of higher frequency CW gravitational waves are rapidly rotating neutron stars that do not have axial symmetry due to cracks in the star's crust or "mountains" that form on the surface causing the rotation of the star to emit GW [57, 165].

GW burst signals are transients that appear simultaneously in multiple detectors but do not fit any inspiral chirp template. Signals of this type are predicted to come from core collapse supernovae [57]. There are also more exotic sources of GW bursts that are predicted to exist, such as GW from cosmic strings [79].

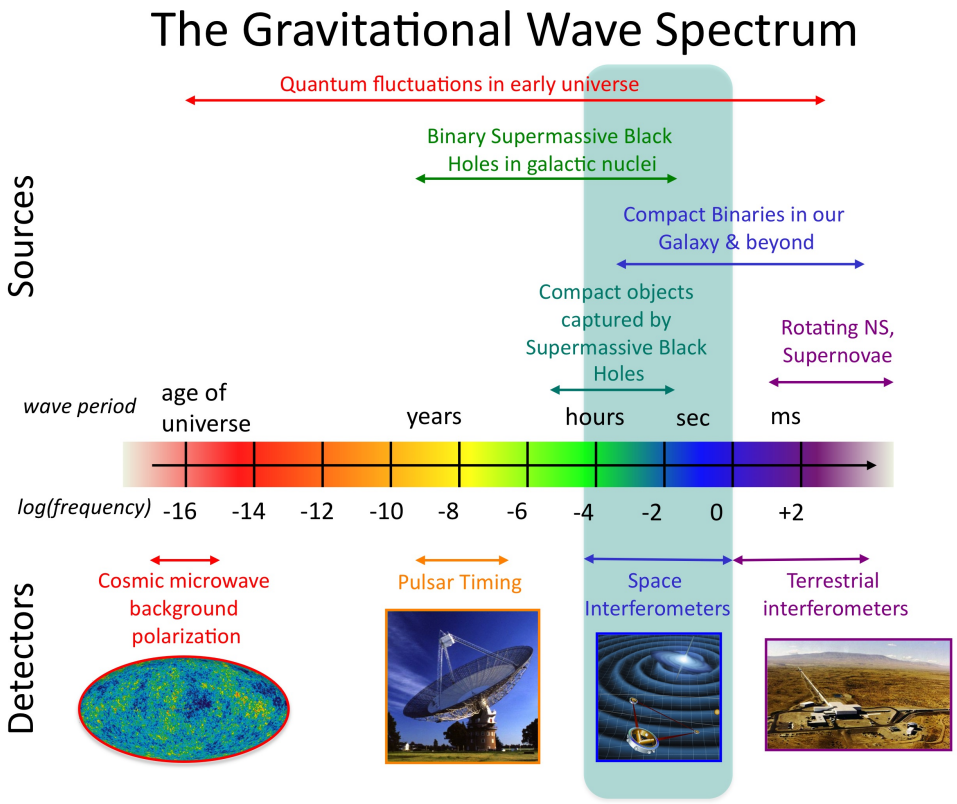

Figure 1.5: Diagram of the gravitational wave frequency spectrum with sources and detectors corresponding to particular frequency ranges. Image source: NASA [116].

Methods of detecting gravitational waves

Gravitational waves can be detected via a number of methods. Ground based interferometers such as LIGO are the focus of this thesis and will be discussed more in-depth in section 1.2. They are sensitive to gravitational waves in the range from several Hz to kHz where it is predicted that most compact binary mergers lie.

Space based interferometers such as the Laser Interferometer Space Antenna (LISA) [64, 105, 155] operate by measuring the time delay between three satellites orbiting the sun. With an arm length of 2.5 million km and a lack of terrestrial noise sources allow the LISA detector to be sensitive to gravitational in the range of 10^{-4} to 10^{-1} Hz [155].

Pulsar timing use the period of rotating neutron stars to study a wide range of astrophysical phenomena. Pulsar timing arrays (PTAs) use sets of extremely well-timed pulsars as a galaxy scale detector with the detector arms extending between Earth and each pulsar in the array [226]. By studying the correlations between the timings in a PTA it should be possible to detect gravitational waves in the range of 10^{-10} to 10^{-6} Hz. This band is of interest for studying inspiralling supermassive binary black holes and cosmic strings [223].

1.2 Detection of gravitational waves using laser interferometry

1.2.1 Michelson interferometer

A Michelson interferometer (shown in figure 1.6) can be used to measure differential arm length change while ignoring any common path length change in the arms. A gravitational wave where the polarization lines up with the Michelson arms induces a purely differential path length change. Noise sources that only couple into common path length change are greatly reduced. This gives the Michelson improved signal to noise for a particular polarization of gravitational waves at the cost of being completely insensitive to the orthogonal polarization where the strain induces zero differential path length change.

A question that is often asked about gravitational wave interferometry is “how is there a

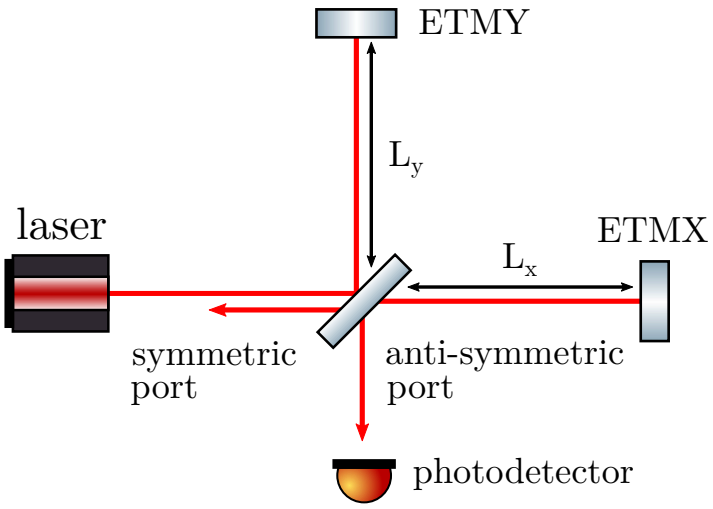

Figure 1.6: A diagram of a Michelson interferometer. By convention in GW interferometry the end mirrors are referred to as the end test masses (ETM). The X and Y arms line up with the h_+ gravitational wave polarization shown in figure 1.2. The $h_\times$ polarization in this case would not produce a signal at the anti-symmetric port.

signal in the detector if a gravitational wave stretches everything including the photons in the detector?". This question has a trivial answer for low frequency gravitational waves: the detector appears stationary from the perspective of a photon travelling from the laser along the Michelson arms to the photodetector at the antisymmetric port. The effect of low frequency gravitational waves on the photons in the detector is negligible and the difference in arm path length is measured as usual. The phase change $\Delta\phi$ in a Michelson under a constant gravitational wave strain h_0 is given by

$$\Delta\phi = \omega_0 \Delta\tau \tag{1.3}$$

$$= \omega_0 \tau h_0 \tag{1.4}$$

where $\omega_0 = 2\pi c/\lambda_0$ where λ_0 is the wavelength of the laser, and $\tau = 2L/c$ is the light travel time in a Michelson with arm length $L = L_x = L_y$.

As the Michelson arms get longer and the time that a photon spends inside the arms increases the overall phase shift that a photon experiences depends on the frequency of the gravitational wave. The change in phase shift that the laser light experiences in a Michelson due to a time dependent gravitational wave strain $h(t)$ is given by

$$\Delta\phi = \omega_0 \int_{t_0-\tau}^{t_0} h(t) dt \tag{1.5}$$

where t_0 is the time at which we measure the signal at the antisymmetric port. Note that if the frequency of the gravitational wave is negligible $h(t) \approx h_0$ then the we get back $\Delta\phi = \omega_0 \tau h_0$ as before. Now we assume that the gravitational wave is a continuous wave at angular frequency ω_{gw} so the strain is

$$h(t) = h_0 \sin\left(\omega_{gw} t + \varphi_{gw}\right) \tag{1.6}$$

where h_0 is the amplitude, and φ_{gw} is an arbitrary phase shift of the gravitational wave corresponding to some initial condition. The accumulated phase change in the Michelson under a continuous gravitational wave is then

$$\Delta\phi = \omega_0 h_0 \int_{t_0-\tau}^{t_0} \sin\left(\omega_{gw} t + \varphi_{gw}\right) dt \tag{1.7}$$

$$= \frac{\omega_0 h_0}{\omega_{gw}} \left(\cos\left(\omega_{gw}(t_0 - \tau) + \varphi_{gw}\right) - \cos\left(\omega_{gw} t_0 + \varphi_{gw}\right)\right) \tag{1.8}$$

using $\cos(a) - \cos(b) = -2\sin(\frac{a-b}{2})\sin(\frac{a+b}{2})$ and simplifying we get

$$\Delta\phi = \frac{2\omega_0 h_0}{\omega_{gw}} \sin\left(\frac{\omega_{gw}\tau}{2}\right) \sin\left(\omega_{gw} t_0 - \frac{\omega_{gw}\tau + \varphi_{gw}}{2}\right) \tag{1.9}$$

which is just a sinusoidal signal in t_0 of the form

$$\Delta\phi = a_0 \sin\left(\omega_{gw} t_0 + \varphi_0\right) \tag{1.10}$$

where the amplitude and phase are

$$a_0 = \frac{2\omega_0 h_0}{\omega_{gw}} \sin\left(\frac{\omega_{gw}\tau}{2}\right) \tag{1.11}$$

$$\varphi_0 = -\frac{\omega_{gw}\tau + \varphi_{gw}}{2} \tag{1.12}$$

A plot of Michelson signal amplitude a_0 as a function of gravitational wave frequency is shown in figure 1.7. The response of Michelson is essentially flat at lower frequencies with the DC level set by $2\omega_0 L/c$. This means that we can improve the sensitivity of the detector by using longer arms. At some point when the gravitational wave frequency is high enough the response begins to decline. This turnover point can be characterized by the first frequency where the Michelson has no response to the gravitational wave.

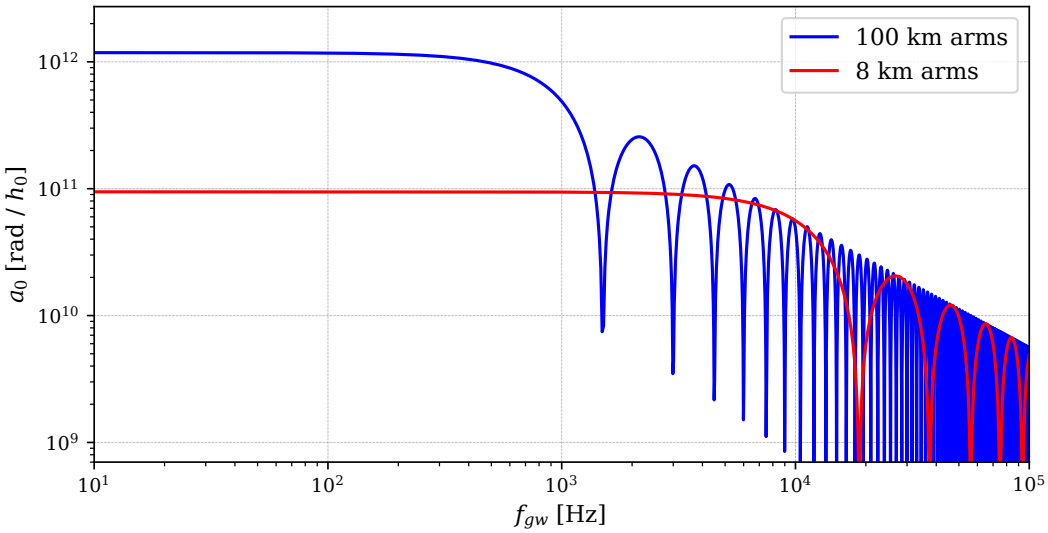

Figure 1.7: Strain amplitude response of a Michelson interferometer with 8 km, and 100 km arm lengths using a 1064 nm laser wavelength.

This happens when the photon travel time coincides with a full period of a gravitational wave. The GW frequencies where this happens are at

$$f_{\text{null}} = \frac{N}{\tau} \tag{1.13}$$

$$= \frac{Nc}{2L} \tag{1.14}$$

where N is any positive integer. These frequencies are shown as the sharp dips in interferometer response in figure 1.7, which goes to exactly zero at those frequencies. The choice of interferometer arm length is then a tradeoff between low and high frequency sensitivity.

Modifications to the Michelson design allow for overall improvements to performance and a greater degree of control over the tradeoff between low and high frequency sensitivity. The culmination of these modifications is the dual recycled Fabry-Perot Michelson interferometer.

1.2.2 Dual recycled Fabry-Perot Michelson interferometer

Current state of the art gravitational wave detectors are dual recycled Fabry-Perot Michelson interferometers. Interferometer design for gravitational wave detection has evolved since the 70's and here we will briefly sketch the development outline. In 1972 Rainer Weiss at Massachusetts Institute of Technology (MIT) did the first detailed noise

study for a gravitational wave detector using Herriot delay lines in the Michelson arms in order to reduce the length of the vacuum tubes [28]. It was found by the Glasgow and Garching groups that incoherent scattering of light from the delay line mirrors caused excessive readout noise [38, 53]. In 1981 Ronald Drever et al. at University of Glasgow and California Institute of Technology (Caltech) proposed to replace the Herriot delay lines with Fabry-Perot cavities [38], where the beam would be confined to a single path inside the arms and hence could use smaller mirrors for a given beam size.

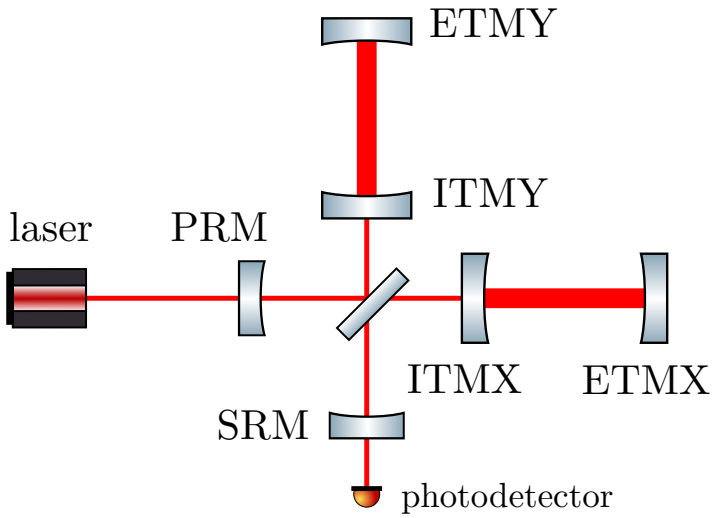

Figure 1.8: Diagram of a dual recycled Fabry-Perot Michelson interferometer (DRFPMI). By convention in GW interferometry the input and end mirror in the Fabry-Perot arm cavities are referred to as the input test mass (ITM) and end test mass (ETM) respectively. The two recycling mirrors in the symmetric and anti-symmetric port are the power recycling (PRM) and signal recycling (SRM) mirrors respectively.

The decision to use Fabry-Perot arms necessitated the stabilization of the laser frequency to a reference cavity. This resulted in the development of the Pound-Drever-Hall locking technique for laser frequency stabilization, published by Drever et al. in 1983 [41], which is now used extensively in precision optical experiments. In 1983 Drever et al. proposed the introduction of a mirror in the symmetric port of the Michelson to increase circulating power and reduce shot noise [40] in a configuration which is now referred to as the power recycled Fabry-Perot Michelson interferometer (PRFPMI).

In 1989 Brian Meers et al. from the University of Glasgow proposed the addition of a mirror to the anti-symmetric port of a PRFPMI in order to shape the frequency response of the detector to optimize it for particular gravitational wave signals [52,

56]. In 1993 Jun Mizuno et al. proposed an alternative to signal recycling where the reflectivity, separation, and tuning of the mirror in the anti-symmetric port is chosen such that the gravitational wave signal is extracted out of the arm cavities faster [61]. This technique is called signal extraction, or resonant sideband extraction (RSE). It decreased the need for power recycling by allowing higher finesse arm cavities to be used to increase arm circulating power. This decreases the power incident on the beamsplitter, which reduces the thermal distortion inside the beamsplitter.

The combination of either signal recycling or signal extraction together with power recycling came to be known as the dual recycled Fabry-Perot Michelson interferometer (DRFPMI), which is shown in figure 1.8. The base DRFPMI design is currently used in most GW interferometers such as LIGO, and Virgo.

1.2.3 The LIGO interferometer

Initial LIGO (iLIGO) began construction in 1992 with the base design being a PRFPMI with an RF readout scheme [58, 227]. In 2006 the enhanced LIGO (eLIGO) upgrade was proposed [102, 107], which switched the RF readout to a DC readout to reduce the coupling from several technical noise sources. It also introduced the output mode cleaner (OMC) to reduce shot noise by removing most of the light that does not contribute to the GW signal. The next major upgrade was Advanced LIGO (aLIGO), which began installation in 2011 [135]. The addition of signal recycling and increased laser power necessitated the redesign of most of the core optics. The recycling cavities were redesigned from marginally stable to geometrically stable by folding the cavities with curved mirrors [104]. This meant that the recycling cavities had a well defined fundamental mode and the detector sensitivity was less susceptible to mirror imperfections [135]. By the time of aLIGO's third observation run (O3) both LIGO detectors were operating with broadband squeezing to reduce shot noise below the standard quantum limit, a description of this was reported in 2019 [192].

At the time of writing LIGO is in between O3 and O4. A comprehensive and up to date review of current aLIGO sensitivity and noise analysis can be found in [218]. The current detector is aLIGO with broadband squeezing which is shown in figure 1.9. The next planned major upgrade is aLIGO+, aka A+, which is the change of broadband to frequency dependent squeezing via a filter cavity [134, 176, 207]. After aLIGO+

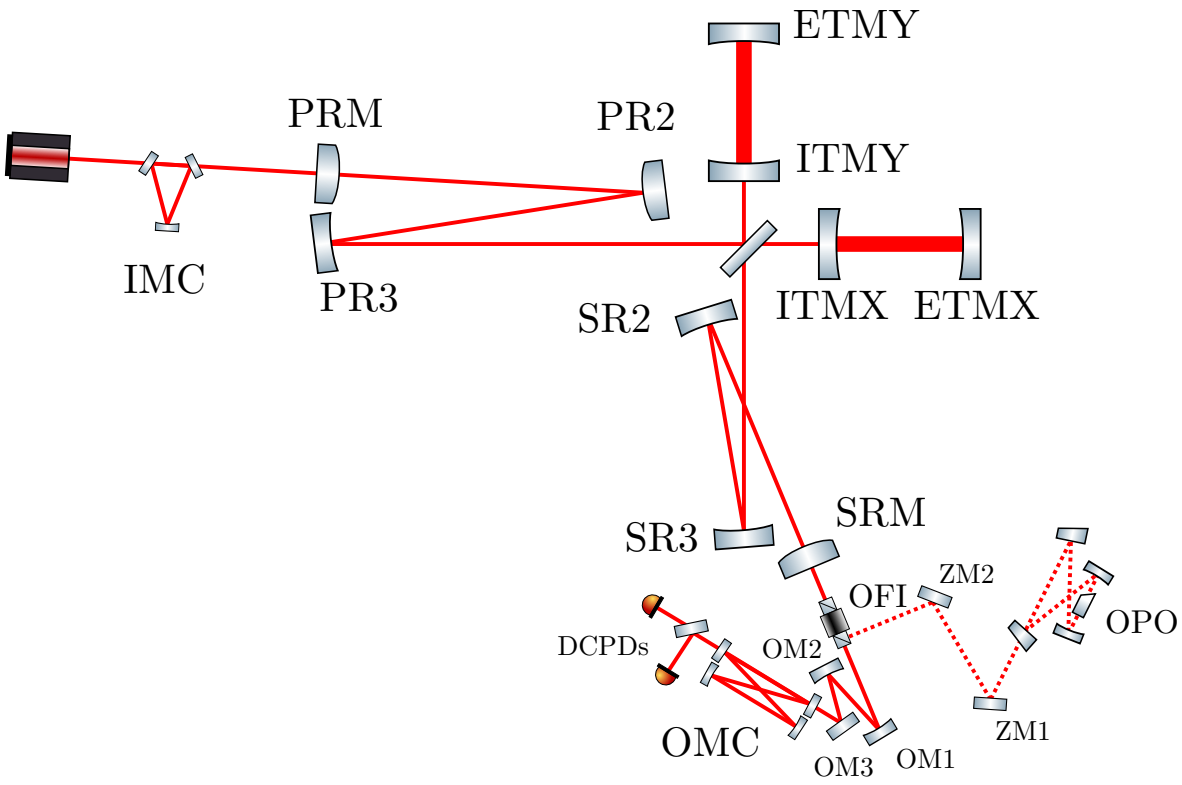

Figure 1.9: A simplified diagram of the current optical layout of aLIGO.

a proposed major upgrade is LIGO Voyager, which plans to replace fused silica test masses with cryogenic silicon at 123 K in order to mitigate thermo-elastic noise [195]. This will necessitate a change in the laser wavelength to somewhere in the 1.5-2 μm range because silicon is opaque to the current 1 μm wavelength.

The significance of GW170817 has shown that there is a compelling science case for more detailed studies of neutron star mergers using gravitational waves. This will require construction of new gravitational wave detectors that are sensitive to higher frequencies in the kilohertz region where it is expected that neutron star postmerger remnants produce gravitational waves [215]. These detectors, which include the upcoming Cosmic Explorer [151, 208, 222] (CE) in the USA, and Einstein Telescope [111] (ET) in Europe are referred to as the third generation (3G) of gravitational wave detectors. To get improved sky localization with 3G detectors it is important for at least one detector to be located in the southern hemisphere [215]. An Australian based detector currently referred to as the Neutron star Extreme Matter Observatory [194] (NEMO) has been proposed, which is aiming to have sensitivity comparable with CE and ET at frequencies around 2 kHz.

The predicted strain sensitivity of all of these upgrades, NEMO, and CE is shown in figure 1.10.

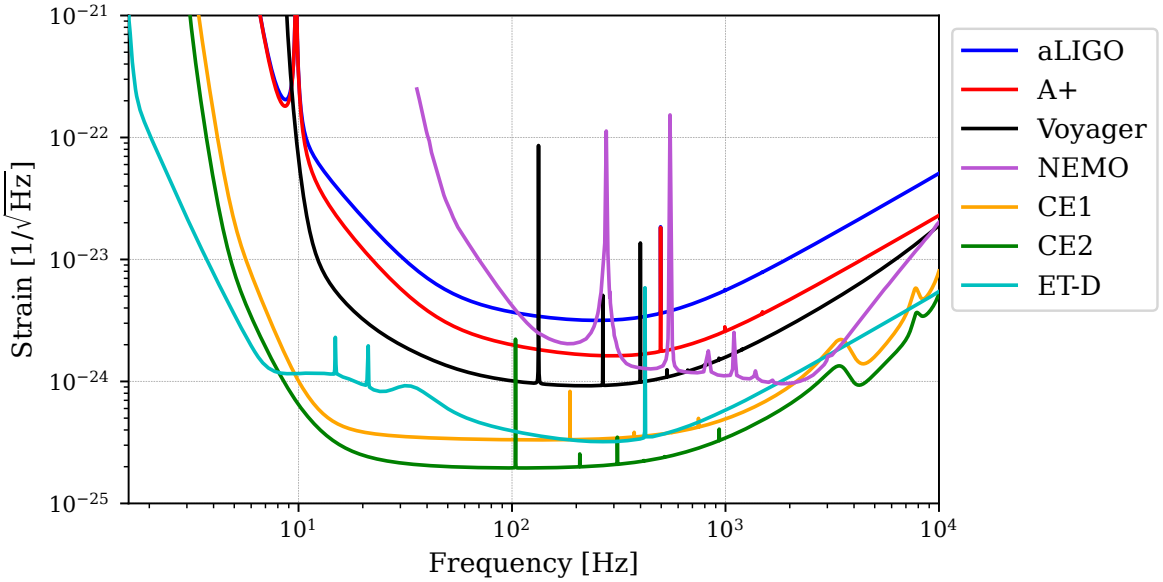

Figure 1.10: The predicted strain sensitivity of aLIGO and its proposed upgrades, NEMO, CE, and ET. The LIGO data was generated using the design parameters from the pygwinc [209] package. NEMO sensitivity data was taken from [194]. Einstein Telescope (ET) sensitivity data was taken from [112].

1.3 Thesis outline

In this thesis we present a new mode matching sensing schemes for the adaptive mode matching actuators planned for aLIGO+ [186, 202] and new optical modelling techniques for simulating detailed scattering effects in coupled cavity interferometers. We believe these will be important in the short term for reaching aLIGO+ design sensitivity, and far into the future where mode matching and optical modelling will play an important role in gravitational wave interferometry and precision optical measurements.

Chapter 2 will review current modelling techniques using Hermite-Gauss (HG) modes and ABCD matrices. It will establish the concept of a HG basis, which is extremely useful when studying mode matching and is used extensively in chapter 6. The relationship between ABCD matrices and HG basis transformations is established, which is required to connect HG modes to the Linear Canonical Transform (LCT) propagation in chapter 3.

Chapter 3 introduces the LCT as an optical modelling tool. It reviews the established applications of using the LCT as a paraxial diffraction integral through an arbitrary ABCD system. A new application of the LCT for solving steady state circulating fields in optical cavities is presented, which is used to model the aLIGO arm cavity loss due to a point absorption defect on the ITM. This work was published in A. A. Ciobanu, D. D. Brown, P. J. Veitch, and D. J. Ottaway. "Modeling circulating cavity fields using the discrete linear canonical transform". In: *Journal of the Optical Society of America A* 38.9 (Sept. 1, 2021). Number: 9, p. 1293. ISSN: 1084-7529, 1520-8532. DOI: 10.1364/JOSAA.433575.

Chapter 4 expands on the LCT model presented in chapter 3 towards modelling coupled cavities such as the dual recycled Fabry-Perot Michelson (DRFPMI). It introduces a formal method of simplifying operator algebra following an established matrix signal flow graph reduction procedure by representing an optical system as a directed cyclic graph. This allows one to write down a generalized notion of a round trip inside an arbitrarily complex coupled cavity, which is necessary for solving the circulating field in these systems.

Chapter 5 presents my commissioning work at the LIGO Hanford detectors during 2018 and 2019. An analysis is presented of the astigmatism present in the output mode cleaner (OMC) that was measured using cavity length scans. It presents a procedure for measuring the transverse mode splitting inside the OMC using OMC cavity length scans and compares to previous results. An analysis of the SR3 rear heater's ability to correct mode mismatch was performed and compared to experimental results.

Chapter 6 introduces a fast radio-frequency (RF) mode matching error signal using second order HG modes. This works because there is an equivalence between the addition of second order HG modes and a change of HG basis, which determines mode matching. This mode matching error signal is simple, not requiring any Gouy phase telescopes and only needing single element photodetectors. An experimental tabletop demonstration of the mode matching error signal is presented where it was able to increase the mode matching of a laser beam to a cavity to 99.9%. This work was published in A. A. Ciobanu, D. D. Brown, P. J. Veitch, and D. J. Ottaway. "Mode matching error signals using radio-frequency beam shape modulation". In: *Applied*

Optics 59.31 (Nov. 1, 2020). Number: 31, p. 9884. ISSN: 1559-128X, 2155-3165. DOI: 10.1364/AO.404646.

Chapter 7 is the conclusion and recaps each chapter while giving an outlook for future research.

Chapter 2

Modelling optical transverse fields

Models are required to make predictions about the behavior of any physical system and optical systems are no different. The fundamental phenomenon that optical models are concerned with is the propagation of light, which is completely described by Maxwell's equations in the classical limit. Despite it being a "solved" problem the direct application of Maxwell's equations is not practical for most optical models, and so approximations are introduced. The most common of these approximations is the paraxial or small-angle approximation, followed by the scalar field approximation. Two popular models arise from the scalar paraxial approximation: the Fresnel diffraction integral and Hermite-Gauss (HG) modes. In chapter 6 we use the HG modes to model a mode matching error signal generated in a tabletop experimental setup. The paraxial diffraction integral approach when combined with paraxial focusing elements forms the Linear Canonical Transform (LCT); a powerful framework capable of efficiently tackling a wide array of optical models. We discuss the application of the LCT in modelling resonant optical systems with hard aperture and point defects in chapters 3 and 4.

In GW modelling the optical models one often works with in practice often fall into two distinct categories, modal and grid based. Grid based models work with the electric field discretely sampled on a grid with propagations given by discrete approximations of diffraction integrals. This style of modelling in GW interferometers has been first developed by Vinet [59] and has seen extensive usage in Virgo [87]. One of the popular grid based optical GW interferometer modelling tools that is currently being used is

SIS [106, 212].

Modal models work representing the electric field as a sum of orthonormal modes, typically the Hermite-Gauss (HG), or Laguerre-Gauss (LG) modes. Currently, some of the popular modal based GW interferometer optical modelling tools are Melody [73, 90], Optickle2 [142, 143], Finesse2 [93, 123, 127, 200]. In writing this thesis we have used Finesse2 and the upcoming Finesse3, and occasionally used SIS for reference.

In this chapter we draw our attention to HG modes, which are a complete and orthonormal set of functions that solve the paraxial wave equation. We use this chapter to set the stage for discussing the mode matching error signal presented in chapter 6, and the work on the linear canonical transform in chapters 3 and 4. This should be review for people familiar with HG modes interspersed with discussion. The discussion is kept brief, delegating a large portion of interesting but not strictly necessary topics to the appendix. This chapter does not present any new results but does allude to them, with the aim being that the new results presented in chapters 3, 4 and 6 and their significance are made clearer with this chapter.

2.1 Hermite-Gauss modes

The HG modes are solutions to the paraxial wave equation, specifically each HG mode is a valid solution to the paraxial wave equation. For a 1D HG mode of order n and wavelength λ propagating along the z axis, the amplitude distribution across a transverse axis x is given by

$$u_n[x, q, \lambda] = \left(\frac{2}{\lambda z_R}\right)^{1/4} \left(\frac{\mathrm{i} z_R}{2^n n! q}\right)^{1/2} \left(\frac{-q^*}{q}\right)^{n/2} H_n\left[\frac{x\sqrt{2}}{w[q,\lambda]}\right] \exp\left[\frac{-\mathrm{i}\pi x^2}{\lambda q}\right] \tag{2.1}$$

where q is the Gaussian beam parameter or simply the q-parameter

$$q = z + \mathrm{i} z_R \tag{2.2}$$

where z is the distance from the waist and z_R is the Rayleigh range, which is the distance distance from the waist where the beam size increases by a factor of $\sqrt{2}$. The

Rayleigh range can be defined in terms of the beam waist size w_0 with

$$z_R = \frac{\pi w_0^2}{\lambda} \tag{2.3}$$

In general the beam size $w[q, \lambda]$ is given by

$$w[q, \lambda] = \sqrt{\frac{\lambda |q|^2}{\pi z_R}} \tag{2.4}$$

The Hermite polynomials $H_n[x]$ can be recursively defined using

$$H_{n+1}[x] = 2xH_n[x] - 2nH_{n-1}[x] \tag{2.5}$$

with the base cases being

$$H_0[x] = 1 \tag{2.6}$$

$$H_1[x] = 2x \tag{2.7}$$

The amplitude distribution of a 2D HG mode is separable in x and y and so can be obtained by taking the outer product of two 1D HG amplitude distributions

$$U_{nm}[x, y, q_x, q_y, \lambda] = u_n[x, q_x, \lambda] u_m[y, q_y, \lambda] \tag{2.8}$$

For brevity we may sometimes omit λ from the list of arguments where in most contexts λ is constant. Additionally we may sometimes only specify a single q-parameter to the 2D U_{nm} distribution. In that case it is implied both q-parameters are equal $q = q_x = q_y$.

The definition of the HG modes in optics can be traced back to Kogelnik in 1966 [18], but this was missing normalization and Gouy phase which can be found in later work by Siegman [50]. Equation (2.1) was reproduced from Siegman [50] equation 16.54. A diagram of the amplitude distribution of the first couple of HG modes is shown in figure 2.1.

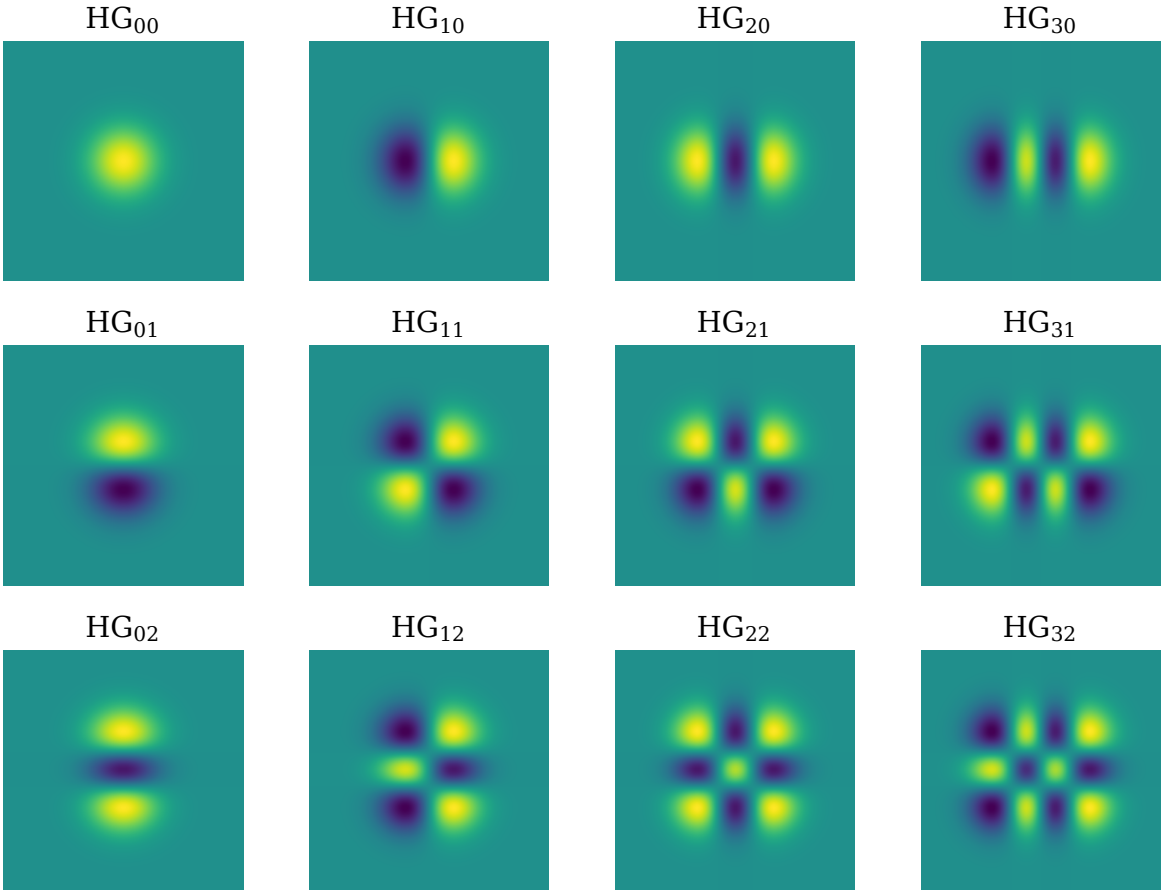

Figure 2.1: Amplitude distributions U_{nm} of the first couple of HG modes. The beam is taken to be at the waist and so the amplitude is purely real. In this colormap yellow is positive amplitude and blue is negative amplitude.

2.1.1 Complete orthonormal set

The 1D and 2D HG modes form a complete orthonormal basis set over the space of all possible square-integrable functions. What this means is that any arbitrary amplitude distribution can be described as a sum of (potentially an infinite number of) HG modes. To find an HG mode coefficient of a particular arbitrary amplitude distribution $E[x, y]$ we can perform the following overlap integral

$$a_{nm}[q_x, q_y] = \iint_{-\infty}^{\infty} E[x, y] U^*_{nm}[x, y, q_x, q_y] dy dx \tag{2.9}$$

In principle to completely describe an arbitrary amplitude $E[x, y]$ with HG modes we would have to perform the integral in equation (2.9) over all possible n and m, which is countably infinite. In practice however only a small number of modes can be used to accurately approximate most amplitude distributions one would work with in practice.

This is because of another property of HG modes; that they are the eigenmodes of optical resonators with spherical mirrors, which we will discuss later.

Often the q-parameter dependence is dropped from the mode amplitudes a_{nm} in equation (2.9). We will also do so but have chosen to include it here to highlight an important point about the nature of HG modes: that they are not unique. For any pair of mode indices (n, m) there is an uncountably infinite number of beams that are described by that HG mode, which differ only by their q-parameters (q_x, q_y). Put another way we can use any pair of q-parameters (q_x, q_y) to decompose an arbitrary amplitude distribution $E[x, y]$ into HG modes using equation (2.9). We choose to call the degree of freedom corresponding to the choice of q-parameters (q_x, q_y) the *basis* of a set of HG modes, or the HG basis. For now will consider HG mode amplitudes in a fixed, but arbitrary choice of HG basis. We will discuss later, ways to make an informed choice of q-parameters (q_x, q_y).

The orthonormality of HG modes means that modes with different mode indices do not interfere or produce any optical beat, provided the modes are all in the same HG basis. Orthonormality can be formally stated as that the HG modes satisfy the following equation

$$\int_{-\infty}^{\infty} u_n[x, q] u_m^*[x, q] dx = \delta_{nm} \tag{2.10}$$

where the Kronecker delta $\delta_{nm} = 1$ if $n = m$ and is otherwise equal to zero. This result trivially generalizes to 2D using the outer product definition in equation (2.8). Orthonormality proves very convenient when calculating the power in a beam. Consider a 1D beam consisting of two mode amplitudes (a_0, a_2).

$$E[x] = a_0 u_0[x] + a_2 u_2[x] \tag{2.11}$$

The power is given by the integral of the intensity distribution

$$P = \int_{-\infty}^{\infty} I[x]dx \tag{2.12}$$
$$= \int_{-\infty}^{\infty} E[x]E^*[x]dx \tag{2.13}$$
$$= \int_{-\infty}^{\infty} \left(|a_0 u_0[x]|^2 + |a_2 u_2[x]|^2 + a_0 a_2^* u_0[x]u_2^*[x] + a_0^* a_2 u_0^*[x]u_2[x]\right) dx \tag{2.14}$$

due to the orthonormality property in equation (2.10) the terms with $u_0[x]u_2^*[x]$ and $u_0^*[x]u_2[x]$ both integrate to zero and so we can drop them

$$P = \int_{-\infty}^{\infty} \left(|a_0 u_0[x]|^2 + |a_2 u_2[x]|^2\right) dx \tag{2.15}$$
$$= \int_{-\infty}^{\infty} |a_0 u_0[x]|^2 dx + \int_{-\infty}^{\infty} |a_2 u_2[x]|^2 dx \tag{2.16}$$
$$= |a_0|^2 \int_{-\infty}^{\infty} |u_0[x]|^2 dx + |a_2|^2 \int_{-\infty}^{\infty} |u_2[x]|^2 dx \tag{2.17}$$

and by the orthonormality property again in equation (2.10) we know that both integrals evaluate to 1 and so we simplify further to

$$P = |a_0|^2 + |a_2|^2 \tag{2.18}$$

which is just the sum of the mode amplitudes squared. This result generalizes to all modes and the general expression for the power of a beam described by HG mode amplitudes is given by

$$P = \sum_n |a_n|^2 \tag{2.19}$$

and similarly in 2D

$$P = \sum_n \sum_m |a_{nm}|^2 \tag{2.20}$$

The HG modes provide a convenient way of computing the power of a beam and much more importantly each mode has a well defined power that does not depend on other modes. This would not be the case if the HG modes were not orthogonal, which is the case when working with eigenmodes of unstable resonators.

2.1.2 Solution of the paraxial wave equation

HG modes are a solution to the paraxial wave equation. An important consequence is that the HG modes in equation (2.8) describe the field across all of 3D space and not just a single plane. To highlight just how useful this is consider the alternative where we do not use HG modes. Begin by considering an arbitrary electric field distribution $E[x, y]$ specified for a particular plane at $z = z_0$. To get the field at any other plane we have to use the paraxial wave equation either directly or indirectly. For now we consider using the paraxial wave equation directly, which tells us that the field at an adjacent plane at an infinitesimal distance ε_z is

$$E[x, y, z_0 + \varepsilon_z] = \left(1 + \frac{\varepsilon_z}{2ik}\left(\partial_x^2 + \partial_y^2\right)\right) E[x, y, z_0] \tag{2.21}$$

To propagate the electric field to a noninfinitesimal distance we then have a number of options. The first is to approximate the infinitesimal step ε_z as small but non-infinitesimal and simply repeatedly apply equation (2.21) to propagate the field to the desired plane. Alternatively, one could construct a noninfitesimal propagator directly from an infinitesimal one by solving for the propagator in the paraxial wave equation as a matrix exponential. This method is not new but is unconventional in optics. It is the same standard method for solving for the time evolution operator in the Schrodinger equation. For readers who are interested we present a derivation in appendix A.3.2. And last but not least one could use the Green's function of the scalar paraxial wave equation to construct a diffraction integral. This diffraction integral is then exactly the Fresnel diffraction integral which can be found in most optics textbooks and is also given in equation (A.32).

We can however sidestep having to worry about any of this by performing an HG mode decomposition of the field $E[x, y, z_0]$ at a single plane using equation (2.9). The field at any other plane is then given by rearranging equation (2.9) and summing over all of the modes

$$E[x, y, z_0 + z] = \sum_n \sum_m a_{nm}[q_x, q_y] U_{nm}[x, y, q_x + z, q_y + z] \tag{2.22}$$

Note that the mode coefficients a_{nm} do not depend on the propagation distance z, only

the HG basis that was used to decompose the field $E[x, y, z_0]$. This is a bit bizarre when compared to the previous propagation methods where it seems like with HG modes we do not have to do any work. The answer is already there. Just multiply the HG functions at another plane by the same mode amplitudes and that is what the field is at that plane. The reason this works is that the HG functions are the solutions to the scalar paraxial wave equation.

On a closer inspection we find that the work that we would have had to do to propagate the field has gone instead into computing the HG mode coefficients. One can see this by considering a field distribution with a sharp edge, such as a field right after interacting with an aperture. In that case the amount of work we have to put into computing the HG mode coefficients is similar if not more than the work we would have done using the other propagation methods. We can gain back some computational performance by neglecting to compute mode amplitudes that are sufficiently small, but then we are back to approximating the propagation. When our field is accurately described by a small number of HG modes computing the HG decomposition is cheap, which is the best case for an HG modal model. Fortunately it is often the case that the fields we work with in practice are described by a small number of HG modes because the HG modes are eigenmodes of geometrically stable optical cavities.

2.1.3 Eigenmodes of a cavity with spherical mirrors

The laser beams that one often interacts with, especially in high precision optical measurements tend to be predominantly very pure Gaussian beams. This is because pure HG_{00} beams are one of the simplest beams to create. One of the best ways to generate high quality beams is by spatially filtering a beam with a resonant geometrically stable optical cavity with spherical mirrors. This is because the eigenmodes of geometrically stable optical cavities with spherical mirrors are precisely the HG modes defined in equation (2.1). To prove this we first consider a cavity comprised of two mirrors separated by a space.

First we will prove that each component of the cavity (in this case free space and reflection off of a mirror) when acting on an HG mode can be thought of as changing the basis of that HG mode. For free space this is trivial since we know that the HG modes are defined to be solutions to the paraxial wave equation and that propagation

of an HG mode is equivalent to changing the real part of the mode's q-parameter, which is a change of basis. The change of basis under a free space propagation of length z is simply given by

$$q_2 = q_1 + z \tag{2.23}$$

For mirror reflection we consider a spherical mirror of radius R_c. Under the paraxial approximation we approximate it as a thin phase plate that applies a quadratic transverse phase.

$$m[x, y] = \exp\left[\frac{i\pi}{\lambda}\frac{2(x^2 + y^2)}{R_c}\right] \tag{2.24}$$

we note that this thin phase plate is separable in to two 1D components in the following way

$$m[x] = \exp\left[\frac{i\pi}{\lambda}\frac{2x^2}{R_c}\right] \tag{2.25}$$

with the original 2D phase plate given by the outer product

$$m[x, y] = m[x]m[y] \tag{2.26}$$

For simplicity we neglect any parity transformations that are produced by a mirror reflection since they do not effect HG basis of the eigenmodes. Because both mirrors and HG modes are separable we will consider a 1D mirror acting on a 1D HG mode. An HG mode after being reflected by the mirror is given by

$$m[x]u_n[x, q_1] = H_n\left[\frac{x\sqrt{2}}{w[q_1]}\right]\exp\left[\frac{\mathrm{i}\pi}{\lambda}\frac{2x^2}{R_c}\right]\exp\left[\frac{-\mathrm{i}\pi x^2}{\lambda q_1}\right] \tag{2.27}$$

$$= H_n\left[\frac{x\sqrt{2}}{w[q_1]}\right]\exp\left[-\frac{\mathrm{i}\pi}{\lambda}\left(\frac{x^2}{q_1} - \frac{2x^2}{R_c}\right)\right] \tag{2.28}$$

$$= H_n\left[\frac{x\sqrt{2}}{w[q_1]}\right]\exp\left[-\frac{\mathrm{i}\pi}{\lambda}\left(\frac{x^2(R_c - 2q_1)}{q_1 R_c}\right)\right] \tag{2.29}$$

We can identify the new basis q_2 as $q_2 = q_1 R_c/(R_c - 2q_1)$. Making that substitution

leaves us with

$$m[x]u_n[x,q_1] = H_n\left[\frac{x\sqrt{2}}{w[q_1]}\right]\exp\left[-\frac{\mathrm{i}\pi x^2}{\lambda q_2}\right] \tag{2.30}$$

There is still the issue that the Hermite polynomial is still scaled by the beam size from the old basis q_1 so we do not yet have a proper change of basis transformation. This turns out to not be a problem since the beam size function $w[q]$ gives the same result for both q_1 and q_2 when reflecting from a mirror. This can be physically intuited by noting that on reflection the beam does not travel any distance and so it has to be the same size as it was before the reflection, but we can also show this is also true strictly from the algebra. To make the algebra simpler we will use an alternate, but equivalent definition of the q-parameter in terms of its reciprocal

$$\frac{1}{q} = \frac{1}{B} - \frac{\mathrm{i}\lambda}{\pi w^2} \tag{2.31}$$

where we can read off a definition of the beam size w as

$$w[q] = \sqrt{\frac{-\pi}{\lambda}\mathrm{Im}\left[\frac{1}{q}\right]} \tag{2.32}$$

which implies that $w[q_1] = w[q_2]$ if the imaginary parts $\mathrm{Im}\left[\frac{1}{q_1}\right] = \mathrm{Im}\left[\frac{1}{q_2}\right]$ are equal. This is not difficult to show

$$\begin{aligned}
\mathrm{Im}\left[\frac{1}{q_2}\right] &= \mathrm{Im}\left[\frac{R-2q_1}{q_1R}\right] && (2.33)\\
&= \mathrm{Im}\left[\frac{R}{q_1R} - \frac{2q_1}{q_1R}\right] && (2.34)\\
&= \mathrm{Im}\left[\frac{1}{q_1} - \frac{2}{R}\right] && (2.35)\\
&= \mathrm{Im}\left[\frac{1}{q_1}\right] - \mathrm{Im}\left[\frac{2}{R}\right] && (2.36)
\end{aligned}$$

The mirror radius of curvature R is purely real so the imaginary part of its reciprocal is zero and so we arrive at $\mathrm{Im}\left[\frac{1}{q_1}\right] = \mathrm{Im}\left[\frac{1}{q_2}\right]$ as required. This completes the proof that spherical mirrors act on HG modes by changing their basis.

We have shown that 1D HG modes are transformed by free space and reflection off of

a mirror by a basis change of q-parameters. This result generalizes to 2D HG modes due to it being separable into an outer product of 1D HG modes using equation (2.8). To show that the HG modes are the eigenmodes of an optical cavity we now seek a sequence of basis change transformations such that completing a single round trip in the cavity results in the same HG basis. The sequence of transformations for a two mirror resonator are as follows

- Free space propagation of length d
- Mirror reflection with radius of curvature R_2
- Free space propagation of length d
- Mirror reflection with radius of curvature R_1

The starting point of these transformations is arbitrary and so their ordering is only determined up to a cyclic permutation. All cyclic permutations should yield equivalent results and so we will continue with this ordering. Starting with q_1 the sequence of basis changes is then

$$q_2 = q_1 + d \tag{2.37}$$

$$q_3 = \frac{q_2 R_2}{R_2 - 2q_2} \tag{2.38}$$

$$q_4 = q_3 + d \tag{2.39}$$

$$q_5 = \frac{q_4 R_1}{R_1 - 2q_4} \tag{2.40}$$

Expanding q_5 in terms of q_1 we get

$$q_5 = \frac{R_1 R_2 (2d + q_1) - 2dR_1(d + q_1)}{2(d + q_1)(2d - R_1) + R_2(R_1 - 4d - 2q_1)} \tag{2.41}$$

To show there is an eigenmode basis we want to find a q_1 such that $q_5 = q_1$. This ends up being equivalent to solving a quadratic equation in q_1 with the solution being

$$q_{\text{eig}} = \frac{-ds_2 \pm \sqrt{s_1 s_2 d(s_1 + s_2 - d)}}{s_1 + s_2} \tag{2.42}$$

which is the HG basis that defines the eigenmodes of a free space cavity with spherical

mirrors where s_1 and s_2 are common subexpressions

$$s_1 = d - R_1 \tag{2.43}$$

$$s_2 = d - R_2. \tag{2.44}$$

The solution is only physical if q_{eig} has some imaginary component as that is what defines the transverse extent of the beam. This is only true if the term inside the square root of equation (2.42) is negative. This condition is related to the geometrical stability of the cavity which indicates if the cavity can support an eigenmode. The two solutions arising from a choice of positive or negative root in equation (2.42) can be reduced down to a single choice. The root should be taken such that the imaginary part of q_{eig} is positive. The root where the imaginary part of q_{eig} is negative corresponds to an unphysical solution of a beam whose intensity exponentially increases to infinity as you move away from the beam axis and so it is discarded.

Equation (2.42) uniquely defines a q-parameter in terms of physical parameters such as the cavity length and mirror curvatures. It is very convenient to work in the cavity basis and it is often the case that the beam is described with very few modes in this basis. This is because when a cavity is on resonance it predominantly transmits only a single, or a small number of HG modes of that cavity and reflects every other HG mode. For a cavity with length d, amplitude reflection coefficients r_1, r_2 and amplitude transmission coefficients t_1, t_2 for the first and second mirror in the cavity respectively, the transmitted HG mode amplitudes b_{nm} are given by

$$b_{nm} = \frac{\mathrm{i}t_1 t_2 a_{nm}}{1 - r_1 r_2 e^{-i2kd}\psi_{nm} a_{nm}} \tag{2.45}$$

where a_{nm} are the incident HG amplitude coefficients in the cavity eigenmode HG basis q_{eig}, and ψ_{nm} is a cavity mode dependent phase shift given by

$$\psi_n = \left(\text{norm}\left[q^*_{\text{eig}} \left(1 + 2d - \frac{2d(1+d)}{R_2} \right) \right] \right)^{(1+n)} \tag{2.46}$$

$$\psi_{nm} = \psi_n \psi_m \tag{2.47}$$

where $\text{norm}[z] = z/|z|$ is a function that normalizes the magnitude of a complex number

to be equal to 1. The mode dependent phase shift ψ_{nm} is often called the *Gouy phase*.

Equation (2.45) is only valid if the mode amplitudes a_{nm} are in the cavity eigenmode basis q_{eig}, which in general will not be the case without deliberately and carefully setting up the incident beam to match the cavity eigenmode basis. To find what set of HG mode amplitudes in one HG basis looks like in the cavity eigenmode HG basis we need to perform the change of HG basis on the HG mode amplitudes, which is not trivial.

Change of HG basis on HG mode amplitudes

The HG basis change transformation from HG basis q_1 to q_2 for a set of mode amplitudes is given by

$$a_m[q_2] = \int_{-\infty}^{\infty} \left(\sum_n a_n[q_1] u_n[x, q_1] u_m^*[x, q_2] \right) dx \tag{2.48}$$

Integration and summation commute so we can swap their order

$$a_m[q_2] = \sum_n a_n[q_1] \int_{-\infty}^{\infty} u_n[x, q_1] u_m^*[x, q_2] dx \tag{2.49}$$

The overlap integral between two HG modes in different bases is not trivial since we cannot use HG mode orthonormality in this case. For now we can give that integral a label

$$k_{nm}[q_1, q_2] = \int_{-\infty}^{\infty} u_n[x, q_1] u_m^*[x, q_2] dx \tag{2.50}$$

where k_{nm} are typically called the mode scattering coefficients. For the 2D mode scattering coefficients we once again use the separability into 1D outer products to write

$$k_{n_1 m_1 n_2 m_2}[q_{1x}, q_{1y}, q_{2x}, q_{2y}] = k_{n_1 n_2}[q_{1x}, q_{2x}] k_{m_1 m_2}[q_{1y}, q_{2y}] \tag{2.51}$$

The integrals in the mode scattering coefficients can be computed numerically relatively quickly since they are 1D overlap integrals where the integrand has an explicit function and so can be evaluated with Gaussian quadrature. Approximate analytical solutions to

equation (2.50) are also relatively straightforward to obtain. These can be obtained by assuming that $q_1 \approx q_2$ and so the integrand in equation (2.50) can be Taylor expanded at q_2 around q_1. The integral for the lowest order terms can be solved with relative ease using symbolic algebra packages and the results have been published in [204], which can also be found in table D.1.

What is remarkable is that the integral in equation (2.50) has been solved without any approximations by F. Bayer-Helms and published in 1984 as equation 18 in [43]. In fact the integral solved by Bayer-Helms was more general than equation (2.50) because his basis change transformation included a change of q-parameters along with the misalignment transformations: translations and rotations about the beam axis.

With the scattering coefficients computed the change of HG basis operation can be written as

$$a_n[q_1] = k_{nm}[q_2, q_1]\, a_m[q_2] \tag{2.52}$$

which is just an index expression for the following matrix-vector multiplication

$$\boldsymbol{a}[q_1] = K[q_2, q_1]\, \boldsymbol{a}[q_2] \tag{2.53}$$

where the scattering coefficients k_{nm} make up the elements of the matrix K and a_n and a_m are the elements of the vectors $\boldsymbol{a}[q_1]$ and $\boldsymbol{a}[q_2]$ respectively.

In 2D the change of HG basis is given by the following index expression

$$a_{n_1 m_1}[q_{1x}, q_{1y}] = k_{n_1 m_1 n_2 m_2}[q_{2x}, q_{2y}, q_{1x}, q_{1y}]\, a_{n_2 m_2}[q_{2x}, q_{2y}] \tag{2.54}$$

which may not appear immediately as a familiar linear algebra operation but the index pair (n_i, m_i) can be mapped to a single index μ_i under the following transformation

$$\mu_i = \frac{1}{2}\left(n_i^2 + 2n_i m_i + n + m_i^2 + 3m_i\right) \tag{2.55}$$

which produces the following mapping

μ_i	0	1	2	3	4	5	6	7	8	9	...
n_i	0	1	0	2	1	0	3	2	1	0	...
m_i	0	0	1	0	1	2	0	1	2	3	...

Table 2.1: A table of the first couple of elements of the one-to-one mapping from a pair of indices (n_i, m_i) to a single index μ_i given in equation (2.55).

with this equation (2.54) then becomes

$$a_{\mu_1}[q_{1x}, q_{1y}] = k_{\mu_1\mu_2}[q_{2x}, q_{2y}, q_{1x}, q_{1y}]a_{\mu_2}[q_{2x}, q_{2y}] \tag{2.56}$$

which is once again an index expression for matrix-vector multiplication but now in terms of μ. Alternatively, we can use the fact that the 2D scattering coefficients are separable to write

$$a_{n_1m_1}[q_{1x}, q_{1y}] = k_{n_1n_2}[q_{2x}, q_{1x}]\, k_{m_1m_2}[q_{2y}, q_{1y}]\, a_{n_2m_2}[q_{2x}, q_{2y}] \tag{2.57}$$

which can be identified as an index expression for the following matrix multiplication

$$A[q_{1x}, q_{1y}] = K[q_{2x}, q_{1x}]\, A[q_{2x}, q_{2y}]\, K^T[q_{2y}, q_{1y}] \tag{2.58}$$

Using separability in this way gives us a more efficient way to compute the 2D HG basis change than the $(n_i, m_i) \to \mu_i$ mapping. In general, operations that use separability will be more efficient since a lot of the internal calculations are reused.

The place where the change of HG basis operation shows up is when computing the interference of two fields in different HG bases. In general this is given by

$$\boldsymbol{a}[q_3] + \boldsymbol{b}[q_3] = K[q_3, q_1]\boldsymbol{a}[q_1] + K[q_3, q_2]\boldsymbol{b}[q_2] \tag{2.59}$$

but often we pick q_3 to coincide with one of the given bases q_1 or q_2 which gives us the following two equivalent expressions

$$\boldsymbol{a}[q_2] + \boldsymbol{b}[q_2] = K[q_2, q_1]\boldsymbol{a}[q_1] + \boldsymbol{b}[q_2] \tag{2.60}$$

$$\boldsymbol{a}[q_1] + \boldsymbol{b}[q_1] = \boldsymbol{a}[q_1] + K[q_1, q_2]\boldsymbol{b}[q_2] \tag{2.61}$$

From here it is easy to spot the following identity about the inverse of the HG basis change operation

$$(K[q_1, q_2])^{-1} = K[q_2, q_1] \tag{2.62}$$

which can be intuitively read as "changing HG basis from q_1 to q_2 and then from q_2 to q_1 is the same as doing nothing". Note that however this is only true with infinite number of modes and in practice, for finite-sized K the relation is only approximate

$$(K[q_1, q_2])^{-1} \approx K[q_2, q_1] \tag{2.63}$$

and the relation does not approach equality as the number of modes increases, which may seem counterintuitive. However, with a small modification the following identity does approach equality as the number of modes increases

$$(K[q_1, q_2])^{-1}\boldsymbol{a}[q_1] \approx K[q_2, q_1]\boldsymbol{a}[q_1], \tag{2.64}$$

for all $\boldsymbol{a}[q_1]$. The reason that equation (2.64) approaches equality and equation (2.63) does not is not trivial and involves arguments about the representation of infinite groups. A proper analysis of this requires to treat the HG basis change as a linear canonical transformation and some discussion is provided in chapter 3.

Circulating field inside a cavity

The fact that HG modes form the eigenmodes of a cavity with spherical mirrors means that we can use HG modes to compute the circulating field with relative ease. Consider a cavity with length d, amplitude reflection coefficients r_1, r_2 and amplitude transmission coefficients t_1, t_2 for the first and second mirror in the cavity respectively. The cavity has an arbitrary incident field $\boldsymbol{a}_{\text{inc}}[q_1]$ with some circulating field $\boldsymbol{a}_{\text{circ}}[q_2]$. The mode amplitudes of the field after a single round trip $\boldsymbol{a}_{\text{rt}}$ are then given by

$$K[q_2, q_3]\boldsymbol{a}_{\text{rt}}[q_3] = e^{-\mathrm{i}2kd} r_1 r_2 \Psi \boldsymbol{a}_{\text{circ}}[q_2] + \mathrm{i}t_1 K[q_2, q_1]\boldsymbol{a}_{\text{inc}}[q_1] \tag{2.65}$$

where Ψ is a diagonal matrix containing the round trip Gouy phases, and q_3 is given by the round trip cavity basis change in equation (2.41) acting on q_2. We can save a

lot of trouble by picking q_2 to be the cavity eigenmode HG basis q_{eig} where we know $q_2 = q_3 = q_{\text{eig}}$. Equation (2.65) then becomes

$$\boldsymbol{a}_{\text{rt}}[q_{\text{eig}}] = e^{-\text{i}2kd} r_1 r_2 \Psi \boldsymbol{a}_{\text{circ}}[q_{\text{eig}}] + \text{i}t_1 K[q_{\text{eig}}, q_1] \boldsymbol{a}_{\text{inc}}[q_1] \tag{2.66}$$

to get the steady state solution we set the circulating field $\boldsymbol{a}_{\text{circ}}$ to be equal to the field after completing a round trip in the cavity $\boldsymbol{a}_{\text{rt}}$

$$\boldsymbol{a}_{\text{circ}} = e^{-\text{i}2kd} r_1 r_2 \Psi \boldsymbol{a}_{\text{circ}} + \text{i}t_1 K \boldsymbol{a}_{\text{inc}} \tag{2.67}$$

we can then rearrange to isolate the circulating field $\boldsymbol{a}_{\text{circ}}$ to the left hand side

$$\boldsymbol{a}_{\text{circ}} - e^{-\text{i}2kd} r_1 r_2 \Psi \boldsymbol{a}_{\text{circ}} = \text{i}t_1 K \boldsymbol{a}_{\text{inc}} \tag{2.68}$$

$$\left(I - e^{-\text{i}kd} r_1 r_2 \Psi\right) \boldsymbol{a}_{\text{circ}} = \text{i}t_1 K \boldsymbol{a}_{\text{inc}} \tag{2.69}$$

where I is the identity matrix. Solving for the circulating field $\boldsymbol{a}_{\text{circ}}$ yields

$$\boldsymbol{a}_{\text{circ}} = \text{i}t_1 \left(I - e^{-\text{i}2kd} r_1 r_2 \Psi\right)^{-1} K \boldsymbol{a}_{\text{inc}} \tag{2.70}$$

We know that Ψ is a diagonal matrix where the elements $\Psi_{ii} = \psi_i$ are the 1D Gouy phases from equation (2.46). This implies that the matrix $\left(I - e^{-\text{i}2kd} r_1 r_2 \Psi\right)$ is also diagonal and so its inverse is given by the reciprocal of the diagonal elements. We can then write the elements of the circulating field in the following way

$$(\boldsymbol{a}_{\text{circ}})_n = \frac{\text{i}t_1 \left(K \boldsymbol{a}_{\text{inc}}\right)_n}{1 - e^{-\text{i}2kd} r_1 r_2 \Psi_{nn}} \tag{2.71}$$

2.2 ABCD matrices

Traditionally ray transfer or ABCD matrices originate from ray tracing. Given a ray with a position x propagating with slope $x' = dx/dz$ to an optical axis we can write

all possible linear transformations acting on that ray as

$$\boldsymbol{r}_2 = M\boldsymbol{r}_1 \tag{2.72}$$

$$\begin{bmatrix} x_2 \\ x_2' \end{bmatrix} = \begin{bmatrix} A & B \\ C & D \end{bmatrix} \begin{bmatrix} x_1 \\ x_1' \end{bmatrix} \tag{2.73}$$

where the matrix M is the ABCD matrix. This is particularly useful as the ABCD matrix cleanly separates the ray transformation from the ray itself, allowing us to work with the composition of ray transformations without a reference to any specific ray. Most basic optical components can be represented with an ABCD matrix, we will list the ones that relevant in this thesis in table 2.2. A more complete list of ABCD matrices can be found in Kogelnik [18] and Siegman [50].

Component	ABCD matrix
Free space of length d	$\begin{bmatrix} 1 & d \\ 0 & 1 \end{bmatrix}$
Thin lens of focal length f	$\begin{bmatrix} 1 & 0 \\ \frac{-1}{f} & 1 \end{bmatrix}$
Curved mirror of radius R_c	$\begin{bmatrix} 1 & 0 \\ \frac{-2}{R_c} & 1 \end{bmatrix}$

Table 2.2: List of ABCD matrices

It is difficult to trace back the origins of using ABCD matrices in ray tracing to a single source though a possible candidate is W. Brouwer in 1964 [13], which is given as the reference for ABCD matrices in ray tracing independently by a number of pioneers in the field: Kogelnik [17, 16, 18], Collins [20], and Siegman [50].

A remarkable fact about these ABCD matrices is that they are equally applicable to HG beam propagation as they are for ray propagation. The ABCD law for transforming HG q-parameters was first given by Kogelnik in 1965 [17]

$$q_2 = \frac{Aq_1 + B}{Cq_1 + D}. \tag{2.74}$$

The derivation that Kogelnik gives for equation (2.74) is not rigorous. He derives it by noting that in the case for a free space and a thin lens the q-parameter transforms the same way as the radius of curvature of a ray, which he defines as the position of the ray divided by its slope

$$R = \frac{x}{x'}. \tag{2.75}$$

From those two special cases Kogelnik extrapolates that the q-parameter transforms the same way as the ray radius of curvature. While it gives the correct q-parameter Kogelnik's derivation completely neglects any treatment of the Gouy phase that is accumulated going through an ABCD system. This is because there is no analogue of Gouy phase for rays. One can easily spot the error by plugging in the q parameter before and after the thin lens into the amplitude of an HG mode given in equation (2.1) and noting that there is a change of Gouy phase. This is incorrect because a beam only accumulates Gouy phase from propagation for which there is none with a thin lens.

Siegman attempts to remedy this by providing an alternative derivation in which he transforms an arbitrary HG mode with the generalized Huygens' integral in [48] (which is Siegman's name for the linear canonical transform). He finds that the q-parameter transforms following the same ABCD law as Kogelnik predicted, but with an additional overall complex scalar for the HG mode. The absolute value of this scalar is just a normalization to conserve energy as the beam changes in size. The phase of the scalar is then the accumulated Gouy phase for propagating through the ABCD system. Siegman states this phase in equation 20.26 of [50] as

$$\psi = \frac{A + B/q_1}{|A + B/q_1|} \tag{2.76}$$

$$\Psi_{nm} = \psi_x^{(1/2+n)} \psi_y^{(1/2+m)} \tag{2.77}$$

which he calls the generalized Gouy phase. There are 2 issues with equation (2.76) that we can see. The first appears to be a relatively minor typo in Siegman's original definition which does not produce the correct Gouy phase shift unless we conjugate

the q-parameter in equation (2.76). We state the corrected generalized Gouy phase as

$$\psi = \frac{A + B/q_1^*}{|A + B/q_1^*|} \tag{2.78}$$

which was deduced by comparing it to diffraction integral calculations and an independent derivation of accumulated Gouy phase by Erden [65] who also used the linear canonical transform to derive the accumulated Gouy phase.

The second issue is present in both the original and corrected forms for the accumulated Gouy phase and that is that it has a sign ambiguity. Unfortunately this sign ambiguity is not trivial and is rooted in the fundamental geometric structure of paraxial optics. In order to fully understand it requires to treat the problem in the framework of group theory which is beyond the scope of this thesis. We will provide a short explanation of the sign ambiguity without requiring any group theory. Fundamentally it stems from the definition of the 1D accumulated Gouy phase being the square root of equation (2.78). The square root is always a double valued function in the complex domain where the two roots differ by a sign. The sign cannot be discarded as it has physical meaning, which essentially reduces to containing information about the history of the optical system. A more in-depth discussion of the sign ambiguity is provided in appendix B.1.

Siegman derived his linear canonical transform by considering the optical path length of rays in an arbitrary ABCD system using Fermat's principle. An alternative derivation of the linear canonical transform that captures the sign ambiguity was presented independently by Bacry [36] and Wolf [95]. The explicit derivation is beyond the scope of this thesis but a simple outline can be presented. It begins by considering transformations that are induced by an arbitrary combination of infinitesimal free space propagation and thin lenses with infinitesimal focal power. One finds that the space of these transformations is locally isomorphic to transformations produced by ABCD matrices, but globally the infinitesimal transformations form a double cover over the ABCD transformations. The two covers differ by an overall sign (180 degrees of phase) applied to the entire field. In other words, an arbitrary combination of free spaces and lenses can reduce to a either a single ABCD matrix and Gouy phase given by (2.78), or the Gouy phase times -1.

In this chapter we have introduced the basics of HG modal propagation models with discussions to broader paraxial wave theory. In the next chapter we will shift the focus to more grid based modelling in the framework of the linear canonical transform. This will ultimately lead into the development of a working LCT model of the circulating field in a gravitational wave interferometer in chapter 4.

Chapter 3

Modelling circulating cavity fields using the discrete linear canonical transform

3.1 Preface

The following work presents a modelling framework for circulating cavity fields using the discrete linear canonical transform [220]. This work has been published in the peer reviewed OSA journal, Journal of the Optical Society of America A.

A. A. Ciobanu, D. D. Brown, P. J. Veitch, and D. J. Ottaway. "Modeling circulating cavity fields using the discrete linear canonical transform". In: *Journal of the Optical Society of America A* 38.9 (Sept. 1, 2021). Number: 9, p. 1293. ISSN: 1084-7529, 1520-8532. DOI: 10.1364/JOSAA.433575.

Fabry-Perot cavities are central to many optical measurement systems. In high precision experiments, such as aLIGO and AdVirgo, coupled cavities are often required leading to complex optical behaviour. We show, for the first time, that discrete LCTs can be used to compute circulating optical fields for cavities in which the optics have arbitrary apertures, reflectance and transmittance profiles, and shape. We compare the predictions of LCT models with those of alternative methods. To further highlight the utility of the LCT, we present a case study of point absorbers on the aLIGO mirrors

and compare with recently published results.

3.2 Introduction

Optical cavities, such as Fabry-Perot interferometers are commonly used in precision optical experiments. The circulating field of any single geometrically stable cavity is a sum of the Hermite-Gauss (HG) modes of the cavity, which are given by analytical expressions [18, 50].

HG decomposition can accurately model the steady state and time domain field that exists in multiple coupled cavities and is extensively used for optical modelling for the advanced gravitational wave detectors [73, 200]. This method however, is not ideally suited for modelling high spatial-frequency features, such as finite mirror apertures and small scale aberrations such as point absorbers [216]. This is because of the large number of HG modes needed to accurately model them [140, 211].

An alternative to HG decomposition is to consider the complex beam amplitude sampled on a uniform cartesian grid. In such a model the spaces in an optical system are represented by diffraction integrals and the optical elements (e.g. mirrors, and lenses) are approximated with thin phase plates. The accuracy of the model is determined by the resolution of the sampled grid. This allows non-Gaussian features to be accurately modelled to the resolution limit of the sampled grid.

In the cartesian basis the diffraction integral becomes a linear operator that couples all points in the input plane to all points in the output plane. This causes the issue that in two dimensions the size of the linear operator grows as the square of the number of grid points, quickly becoming too large for practical simulations due to memory limitations. A common optimization is to perform the diffraction integrals in the Fourier domain where the convolution in the diffraction integral becomes multiplication in the Fourier domain, and hence cheaper to compute. This optimization has led to the use of iterative algorithms for solving for circulating fields in the cartesian basis [106].

The first known usage of an iterative algorithm for solving steady state circulating fields is the *Fox-Li method* demonstrated in 1961 [11]. The method involves taking a guess at a circulating field and repeatedly computing round trip propagations inside

the cavity until the circulating field converges to a steady state, with the number of iterations typically scaling with the finesse of the cavity [59]. The speed of each iteration is typically limited by the diffraction integral. Fast Fourier transforms (FFTs) can be used to efficiently compute the diffraction integrals, which has in turn led to this class of models being colloquially called *FFT models*. The number of iterations is reduced with a better initial guess of the circulating field or by accelerating the rate of convergence by using a modified iteration scheme [67, 91, 129]. The Fox-Li method has also been used in modelling eigenmodes of unstable resonators [82, 81].

FFT models can be used to model more complicated optical systems involving multiple coupled cavities, such as the Fabry-Perot power recycled Michelson interferometers (FPPRMI) used in Gravitational Wave (GW) detectors as modeled by Bochner et al. in 2003 [91]. Bochner et al. additionally state that FFT models are difficult to implement in code and that accelerating the rate of convergence of their FFT models often leads to instability—which was also found to be an issue by Day et al. [129]. A 2017 review of unstable resonator eigenmode modelling by New [163] showed that the Fox-Li method can be outperformed by general purpose linear algebra algorithms available in MATLAB in cases where the sampling grid resolution is not larger than 512×512.

Linear Canonical Transforms (LCT) provides an alternative modeling formalism to modal and FFT models. The LCT was first introduced to the optical modelling community in 1970 by Collins [20] and has been widely used to derive beam propagation formulas and model single pass optical systems. Recently the LCT has been applied in modelling 1D unstable cavity eigenmodes [120], and propagation in Herriott cells [154]. Over the past 20 years there have been many efforts to refine discrete approximations of the LCT across multiple disciplines [83, 147, 175, 188].

In this paper we apply the discrete LCT (DLCT) for modeling circulating fields in resonant cavities, for the first time to the best of our knowledge. A particular benefit of the LCTs is that it enables us to use highly optimized general purpose linear algebra algorithms instead of the Fox-Li method. The paper is laid out as follows: in section 3.3 we define the continuous LCT and some of its properties. Section 3.4 covers a brief review of the application of the LCT in optical propagation in ABCD optical systems.

Section 3.5 demonstrates a new application of the LCT to calculate the circulating field of single linear and ring cavities, as well as linear cavities with finite apertures and mirror deformations including point absorbers. Appendix B.1 also contains a discussion on the metaplectic nature of the LCT, which is used to derive new expressions for accumulated Gouy phase of HG modes in ABCD optical systems.

3.3 Linear Canonical Transform

The history of the linear canonical transform (LCT) can be traced back to two independent origins [159, 150]; one in optics [20], and one in quantum mechanics [24]. In optics alone the LCT has appeared under a number of other names such as: the generalized Huygens' integral [48], and the affine Fourier transform [62]. More abstractly the LCT is a faithful representation of the metaplectic group acting on phase space [36, 95].

The LCT is a paraxial diffraction integral that models the propagation of an arbitrary electric field through an optical system that is represented by an ABCD matrix [48]. Formally, the LCT is a family of integral transforms, which include the Fourier and fractional Fourier transforms, as well as Laplace transforms, and the Fresnel integral. Any particular LCT can be parameterized up to an overall sign by four complex numbers denoted A, B, C, D, and one constraint $AD - BC = 1$ [85, 144].

3.3.1 Continuous LCT

The continuous LCT, $g(x)$, of a function $f(x)$ is defined as

$$g(x_2) = \int_{-\infty}^{\infty} \mathcal{L}(x_1, x_2) f(x_1) dx_1 \tag{3.1}$$

where $\mathcal{L}$ is a linear operator and the kernel of the LCT integral transform

$$\mathcal{L}(x_1, x_2) = \begin{cases} \sqrt{\dfrac{\mathrm{i}}{B\lambda}} \times \exp\left[\dfrac{-\mathrm{i}\pi}{B\lambda}\left(Ax_1^2 - 2x_1x_2 + Dx_2^2\right)\right] \\ \sqrt{D} \times \exp\left[\dfrac{-\mathrm{i}\pi C}{\lambda D} x_2^2\right] \delta(x_1 - Dx_2) \qquad \text{if } B = 0 \end{cases} \tag{3.2}$$

where λ is the optical wavelength, $\{A, B, C, D\}$ are the LCT parameters, and $\delta(x)$ is the Dirac delta function.

3.3.2 Discrete LCT

A discrete LCT can be obtained by taking N samples of (3.1) at regular intervals Δx

$$g(x_k) = \Delta x \times \sum_{j=1}^{N} \mathcal{L}(x_j, x_k) f(x_j) \tag{3.3}$$

where $\Delta x = \mathrm{x_{i+1}} - \mathrm{x_i}$, and $f(x) \to 0$ for $x < x_1$ and $x > x_N$.

We can simplify the notation by introducing the following N-vector $\mathbf{x}$

$$\mathbf{x} = \left[\mathrm{x}_1, \mathrm{x}_2, \ldots, \mathrm{x}_{N-1}, \mathrm{x}_N\right]^T. \tag{3.4}$$

Then (3.3) can be rewritten as a matrix-vector product

$$\mathbf{g} = \Delta x \times \mathbf{L}\mathbf{f} \tag{3.5}$$

where $\mathbf{f} = f(\mathbf{x})$, $\mathbf{g} = g(\mathbf{x})$ are N-vectors, and $\mathbf{L}$ is an $N \times N$ matrix. The matrix $\mathbf{L}$ is given by

$$\mathbf{L} = \sqrt{\frac{\mathrm{i}}{B\lambda}} \times \exp_\circ\left[\frac{-\mathrm{i}\pi}{B\lambda}\left(A\mathbf{X_1}^2 - 2\mathbf{x}\mathbf{x}^T + D\mathbf{X_2}^2\right)\right] \tag{3.6}$$

where $B \neq 0$, $\exp_\circ[\mathbf{X}]$ is an element-by-element exponentiation,

$$\mathbf{X_1}^2 = \begin{bmatrix} x_1^2 & \ldots & x_N^2 \\ \vdots & \ddots & \vdots \\ x_1^2 & \ldots & x_N^2 \end{bmatrix}, \qquad \mathbf{X_2}^2 = \begin{bmatrix} x_1^2 & \ldots & x_1^2 \\ \vdots & \ddots & \vdots \\ x_N^2 & \ldots & x_N^2 \end{bmatrix}, \tag{3.7}$$

and $\mathbf{x}\mathbf{x}^T = \mathbf{x} \otimes \mathbf{x}$ is an outer product.

This DLCT implementation is sometimes called the "direct" implementation [83, 147]. It accurately approximates the continuous LCT except when $|B| \ll 1$, for which the magnitude of the exponent in (3.2) become large and thus a higher resolution array of samples is required to avoid aliasing in the kernel $\mathbf{L}$.

A number of alternative DLCT implementations have been constructed over the years, most of which are well-behaved for $|B| \ll 1$ [147, 188]. However, it appears there is no

single DLCT implementation that has a consistently lower approximation error for all possible LCT parameters and input functions.

For modelling geometrically stable resonant optical cavities where $|A+D| < 2$, and $|B|$ is not close to zero [47, 49] we find that the "direct" implementation in (3.3) performs adequately.

3.3.3 LCT Composition

Composition is perhaps the most powerful property when working with LCTs. For optical models the composition property allows for any arbitrary ABCD optical system to be accurately modelled with a single LCT. This drastically reduces the amount of computation compared to equivalent FFT models, which require each optical component in a system to be modelled individually.

We adopt the standard convention of packaging the $\{A, B, C, D\}$ parameters into a matrix $\mathbf{M} = \left[\begin{smallmatrix} A & B \\ C & D \end{smallmatrix}\right]$. These matrices use the "reduced" ray slope method defined in [47]. They are identical to the standard ABCD matrices [18], except for the case where a refractive index change occurs. The ABCD matrix elements are real in most optical models, but can be complex if the model contains soft Gaussian apertures [48].

The composition property states that composing two LCTs is the same as single LCT (up to a sign difference) whose ABCD matrix is given by the matrix product of the ABCD matrices of the composed LCTs [44]

$$\mathcal{L}_{\mathbf{M_2}}\mathcal{L}_{\mathbf{M_1}} = \sigma\mathcal{L}_{\mathbf{M_2}\mathbf{M_1}}, \tag{3.8}$$

where $\sigma \in \{-1, 1\}$ is the metaplectic sign. In general, when composing ABCD matrices it is necessary to keep track of the metaplectic sign σ. Failing to do so may introduce erroneous minus signs in the calculation of the accumulated Gouy phase. Further discussions on the metaplectic sign, as well as instructions on how to compute it are presented in appendix B.1.

Unfortunately, all known DLCT implementations only satisfy composition approxi-

mately [148, 188].

$$\mathbf{L_{M_2}} \mathbf{L_{M_1}} \approx \sigma \, \mathbf{L_{M_2 M_1}} \tag{3.9}$$

Exact composition for specific subsets of LCT parameters can be recovered in some DLCT implementations [137]. This approximation error can be made arbitrarily small by using higher resolution DLCT matrices $\mathbf{L_M}$. This is similar to how the accuracy of an FFT based model scales with grid resolution.

3.4 Optical propagation using the LCT

Here we review a well known application of the LCT: the propagation of paraxial electric fields through an ABCD optical system. We discuss both analytical solutions of the LCT and its discrete approximations to 1D and separable 2D systems.

3.4.1 1D propagation

An 1D paraxial electric field $E_{\text{in}}(x)$ at an input plane can be propagated through a paraxial optical system represented by an ABCD matrix $\mathbf{M}$ using (3.1)

$$E_{\text{out}}(x') = \int_{-\infty}^{\infty} \mathcal{L}_{\mathbf{M}}(x, x') E_{\text{in}}(x) dx \tag{3.10}$$

where $E_{\text{out}}(x)$ is the electric field at the output plane.

In the discrete case, the N samples of the output electric field $\mathbf{u}_{\text{out}}$ can be calculated by matrix multiplying an N-vector representation of the input electric field $\mathbf{u}_{\text{out}}$ by $N \times N$ DLCT matrix $\mathbf{L_M}$

$$\mathbf{u}_{\text{out}} = \mathbf{L_M} \mathbf{u}_{\text{in}}. \tag{3.11}$$

The DLCT provides a simple framework for viewing optical propagation as a product of matrices, each corresponding to a basic optical component, to yield a single DLCT matrix for the overall optical system as illustrated in figure 3.1.

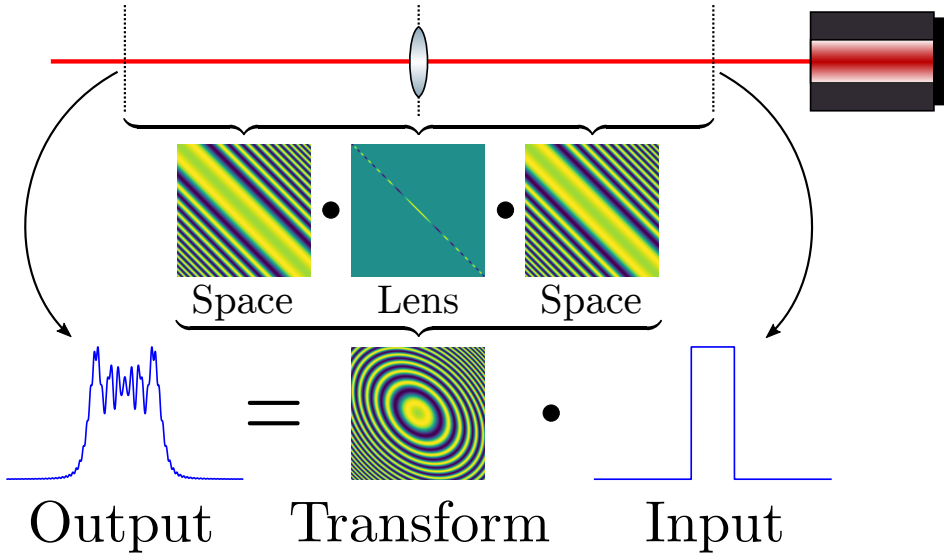

Figure 3.1: A visualization of a 1D DLCT where the electric field propagates from right-to-left to maintain consistency with the matrix-vector multiplication in the bottom row. The optical system consists of 3 ABCD matrices, each of which yields a DLCT kernel, the real part of which is shown. The overall kernel is determined using (3.9), and used to propagate a tophat beam from the input plane to the output plane using (3.11).

3.4.2 Separable 2D propagation

In general, a 2D propagation through a paraxial system is given by the following integral

$$E_{\text{out}}(x', y') = \iint_{-\infty}^{\infty} \mathcal{L}_{\mathbf{M}}(x, x', y, y') E_{\text{in}}(x, y) dx dy \tag{3.12}$$

where $\mathbf{M}$ is a 4×4 2D ABCD matrix. The definition of the 2D LCT kernel $\mathcal{L}_{\mathbf{M}}(x, x', y, y')$ is given in [20, 98].

In optics it is often the case that instead of a 4×4 ABCD matrix $\mathbf{M}$ we have two 2×2 ABCD matrices $\mathbf{M}_x$ and $\mathbf{M}_y$, one for each axis. The 2D LCT kernel is then separable in the two axes and can therefore be written as a product of two 1D LCT kernels.

$$\mathcal{L}_{\mathbf{M}}(x, x', y, y') = \mathcal{L}_{\mathbf{M}_x}(x, x') \mathcal{L}_{\mathbf{M}_y}(y, y') \tag{3.13}$$

The propagation through a 2D separable paraxial optical system is then given by

$$E_{\text{out}}(x', y') = \int_{-\infty}^{\infty} \mathcal{L}_{\mathbf{M}_y}(y, y') \left(\int_{-\infty}^{\infty} \mathcal{L}_{\mathbf{M}_x}(x, x') E_{\text{in}}(x, y) dx \right) dy. \tag{3.14}$$

In the discrete approximation of equation (3.14), the $N \times M$ samples of the output electric field $\mathbf{U}_{\text{out}}$ using

$$\mathbf{U}_{\text{out}} = \Delta x \Delta y \times \mathbf{L}_{\mathbf{M}_y} \mathbf{U}_{\text{in}} \left(\mathbf{L}_{\mathbf{M}_x}\right)^T \tag{3.15}$$

where $\mathbf{L}_{\mathbf{M}_y}$ is an $N \times N$ 1D DLCT matrix for the y-axis and $\left(\mathbf{L}_{\mathbf{M}_x}\right)^T$ is the transpose of an $M \times M$ 1D DLCT matrix for the x-axis.

In the case where the 2D LCT kernel is not separable equation (3.12) has to be discretized differently in order to obtain the 2D non-separable DLCT [148, 193]. This is necessary if one is interested in modelling *general astigmatism* [19, 99] using ABCD matrices, which comes about from propagation through rotated astigmatic lenses [97]. Throughout the rest of this paper we will only consider separable 2D LCTs.

3.5 Circulating field in ideal resonant cavities

3.5.1 Linear cavities

The circulating field in a stable optical cavity is determined by generalizing the strategy used by Siegman [46] for plane waves.

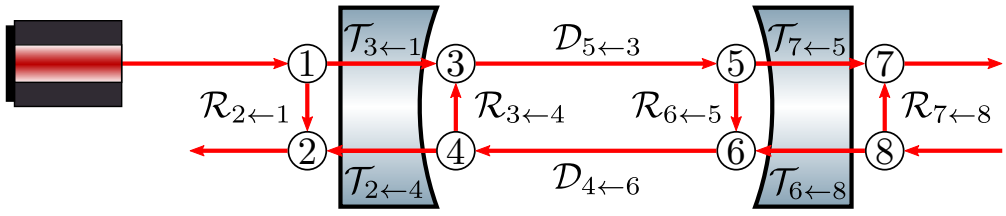

Figure 3.2: A directed network graph of a Fabry-Perot cavity. Each node corresponds to a distinct electric field, and each edge/red arrow corresponds to a linear operator that transforms a field from the input to the output node. Multiple edges leading into a single node are summed together to obtain the field at that node.

For the cavity shown in figure 3.2 the circulating field at node 3 is given by

$$E_3 = \mathcal{R}_{3\leftarrow 4}\mathcal{D}_{4\leftarrow 6}\mathcal{R}_{6\leftarrow 5}\mathcal{D}_{5\leftarrow 3}E_3 + \mathcal{T}_{3\leftarrow 1}E_1, \tag{3.16}$$

where we assume $E_8 = 0$. The definition of symbols that convert (3.16) into an LCT model for an ideal cavity is given in table 3.1, where $r_1, r_2, \mathbf{M}_{R_1}, \mathbf{M}_{R_2}$ are amplitude

Edge	Analytical	Discrete 1D	Discrete 2D
$\mathcal{T}_{3\leftarrow 1}[\mathbf{X}]$	$\mathrm{i}t_1\mathcal{L}_{\mathbf{M}_{T_1}}[\mathbf{X}]$	$\mathrm{i}t_1\mathbf{L}_{\mathbf{M}_{T_1}}\mathbf{X}$	$\mathrm{i}t_1\mathbf{L}_{\mathbf{M}_{T_{1y}}}\mathbf{X}\left(\mathbf{L}_{\mathbf{M}_{T_{1x}}}\right)^T$
$\mathcal{R}_{3\leftarrow 4}[\mathbf{X}]$	$r_1\mathcal{L}_{\mathbf{M}_{R_1}}[\mathbf{X}]$	$r_1\mathbf{L}_{\mathbf{M}_{R_1}}\mathbf{X}$	$r_1\mathbf{L}_{\mathbf{M}_{R_{1y}}}\mathbf{X}\left(\mathbf{L}_{\mathbf{M}_{R_{1x}}}\right)^T$
$\mathcal{R}_{6\leftarrow 5}[\mathbf{X}]$	$r_2\mathcal{L}_{\mathbf{M}_{R_2}}[\mathbf{X}]$	$r_2\mathbf{L}_{\mathbf{M}_{R_2}}\mathbf{X}$	$r_2\mathbf{L}_{\mathbf{M}_{R_{2y}}}\mathbf{X}\left(\mathbf{L}_{\mathbf{M}_{R_{2x}}}\right)^T$
$\mathcal{D}_{4\leftarrow 6}[\mathbf{X}]$	$e^{\mathrm{i}\phi/2}\mathcal{L}_{\mathbf{M}_d}[\mathbf{X}]$	$e^{\mathrm{i}\phi/2}\mathbf{L}_{\mathbf{M}_d}\mathbf{X}$	$e^{\mathrm{i}\phi/2}\mathbf{L}_{\mathbf{M}_d}\mathbf{X}\left(\mathbf{L}_{\mathbf{M}_d}\right)^T$
$\mathcal{D}_{5\leftarrow 3}[\mathbf{X}]$	$e^{\mathrm{i}\phi/2}\mathcal{L}_{\mathbf{M}_d}[\mathbf{X}]$	$e^{\mathrm{i}\phi/2}\mathbf{L}_{\mathbf{M}_d}\mathbf{X}$	$e^{\mathrm{i}\phi/2}\mathbf{L}_{\mathbf{M}_d}\mathbf{X}\left(\mathbf{L}_{\mathbf{M}_d}\right)^T$

Table 3.1: Definition of symbols in (3.16) for modelling an ideal linear cavity in an analytical, 1D and 2D discrete LCT models. The symbol $\mathbf{X}$ is either an analytical expression, a vector, or a matrix respectively.

reflection coefficients and ABCD matrices of the input and end mirror respectively, t_1 and $\mathbf{M}_{T_1}$ is the amplitude transmission coefficient, and ABCD matrix for the input mirror, $\mathbf{M}_d$ is the free-space propagation ABCD matrix for the distance between the mirrors, and $\phi = 2kd$ is the accumulated round-trip plane-wave phase.

Substituting in the LCT operators gives

$$E_{\text{circ}} = e^{\mathrm{i}\phi} r_1 r_2 \mathcal{L}_{\mathbf{M}_{R_1}} \mathcal{L}_{\mathbf{M}_d} \mathcal{L}_{\mathbf{M}_{R_2}} \mathcal{L}_{\mathbf{M}_d} E_{\text{circ}} + \mathrm{i}t_1 \mathcal{L}_{\mathbf{M}_{T_1}} E_{\text{inc}}. \tag{3.17}$$

We can use the LCT composition property to simplify the sequence of LCTs $\mathcal{L}_{\mathbf{M}_{R_1}} \mathcal{L}_{\mathbf{M}_d} \mathcal{L}_{\mathbf{M}_{R_2}} \mathcal{L}_{\mathbf{M}_d}$ into a single round-trip LCT $\mathcal{L}_{\mathbf{M}_{\text{RT}}}$, and thus

$$E_{\text{circ}} = e^{\mathrm{i}\phi} r_1 r_2 \mathcal{L}_{\mathbf{M}_{\text{RT}}} E_{\text{circ}} + \mathrm{i}t_1 \mathcal{L}_{\mathbf{M}_{T_1}} E_{\text{inc}} \tag{3.18}$$

Rearranging for E_{circ} gives us

$$E_{\text{circ}} = \mathrm{i}t_1 \left(\mathcal{I} - e^{\mathrm{i}\phi} r_1 r_2 \mathcal{L}_{\mathbf{M}_{\text{RT}}} \right)^{-1} \mathcal{L}_{\mathbf{M}_{T_1}} E_{\text{inc}} \tag{3.19}$$

where $\mathcal{I}$ is the identity operator ($\mathcal{I}x = x$).

Unfortunately, the $\left(\mathcal{I} - e^{\mathrm{i}\phi} r_1 r_2 \mathcal{L}_{\mathbf{M}_{\text{RT}}}\right)$ operator has no known closed form inverse, but it can be approximated with discrete numerical methods. Rewriting (3.19) in the 1D discrete case yields the following matrix-vector equation

$$\mathbf{u}_{\text{circ}} = \mathrm{i}t_1 \left(\mathbf{I} - e^{\mathrm{i}\phi} r_1 r_2 \mathbf{L}_{\mathbf{M}_{\text{RT}}} \right)^{-1} \mathbf{L}_{\mathbf{M}_{T_1}} \mathbf{u}_{\text{inc}} \tag{3.20}$$

where $\mathbf{I}$ is an $N \times N$ identity matrix. (3.20) can be trivially computed with a matrix inverse algorithm.

For 2D the solution is more complicated. Starting from (3.18) the $N \times N$ 2D discrete circulating field $\mathbf{U}_{\text{circ}}$ is given by

$$\mathbf{U}_{\text{circ}} - e^{\mathrm{i}\phi} r_1 r_2 \mathbf{L}_{\mathbf{M}_{\text{RT}_y}} \mathbf{U}_{\text{circ}} (\mathbf{L}_{\mathbf{M}_{\text{RT}_x}})^T = \mathrm{i} t_1 \mathbf{L}_{\mathbf{M}_{T_{1y}}} \mathbf{U}_{\text{inc}} (\mathbf{L}_{\mathbf{M}_{T_{1x}}})^T. \tag{3.21}$$

(3.21) is of the form where the left-hand-side (LHS) consists of purely linear operations on the unknown $\mathbf{U}_{\text{circ}}$ and the right-hand-side (RHS) contains only known quantities. Therefore, (3.21) is equivalent to an $N^2 \times N^2$ system of linear equations given by $\mathbf{Ax} = \mathbf{b}$. However, the $\mathbf{Ax} = \mathbf{b}$ form is not practical due to memory limitations arising from the $N^2 \times N^2$ dimensionality.

(3.21) can be rewritten as a Sylvester equation $\mathbf{AX} + \mathbf{XB} = \mathbf{Q}$, where $\mathbf{X}$ is unknown, and $\mathbf{A}, \mathbf{B}, \mathbf{Q}$ are known $N \times N$ matrices, which can be solved efficiently by the Bartels-Stewart algorithm [26] in LAPACK [54]. Alternatively (3.21) can be solved using iterative sparse linear solvers such as GMRES [45], which can also be used to model cavities with mirror surface imperfections and is discussed in more detail in section 3.6.

3.5.2 Ring cavities

The approach to modelling ring cavities is similar to the linear cavity except that the reflection operators have to be modified to include a parity transformation for the reflected electric field. This parity transformation is also present in linear cavities, however is often neglected as the parity from each mirror cancels in the round trip.

The triangular cavity is an interesting example as it is the simplest cavity with an odd number of mirrors, which has an overall parity in the round trip and hence splits the resonances of its horizontal and vertical eigenmodes [15, 14, 71]. Typically, this phenomenon is modelled in HG models by explicitly counting the number of mirrors and manually applying a minus sign in specific equations to produce the desired transverse mode splitting.

For both LCT and FFT models the transverse mode splitting in triangular cavities is generated by parity operators $\mathcal{P}$ that swap the left and right side of the electric field on

reflection $\mathcal{P}[E(x,y)] = E(-x,y)$ to maintain a consistent coordinate system [47]. We can identify the mirror counting behavior by noting that the parity operator commutes with the LCT $\mathcal{P}\mathcal{L}_{\mathbf{M}} = \mathcal{L}_{\mathbf{M}}\mathcal{P}$. The parity operators can thus all be commuted to one side where we only need to consider whether there are an odd or even number of parity operators (i.e. odd or even number of mirrors) because the parity operator is its own inverse $\mathcal{P}\mathcal{P} = \mathcal{I}$. In the case of a round trip in a triangular cavity we are then left with a single overall parity operator $\mathcal{P}$, which flips the sign of the odd part of the electric field along the x-axis. Decomposing the parity operator into the HG basis we find all $\mathrm{HG}_{n,m}$ modes that have an odd mode order index n for the x-axis pick up an additional minus sign.

For the LCT we can simplify this analysis since the parity operation $\mathcal{P}$ is a subset of the LCT that can be represented by an ABCD matrix, namely the negative identity matrix

$$\mathbf{M}_{\mathcal{P}} = \begin{bmatrix} -1 & 0 \\ 0 & -1 \end{bmatrix}, \tag{3.22}$$

which can be interpreted as the reflection off of a flat mirror. It should be noted that in separable 2D models the parity operation should only be included in the x-axis ABCD matrix. So for example the ABCD matrices for reflecting off of a curved mirror in the x and y axis respectively are given by

$$\mathbf{M}_x = \begin{bmatrix} -1 & 0 \\ \frac{2}{R_x} & -1 \end{bmatrix}, \qquad \mathbf{M}_y = \begin{bmatrix} 1 & 0 \\ \frac{-2}{R_y} & 1 \end{bmatrix}, \tag{3.23}$$

where R_x and R_y are the radii of curvature of the mirror in the x and y axes respectively.

This approach of encoding the parity transformations with the ABCD matrix allows (3.21) to be valid for both linear and ring cavities. It has also previously been justified by Siegman based on purely geometrical arguments in figure 15.8 of [47], and by Arai [121] for computing the transverse mode splitting in ring cavities.

It should be noted that encoding the parity operator into the ABCD matrix introduces 90° of phase on reflection to the entire electric field from the $\sqrt{D}$ term in (3.2). This

affects the phase relationship between reflection and transmission that is needed to maintain conservation of energy (section 2.4 in [140]). However, it can be trivially accounted for by defining all scalar amplitude reflectivities to have an additional -90° of phase to counteract the 90° from the LCT parity operation.

3.5.3 Results

The normalized circulating power predicted by (3.21) as the round trip phase, ϕ, is varied is plotted in figure 3.3 for a linear and ring cavity. The incident field consists of the sum of equal power HG_{00}, HG_{22}, and HG_{33} modes. Note that for the HG_{33} the resonance phase differs in the linear and ring cavities by 180° due to the overall parity operator in the round trip in a ring cavity with an odd number of mirrors.

The circulating power as computed in the LCT model is compared to an equivalent HG modal model calculated using the FINESSE optical modelling package [93, 123, 128, 200]. figure 3.3 shows that the LCT and HG model agree to at least 10^{-8} of the circulating power in the test case shown.

The difference between the two models seen in figure 3.3 can be attributed entirely due to the limited resolution in the LCT grid as the HG model in this case corresponds to the complete analytic solution.

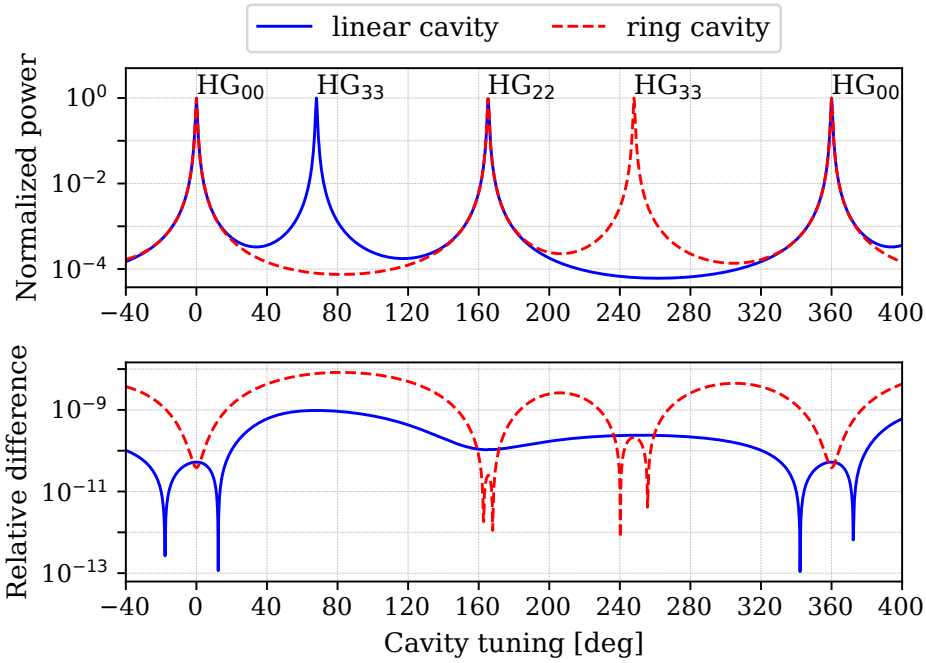

Figure 3.3: The upper plot shows the calculated circulating power inside a linear (solid blue) and triangular (red dashed) cavity with infinite mirrors versus cavity tuning ϕ. The free spectral range (FSR) and round trip Gouy phase identical to a 4 km aLIGO arm cavity. The power is normalized so that on-resonance the circulating power is 1. The LCT model uses a 200×200 grid. The circulating power computed by both models is indistinguishable by eye and so only the LCT solution is shown in the upper plot. The relative difference between the LCT and FINESSE models are shown in the lower plot.

3.6 Linear cavity with apertures and mirror defects

We have only considered optical models that are able to be completely described by ABCD matrices and hence use mirrors of infinite extent.

The LIGO arm cavities are tightly constrained with respect to their resonant eigenmode. The beam size at the test masses should be as large as possible to reduce thermal coating noise by averaging over more of the coating [69, 88, 101]. The beam size cannot be too big however since too much power would be lost to mirror aperture scattering. In the design of the LIGO arm cavity a balance was found between the various constraints.

Recently there has been an increased interest in modelling the field inside the arms with attention on how the intensity distribution changes with aperture scattering and

different mirror polishing profiles. The aim is to design a mirror polishing profile that further optimizes the performance of the detector.

Modelling these kind of effects is well suited to grid based FFT models such as SIS. To ensure that a model is correct it should be compared to experimental data. However in cases where experimental data is difficult or impossible to obtain, the next best method of model validation is consensus with other models. If many independent models agree on the same result then that result is more likely to be accurate. Typically FFT models are compared against HG models. This poses a challenge since HG models tend to converge slowly when hard apertures are involved. Often to get good agreement an impractically large number of HG modes have to be used.

LCT models provide another way of simulating the circulating field in optical systems. The calculation is independent and different to the methods used in FFT models, making them suitable for validating existing FFT models. This section describes an LCT model of the circulating field in the LIGO arm cavity with apertures.

To incorporate finite aperture mirrors into the DLCT framework we need to formulate the action of an aperture as a linear operator. For an electric field $\mathbf{X}$ sampled on a 2D $N \times N$ grid, apertures (and most mirror surface maps) become diagonal $N^2 \times N^2$ matrices when implemented as a linear operator. The off-diagonal elements become non-zero when propagating the beam away from the mirror and so in general all $N^2 \times N^2$ elements are non-zero in any optical model. This poses a technical challenge as the computer storage requirements of an $N^2 \times N^2$ matrix are prohibitively large for current consumer hardware for $N > 200$. Specifically for 128-bit complex floating point numbers, the amount of memory required to store an $N^2 \times N^2$ matrix is $N^4 \times 1.6 \times 10^{-8}$ GB. This $\mathcal{O}(N^4)$ scaling in storage requirements has been documented as a primary bottleneck in similar linear operator based approaches [163].

The approach to 2D we have described in sections 3.4 and 3.5 avoids this $\mathcal{O}(N^4)$ space complexity by exploiting the structure of the separable 2D DLCT kernel as described in appendix B.2. Specifically, our approach has an $\mathcal{O}(N^2)$ space complexity since we only store the $N \times N$ matrices and never explicitly construct the full $N^2 \times N^2$ 2D propagation matrix. The apertures can also be incorporated as an element-wise product a.k.a Hadamard product of the aperture map with the incident field. This is

similar to how FFT models implement their apertures and mirror maps, which also achieve the same $\mathcal{O}(N^2)$ space complexity.

To compute the circulating field with apertures we first consider the general operator solution in (3.16). The reflection and transmission operators are given by

$$\mathcal{T}_{3\leftarrow 1}[\mathbf{X}] = \mathbf{T}_1 \circ \mathbf{X} \tag{3.24}$$

$$\mathcal{R}_{6\leftarrow 5}[\mathbf{X}] = \mathbf{R}_2 \circ \mathbf{X} \tag{3.25}$$

$$\mathcal{R}_{3\leftarrow 4}[\mathbf{X}] = \mathbf{R}_1 \circ \mathbf{X} \tag{3.26}$$

where $\circ$ is the Hadamard product (a.k.a. element-by-element array product), $\mathbf{T}_1$ is the complex amplitude transmission map of the input mirror $\mathbf{R}_1$ and $\mathbf{R}_2$ are complex amplitude reflection maps of the input and output mirror respectively. There are no structural requirements on these reflection and transmission maps and as such they can be used to model any arbitrary aperture, reflectivity, and height maps. The space propagation edges $D_{4\leftarrow 6}$ and $D_{5\leftarrow 3}$ are the same as the last column of table 3.1.

To solve (3.16) it is more convenient to rewrite it into a familiar form

$$\mathcal{A}[\mathbf{X}] = \mathbf{B} \tag{3.27}$$

where we relabel the circulating field $\mathbf{E}_3$ to $\mathbf{X}$, $\mathbf{B} = \mathcal{T}_{3\leftarrow 1}[\mathbf{E}_1]$, and $\mathcal{A}$ is a procedure given by

$$\mathcal{A}[\mathbf{X}] = \mathcal{I}[\mathbf{X}] - \mathcal{R}_{3\leftarrow 4}\mathcal{D}_{4\leftarrow 6}\mathcal{R}_{6\leftarrow 5}\mathcal{D}_{5\leftarrow 3}[\mathbf{X}]. \tag{3.28}$$

(3.27) can be interpreted as a linear equation in $\mathbf{X}$ as $\mathcal{A}$ is made up of only linear operations it itself must be a linear operator where $\mathcal{A}[\mathbf{x}+\mathbf{y}] = \mathcal{A}[\mathbf{x}] + \mathcal{A}[\mathbf{y}]$ for all $\mathbf{x}$ and $\mathbf{y}$. The round trip part of equation (3.28) is expanded at the end of of appendix B.2.

Since equation (3.28) contains a mix of matrix and Hadamard products equation (3.27) cannot be rewritten into a Sylvester equation like equation (3.21). A number of algorithms are available to solve equation (3.27) using only the procedure that computes the matrix-vector product $\mathcal{A}[\mathbf{X}]$. These algorithms typically employ the use of a Krylov subspace such as GMRES [45], and BICGSTAB [60], both of which have easy to use

python wrappers available in scipy [210].

3.6.1 Example: aLIGO linear cavity with finite-aperture mirrors

Cavity scan

For the numerical comparison we once again perform a cavity scan on the aLIGO arm cavity as in figure 3.3, except now we add 34 cm circular apertures to both mirrors in the arm cavity, corresponding to the diameter of the aLIGO arm cavity mirrors. We change our incident beam to be composed of equal parts HG_{00}, HG_{10}, and HG_{60}. The resulting cavity scan is shown in figure 3.4.

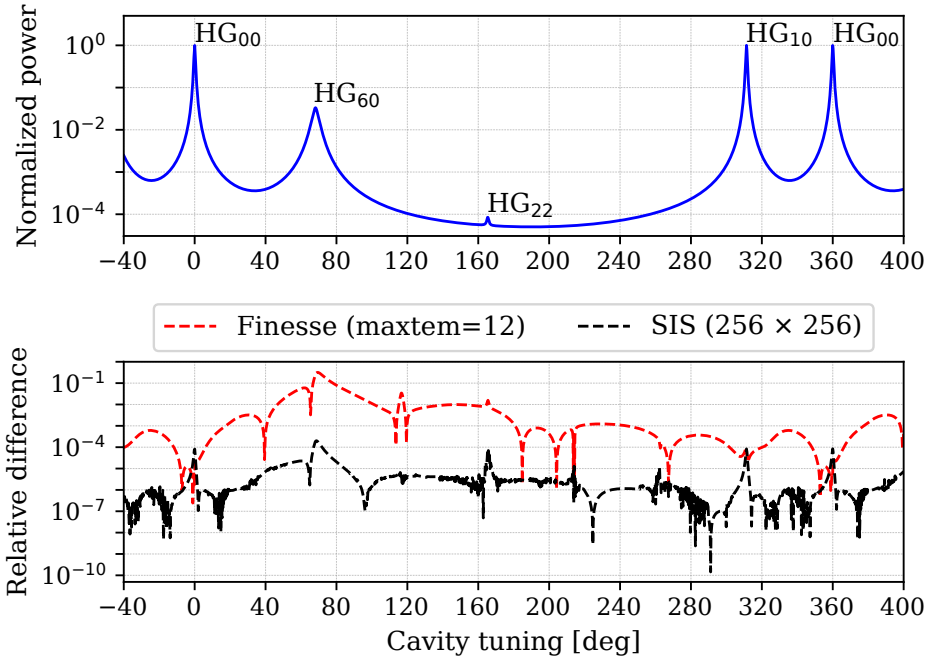

Figure 3.4: The upper plot is the circulating power inside an aLIGO arm cavity with 34 cm diameter mirrors as a function of cavity tuning ϕ. The difference between each model is indistinguishable by eye and so only the LCT circulating power is plotted. The lower plot shows the relative difference between the LCT model and an HG model Finesse (dashed red) and the SIS [106] FFT model (dashed black). The *maxtem* N parameter tells FINESSE to only model the HG_{nm} modes that have their mode order $n + m \leq N$. FINESSE, SIS, and the LCT model use the same 256 × 256 grid.

The HG_{10} and HG_{60} modes that were chosen primarily for their difference in physical extent. The larger HG_{60} interacts more strongly with the aperture than the HG_{10} and is therefore expected to have a higher clipping loss. This can be seen in figure 3.4 where

the HG_{60} resonance is both smaller and wider than the HG_{10} resonance. Additionally, a small resonance can be seen 165 degrees that corresponds to a fourth order mode. This resonance is explained by the mode scattering of the HG_{60} by the aperture to produce fourth order modes.

The LCT prediction is compared in figure 3.4 (lower) with the modal-based: Finesse, and an FFT-based model: SIS, which is typically used for modelling high spatial frequency effects in optical cavities. To maintain consistency between the models we used the same 256×256 grid in all 3 models to describe the aperture maps in figure 3.4. While the LCT and SIS models agree to within about 1 ppm, the disagreement between Finesse and LCT is several orders of magnitude worse, particularly at the heavily-clipped HG_{60} mode.

This disagreement is perhaps expected as in FINESSE an aperture is represented by a scattering matrix where each element describes how the amplitude of each apertured HG mode couples to each HG modes. The elements of this scattering matrix are given by overlap integrals, which are computed numerically. The accuracy of an HG model with apertures is then dependent on the numerical accuracy of the scattering matrix element integration, and the number of HG modes used.

Circulating field intensity distribution

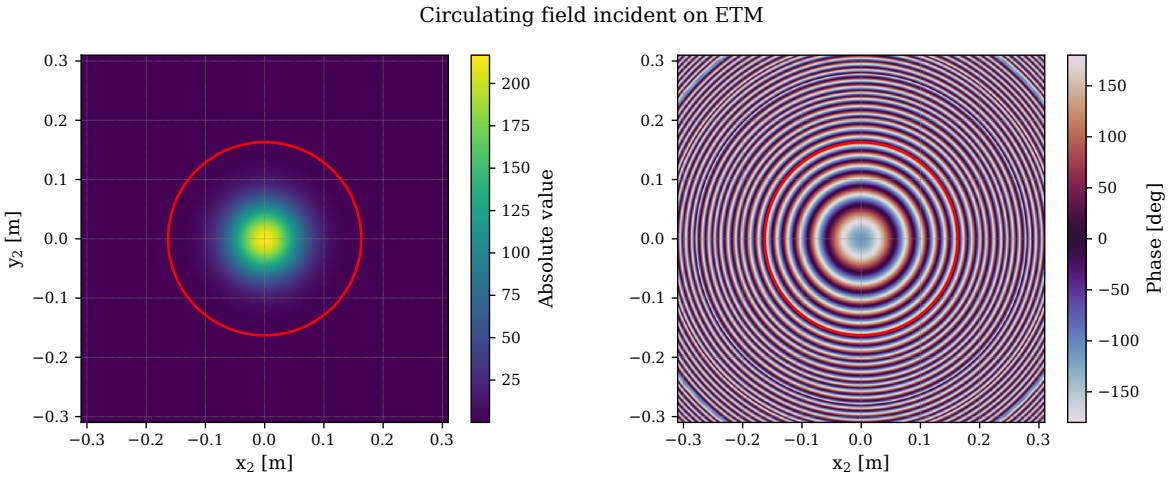

Figure 3.5: Circulating field incident onto the ETM as modelled by the LCT. The ETM aperture edge is outlined in red.

Figure 3.5 shows the complex amplitude of the circulating field incident onto the ETM. The input field is a pure HG_{00} of the arm cavity eigenmode and the arm cavity itself

is locked to the HG_{00} resonance. The field appears identical to the eigenmode of the cavity, however three orders of magnitude below what is shown in figure 3.5 are the diffraction effects caused by the finite test mass aperture. This is shown in figure 3.6 which is the same field incident onto the ETM as shown in figure 3.5 but with the field inside the ETM aperture set to zero to highlight the aperture scattering effects.

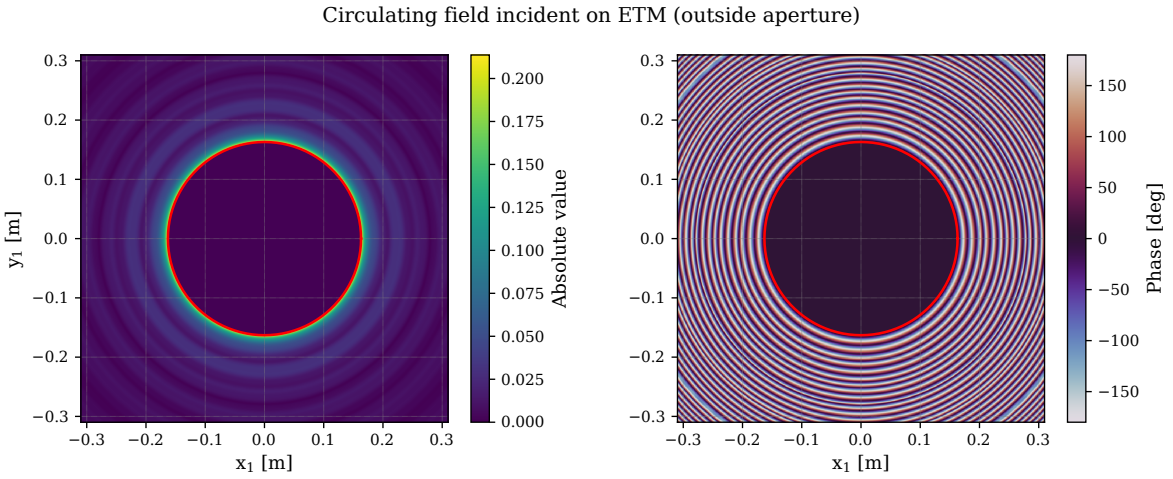

Figure 3.6: Circulating field incident onto the ETM as modelled by the LCT with the field inside the ETM aperture set to zero. The ETM aperture edge is outlined in red.

Since the diffraction effects are radially symmetric due to the circular aperture we can take a 1D cross section through figure 3.5 without losing any information. In figure 3.7 we plot the cross section of the log of the intensity against the radial distance squared. In this plot the log of the intensity of a HG_{00}, given by I_{00} is a straight line with respect to r^2.

$$\log\left[I_{00}(r)\right] = \log\left[a\exp\left[-r^2/(2w)\right]\right] \tag{3.29}$$

$$= \log\left[a\right] - \frac{r^2}{2w} \tag{3.30}$$

with the slope is given by the beam size w, and the y-intercept by the peak intensity a. This makes it easy to visually identify when the intensity begins to deviate from HG_{00}.

We see that all models agree that inside the ETM aperture the field is well described by a HG_{00}. As we move beyond the ETM aperture edge we start to see deviation from a HG_{00}. The FFT based SIS and LCT model broadly agree on the field beyond the aperture edge. The early break in the SIS data was because it was ran with a smaller grid than the LCT model. As expected the modal Finesse model has a hard

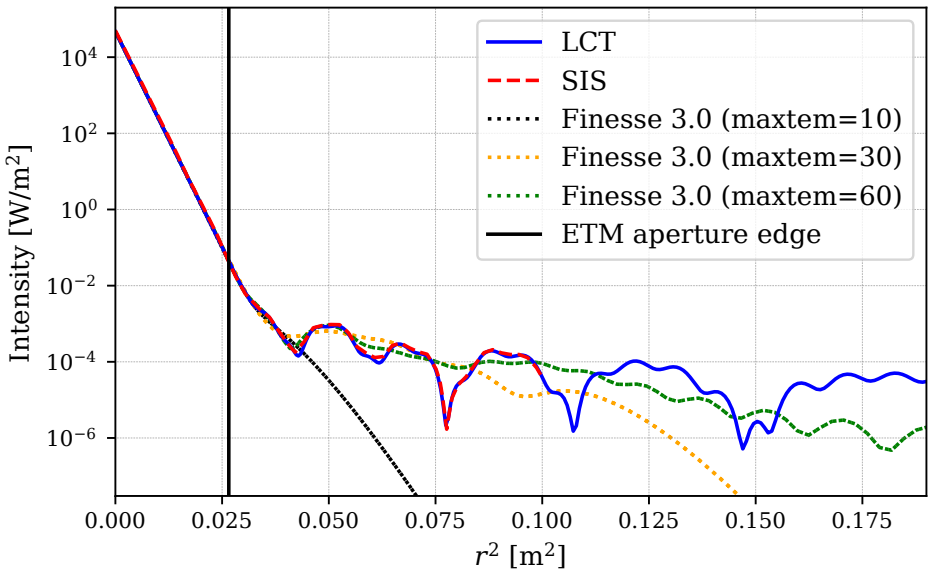

Figure 3.7: Cross section of the arm cavity circulating field incident on the ETM as modelled by an LCT model, SIS, and Finesse for varying number of HG modes.

time describing the field beyond the aperture with a small number of modes, but does appear to tend to the FFT/LCT result as the number of modes increases. It should be noted that at `maxtem=60` Finesse runs several times slower than the LCT model with a 500×500 grid.

We have applied the LCT modelling framework to model how finite apertures in the LIGO arm cavity effect the circulating field distribution. We find that it shows good agreement with previous FFT models. This demonstrates that the LCT can be used to validate FFT models in cases where modal models converge slowly.

3.6.2 Case study: aLIGO point absorbers

Example 3.6.1 assumed that the reflection maps for the mirrors described a uniform reflectivity, spherical mirror with a finite circular clear aperture. Here, we consider the effect of a point-like absorbing defect on the mirror surface, such as those discovered in the aLIGO arm-cavity mirrors [135]. These point absorbers caused a large decrease in the power recycling gain (PRG) as the power stored in the arms increased [201]. An analysis of this effect has recently been published by Brooks et al. [216]

The complex amplitude reflection map for a mirror m; $\mathbf{R}_m$ is given by

$$(\mathbf{R}_m)_{ij} = \begin{cases} 0 & \text{if } \sqrt{x_j^2 + y_i^2} \geq \dfrac{D_m}{2} \\ r_m \times \exp\left[-\dfrac{\mathrm{i}4\pi}{\lambda}\left[(\mathbf{S}_m)_{ij} + (\mathbf{C}_m)_{ij}\right]\right] & \text{otherwise,} \end{cases} \tag{3.31}$$

where r_m is the amplitude reflection coefficient, D_m is the diameter of the mirror,

$$(\mathbf{C}_m)_{ij} = -\frac{x_j^2}{2R_{m,x}} - \frac{y_i^2}{2R_{m,y}} \tag{3.32}$$

is the curvature height map and $R_{m,x}$, and $R_{m,y}$ are the radii of curvature along the x, and y-axis respectively. The point absorber height map $\mathbf{S}_m$ is derived using Eq. B8 and B9 in [216].

$$(\mathbf{S}_m)_{ij} = \begin{cases} -\dfrac{\alpha P_{\text{abs}}}{2\pi\kappa}\left(\dfrac{r_{ij}}{\sqrt{2}\omega}\right)^2 \\ \dfrac{\alpha P_{\text{abs}}}{2\pi\kappa}\left(-\dfrac{1}{2} + \log\left[\dfrac{\omega\left(h_m^2 + \sqrt{h_m^2 + r_{ij}^2}\right)}{r_{ij}\left(h_m^2 + \sqrt{h_m^2 + \omega^2}\right)}\right]\right) \end{cases} \tag{3.33}$$

where the top case is for $r_{ij} \leq \omega$ and the bottom case is for $r_{ij} > \omega$. The radial coordinate r_{ij} is given by

$$r_{ij} = \sqrt{\left(x_j - x_0\right)^2 + \left(y_i - y_0\right)^2} \tag{3.34}$$

and x_0, y_0 is the location of the point absorber, ω is the radius of the point absorber, h_m is the thickness of the mirror, P_{abs} is the absorbed power, and $\frac{\alpha}{2\pi\kappa} \approx 6.3 \times 10^{-8}$ m/W is a scaling factor derived from the thermal expansion coefficient α and thermal conductivity κ of fused silica.

A map of a surface bump due to a 40 μm diameter point absorber offset by 3 cm from the center of a 34 cm diameter, 20 cm thick mirror and 20 mW of absorbed power is shown in figure 3.8. The eigenmodes and eigenvalues of (3.28) were computed using the Arnoldi method in ARPACK [68] for a range of absorbed powers and defect locations. While the shape of the lowest-order eigenmode is almost identical to the HG_{00} mode,

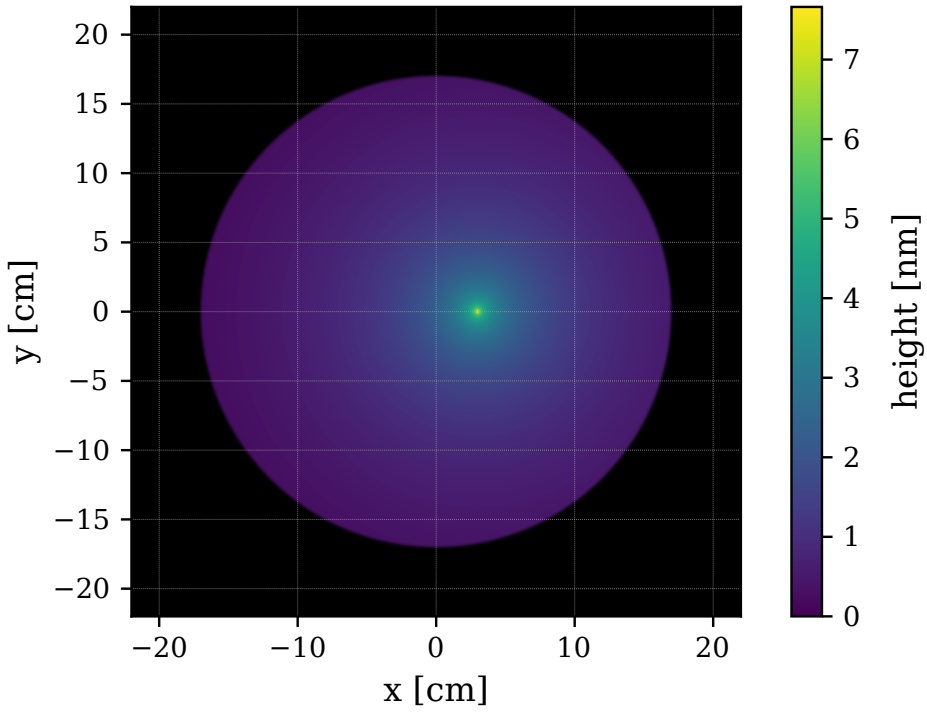

Figure 3.8: A height map of a 34 cm mirror with a 40 μm diameter point absorber with 20 mW of absorbed power offset 3 cm in the x-axis from the center of the optic.

its eigenvalue varies significantly with point absorber position and mirror diameter as shown in figure 3.9.

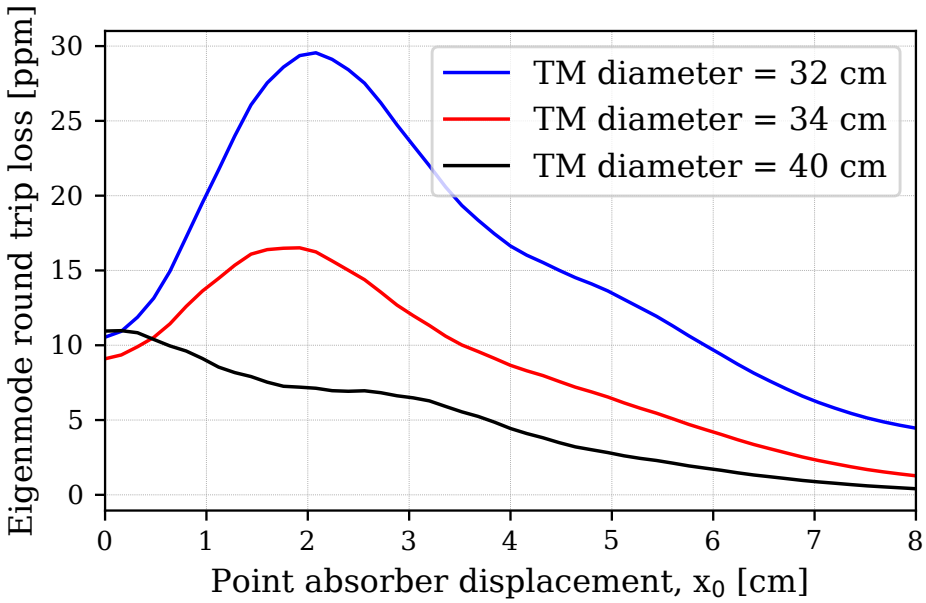

Figure 3.9: A plot of round trip loss for the lowest order mode in the aLIGO arm cavity versus point absorber position along the x-axis for three different arm cavity test mass (TM) mirror diameters: 32 cm (blue), 34 cm (red), and 40 cm (black). The loss is explicitly computed as $1 - |\gamma_0|^2$.

We can compute the decrease in PRG that would result from this point absorber loss by using Eq. 6 in [145]

$$\mathrm{PRG} = \left(\frac{t_p}{1 - r_p r_a} \right)^2 \tag{3.35}$$

where t_p and r_p are the amplitude transmission and reflection coefficients of the power recycling mirror (PRM) respectively. In this equation and following two, $r = \sqrt{1 - t^2}$. We define the effective arm cavity amplitude reflection coefficient r_a as

$$r_a = \frac{1}{r_i} \left(\frac{g_{\mathrm{rt}} - r_i^2}{1 - g_{\mathrm{rt}}} \right) \tag{3.36}$$

where t_i and r_i are the amplitude transmission and reflection coefficients of the input test mass (ITM) and g_{rt} is the round trip arm gain on resonance, given by

$$g_{\mathrm{rt}} = r_i r_e |\gamma_0| \sqrt{1 - \Gamma} \tag{3.37}$$

where r_e is the amplitude reflectivity of the end test mass (ETM) mirror, γ_0 is the round trip eigenvalue of the u_0 arm cavity eigenmode, and Γ is an additional round trip loss factor. Taking the absolute value of the eigenvalue γ_0 is effectively equivalent to making the arm cavity resonant for the u_0 eigenmode.

A summary of the necessary constant parameters needed to compute the PRG are given in table 3.2.

t_p^2	t_i^2	t_e^2	Γ
0.03	0.014	5×10^{-6}	60×10^{-6}

Table 3.2: Relevant aLIGO parameters for computing the PRG.

In this study we assume the point absorber has a negligible effect on all previously mentioned parameters with the exception of γ_0. Computing the PRG as a function of point absorber absorbed power for three different absorber positions is shown in figure 3.10. The additional round trip loss Γ was set to 60 ppm to match the experimentally observed PRG at low power. We assume that for less than 40 mW of absorbed power the height map is linearly proportional to the absorbed power. This is to be

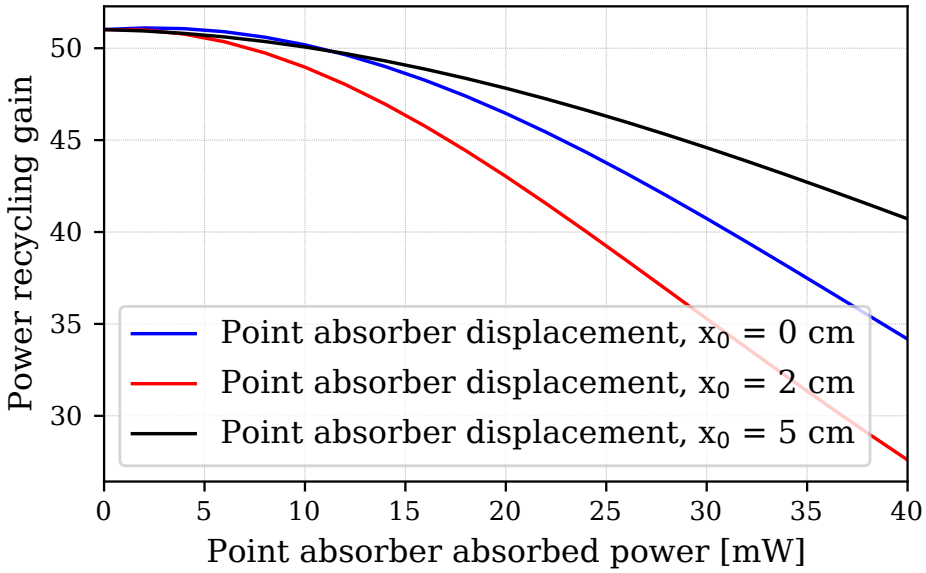

Figure 3.10: A plot of the PRG decreasing with increased power absorbed by a 40 μm point absorber located at 0 cm (blue), 2 cm (red), and 5 cm (black) away from the center of the optic.

compared to figure 4 in [216], which shows a similar trend for PRG decreasing as a function of circulating power in the arm cavity.

Perhaps surprisingly the loss increases initially as the point absorber moves away from the center of the optic, peaking at about 2 cm where afterwards it monotonically decreases. This is better shown in figure 3.9 where the point absorber power is kept constant at 20 mW as it is moved across the optic. This loss peak at 2 cm is very sensitive to the arm cavity mirror size.

The explanation for the peak in arm cavity loss at 2 cm seen in figure 3.9 is that the point absorber scattering maximizes scattering the HG_{00} into 7th order modes. The 7th order modes resonate nearly at the same phase as the HG_{00} and so are partially resonantly enhanced when the arm cavity is locked onto the HG_{00}. This can be most clearly seen by performing an HG decomposition on the arm cavity circulating field as was done in figure 3.11.

The explanation behind the dependence on mirror size then follows as the larger 7th order modes interact strongly with the edges of the hard aperture. Decreasing the size of the mirrors increases the loss on the 7th order modes, thus broadening their resonance, allowing for more resonant enhancement from the HG_{00}. Conversely, increasing the

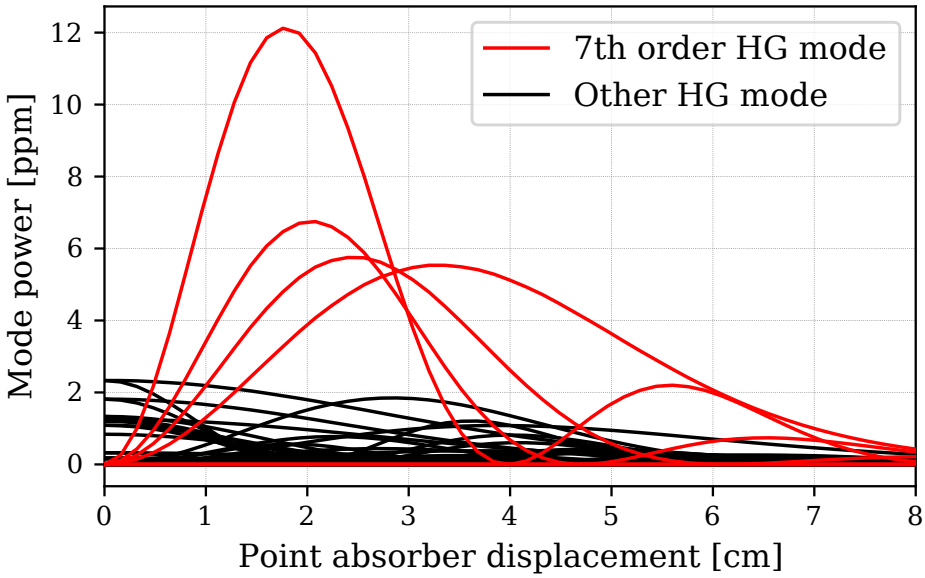

Figure 3.11: An HG decomposition of the arm cavity circulating field with 34 cm mirrors. The seventh order modes are highlighted in red. The power in all $HG_{n,m}$ with $n + m \leq 10$ are plotted with the exception of the HG_{00} mode.

size of the mirrors narrows the 7th order resonance, decreasing the enhancement from the HG_{00}.

A similar conclusion about the contribution of 7th order modes to the loss was made by Brooks et al. [216], though following a different formalism. This case study demonstrates that a combination of apertures, reflection maps, and resonant conditions must be modelled sufficiently to see these HOM loss effects.

3.7 Conclusion

We have presented an introduction to LCTs and their application to free-space wave propagation through first order optical systems [220]. A new application of the LCT for solving the circulating field in a Fabry-Perot cavity using general purpose sparse linear algebra algorithms was demonstrated. The LCT method shows good numerical agreement with analytical solutions and established FFT-models, as well as reproducing results from recent aLIGO point absorber models. This highlights how such modeling tools can be used in designing future detectors to avoid such problems. Future work will need to extend the LCT method to coupled cavities to allow us to model complete interferometric systems. Further work is also needed to identify which linear algebra methods optimally solve the LCT matrices as well as packaging it up into a usable

tool, such as FINESSE or SIS.

Chapter 4

Towards coupled cavity LCT models

The next step in developing the LCT modelling framework is to extend it from solving the circulating field in a single cavity to solving the circulating fields in coupled cavities. We achieve this by treating an optical system as a matrix signal flow graph (MSFG), which yields a small system of linear matrix equations after applying a graph reduction procedure. The system of linear matrix equations can then be solved using Krylov subspace methods on their structured matrix representations, similar to what was described section 3.6.

A significant portion of this chapter relies on graph theory and frequently uses their terminology. We make the assumption that the reader is not familiar with graph theory and so we dedicate the following subsection to defining basic graph theoretic terms. The reader may skip to the next section and refer back when an unfamiliar graph theoretic term is used.

Graph theory introductory summary

A graph or network is a collection of nodes connected in pairs by edges. A node is a fundamental graph element that in our use case denotes a variable in a linear equation. An edge is the other fundamental graph element that represents a connection between two nodes. We only use directed edges, where the input and output nodes are distinct from each other. In our use case an edge denotes a linear transformation of the variable

from the input node to the variable at the output node. It is convenient to draw a directed edge as an arrow where the tail of the arrow connects to the input node and the head of the arrow connects to the output node. The numerical value of a node or edge is called the node weight and edge weight respectively.

Some special cases of nodes and edges have names associated to them. A source node is a node that has no edges going into it. Conversely, a sink node is a node that has no edges coming out of it. A loop, or self-loop is a name for an edge that starts and ends at the same node.

4.1 Signal flow graphs

The input/output relations of a field interacting with an optical component can often be described by a set of linear equations. These linear equations can be represented by a transfer matrix acting on a field vector. The usage of transfer matrices to model circulating cavity fields is well described in chapter 2 of [140].

A system of coupled transfer matrices can be rewritten as a single matrix describing the couplings between all fields in an optical system. This matrix is called the system transfer matrix, or the interferometer matrix. Any system transfer matrix can be interpreted as the adjacency matrix of a graph, with the matrix elements corresponding to weights of the graph edges. This is shown in figure 4.1.

$$\begin{bmatrix} A & 0 & B \\ C & 0 & 0 \\ 0 & D & 0 \end{bmatrix} \begin{bmatrix} a_0 \\ b_0 \\ c_0 \end{bmatrix} = \begin{bmatrix} a_1 \\ b_1 \\ c_1 \end{bmatrix} \quad \Longrightarrow$$

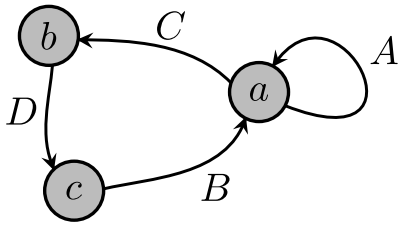

Figure 4.1: A system of linear equations from a weighted adjacency matrix multiplied with the node vector and its corresponding graph.

It should be noted that some authors define the adjacency matrix as the transpose of the matrix in figure 4.1. This difference comes from the choice whether to map the (input, output) node pairs on to (row, column) or (column, row) indices. We map (input, output) nodes to (column, row) indices because the resulting adjacency matrix can then be multiplied with the node vector to produce the system of equations that

describe that graph as was done in figure 4.1.

The matrix representation is equivalent to the graph picture with one exception; the matrix implicitly encodes an ordering on the nodes (in figure 4.1 the order is (a, b, c)), whereas the nodes in the graph are unordered. For figure 4.1 there are a total of 6 distinct matrix-vector equations that produce the same graph. They can be obtained by rearranging the nodes (a, b, c) and swapping the matrix rows and columns such that they produce the same set of linear equations. The fact that a set of single set of linear equations maps to a single graph regardless of how the equations are ordered gives a distinct advantage to the graph picture over the matrix representation. Another benefit of graphs is that operations add or remove nodes are expressed relatively cleanly whereas in the matrix representation those operations would change the size of the matrix, which is inelegant, and more importantly computationally inefficient.

A directed graph with edge weights like the one shown in figure 4.1 is sometimes called a *signal flow graph* (SFG). Signal flow graphs have commonly been used to model electronic circuits and control systems. The transfer function of the system at any node can be obtained by *Mason's gain formula* [8, 9]. In optics, scalar signal flow graphs together with Mason's gain formula have been used for planar optical models [22, 31, 63, 66, 114, 122, 214]. Despite their benefits, the usage of signal flow graphs has diminished for modelling electronic circuits in favor of sparse matrix methods, likely due to readily available and highly efficient sparse matrix libraries.

Unlike electrical circuits, optical models have an extra layer of complexity that makes signal flow graphs particularly useful. The value or weight at an optical node is in general not a scalar but a vector, where the elements of the vector describe the different components of the transverse extent of the optical field. A natural choice is to use higher order mode amplitudes as the elements of an optical node weight vector. Following this description the edges in an optical model become linear operators that transform the field vectors between nodes. In the sparse matrix formalism these vectorial optical models correspond to sparse matrices with dense submatrix blocks, also known as block sparse matrices. These block sparse matrices can be solved using the same sparse matrix solvers as electrical circuits but often the dense blocks are handled poorly, resulting in slower models.

Extending the signal flow graph formalism to deal with vectors and linear operators results in *matrix signal flow graphs* (MSFGs) [10, 12, 25, 27]. Solving MSFGs requires a different approach as Mason's gain formula is only valid for scalar signal flow graphs and cannot be used to solve a MSFG. Recently Stone et. al. have demonstrated that MSFGs can be used to model higher order mode conversion in resonant coupled cavities [225]. We show that a relatively unoptimized graph reduction procedure acting on an MSFG can outperform highly optimized sparse matrix solvers when the number of higher order transverse modes is large enough.

4.1.1 Graph reduction

A general method for solving both scalar and matrix SFGs is *graph reduction*, which is a method for procedurally simplifying an SFG based on a handful of simple rules until a irreducible graph is obtained. The irreducible graph is then a collection of sinks, sources, and possibly self-loops where the solution can then be read off from the paths connecting the sources to the sinks and inverting any self-loops if they are present.

There are a total of three graph reduction rules for reducing any MSFG. They are the product rule, sum rule, and the self-loop rule.

Product rule

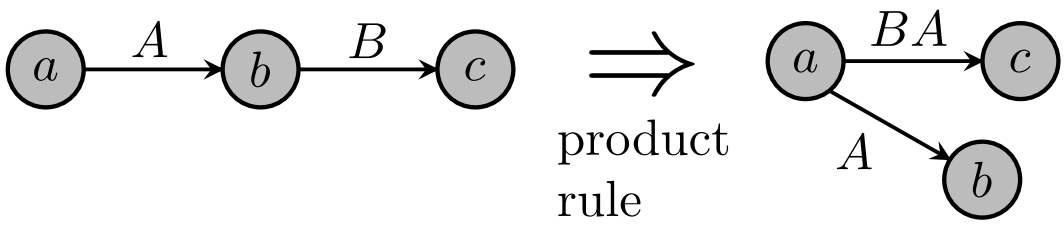

Figure 4.2: Product rule for graph reduction

The product rule states that two edges in series can be combined into a single edge where the new edge weight is applying the two operators one after each other. If the operators are matrices then this is a matrix product of the two matrices. If the operators are scalars then this just becomes a product of the two edges.

The product reduction rule can be expressed in a form that either eliminates or preserves nodes. The eliminated nodes are always sinks and so do not contribute to the

result. We use the node preserving form since these sink nodes correspond to viewing the optical field at another point in the optical system, which can be useful. For large graphs the sink nodes can lead to a cluttered diagram and in those cases we will remove the sink nodes for clarity.

Sum rule

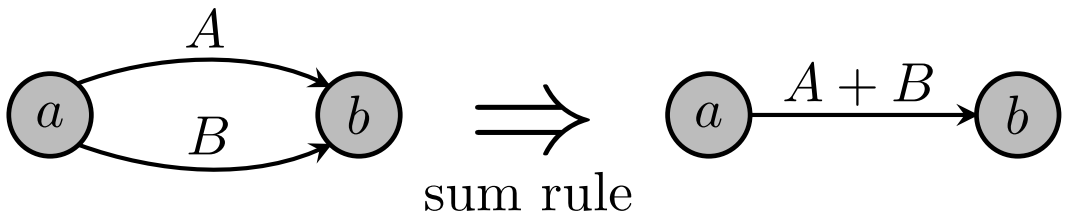

Figure 4.3: Sum rule for graph reduction.

The sum rule states that two parallel edges can be combined into a single edge where the new edge weight is given by the summing the result of applying each operator individually. If the operators are matrices then this is the sum of the matrices. If the operators are scalars then this is the sum of the scalars.

Self-loop rule

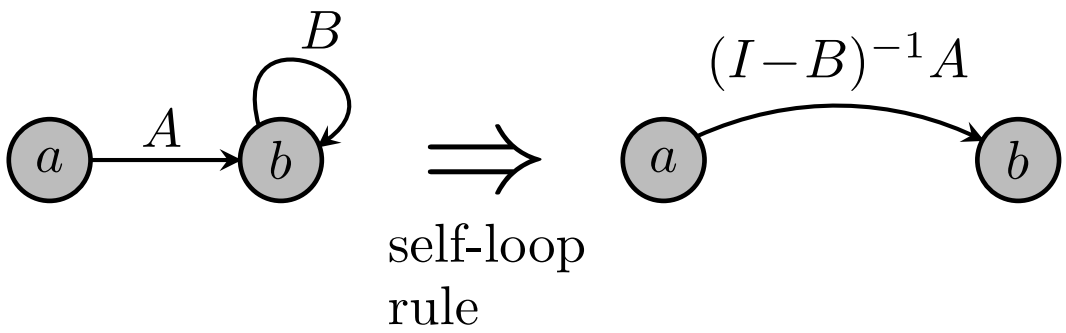

Figure 4.4: Self-loop rule for graph reduction. A short derivation of the self-loop rule is shown in equation (4.1)

$$
\begin{aligned}
b &= Bb + Aa \qquad (4.1)\\
(I - B)b &= Aa \\
b &= (I - B)^{-1}Aa
\end{aligned}
$$

The self-loop rule states that a self-loop can be transformed into an edge whose weight is given by the inverse of the identity minus the loop operator. This rule is straightforward to implement if the loop operator is a matrix. In the case of our LCT models where the operators are given by structured matrix multiplication algorithms. The inverse in our case is not readily available and so we do not include the self-loop rule in our graph reduction procedure. The self-loops instead are all solved simultaneously at a later stage.

4.1.2 Single linear cavity

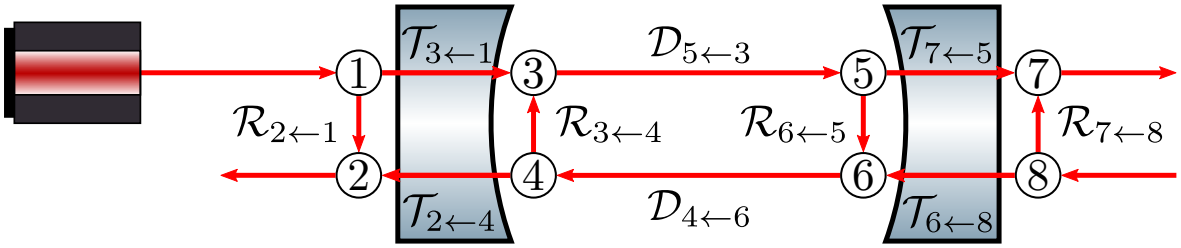

Figure 4.5: Network graph of a cavity. Reproduced from figure 3.2.

Taking the graph from figure 4.5 we can obtain a irreducible graph from the following graph reductions:

1. product rule at node 4
2. product rule at node 5
3. product rule at node 6

The resulting reduced graph shown in figure 4.6 contains only sources, sinks, and a single self-loop at node 3. The graph can be made visually clearer by removing all sink nodes since they do not contribute to the circulating field.

The edge weight of the self-loop is identical to the round-trip operator given in equation (3.18). Applying the self-loop rule results in equation (3.19), which can be solved in a number of ways as described in section 3.5. These equations were originally obtained using algebraic manipulation of operator expressions, which is not trivial to write as a computer program. Whereas the graph reduction method allows one to obtain the same expressions from a given signal flow graph by following two or three rules, making for a relatively simple computer implementation. For a single cavity the benefit of obtaining operator expressions from a computer algorithm is minimal, however for more

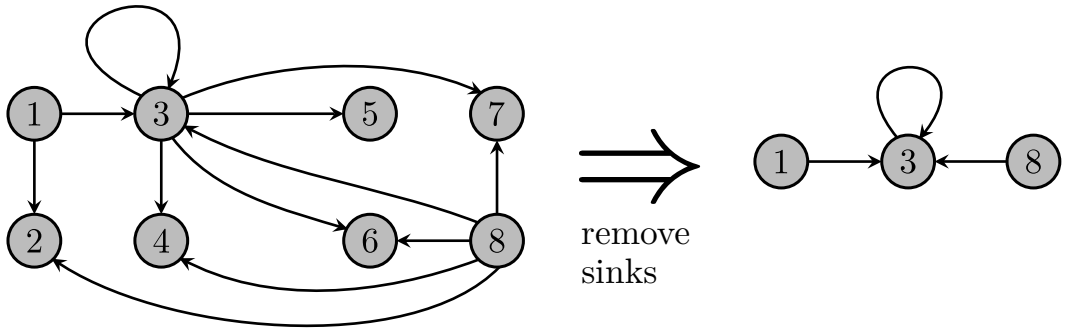

Figure 4.6: Left is the result of graph reduction applied to figure 4.5. The resulting operators are omitted from the diagram for brevity. Right is the same reduced graph with all of the sink nodes removed.

complicated optical systems with multiple coupled cavities the expressions become too unwieldy to manipulate by hand and the algorithm becomes helpful.

It should be noted that this graph reduction is not unique. The ordering of graph reduction steps is arbitrary. A different sequence of reduction steps can result in a different but equivalent irreducible graph. That is, the graph may look different but should produce nearly identical numerical results when solved. The LCT composition rule complicates this somewhat since it is not satisfied in the discrete case and can make the differences between equivalent graph reductions much larger than floating point precision unless a sufficiently fine LCT grid is used.

It is worth noting that the number of self-loops in an irreducible graph is not guaranteed to be constant. In most optical systems the number of self-loops often maps directly onto the number of cavities and this is the case for the optical systems covered here. However, Riegle showed a simple graph with 7 nodes in figure 3 of [27] that when reduced can have either 2 or 3 self-loops depending on the order of reduced nodes. The simplest optical systems that exhibit a variable number of self-loops when reduced typically include multiple beamsplitters where the reflected and transmitted ports are connected to each other in such a way that there is not an easy way to identify distinct cavities. Riegle formulated the problem of finding the optimal reduction as the one that produced the smallest number of self-loops, which he related to finding the minimum feedback vertex set of the graph. More work is needed to be able to make definitive statements about the number of self-loops in a reduced graph and the physical interpretation of these self-loops. For our applications the most complicated optical system

is the dual recycled Fabry-Perot Michelson, which has only one beamsplitter and so the equivalence of self-loops to cavities is adequate.

After applying the self-loop rule to node 3 in figure 4.6 the field at every other node cavity such as the cavity reflection and transmission can be obtained from linear combinations of the source and circulating fields. If the node preserving form of the graph reduction rules was used then the nodes still exist as sinks. The edges that connect the sources and circulating fields to the sinks in the irreducible graph are the propagation matrix elements in equation (4.2).

The field at the remaining nodes is then given by

$$\begin{bmatrix} E_2 \\ E_4 \\ E_5 \\ E_6 \\ E_7 \end{bmatrix} = \begin{bmatrix} M_{2\leftarrow 1} & M_{2\leftarrow 3} & M_{2\leftarrow 8} \\ M_{4\leftarrow 1} & M_{4\leftarrow 3} & M_{4\leftarrow 8} \\ M_{5\leftarrow 1} & M_{5\leftarrow 3} & M_{5\leftarrow 8} \\ M_{6\leftarrow 1} & M_{6\leftarrow 3} & M_{6\leftarrow 8} \\ M_{7\leftarrow 1} & M_{7\leftarrow 3} & M_{7\leftarrow 8} \end{bmatrix} \begin{bmatrix} E_1 \\ E_3 \\ E_8 \end{bmatrix} \tag{4.2}$$

Where the propagation matrix elements for field E_1 are

$$\begin{aligned} M_{2\leftarrow 1} &= \mathcal{R}_{2\leftarrow 1} \\ M_{4\leftarrow 1} &= 0 \\ M_{5\leftarrow 1} &= 0 \\ M_{6\leftarrow 1} &= 0 \\ M_{7\leftarrow 1} &= 0 \end{aligned}$$

where we adopt the convention that a lack of an edge between nodes i and j corresponds to a zero or null operator for that propagation matrix element. The matrix propagation

elements for field E_3 are

$$M_{2\leftarrow 3} = \mathcal{T}_{2\leftarrow 4}\mathcal{D}_{4\leftarrow 6}\mathcal{R}_{6\leftarrow 5}\mathcal{D}_{5\leftarrow 3}$$
$$M_{4\leftarrow 3} = \mathcal{D}_{4\leftarrow 6}\mathcal{R}_{6\leftarrow 5}\mathcal{D}_{5\leftarrow 3}$$
$$M_{5\leftarrow 3} = \mathcal{D}_{5\leftarrow 3}$$
$$M_{6\leftarrow 3} = \mathcal{R}_{6\leftarrow 5}\mathcal{D}_{5\leftarrow 3}$$
$$M_{7\leftarrow 3} = \mathcal{T}_{7\leftarrow 5}\mathcal{D}_{5\leftarrow 3}$$

and the propagation matrix elements for field E_8 are

$$M_{2\leftarrow 8} = 0$$
$$M_{4\leftarrow 8} = 0$$
$$M_{5\leftarrow 8} = 0$$
$$M_{6\leftarrow 8} = 0$$
$$M_{7\leftarrow 8} = \mathcal{R}_{7\leftarrow 8}$$

Though the matrix elements may seem obvious from a visual inspection of the graph, they quickly becomes unobvious in more complicated systems. The approach outlined here generalizes to arbitrarily complicated optical systems and so we will summarize the algorithm here.

1. Construct a graph from coupling component-wise linear equations for the incoming and outgoing fields as described in chapter 2 of [140].
2. Loop over every node in the graph and apply the product graph reduction rule if it applies
3. Loop over every pair of nodes in the graph and apply the sum graph reduction rule if it applies
4. Solve the linear system given by the irreducible graph
5. Propagate the solved and source fields to every remaining node in the graph

Steps 2 and 3 imply some kind of ordering on the nodes in the graph to loop over,

which in general is arbitrary. In principle any ordering can be used provided the graph at the end is reduced to sources, sinks, and self-loops. Step 4 is not illustrated well by the single cavity example shown here, but is more clear for the power recycled cavity discussed below.

4.1.3 Power recycled Fabry-Perot cavity

For the next step up in complexity we will consider the aLIGO power recycling cavity into one of the arm cavities as an example of a coupled cavity. The graph for this optical system is given in figure 4.7.

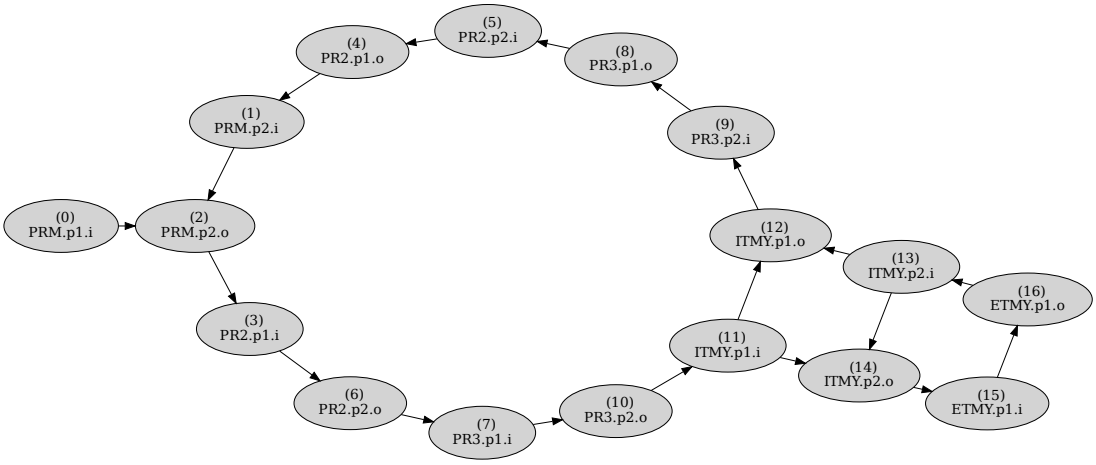

Figure 4.7: Graph of a power recycled arm cavity.

The node naming convention is adopted from `Finesse3` where the node name has three parts delimited by dots. The first part is the component name (e.g. PRM, PR2, PR3, ITMY, ETMY). The second part is the port number of the component, which in this case maps onto either the front or back surface of a mirror. For example `ITMY.p1` maps onto the back surface of the ITMY whereas `ETMY.p1` maps onto the front surface of the ETMY. The third part determines if the field is incoming or outgoing relative to the port. We also assign a unique integer to each of the nodes, which we will use as a shorthand when referring to that node. The integer labelling in general is arbitrary, we used the order in which the nodes were added to the graph.

To explain the visual appearance of figure 4.7, specifically the positioning of the nodes we first have to note that the drawing of graphs is in general arbitrary. The nodes and edges can be drawn by hand in a way that highlights some kind of physical intuition

as was done in figures 3.2 and 4.6. However, for large graphs and in general it is more appropriate to use a general purpose graph layout method for determining the position of nodes when drawing these graphs. We provide a short summary of the technicalities of graph layout methods below. The reader may skip to the next section where we discuss how to analyze the graph.

Graph layout algorithms

The main general purpose graph layout methods come in two varieties: *force-directed*, and *energy minimizing*. Both are similar in that they determine the positions of the nodes by treating the graph dynamical system where all nodes experience a repulsive and attractive force that has to be balanced. In this scheme it is common to model the nodes as point charges and the edges as springs but other forces can be used to produce a visually different layout. For instance in the Kamada-Kawai graph layout [55] every node is connected to every other node by a spring regardless if there is an edge connecting them or not. The natural length of the spring between two nodes is given by the graph theoretic distance between them, which is the number of edges in the shortest path connecting the two nodes.

Most graph layouts begin with the nodes initially placed, often in randomly generated positions. The position of the nodes are then iteratively updated by the modelled forces until the graph reaches a stationary state where each node experiences zero net force. In energy minimizing layouts the forces give rise to a potential energy which is fed into a minimization algorithm such as gradient descent to determine the optimal position of the nodes that minimizes this potential energy.

Both methods produce similar results, but the force-directed layouts often run into the issue that they settle on some kind of local minimum that might not look visually pleasing. The energy minimizing method can also get stuck on local minima, but global minimization methods can be used to alleviate this whereas the force-directed method can only guarantee to settle on a local minimum. A spring-electrical force-directed layout and an energy minimizing Kamada-Kawai layout is available in the `graphviz` package [92] through the `fdp` and `neato` binaries respectively. For the graph diagrams presented here we chose to use the `neato` layout, which produced the most visually clear and aesthetically pleasing diagrams.

Graph reduction

We begin by applying the product rule on the path from `PRM.p2.o` to `ITMY.p1.i`, and the path from `ITMY.p1.o` to `PRM.p2.o`. This corresponds to applying the product rule on the following nodes {3,6,7,10,11,12,9,8,5,4,1}. The next step is to reduce the arm cavity by applying the product rule to nodes {15,16,13}, which is the same reduction that was done in section 4.1.2.

The resulting irreducible graph is then a source node `PRM.p1.i`, two coupled self-loops at `PRM.p2.o` and `ITMY.p1.o`, and a bunch of sink nodes. This graph is shown in figure 4.8.

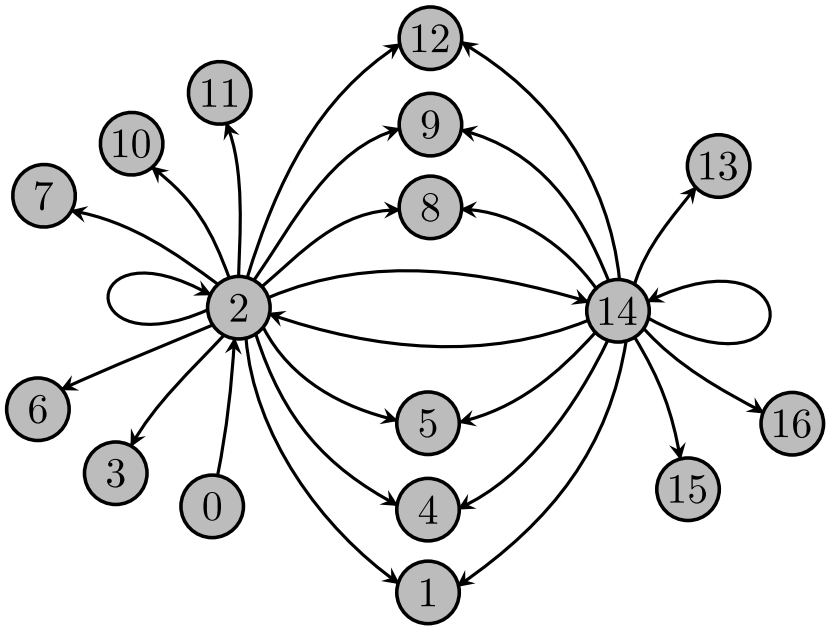

Figure 4.8: Resulting graph from applying the graph reduction procedure to the power recycled cavity graph from figure 4.7.

For clarity we can remove all the sink nodes from the graph since they have no causal influence on the graph. The sinkless reduced graph is shown in figure 4.9.

At this point the only graph reduction rule that applies is the self-loop elimination, which we can only use for matrix and scalar edges. In our case the edges are operators and so the self-loops ca not be removed at this stage.

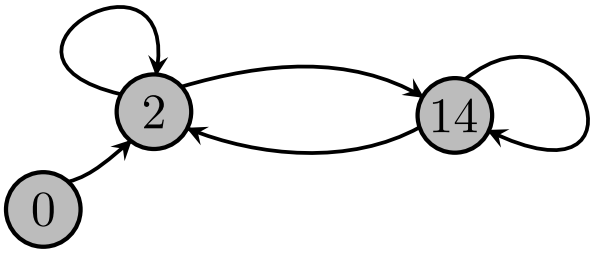

Figure 4.9: Reduced power recycled cavity graph from figure 4.8 with all of the sink nodes removed.

Graph solving

To solve figure 4.8 we only consider the nodes with self-loops. We have labelled `PRM.p2.o` as node 2 and `ITMY.p1.o` as node 14. From there we construct the following linear operator equation

$$\begin{bmatrix} a_2 \\ a_{14} \end{bmatrix} = \begin{bmatrix} M_{2\leftarrow 2} & M_{2\leftarrow 14} \\ M_{14\leftarrow 2} & M_{14\leftarrow 14} \end{bmatrix} \begin{bmatrix} a_2 \\ a_{14} \end{bmatrix} + \begin{bmatrix} b_2 \\ b_{14} \end{bmatrix} \tag{4.3}$$

where $[a_2, a_{14}]^T$ is the vector containing the circulating fields at nodes 2 and 14 respectfully. $[b_2, b_{14}]^T$ is the vector containing the sum of all source fields propagated to nodes 2 and 14 respectively. The matrix elements $M_{i\leftarrow i}$ describe the self-loop operators and $M_{i\leftarrow j}$ where $i \neq j$ describes how the self-loops couple to each other. Equation (4.3) is just a generalization of equation (3.16) to coupled cavities. We now list the explicit form of the path operators.

$$\begin{aligned}
M_{2\leftarrow 2} &= \mathcal{R}_{2\leftarrow 1}\mathcal{D}_{1\leftarrow 4}\mathcal{R}_{4\leftarrow 5}\mathcal{D}_{5\leftarrow 8}\mathcal{R}_{8\leftarrow 9}\mathcal{D}_{9\leftarrow 12}\mathcal{R}_{12\leftarrow 11}\mathcal{D}_{11\leftarrow 10}\mathcal{R}_{10\leftarrow 7}\mathcal{D}_{7\leftarrow 6}\mathcal{R}_{6\leftarrow 3}\mathcal{D}_{3\leftarrow 2} \\
M_{14\leftarrow 2} &= \mathcal{T}_{14\leftarrow 11}\mathcal{D}_{11\leftarrow 10}\mathcal{R}_{10\leftarrow 7}\mathcal{D}_{7\leftarrow 6}\mathcal{R}_{6\leftarrow 3}\mathcal{D}_{3\leftarrow 2} \\
M_{2\leftarrow 14} &= \mathcal{R}_{2\leftarrow 1}\mathcal{D}_{1\leftarrow 4}\mathcal{R}_{4\leftarrow 5}\mathcal{D}_{5\leftarrow 8}\mathcal{R}_{8\leftarrow 9}\mathcal{D}_{9\leftarrow 12}\mathcal{T}_{12\leftarrow 13}\mathcal{D}_{13\leftarrow 16}\mathcal{R}_{16\leftarrow 15}\mathcal{D}_{15\leftarrow 14} \\
M_{14\leftarrow 14} &= \mathcal{R}_{14\leftarrow 13}\mathcal{D}_{13\leftarrow 16}\mathcal{R}_{16\leftarrow 15}\mathcal{D}_{15\leftarrow 14}
\end{aligned}$$

The source terms are

$$b_2 = \mathcal{T}_{2\leftarrow 0} E_0$$
$$b_{14} = 0$$

Rearranging into a more familiar form

$$\left(\begin{bmatrix} I & 0 \\ 0 & I \end{bmatrix} - \begin{bmatrix} M_{2\leftarrow 2} & M_{2\leftarrow 14} \\ M_{14\leftarrow 2} & M_{14\leftarrow 14} \end{bmatrix} \right) \begin{bmatrix} a_2 \\ a_{14} \end{bmatrix} = \begin{bmatrix} b_2 \\ b_{14} \end{bmatrix} \tag{4.4}$$

where I is the identity operator. Equation (4.4) is then of the form $Ax = b$, where $A = I - M$. The M operator can be thought of as a generalization of the round trip operator in coupled cavities.

This operator equation can be solved using the same Krylov subspace methods as in section 3.6. The difficulty is turning the A operator, which is a composite object consisting of linear combinations of operators into something that looks like a first-class operator. This will typically require some kind of method overloading for matrix-vector multiplication. The scipy [210] library provides an API for defining arbitrary structured linear operators using `scipy.sparse.linalg.LinearOperator`, which is what we use with scipy's Krylov solvers.

4.1.4 Dual recycled Fabry-Perot Michelson interferometer

The dual recycled Fabry-Perot Michelson interferometer (DRFPMI) is a more complicated optical system than the power recycled Fabry-Perot cavity. The DRFPMI serves as the base optical layout in current generation gravitational wave detectors such as aLIGO and AdVirgo. The network graph of a DRFPMI is shown in figure 4.10.

To obtain the irreducible graph we apply the product rule on every node except `PRM.p1.i`, `PRM.p1.o` `PRM.p2.o`, `ITMX.p2.o`, `ITMY.p2.o`, and `SRM.p1.i`, corresponding to nodes 0, 2, 28, 22, and 39 respectively. The order in which the product rule is applied seems to not change the final graph. We used the increasing order based on the integer node label.

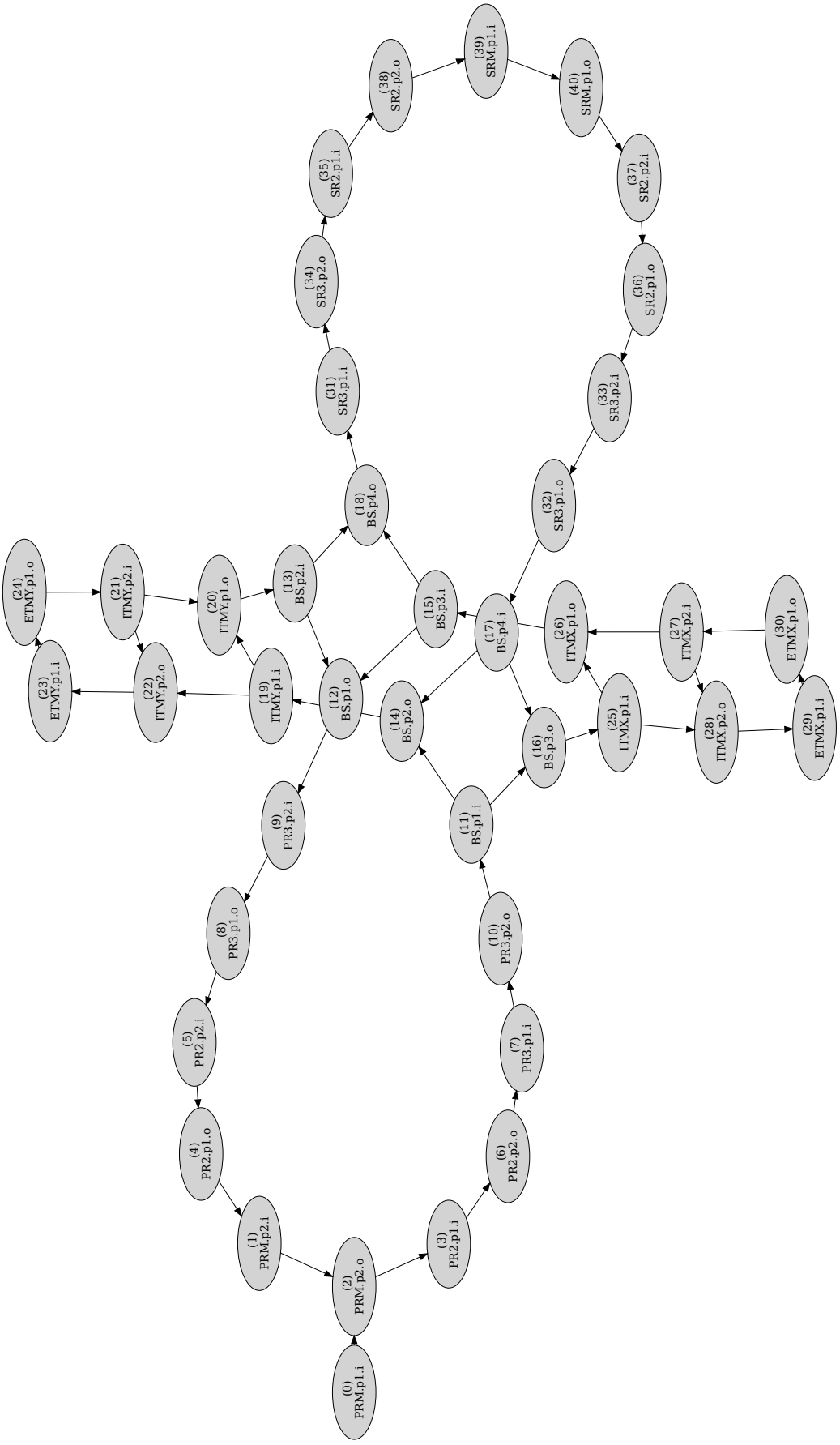

Figure 4.10: Graph of a dual recycled Fabry-Perot michelson interferometer.

The irreducible graph then consists of 4 coupled self-loops located at nodes {2,28,22,39}, a source node at node 0 with every other node being a sink. The corresponding reduced DRFPMI graph is shown in figure 4.11. For clarity we omit drawing any of the 36 sink nodes.

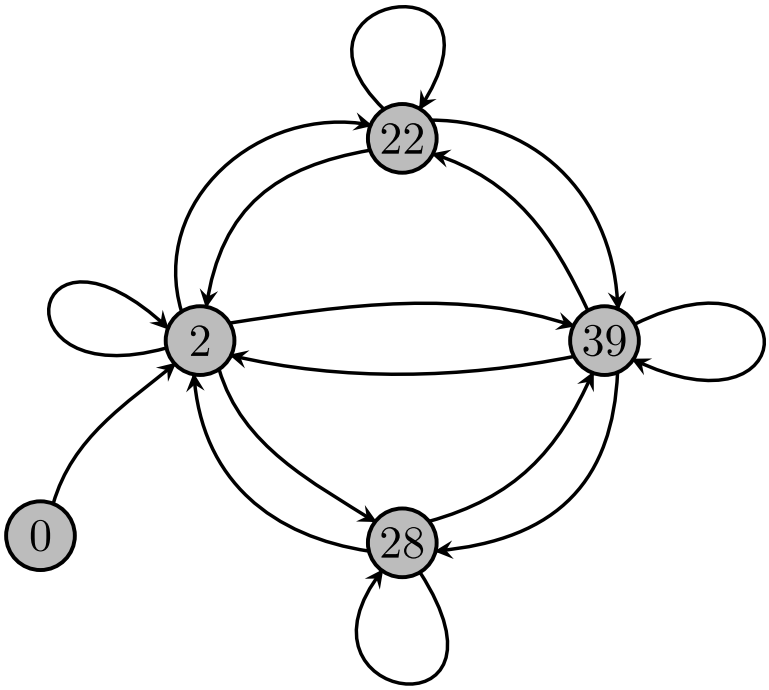

Figure 4.11: An irreducible graph of a dual recycled Fabry-Perot michelson interferometer with integer node labels and all sink nodes removed.

To solve the graph we then apply the exact same procedure as before and write out the linear equation describing the irreducible graph.

$$\begin{bmatrix} a_2 \\ a_{28} \\ a_{22} \\ a_{39} \end{bmatrix} = \begin{bmatrix} M_{2\leftarrow 2} & M_{2\leftarrow 28} & M_{2\leftarrow 22} & M_{2\leftarrow 39} \\ M_{28\leftarrow 2} & M_{28\leftarrow 28} & M_{28\leftarrow 22} & M_{28\leftarrow 39} \\ M_{22\leftarrow 2} & M_{22\leftarrow 28} & M_{22\leftarrow 22} & M_{22\leftarrow 39} \\ M_{39\leftarrow 2} & M_{39\leftarrow 28} & M_{39\leftarrow 22} & M_{39\leftarrow 39} \end{bmatrix} \begin{bmatrix} a_2 \\ a_{28} \\ a_{22} \\ a_{39} \end{bmatrix} + \begin{bmatrix} b_2 \\ b_{28} \\ b_{22} \\ b_{39} \end{bmatrix} \tag{4.5}$$

For the sake of brevity we will write out the matrix elements in a more compact form where the series of operators are denoted by a node path through the graph.

$$M_{2\leftarrow 2} = (2, 1, 4, 5, 8, 9, 12, 13, 20, 19, 14, 11, 10, 7, 6, 3, 2)$$

$$
\begin{aligned}
&+ (2,1,4,5,8,9,12,15,26,25,16,11,10,7,6,3,2) \\
M_{2\leftarrow 28} &= (2,1,4,5,8,9,12,15,26,27,30,29,28) \\
M_{2\leftarrow 22} &= (2,1,4,5,8,9,12,13,20,21,24,23,22) \\
M_{2\leftarrow 39} &= (2,1,4,5,8,9,12,13,20,19,14,17,32,33,36,37,40,39) \\
&+ (2,1,4,5,8,9,12,15,26,25,16,17,32,33,36,37,40,39) \\
M_{28\leftarrow 2} &= (28,25,16,11,10,7,6,3,2) \\
M_{28\leftarrow 28} &= (28,27,30,29,28) \\
M_{28\leftarrow 22} &= 0 \\
M_{28\leftarrow 39} &= (28,25,16,17,32,33,36,37,40,39) \\
M_{22\leftarrow 2} &= (22,19,14,11,10,7,6,3,2) \\
M_{22\leftarrow 28} &= 0 \\
M_{22\leftarrow 22} &= (22,21,24,23,22) \\
M_{22\leftarrow 39} &= (22,19,14,17,32,33,36,37,40,39) \\
M_{39\leftarrow 2} &= (39,38,35,34,31,18,13,20,19,14,11,10,7,6,3,2) \\
&+ (39,38,35,34,31,18,15,26,25,16,11,10,7,6,3,2) \\
M_{39\leftarrow 28} &= (39,38,35,34,31,18,15,26,27,30,29,28) \\
M_{39\leftarrow 22} &= (39,38,35,34,31,18,13,20,21,24,23,22) \\
M_{39\leftarrow 39} &= (39,38,35,34,31,18,13,20,19,14,17,32,33,36,37,40,39) \\
&+ (39,38,35,34,31,18,15,26,25,16,17,32,33,36,37,40,39)
\end{aligned}
\tag{4.6}
$$

The DRFPMI matrix elements have two new features when compared to the power recycled arm cavity matrix elements. The first is that two of the matrix elements $M_{28\leftarrow 22}$ and $M_{22\leftarrow 28}$ are exactly zero, denoting that there is no direct path between these two nodes in the irreducible graph. These two edges describe the coupling between XARM and YARM. Them being zero means that to first order there is no coupling between the field circulating in the XARM and the field circulating in the YARM. The second new feature is that there are two edges (a second degree multi-edge) for every coupling between nodes 2 and 39. Following the addition graph reduction rule these multi-edges are replaced by a single edge, whose operator is the sum of the operators

in the multi-edge. Nodes 2 and 39 correspond to the PRC and SRC respectively. The multi-edges between the PRC and SRC denote that their round trips and couplings are comprised of a sum of the contribution the path interacting with ITMX and the path interacting with ITMY.

To obtain the field at every one of the 41 nodes in the DRFPMI graph we can use the 36×5 matrix to propagate the one source and four circulating fields to every other node in the graph. For the sake of brevity we will not list all of the 180 propagation matrix elements but they can be trivially obtained from the edge operator weights to these sink nodes.

4.2 Results

To validate the matrix signal flow graph formalism presented here we use it to solve an HG model and compare it to the same HG model solved using traditional matrix solving methods. Each optical model was initially created by hand in `Finesse3`, which handled defining all model matrix elements based on given components. Those matrix elements were then converted to the corresponding matrix signal flow graph. The graph was reduced following the graph reduction rules presented section 4.1. The final self-loop solving stage and propagation to all the sink nodes was done using dense matrix algebra in the `numpy` [205] package. We recorded the end-to-end execution time as the time taken from the beginning of graph reduction to when the solved fields were propagated to all the sink nodes.

We compared the graph reduction solver to 2 alternatives: KLU and the `numpy` dense matrix solver. KLU [100, 109] is a highly optimized sparse matrix solver from the `SuiteSparse` library based on LU factorizations that is used in `Finesse2` and `Finesse3`. The dense solver is included as a worst case. In all cases the solved field given by the graph solver was within floating point precision of both the dense solver and KLU.

We see from the following figures that the graph reduction solver starts off being the slowest with nearly a constant time taken for $N < 10$. This is most likely due to python overhead associated with the graph operations. At $N = 100$ the graph reduction solver and KLU both perform about the same for all 3 optical systems tested with the graph

solver outperforming KLU for $N > 100$.

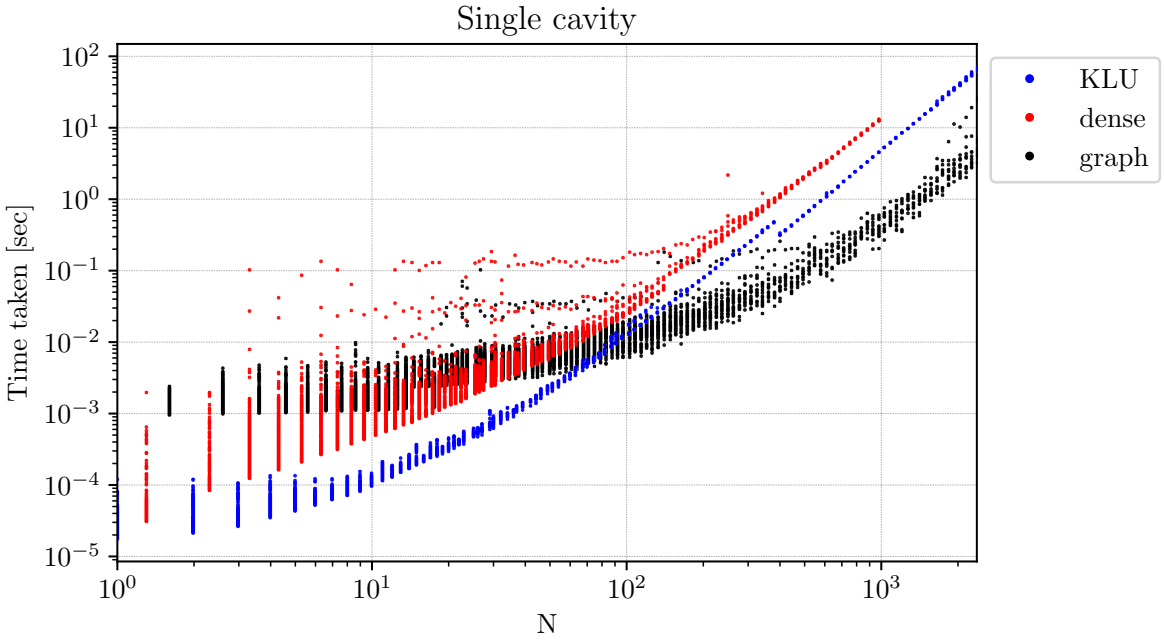

Figure 4.12: Time taken to solve the model shown in figure 4.5 for various solvers.

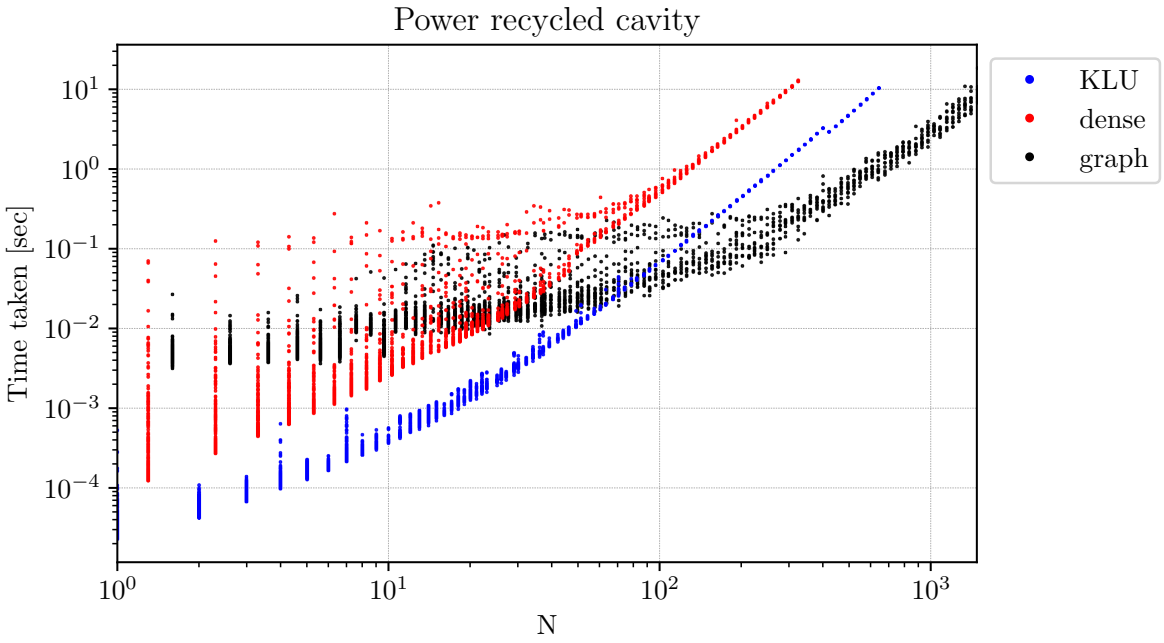

Figure 4.13: Time taken to solve the model shown in figure 4.7 for various solvers.

The speedup from the graph solver can be attributed to the fact that the size of the matrix inverse that is computed is 10 times smaller than the matrix inverse that is computed in the dense and KLU solver. The graph solver effectively separates the single large block sparse inverse into a smaller dense inverse and a dense matrix

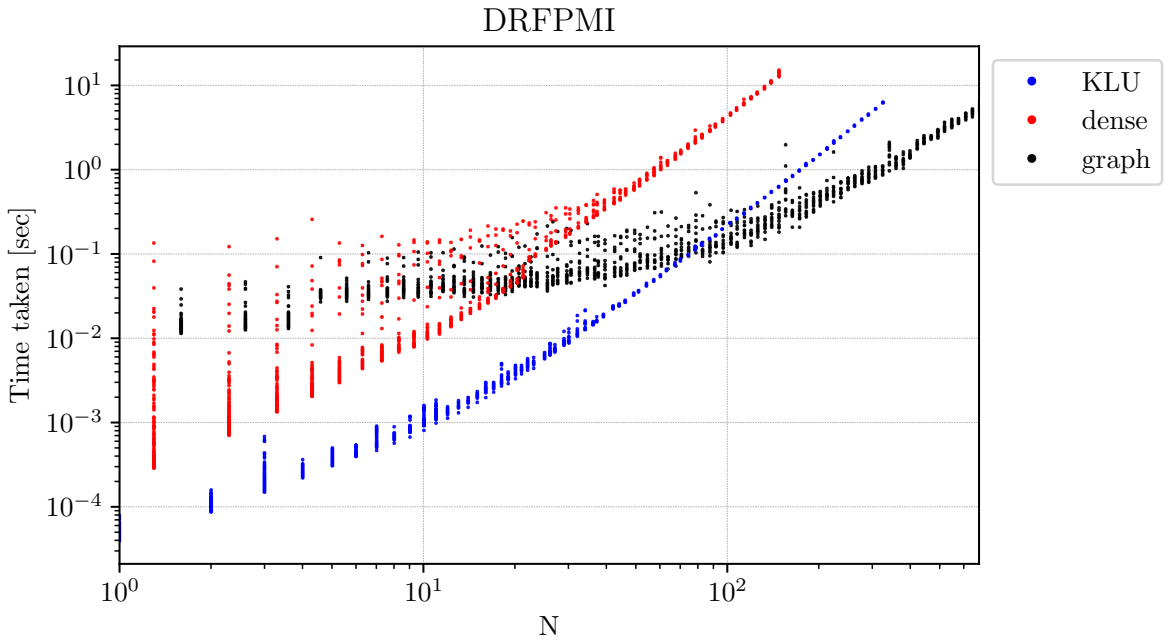

Figure 4.14: Time taken to solve the model shown in figure 4.10 for various solvers.

multiplication. We can see that in the best case there is nearly a 100 times speedup over the dense solver and a 10 times speedup over KLU.

This highlights a potential application of using graph reduction as the solver in HG modelling packages such as `Finesse`. The graph structure inherently lends itself to a parallel implementation. More work needs to be done to optimize the graph solver for smaller models where the runtime is dominated by python overhead.

4.3 Summary and future work

We have shown a potential extension of LCT models for coupled cavities by converting optical models into signal flow graphs. Applying graph reduction rules allows one to construct a linear operator equation for coupled cavities that looks like an equation for a single cavity, which can be solved using the same methods that we have presented in chapter 3. This also allows us to define a generalization of the round trip operator in coupled cavities that is model independent, which may prove valuable in HG and FFT based optical models. The remaining work to write the code for an implementation of a coupled cavity solver graph solver using LCTs.

Chapter 5

Commissioning for Advanced LIGO

This chapter describes the various contributions to commissioning efforts for Advanced LIGO that I undertook during my PhD. For LIGO commissioning periods are between observation runs where the detector is adjusted or modified to improve performance. I was involved in LIGO commissioning in 2018 and 2019 with a focus on modelling and understanding the issues related to mode matching between the various LIGO subsystems. The two main activities presented here were the analysis of OMC astigmatism from measurements of the OMC transverse mode splitting, and a measurement of the SR3 rear heater's ability to correct mode mismatch.

5.1 Squeezer beam and LHO OMC astigmatism

During commissioning leading up to LIGO's third observation run (O3) it was found that the squeezer beam was noticeably astigmatic going into the OMC [174]. This limits the overall mode matching that can be achieved and generally degrades squeezing performance. While the squeezer beam was profiled I analyzed the OMC cavity scans to quantify the mode mismatch and investigate how it was impacted by the beam astigmatism. The mode mismatch is obtained by measuring the ratio of the second order mode peak height to the fundamental mode peak height during a cavity length scan.

One of the OMC scans I took is shown in figure 5.1. The ratio between HG_{02} and HG_{00} peaks is roughly 0.1, which yields a mode mismatch of 10%. The mode order

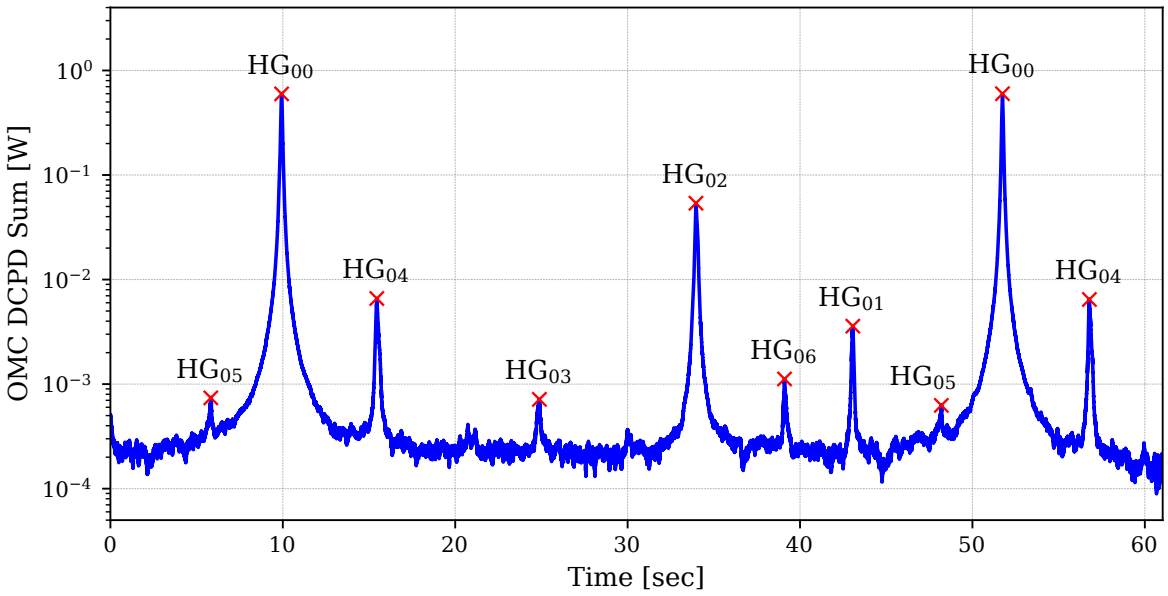

Figure 5.1: A full period of an LHO OMC cavity length scan of the squeezer beam. All known peaks are labelled based on the relative location of higher order mode resonances based on OMC cavity geometry. The label HG_{0n} is intended to denote all the n'th order higher modes that should resonate at, or close to that frequency.

of a resonant peak is determined by their relative distance to the fundamental mode peak and the design parameters of the OMC cavity geometry. The incident beam is single frequency and so every peak in the cavity scan corresponds to a higher order transverse mode of the incident beam in the OMC eigenmode basis.

If the OMC was operating to design the three second order peaks (HG_{02}, HG_{11}, HG_{20}) should be nearly degenerate and hence should not be resolvable. In this case when the incident beam is astigmatic the ratio between the fundamental and second order peaks should give an estimate for the average mode mismatch between the vertical and horizontal axes, but this was not what I found. Instead the resonant power around the resonance for the second order modes took an odd shape, which remained consistent from scan to scan.

A close-up on the second order resonance peak is shown in figure 5.2 along with a least-squares fit of a Lorentzian function, which closely approximates the line shape of a single mode or degenerate multi-mode cavity resonance. The Lorentzian function

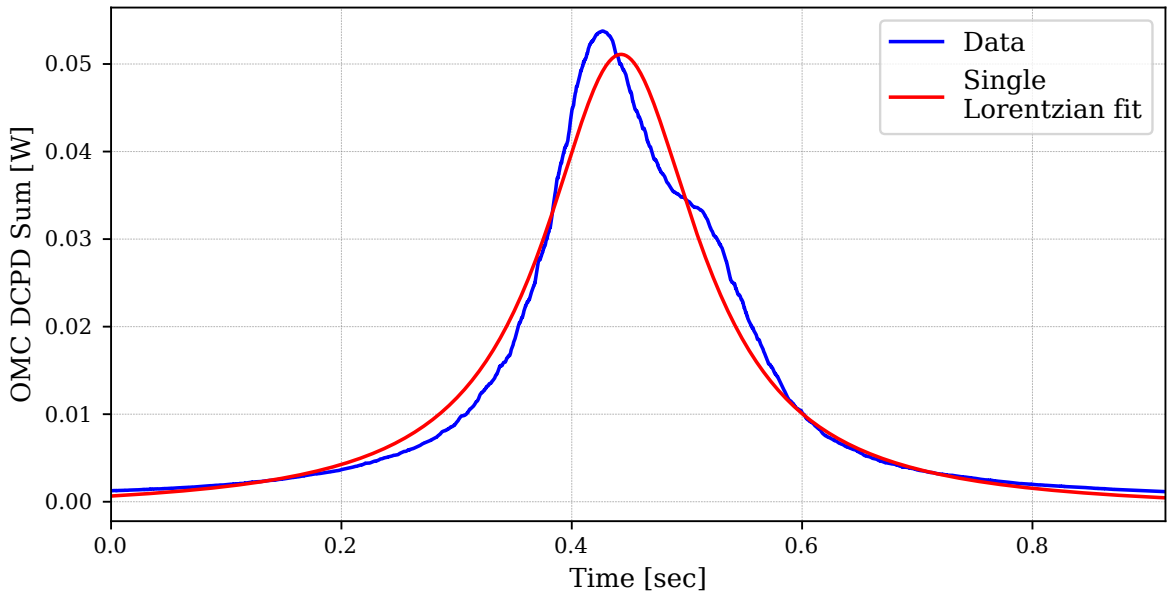

Figure 5.2: The second order OMC resonance with a strongly astigmatic beam.

with a full-width-half-maximum (FWHM) Γ is given by

$$L(x, \Gamma) = \frac{\left(\frac{\Gamma}{2}\right)^2}{x^2 + \left(\frac{\Gamma}{2}\right)^2} \tag{5.1}$$

This definition is chosen such that the maximum value of the Lorentzian is $L(0, \Gamma) = 1$.

The single Lorentzian fit in figure 5.2 is quite bad making it difficult to accurately predict the resonant amplitude. Introducing a second Lorentzian function improves the fit substantially, as shown in figure 5.3.

The two peaks in figure 5.3 correspond to the HG_{20} and HG_{02} modes respectively. They are resolvable because the OMC cavity is more astigmatic than the design, which breaks the frequency degeneracy for higher order modes. The resonance frequency for vertical higher order modes is slightly shifted with respect to the horizontal higher order modes. The difference in the heights of these two peaks gives a measure of beam astigmatism, and the separation frequency of these two peaks gives a measure of the cavity astigmatism.

This cavity astigmatism can be rephrased in terms of splitting of the transverse mode spacing (TMS), which can be directly computed from the fits in figure 5.3. The TMS

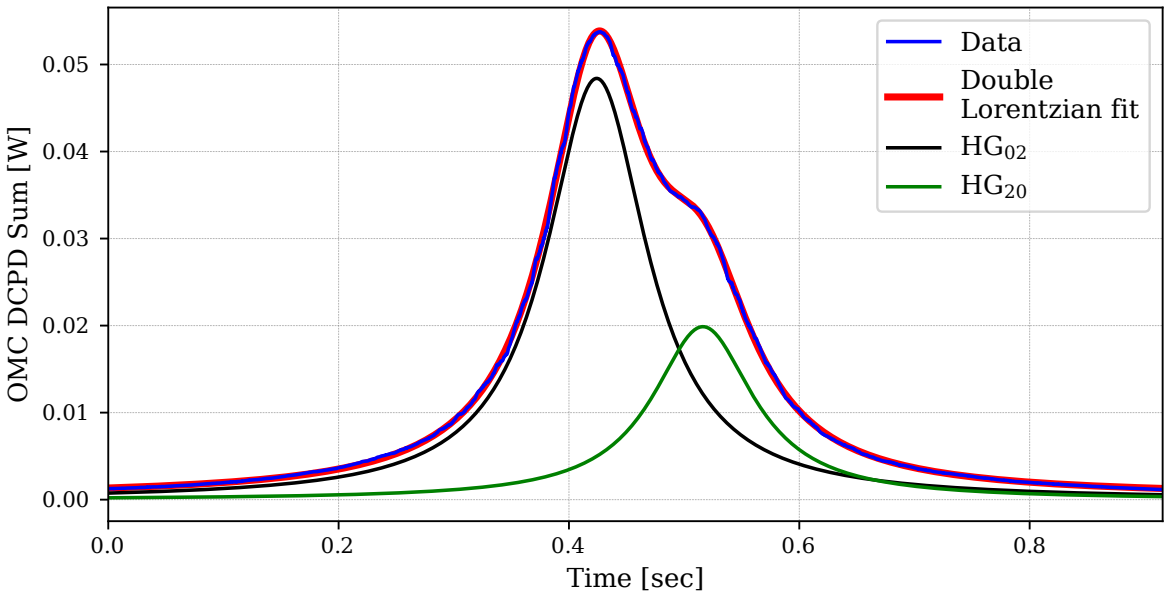

Figure 5.3: Two Lorentzians fitted to a second order OMC resonance with a strongly astigmatic beam.

splitting is a unitless quantity given by

$$\text{TMS splitting} = \frac{|x_{02} - x_{20}|}{2\Gamma} \tag{5.2}$$

where x_{02} and x_{20} are the locations of the HG_{02} and HG_{20} resonance peaks respectively. The factor of 2 on the denominator comes from the fact that we are measuring the TMS splitting using second order modes. The TMS splitting from figure 5.3 is about 0.43. To convert it to a frequency splitting the TMS splitting should be multiplied by the FWHM of the OMC.

In principle in figure 5.3 there should be a another higher order mode: the HG_{11} mode, whose resonance frequency sits exactly between the HG_{20} and HG_{02} modes. However the amplitude of the HG_{11} mode was small enough here as to be negligible. This can be justified by noting that the scattering into the HG_{11} mode primarily happens through misalignment; mode mismatch only changes the strength of the misalignment coupling [43]. Similar to mode mismatch, misalignment is obtained by taking the ratio of the HG_{01} peak to the HG_{00} peak in a cavity length scan.

Figure 5.1 shows that the HG_{01} peak is about an order of magnitude smaller than the HG_{02} peak. Since the mode mismatch was 10% this indicates that the beam was misaligned to the cavity to less than 1%. The peak height for the HG_{11} mode is

expected to be around 10^{-4} W, less than the noise floor and so its contribution to the profile of the second order peak in figure 5.3 is negligible.

The least-squares fits to cavity scan peaks are accurate but difficult to automate for commissioning due to requiring human expert knowledge to provide a reasonable guess for initial fit parameters. Cases like figure 5.1 are relatively simple for an expert where the beam has a single frequency and is well mode matched and aligned. Despite that automatically identifying peaks is challenging even in simple cases since the relationship between PZT voltage and cavity length is not exactly linear. This shifts the position of the peaks relative to each other and can result in misidentified peaks.

These challenges make computer aided tools unappealing in comparison to estimating the resonant amplitude by the maximum height of the resonant peak, especially when quick answers important to keep up the pace of commissioning. Estimating mode mismatch with peak heights in this case produces systematic underestimation as illustrated by figure 5.4.

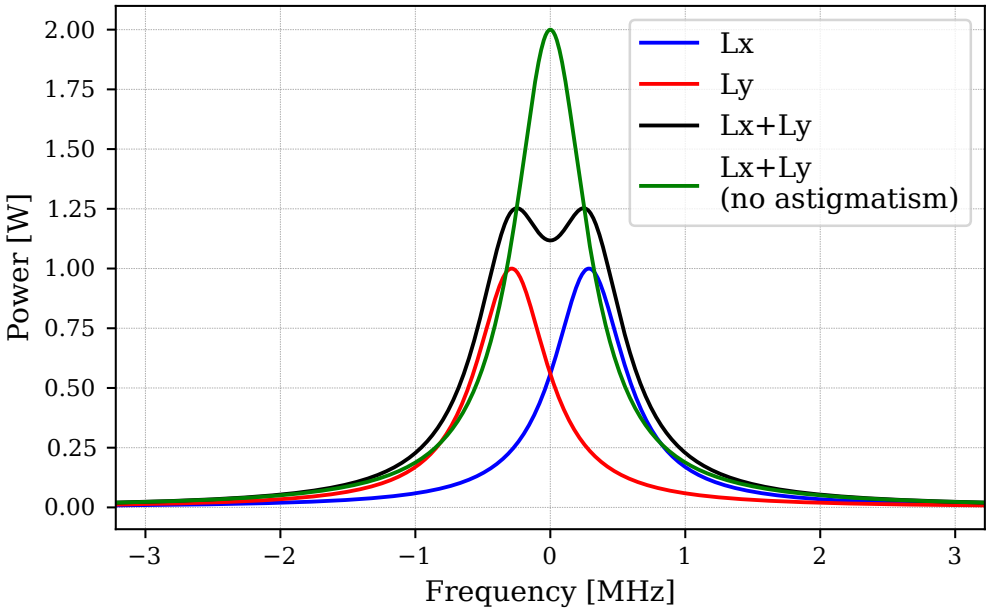

Figure 5.4: A demonstration that the peak of the sum of two Lorentzians is reduced if the Lorentzians are not on top of each other. The Lorentzian separation used here is the same as was measured in the LHO OMC cavity scan in figure 5.3.

The maximum of the split peak in figure 5.4 is about 1.6 times less than if the OMC had no astigmatism, which means that mode mismatch estimates need to be multiplied by that amount to compensate. This correction factor is not constant and depends on

the relative height of the two peaks, which in turn depends on the astigmatism of the beam relative to the cavity. The correction factor as a function of the relative height difference between the second order peaks is shown in figure 5.5. Zero mode mismatch

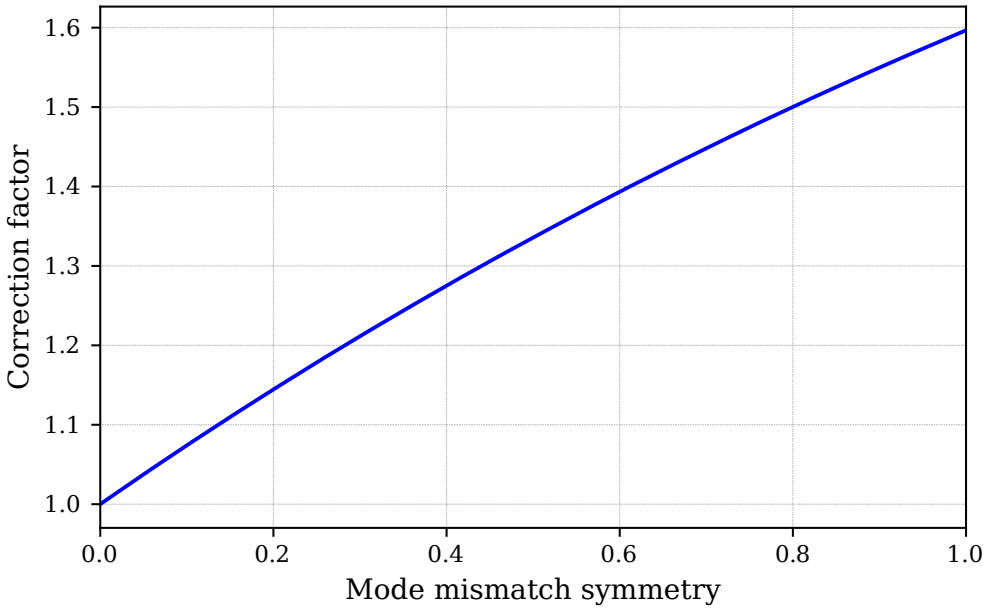

Figure 5.5: A plot of the peak height correction factor as a function of relative height difference between the two peaks. The Lorentzian separation used here is the same as was measured in the LHO OMC cavity scan in figure 5.3.

symmetry corresponds to the height of one of the HG_{02} or HG_{20} to be exactly zero, in which case the height of the remaining peak gives an accurate estimate of mode mismatch and hence the correction factor is exactly 1. A mode mismatch symmetry of 1 corresponds to the HG_{02} and HG_{20} peaks having the same height, which is the case depicted in figure 5.4 with the correction factor of 1.6. In general the mode mismatch symmetry is given by

$$\text{mode mismatch symmetry} = \frac{\min\left[P_{02}, P_{20}\right]}{\max\left[P_{02}, P_{20}\right]} \tag{5.3}$$

where P_{02} and P_{20} are the powers in the HG_{02} and HG_{20} modes respectively.

5.1.1 Comparison of LHO and LLO astigmatism

Here we compare the astigmatism of the LHO OMC to the LLO OMC using the same method as section 5.1. A sample of second order resonance peaks from both detectors was extracted from OMC cavity scans performed by on-site commissioners

for a different purpose in early 2019. These are shown in figure 5.6. The LHO and LLO cavity scans were ran for six and two cycles respectively. Two Lorentzians were fit to each resonance peak and the residuals are shown in figure 5.7.

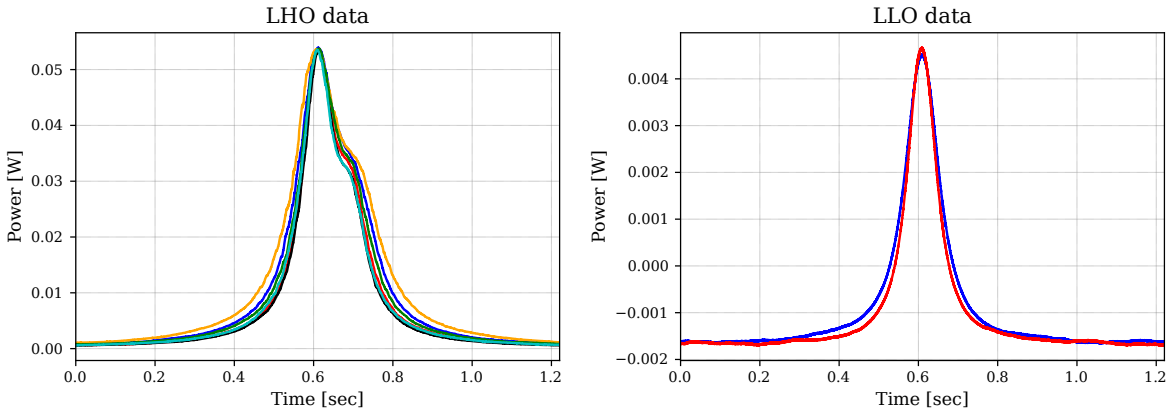

Figure 5.6: A plot of OMC second order resonance peaks in the LHO (left) and LLO (right) GW detectors.

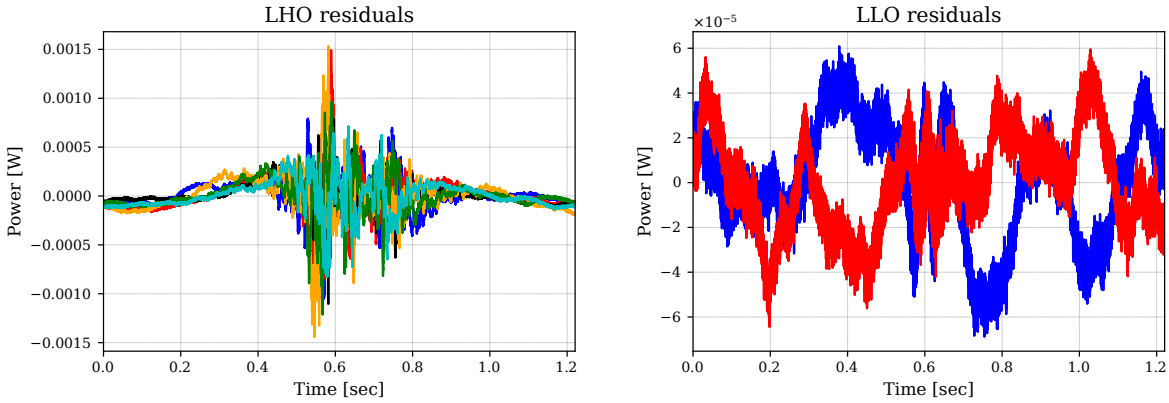

Figure 5.7: Residuals for the Lorentzian fits to the second order OMC resonance peaks shown in figure 5.6. The colors of the traces correspond to the same traces from figure 5.6.

We find that the LLO OMC is significantly less astigmatic than the LHO OMC, and slightly less astigmatic than the aLIGO OMC design. It is known that the OMCs in LHO and LLO differ slightly in their as built parameters, though direct measurements of these parameters in-situ is difficult. This measurement of OMC TMS splitting gives a way to directly measure the impact of some of these parameters. We find that the TMS splitting in LHO and LLO are 0.44 and 0.17 respectively. A summary plot of the measured OMC TMS splitting is shown in figure 5.8.

The time of the measured peaks was used to obtain the PZT voltage on PZT2, which

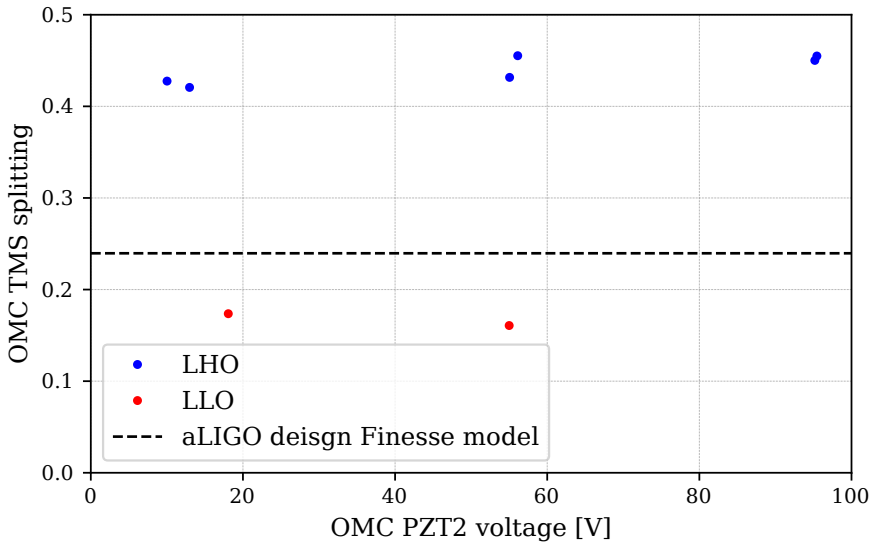

Figure 5.8: Calculated OMC TMS splitting using equation (5.2) for both LHO and LLO based on the separation of the two fitted Lorentzians to the transverse second order OMC resonances in figure 5.6. The dashed line is the predicted TMS splitting calculated by Finesse based on the aLIGO design parameters for the OMC.

was used to scan the OMC cavity length. The other PZT in the OMC — PZT1 was set to 10 V is both detectors during that time. The nearby points in the LHO data show the reproducibility of our method, which we estimate is about ± 0.02. The uncertainty estimates for each measurement point based on the least squares fits are orders of magnitude less, indicating some degree of model misspecification.

Based on the results in figure 5.7 we conclude that that the TMS splitting and hence OMC astigmatism does not strongly depend on the applied PZT voltage in both detectors. This dependence broadly agrees with results published by Arai [133], who measured the TMS splitting in both OMCs prior to them being installed in each detector. His measured value for the TMS splitting for all OMCs was about 0.218, which is closer to the aLIGO design than either the measured LLO or LHO TMS splitting shown in figure 5.8.

To discuss this measured difference it is important to note that the TMS splitting is only dependent on the cavity geometry, which is given by the lengths between each mirror, the mirror radius of curvature, and angle of incidence (AOI) on each mirror. Out of any of these the AOI seems the most likely to differ from design. The OMC input coupler (IC) and output coupler (OC) are flat and so their AOI does not directly contribute to the TMS splitting. Changing the angle of the IC and OC can change the

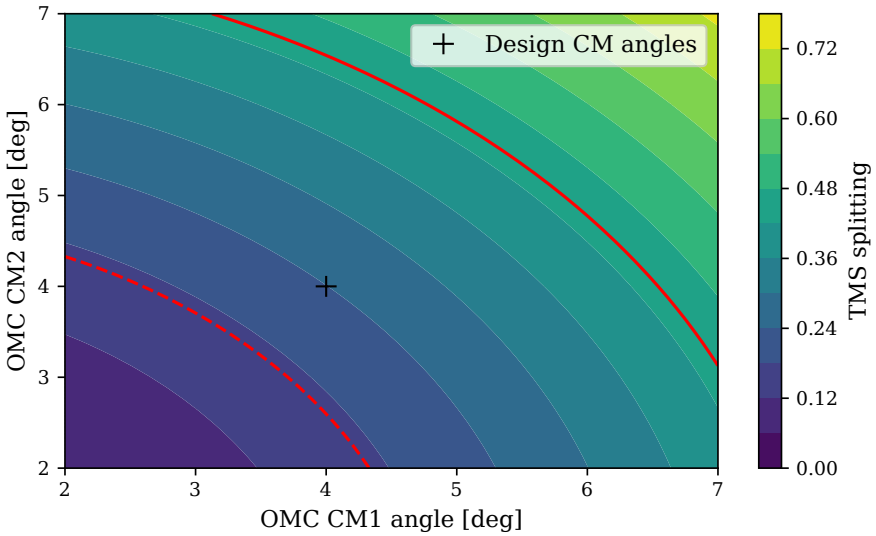

Figure 5.9: OMC TMS splitting as a function of angle of incidence on the OMC curved mirrors (CMs). The red dashed line is the measured LLO TMS splitting and the red solid line is the measured LHO TMS splitting.

cavity round trip beam path so that the beam hits the CMs off-center, which means the beam will see a different angle and hence lead to a change in the TMS splitting. We neglect this effect and only look at the TMS splitting purely as a function of AOI on the CMs to get a sense of scale of the TMS splitting in more concrete terms. In figure 5.9 we show how the TMS splitting changes when the AOI on the curved mirrors (CM) changes in an aLIGO design OMC. We see that to get the TMS splitting that was measured for LHO the AOI on both CMs has to increase from their design by about 1.5 degrees. Similarly the LLO TMS splitting can be obtained by decreasing both the AOI on both CMs by about 0.5 degrees.

At the time of writing we do not know how this change in TMS splitting came about in the time between being measured by Arai before installation and the in-situ measurements we presented here. The difference that we report is small and likely has a negligible impact on the mode cleaning capabilities of either OMC.

5.2 Beam shape inference from SR3 rear heater scans

As part of the commissioning effort for the third observation run (O3) I investigated how the SR3 rear heater impacted the mode matching from the SRC to the OMC.

High mode matching is important for minimizing squeezing losses and at the time the SR3 rear heater provided the only method of mode matching actuation from inside the signal recycling cavity (SRC). During this measurement the interferometer was in a "single bounce" state, where the PRM, SRM, ITMX, ETMX, and ETMY are all misaligned in figure 5.10. This allows us to analyze the impact of the SR3 rear heater on a beam that somewhat approximates the arm cavity mode without involving any cavities in the interferometer. This allows us to operate without worrying about lock loss. In practice, the dual recycled Fabry-Perot Michelson beam will differ in shape to the "single bounce" beam due to mode mismatches between the internal cavities within the interferometer, but the "single bounce" beam should be a good approximation when all the cavities inside the interferometer are well mode matched.

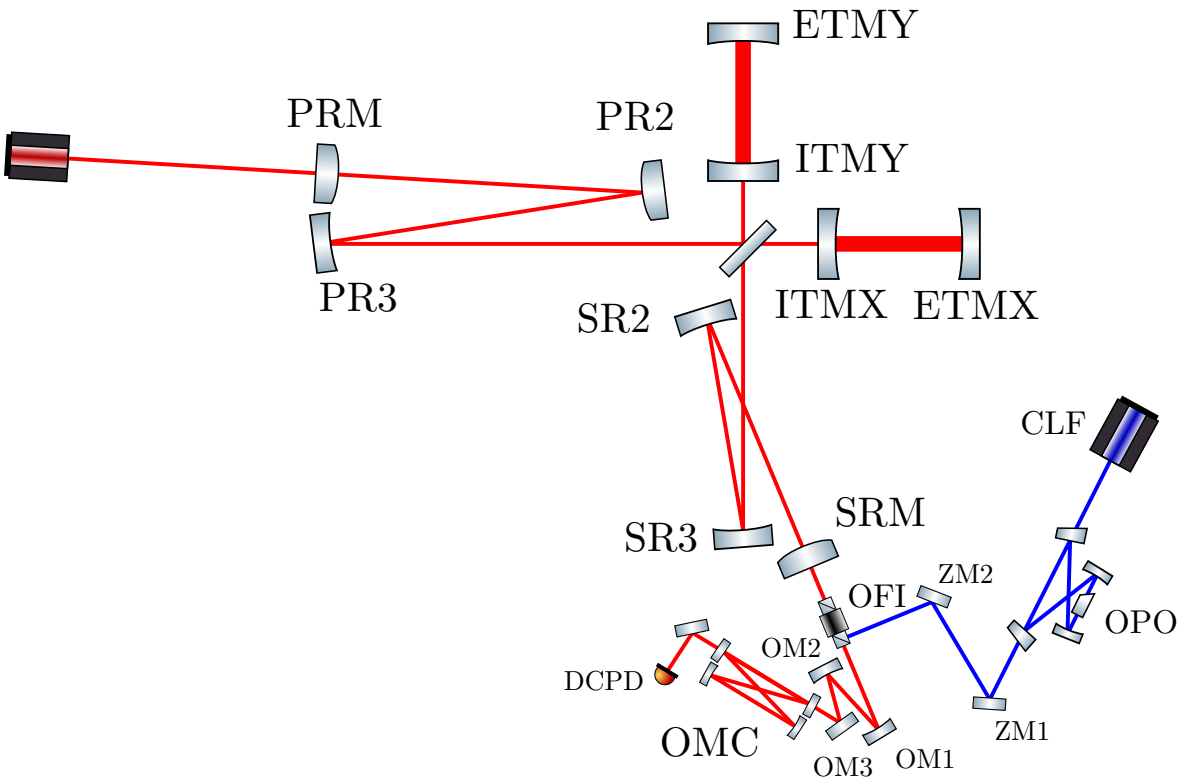

Figure 5.10: Dual recycled Fabry-Perot Michelson (DRFPMI) layout of the aLIGO interferometer.

The SR3 rear heater — shown in figure 5.11 is a radiative heater mounted directly against the back surface of the SR3 mirror. The heater has a max operating temperature of 360 K, or about 86°C, which is modelled to increase the radius of curvature of the SR3 mirror by 32 mm via thermoelastic deformation [132]. The nominal radius of curvature of the SR3 is roughly 36 m and so the rear heater is equivalent to a 25 μD

lens. The thermal time constant of the heater is about 15 minutes, which is the time it takes for the difference between the current temperature and the target temperature to drop by $1/e$.

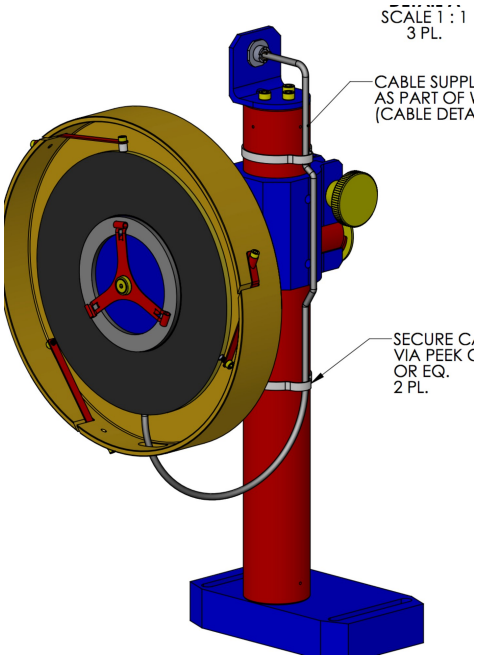

Figure 5.11: A diagram of the SR3 rear heater. Taken from [132].

The rear heater temperature was steadily increased from 25 to 70°C over the period of about 4 hours. During that time the OMC cavity length was continuously scanned by driving the PZT with a sawtooth wave voltage signal. The mode mismatch into the OMC was estimated by a peak detection algorithm running on the realtime data. This peak detection algorithm picked out the HG_{00} and second order resonance peak height each OMC scan period by a combination of heuristics and user guidance. The initial guess for the position of the HG_{00} and second order peak positions are specified by the user. The heuristic was derived from the assumption that the PZT voltage of each OMC resonance peak changes very little from scan to scan, and so each scan period the new peaks were acquired using their previously recorded PZT voltage. The raw data for the SR3 heater element temperature and the OMC mode mismatches as a function of time are shown in figure 5.12. The SR3 heater element temperature was set by hand by setting the target temperature and waiting for the rear heater equilibrate before increasing the target temperature again. The break in the data is in figure 5.12 corresponds to a lunch break when the experiment was not running.

After the experiment was finished the measured OMC mismatch was plotted against

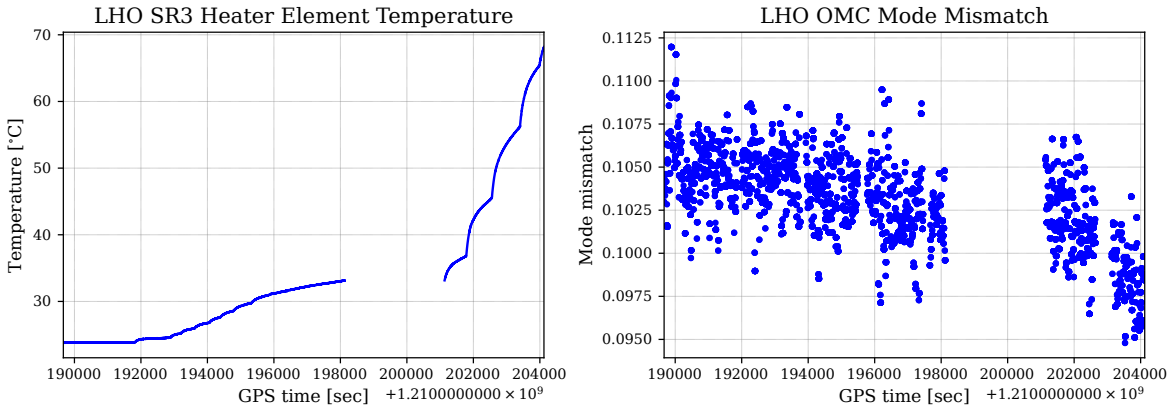

Figure 5.12: Plot of SR3 heater element temperature as a function of time (left). Plot of measured mode mismatch into the OMC as a function of time during that period (right).

the SR3 heater element temperature, which is shown in figure 5.13. The noise in

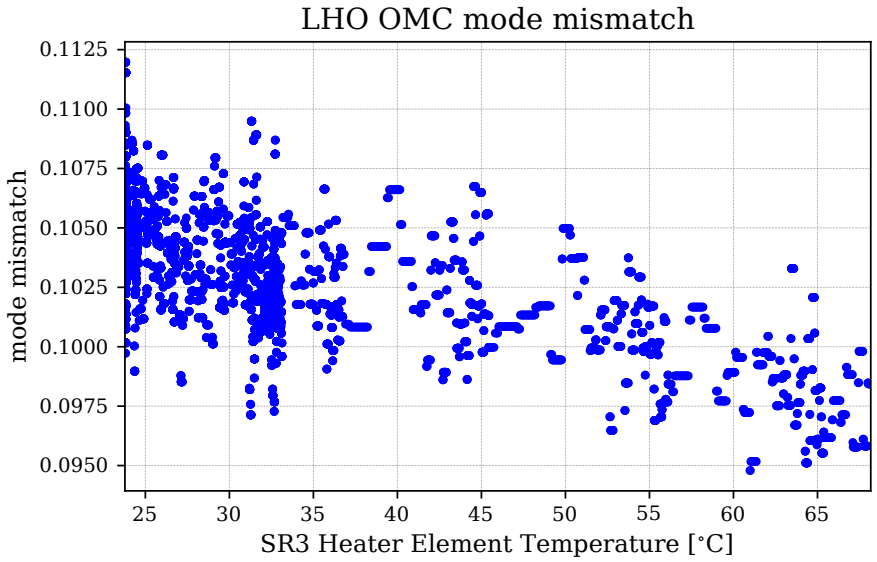

Figure 5.13: A plot of measured OMC mismatch as a function of SR3 heater element temperature.

the mode mismatch data was likely caused by intensity noise on the laser, which was not intensity stabilized throughout the experiment. Intensity noise has an effect on mode mismatch measurements since the intensity readings for the HG_{00} and HG_{20} peaks happen at different times, typically seconds apart, which means that the noise is uncorrelated. This means that the impact of intensity noise on the measured mode mismatch is significant.

However, despite the noise, through the sheer number of data points a trend is visible

in figure 5.13. The data shows a near linear decrease in mode mismatch from about 10.5% at 25°C to 9.75% at 65°C. This decrease in OMC mode mismatch due to increase in SR3 curvature is small, but the fact that it is small over that range can be used to infer information about the beam parameter going in to the OMC. A parameter map of how 10% mode mismatched beam parameters at the SRM change as the SR3 radius of curvature is increased is shown in figure 5.14. This map was generated by

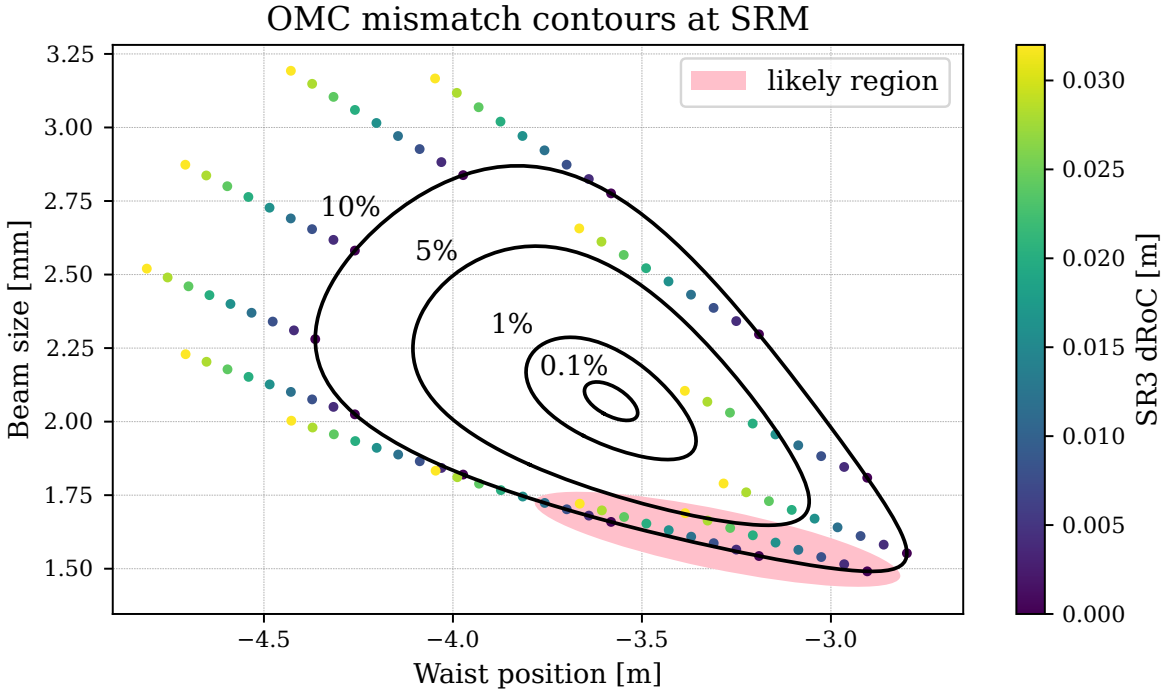

Figure 5.14: A map in beam parameter space at the SRM close to mode matching to the OMC. Contours are shown for 0.1%, 1%, 5%, 10% mode mismatches. The region highlighted in pink corresponds to the area where the SR3 actuator has a small improvement on the mode matching of a 10% mismatched beam, which is similar to what was seen in the measurement in figure 5.13. This means the measured beam parameter is likely to be from that region.

taking a uniform sample of beam parameters that are 10% mode mismatched to the OMC eigenmode. What we would like to know is what these beam parameters would look like right before the SR3 so that we can model how they change when the SR3 curvature is increased. For this we need to reverse propagate the beam at the OMC to the SR3 using inverse ABCD matrices.

After the mismatched OMC beam parameters are inverse propagated back to the SR3, the SR3 curvature is changed and the beam is forward propagated to the SRM, which is a common reference point for OMC mode matching used in commissioning. This is

repeated for a range of SR3 curvatures. The resulting beam parameters that have been transformed by different SR3 curvatures are shown as the points in figure 5.14.The plot is a 2D map in beam parameter space where the x-axis is the beam's waist position and the y-axis is the beam's beam size. These two degrees of freedom uniquely specify a beam parameter.

We can see that for certain initial beam parameters it is possible to see a relatively small decrease in mode mismatch as the SR3 rear heater temperature is increased, corresponding to a beam parameter that has a waist position at -3.2 m and a beam size at the SRM of about 1.55 mm. The information about the beam parameter from scanning a mode matching actuator can be combined with other measurements, such as beam profiles to further constrain the space of possibility.

Using the model in figure 5.14 we conclude that in the best case the SR3 heater is able to fix mode mismatch of up to 5%. If the SR3 heater is operated at its middle point, which is about 55°C then we expect it to fix mismatches of about 2% on either side of the SR3 actuation axis.

To be able to effectively actuate on an area of beam parameters and not just one line a second mode matching actuator is required. This actuator should ideally be orthogonal to the SR3 actuator, where orthogonal means that the axis on which it moves the beam parameters is 90 degrees to the SR3 actuation axis in figure 5.14. This can be achieved by having the actuator separated from the SR3 actuator by 90 degrees of Gouy phase, where the Gouy phase is defined as

$$\Psi = \arctan\left[\frac{z}{z_R}\right] \tag{5.4}$$

where z and z_R are the waist position and Rayleigh range of the beam at the actuator. In figure 5.15 we computed the accumulated Gouy phase in the signal recycling cavity with Finesse3 using design aLIGO parameters. Unfortunately both SR2 and the ITMs are close in Gouy phase as SR3, making them a poor choice for a pair of actuators in the signal recycling cavity. The remaining optic is the SRM, which is somewhat orthogonal to the SR3 by about 20 degrees of Gouy phase. Unfortunately the SRM is used in both reflection and transmission. This is a problem since any thermal actuation on the SRM will induce both a thermoelastic and thermorefractive deformation with

the latter being undesirable in this case. The thermorefractive actuation will then need to be compensated for in the OMC and squeezer paths to maintain good mode matching to both of these subsystems.

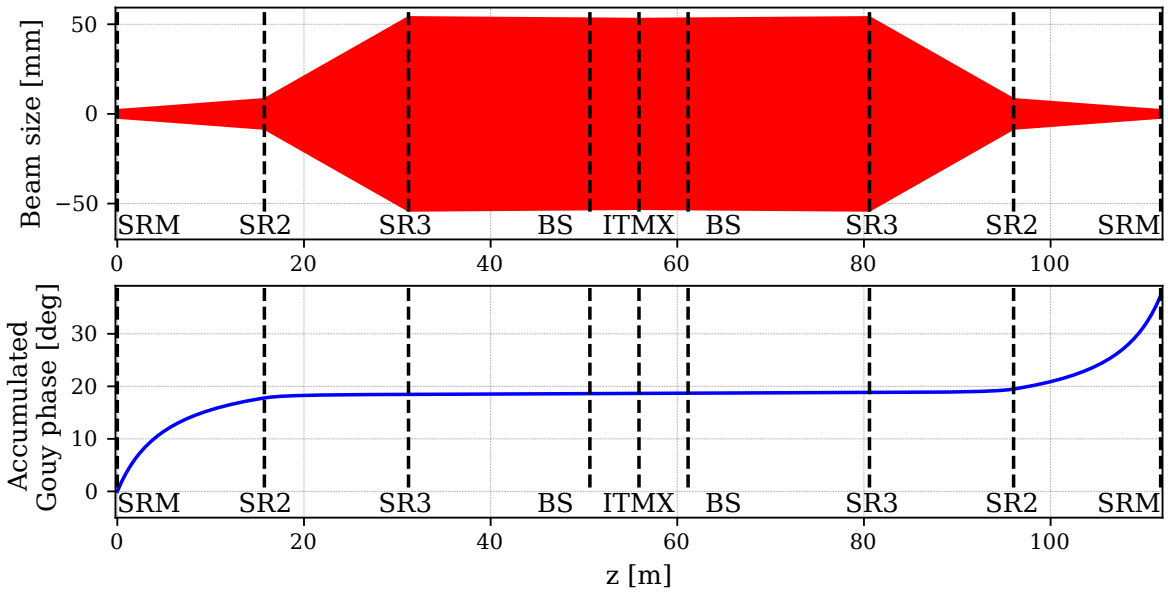

Figure 5.15: A plot of the beam size and accumulated Gouy phase in a round trip of the SRC through the ITMX using aLIGO design parameters.

In summary, we have used the SR3 actuator combined with OMC cavity scans to constrain the single bounce beam parameter to lie on a small section of the mode mismatch contour in parameter space. From actuation data we found that in a model of the design aLIGO the SR3 heater is able to correct mode mismatches of up to 5%. A second orthogonal actuator inside the signal recycling cavity is needed to be able to actuate on an area in beam parameter space. We have investigated the suitability of each possible actuator and found that the SRM can provide the most orthogonal actuator to the existing SR3 rear heater. We discussed the possibility of using the SRM with a thermal actuator and the mode mismatch that is introduced on transmission due to the thermorefractive effect, which affects the mode matching of the interferometer beam going into to the OMC and the squeezer beam entering the interferometer.

5.3 Concluding remarks

We have shown in section 5.1 that using OMC cavity length scan data it is possible to precisely measure the transverse mode spacing (TMS) splitting due to OMC astigma-

tism by fitting two lorentzians to the second order transverse resonance of the OMC. Using this technique we have found that the LHO OMC is more astigmatic than the aLIGO design, and the LLO OMC is less astigmatic than the aLIGO design.

In section 5.2 we showed that information can be obtained about the beam parameter coming out of the SRC by scanning the SR3 rear heater temperature while measuring OMC mode mismatch from OMC scans. This mismatch data can be used to fit a beam parameter from an ABCD model of SR3 with different radii of curvature. We investigated the suitability of a second actuator inside the signal recycling cavity to further improve mode matching in the signal recycling cavity.

Chapter 6

Mode matching error signals using radio-frequency beam shape modulation

6.1 Preface

This chapter presents a fast optical mode matching dither signal generated by an electro-optical modulation that is filtered by an optical cavity. A large portion of this chapter has been published as a paper [204] in the peer reviewed OSA journal, Applied Optics.

A. A. Ciobanu, D. D. Brown, P. J. Veitch, and D. J. Ottaway. "Mode matching error signals using radio-frequency beam shape modulation". In: *Applied Optics* 59.31 (Nov. 1, 2020). Number: 31, p. 9884. ISSN: 1559-128X, 2155-3165. DOI: 10.1364/AO.404646.

Precise mode matching is needed to maximize performance in coupled cavity interferometers such as Advanced LIGO. In this chapter we present a new mode matching sensing scheme that uses a single radio-frequency higher-order-mode sideband and single-element photodiodes. It is first order insensitive to misalignment and can serve as an error signal in a closed loop control system for a set of mode matching actuators. We also discuss how it may be implemented in Advanced LIGO. The proposed mode

matching error signal has been successfully demonstrated on a tabletop experiment, where the error signal increased the mode matching of a beam to a cavity to 99.9%.

6.2 Introduction

Precise control of mode matching is desirable in many high precision optical cavity experiments to minimise optical losses. This is especially true for advanced gravitational wave (GW) detectors that use multiple coupled cavities and squeezed light injection to maximize sensitivity [185], such as Advanced LIGO [135], and Advanced Virgo [136]. figure 6.1 depicts the degradation when using 6 dB of frequency-independent squeezing due to varying percentages of mode mismatches. A mode mismatch of only 10% can almost completely nullify the expected improvement from squeezing.

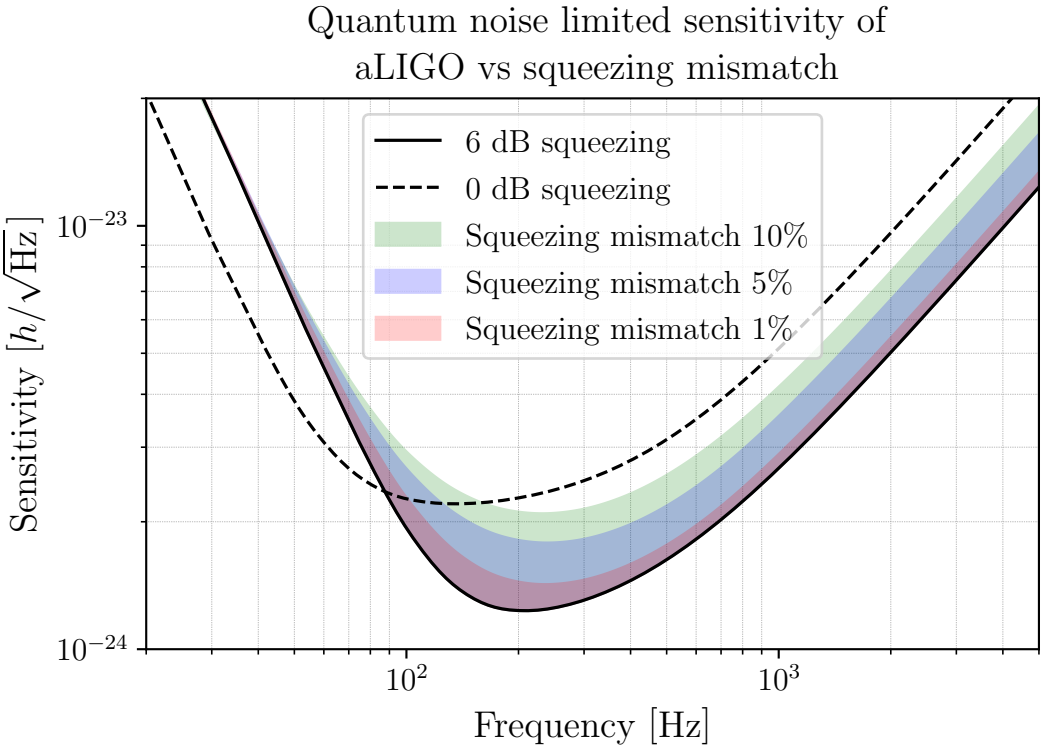

Figure 6.1: Shown is the reduction in quantum noise limited sensitivity if the squeezer is mismatched by 1%, 5%, or 10% in an aLIGO like detector setup with 6 dB of frequency independent squeezing using FINESSE [128, 200]. The worst case scenarios are shown, as a mismatch of 10% can be distributed between beam waist and position mismatch. Thus for a given mismatch the sensitivity can lie somewhere between the upper coloured bound and the solid-black 6 dB line.

A diagram of the simplified problem being considered is illustrated in figure 6.2. The squeezer here has been simplified to a single laser source (SQZ), which is injected

into the main interferometer (IFO) through the output faraday isolator (OFI). The gravitational wave signal is then filtered by the output mode cleaner (OMC) cavity, whose purpose it is to remove junk light and radio-frequency sidebands that do not contribute to the gravitational readout. The GW signal is measured by the photodiode DCPD.

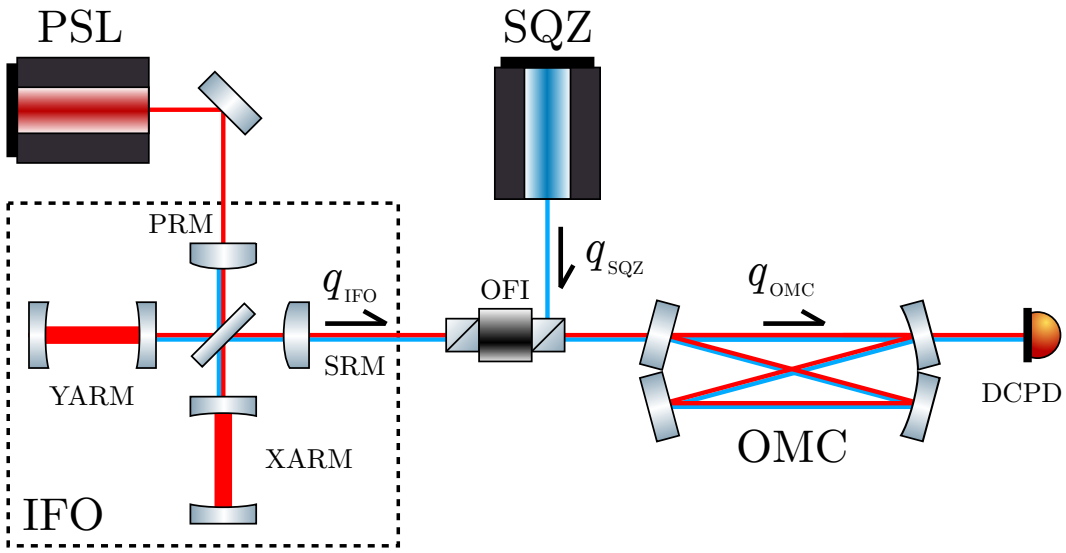

Figure 6.2: A simplified diagram of a gravitational wave interferometer with squeezing for illustrating the mode matching problem that is being considered in this paper. The interferometer and squeezer beam both need to be simultaneously mode matched to each other and the output mode cleaner (OMC). The mode matching problem reduces to making all of the q parameters equal $q_{\mathrm{IFO}} = q_{\mathrm{SQZ}} = q_{\mathrm{OMC}}$. The definition of the q parameter and its application to mode matching is given in section 6.3.

The modes of the OMC cavity, IFO and SQZ beam are parameterized by the q parameters q_{OMC}, q_{IFO}, and q_{SQZ} respectively. To minimise the squeezing losses due to mode mismatch it is necessary to minimise the difference between all three q parameters when the beams are overlapped. Current plans for upgrades and future designs will implement additional optical cavities called *filter cavities* [207]—which also require mode matching to. These will provide frequency-dependent squeezing for a broadband reduction in quantum noise, as opposed to frequency-independent squeezing as shown in figures 6.1 and 6.2.

Mode matching the squeezer to the IFO becomes increasingly challenging due to the ever increasing requirements for optical power stored in the interferometer. The increased power introduces significant thermal lensing which varies over time and must

be actively compensated for [141]. Various actuators are available to correct for this [89, 118] however accurate sensors for measuring the distortion to the optical fields are not as prevalent.

Heterodyne wavefront sensing techniques using quadrant-photodiodes can be used to sense both alignment [70] and shape [190] distortions in optical fields. Annularly segmented diodes, known as *bullseye-detectors*, can also be used [80, 117]. However, these schemes require the use of multiple sensors and *gouy-phase telescopes* to sense each of degree of freedom: translation, displacement, size, and curvature of the beam. An alternative method proposed by Fulda et.al. [157] uses an electro-optic beam deflector to generate a Hermite-Gaussian HG_{10} sideband that can be used as a reference for alignment sensing. This simplifies an experiment by using single-element photodiodes and does not require any Gouy-phase telescopes. Segmented photodiodes and higher order Hermite-Gaussian modes have additionally been used to generate DC cavity length error signals [75, 130].

In this paper we demonstrate a new heterodyne scheme that uses a single HG_{20+02} sideband selected by a resonant cavity from a phase modulated, mode mismatched beam. This HG_{20+02} sideband beats with a HG_{00} carrier to produce mode matching error signals for both degrees of freedom on a single photodiode with no Gouy-phase telescopes. Experimentally we show how this can be used to match a beam's shape to an optical cavity to 99.9%. This scheme allows multiple sequential cavities to be mode matched together and can be applied for mode matching the squeezed light source, filter-cavity, interferometer, and the OMC in current and future GW detectors.

Firstly, in section 6.3 we present the theory of the mode matching error signal as well as a simpler model in section 6.3.2 that can compute the mode matching error signal to first order in mismatch. In section 6.4 an experimental demonstration of the proposed mode matching scheme is described followed by an analysis of the results in section 6.5. Finally, in section 6.6 we present how this mode matching error signal can be applied to Advanced LIGO [135].

6.3 Theory

6.3.1 Ideal mode matching error signal

Mode matching, as defined in the context of optical cavities is the process of changing the incoming beam shape to match the eigenmode of a cavity. The eigenmode of a stable cavity is parameterized by a single complex number $q = z + \mathrm{i} z_R$, often referred to as the beam parameter [50], where z is the distance to the beam waist, and $z_R = \pi w_0^2/\lambda$ is the Rayleigh range of a beam with waist size w_0 and wavelength λ.

Mode matching is achieved when the waist position and size of the input beam matches the eigenmode of the cavity, which can be done by minimizing the quantities Δw_0 and Δz illustrated in figure 6.3. These two quantities form the two orthogonal degrees of freedom for mode matching. Both must be measured simultaneously in any mode matching sensing scheme. This is analogous to alignment sensing where the two degrees of freedom to be minimised are tilt γ and displacement δ as illustrated in figure 6.3.

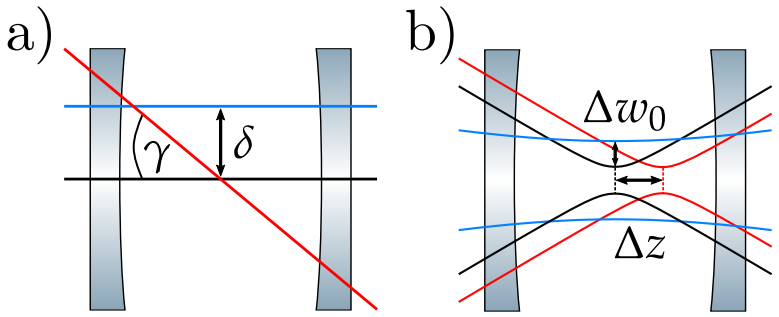

Figure 6.3: a) The two misalignment degrees of freedom: tilt γ (red), and displacement δ (blue) with respect to the cavity axis (black). b) The two mode matching degrees of freedom: waist position Δz (red), and waist size Δw_0 (blue) with respect to the cavity eigenmode (black).

An idealised mode matching error signal would indicate for a given q_1 and q_2 what is the mode mismatch between them, and more importantly the direction in q space along which they lie. One can define a quantity $\mathcal{M}$, which we call the *ideal mode matching error signal* that has the required properties

$$\mathcal{M}(q_1, q_2) = \frac{q_2 - q_1}{q_2 - q_1^*} \tag{6.1}$$

where the mode mismatch is given by $\mathrm{M} = |\mathcal{M}|^2$ [43] . The mode mismatch M between two Gaussian beam parameters q_1 and q_2 is defined by the fraction of HG_{00} power in q_1 that appears as higher order HG modes in q_2.

From the definition of mode mismatch M it is evident that it can be satisfied by more than one value of q_2 for any q_1 and nonzero M. The set of q_2's that satisfy $\mathrm{M} = |\mathcal{M}|^2$ are called the M *mode matching contour of* q_1. The contour of q_2's for $q_1 = z_1 + \mathrm{i}z_{R1}$ can be completely described by

$$q_2 = q_1^* + \frac{2\,\mathrm{i}\,z_{R1}}{1 + \sqrt{\mathrm{M}}\exp(\mathrm{i}\theta)} \tag{6.2}$$

where $0 \leq \theta < 2\pi$ is the angular position along the contour of constant mode mismatch M in q-space.

To first order in mode mismatch $\mathcal{M}$ is

$$\mathcal{M}(q_1, q_2) = \frac{\varepsilon_q(q_1, q_2)}{2} + \mathcal{O}\left(\varepsilon^2\right) \tag{6.3}$$

where ε_q is a relative change in beam parameters. It is defined as

$$\varepsilon_q(q_1, q_2) = \frac{q_2 - q_1}{z_{R,1}} = \varepsilon_z(q_1, q_2) + \mathrm{i}\varepsilon_{z_R}(q_1, q_2) \tag{6.4}$$

where $z_{R,1}$ is the imaginary part of q_1[1]. The real part of this ε_z represents a waist position mismatch, and ε_{z_R} Rayleigh range mismatch between the q_1 and q_2; these are also referred to as the orthogonal *mode matching quadratures*. We show in section 6.3.2 that the proposed mode matching error signal approximates the ideal mode matching error signal to first order in mode mismatch up to a constant factor.

6.3.2 Single sideband error signal

Here we provide a broad overview of our technique and detailed mathematical derivations can be found in appendix D.3. In order to understand how our scheme can be applied to an arbitrarily complicated optical system such as a gravitational wave detector we must first cover two key cases. The first being the mode matching between two beams as in figure 6.2 between q_{IFO} and q_{SQZ}. The second being the mode matching between a beam and a cavity as in figure 6.2 between q_{IFO} and q_{OMC}. Additional instances that require mode matching error signals in Advanced LIGO can be obtained from these two cases and are discussed in more detail in section 6.6. For example mode

[1]The Rayleigh range in (6.4) can be for either q_1 or q_2 as they are approximately equal for small mode mismatches. The lowest numerical error is achieved using $(z_{R,1} + z_{R,2})/2$

matching to a filter cavity in the planned A+ upgrade [176] to Advanced LIGO would require the application of the second case.

For both cases, let us consider the behaviour of a beam consisting of a HG_{00} carrier at the optical frequency ω_0 with a beam parameter q_1 and a $\mathrm{HG}_{02,20}$ single sideband with a beam parameter q_2 at a frequency offset Ω,

$$E = \left[U_{00}(q_1) + (U_{20}(q_2) + U_{02}(q_2))e^{\mathrm{i}\Omega t}\right] e^{\mathrm{i}\omega_0 t}. \tag{6.5}$$

Here U_{nm} are the 2D transverse mode shape for the nm-th Hermite Gaussian modes. In the case $q_1 = q_2$, this beam would look as if the carrier q_1 parameter is being modulated in both waist position and size at a frequency Ω, forming a beam with pure *beam shape modulation* at frequency Ω. This is due to the fact that a HG_{00} beam combined with a small amount of HG_{02} can be considered to be a pure HG_{00} but with a slightly different q parameter [42] and a single sideband implies a modulation in both quadratures.

Mode matching error signal between two beams

For the first case, the optical field (6.5) incident on a photodiode will generate a photocurrent $\mathcal{I} \propto |E|^2$. To compute the mode matching error signal we must first ensure all optical fields are represented in the same q basis—here we choose to project the $\mathrm{HG}_{02,20}$ in the basis q_2 into q_1, as depicted in figure 6.4. When the carrier and sideband have the same $q_1 = q_2$ parameter the HG_{00} and $\mathrm{HG}_{02,20}$ are orthogonal and produce no beat. In general the carrier and sideband would travel through separate optical systems such that $q_1 \neq q_2$ when they are combined on a beamsplitter. Demodulating $\mathcal{I}$ at a frequency Ω and low-passing the output results in the complex-valued signal

$$\mathcal{Z}_{\mathrm{beam}} = -\mathrm{i}\sqrt{P_{00}P_{02}}\frac{\sqrt{2}}{2}\varepsilon_q(q_1, q_2) + \mathcal{O}\left(\varepsilon^2\right). \tag{6.6}$$

We derive this expression in detail in appendix D.3.1. Here P_{00} and P_{02} are the power in the carrier and reference sideband respectively. The measured error signal at some demodulation phase ϕ is then given by $\mathrm{Re}(\mathcal{Z}e^{\mathrm{i}\phi})$. Thus we can easily select either the real or imaginary part of the mode matching error signal using the demodulation phase.

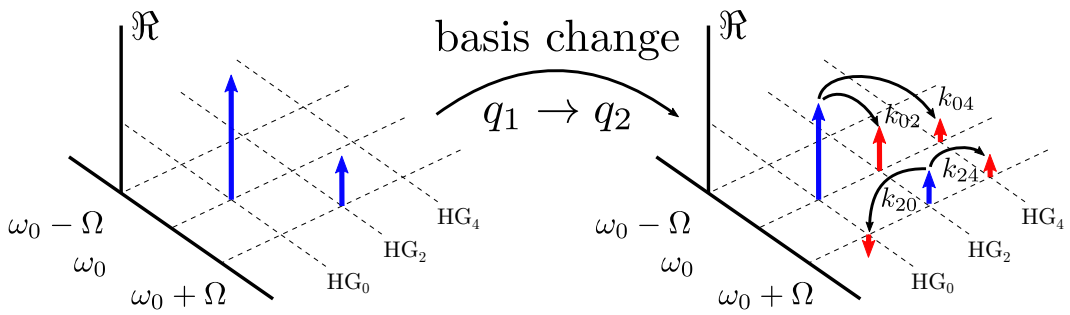

Figure 6.4: An example of a basis change. The two mode spectra on the left and on the right describe the same beam but in bases q_1 and q_2 respectively. The new Hermite-Gauss modes that are generated during the basis change are indicated with red arrows. The coupling coefficients k_{nm} used to scatter fields to other Hermite-Gaussian modes in a basis change are listed in Table D.1.

Mode matching error signal on reflection of a resonant cavity

For mode matching between a beam and a cavity, which is the second case described in section 6.3.2 we must consider when (6.5) with $q_1 = q_2$ is reflected off of an optical cavity with eigenmodes parameterised by q_{cav} . The cavity is held on resonance for the HG_{00} carrier, the resonating field has a shape defined by q_{cav}. To compute the mode matching error signal we are required to project all components of the incident field into the q_{cav} basis. The complex-valued error signal is this case is found to be

$$\mathcal{Z}_{\mathrm{cav}} = -\mathrm{i}\sqrt{P_{00}P_{02}}\,(R_{\mathrm{cav}} - 1)\,\frac{\sqrt{2}}{2}\varepsilon_q(q_1, q_{\mathrm{cav}}) + \mathcal{O}\left(\varepsilon^2\right), \tag{6.7}$$

where ε_q is now the mismatch between q_1 and q_{cav}, and R_{cav} is the reflectivity of the cavity for the carrier. R_{cav} depends on whether the cavity is over-coupled, impedance matched, or under-coupled [140]

$$R_{\mathrm{cav}} = \mathrm{sign}(R_1 - R_2)\left(\frac{R_1 - R_2}{R_1 + R_2 - 2}\right)^2, \tag{6.8}$$

where $R_{1,2}$ are the reflectivity of the input and output mirrors. For over-coupled, impedance matched, and under-coupled cavities R_{cav} takes the values $-1 < R_{\mathrm{cav}} < 0$, $R_{\mathrm{cav}} = 0$, and $0 < R_{\mathrm{cav}} < 1$ respectively.

If $q_1 = q_{\mathrm{cav}}$ there is again no optical beat measured at the reflected photodiode due to the HG modes of the incident and circulating fields being perfectly orthogonal. In the

case where the incident beam is mismatched this orthogonality between the modes is broken and an optical beat is measurable.

Generating a single HG_{nm} sideband

There are multiple ways in which a single sideband can be generated. In this work we will produce the single sideband field as described by (6.5) by using a Mach-Zender interferometer. One of the paths will contain a Fabry-Perot cavity which is locked to the HG_{20+02} mode of phase modulated sideband generated by an electro-optic modulator (EOM). This is then combined with the original unmodulated carrier field to produce the final field. Although simple the q of the carrier and sideband will not be identical, thus care must be taken to mode match and align them well. The downside of this method is that it is not particularly efficient as the vast majority of the power resides in the carrier frequency, the non-transmitted sideband, and in the HG_{00} mode.

An alternative method would be to use a modulated mode-mismatched beam where the frequency of the sidebands are chosen so that $HG_{20,02}$ higher order mode of sidebands resonates simultaneously with the HG_{00} at the carrier frequency. Both then have the same q parameter and are transmitted through the cavity ensuring the carrier and sideband are aligned, as well as mode and phase matched. The efficiency of sideband generation is identical to our Mach-Zender method. However unlike the Mach-Zender method the choice of modulation frequency is fixed for a particular cavity, and for short cavities the modulations frequencies can also be prohibitively high unless a cavity near to geometric instability is used.

A more efficient approach could be to use an EOM with specifically designed electrodes that shape the electric field inside the electro-optic crystal in such a way that it lenses a beam passing through it—similar to Fulda et.al's [157] modulator. A disadvantage with this method is that the lensing created by such a modulator would likely be almost purely astigmatic due to the fact that external electrodes require the divergence of the electric field inside the crystal to be zero. Then to sense mode mismatch an astigmatic cavity can be used to select out either the horizontal or vertical higher order mode, alternatively an astigmatic Gouy-phase telescope [190] can be used to to correct the phase difference between the vertical and horizontal modes to obtain a cylindrically symmetrical modulation.

6.3.3 Mode matching actuators

For the mode matching error signal to be useful it is necessary to be able to actuate on the mode matching of a beam to a cavity. This can be achieved by either changing the position of a focusing optic or the focal power of an optical element. Mode matching has two degrees of freedom and so to fully actuate on mode matching two orthogonal actuators are required. The distances that fixed focal length lenses or mirrors needed to be translated is typically up to tens of centimeters. Focus adjustable lenses or mirrors are an attractive option for a mode matching actuator since the optic can remain in one place.

The mode matching actuator used in this experiment was a liquid lens on a manual translation stage. The position and focal power of the lens served as the two orthogonal mode matching degrees of freedom. This was chosen as a compromise between cost and usability. The mode matching actuator needed to respond quickly in order to map out the mode matching error signal in actuator space in a reasonable amount of time. Two static lenses on translation stages would have been too slow and two liquid lenses per mode matching stage was beyond the budget of the experiment. To scan the parameter space the liquid lens would be manually moved to each point, which was slow, and then the current of the liquid lens would be swept, which was fast.

The position of the liquid lens and translation stage was determined using an optimization algorithm such that each mode matching stage achieves about 20% mode mismatch from ideal mode matching at the edge of the actuation range. The model used in the optimization was a beam tracing ABCD matrix model with estimates for the input and target beam parameter determined from cavity geometry and beam profiles. It was found to satisfy the requirement of relatively uniform actuation 20% mode matching actuation the addition of a 30 cm offset lens was necessary to both liquid lenses. This offset lens was mounted to the liquid lens via a short lens tube. The input beam had to be carefully aligned through the lens tube had to prevent misalignments when translated and when the liquid lens focal length changed. This misalignment proved to be extremely difficult if not impossible to eliminate completely. For any position on the translation stage the misalignment due to focal length change can be eliminated completely by walking the input beam position and angle such that the beam spot

motion is minimized in both the near and far field. However once the liquid lens is translated the misalignment due to focal length change returned and the input beam alignment has to be readjusted. This is most likely due to misalignments between the lens tube axis and the translation axis, for which we had no method of aligning to the degree needed to remove misalignments when the mode matching is changed.

The tube and translation axis misalignment was minimized using irises, which improved the situation but could not eliminate the misalignment completely. The remainder of the induced misalignment from the mode matching actuator was compensated for by hand with two beam steering mirrors sitting between the liquid lens telescope and the triangular mode cleaner. For each measurement of the mode matching error signal the alignment was adjusted with those mirrors to minimize the HG_{01} and HG_{10} resonances in the triangular mode cleaner cavity. An automatic alignment control system to the input of the mode cleaner could be used here to eliminate the residual misalignment.

6.4 Experimental Demonstration

To test the proposed mode matching error signal an experiment as depicted in figure 6.5 was performed where the goal is to mode match q_{NPRO} to q_{cav}. Additionally, it was designed to replicate the parts of the aLIGO output in figure 6.2 that would be relevant for the mode matching error signal. The goals of this experiment were to show that zeroing the error signal optimizes the mode matching metrics: maximizing the transmission through a resonant cavity, and minimizing the amount of HG_{02+20} circulating in the cavity. We show that to achieve this careful consideration of mode matching error signal, offsets are required.

The experiment description presented here is split into descriptions of the optical and electronic paths.

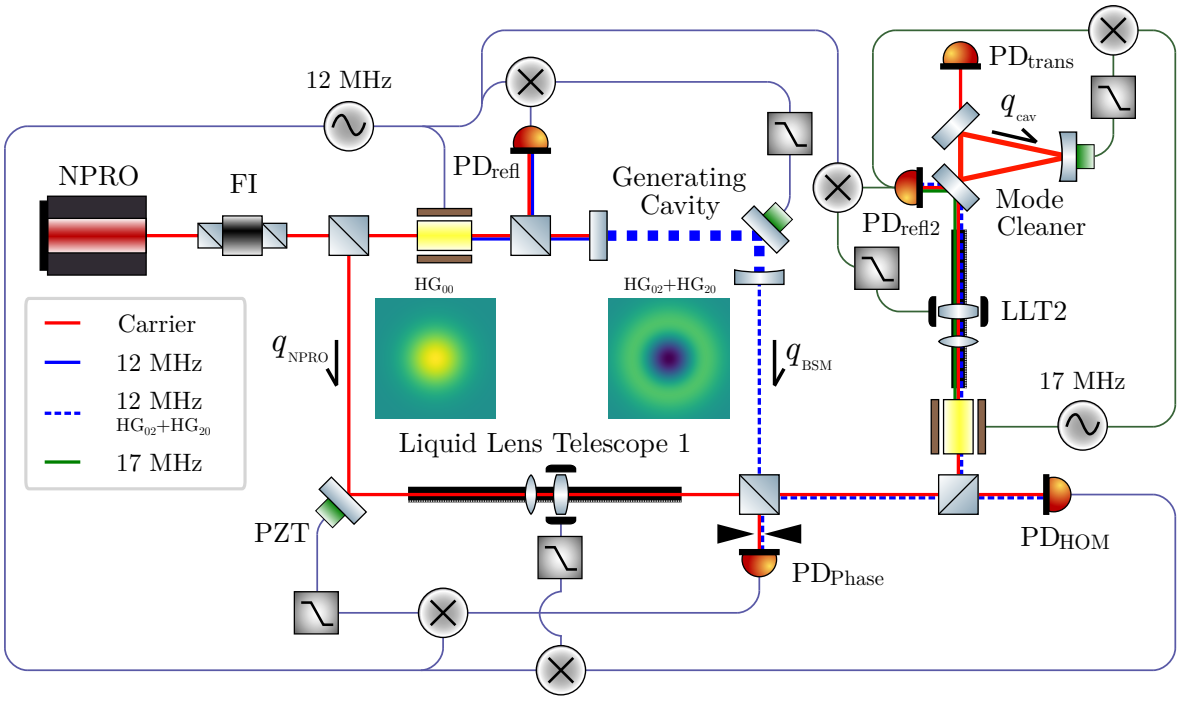

Figure 6.5: Diagram of the tabletop experiment performed to verify the mode matching error signal. It has been designed to simulate the optical layout of the output of an advanced gravitational wave detector. The generating cavity plays the part of the OPO cavity in figure 6.16. The triangular mode cleaner works as the OMC, and the NPRO as the interferometer beam. The RF signal generation, mixing, and lowpass filtering was all done on STEMlab 125-14 FPGAs by Red Pitaya [191] running the PyRPL package [162].

6.4.1 Optical path

A beam from a 1064 nm non-planar ring oscillator (NPRO) (Innolight Mephisto [153]) was split into two paths in a Mach-Zehnder configuration before being recombined and incident onto a triangular cavity. One of the paths was intended to represent the interferometer beam, which goes through an adjustable focal length liquid lens (EL-10-30-C-NIR-LD by Optotune [224]) on a translation stage. The NPRO beam was intentionally not spatially filtered in any way in order to mimic the fact the interferometer beam is not a pure HG_{00} [113]. The liquid lens telescope allows us to change the q_{NPRO} parameter to match it to q_{BSM} when the beams combine on the beamsplitter.

The other path goes through a 12 MHz New Focus 4005 EOM [126], which adds a pair of 12 MHz phase modulation sidebands to the beam. These sidebands are typically used to provide a PDH error signal to lock a cavity to a resonance of the carrier beam

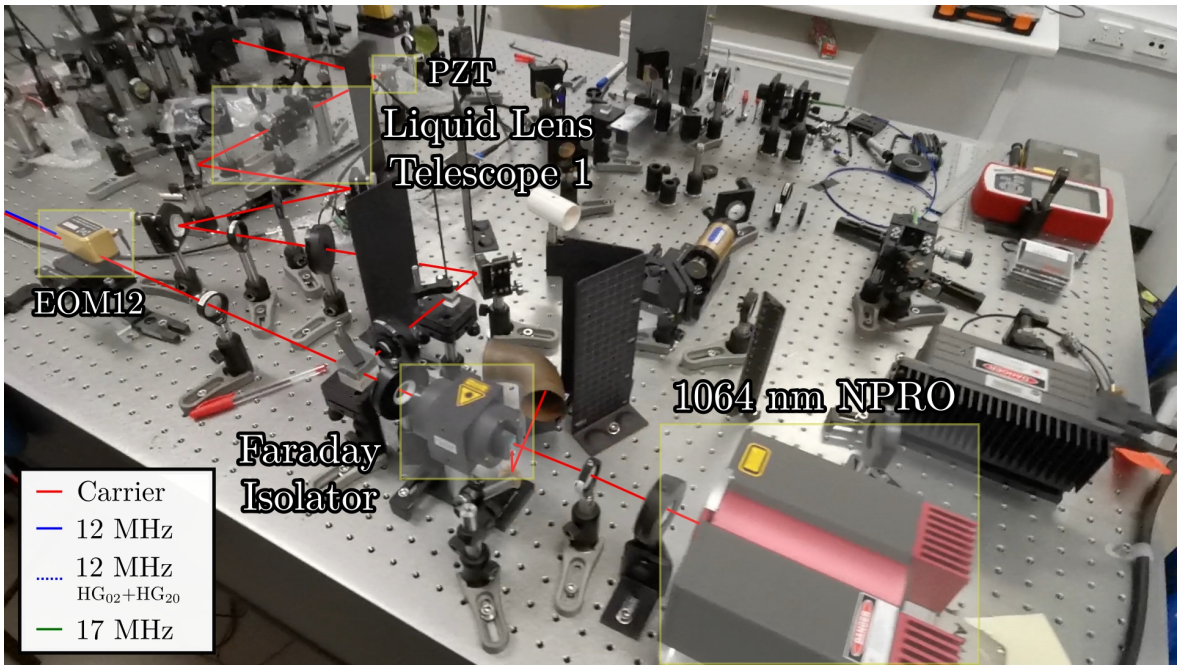

Figure 6.6: Annotated photo of the NPRO laser side of the tabletop mode matching error signal experiment.

[41, 84]. Typically, the PDH error signal is used to lock to the HG_{00} of the carrier beam. Here the PDH error signal is used to lock the length of the *generating cavity* in figure 6.5 to the HG_{02} mode of a 12 MHz sideband. The HG_{20} mode is also resonant at the same frequency.

About 1% of carrier HG_{00} power was transmitted through the generating cavity as 12 MHz HG_{02}, which was sufficient for demonstrating the mode matching error signal. The theoretical maximum conversion efficiency for this process is about 4.2%, which can be obtained by using about about 67% of input mode mismatch into the generating cavity, and an EOM modulation depth of about 1.8.

The generating cavity in this experiment is a 20 cm long L-shaped hemispherical cavity with a flat input coupler and a 50 cm output coupler, both at 99% reflectivity. The corresponding finesse and free spectral range (FSR) are 310, and 750 MHz respectively. The L-shape was chosen to facilitate the available PZTs for cavity length tuning, which only worked on reflection and so could not be mounted on either the input or output coupler. The intermediate mirror in the L-bend is a flat HR mirror with a Thorlabs PK25LA2P2 [167] PZT stack located about 5 cm away from the input coupler. The waist of the cavity is located at the input coupler and has a design size of 290 um.

The two arms of the Mach-Zehnder are recombined with a 50:50 beamsplitter. For convenience we will call the beam that is still in the fundamental mode the *optical local oscillator* and the 12 MHz offset HG_{02+20} beam as the *mode modulation beam*. One of the output ports of the Mach-Zehnder is incident on a photodiode PD_{phase} with an iris. The iris clips the beam around the center to break the orthogonality between the optical local oscillator and the mode modulation beam. This is used to provide a phase error signal for the microscopic path length changes between the two arms of the Mach-Zehnder.

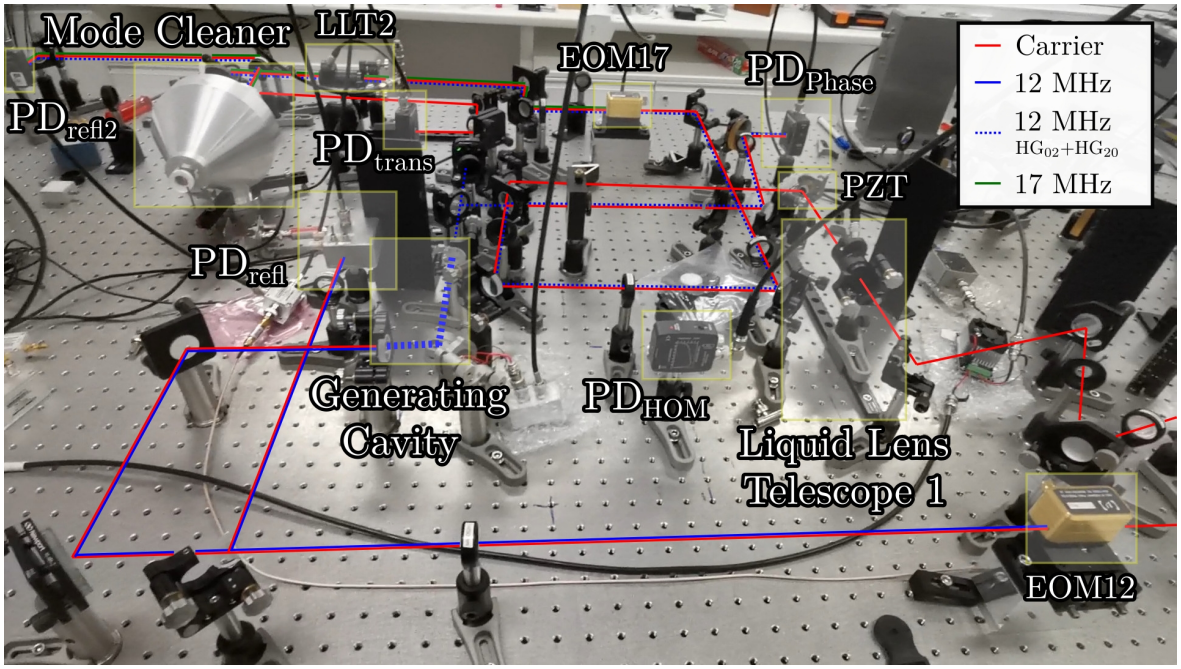

Figure 6.7: Annotated photo of the generating cavity and Mach-Zehnder side of the tabletop mode matching error signal experiment.

The phase error signal is used to drive a Thorlabs PK25LA2P2 PZT [167] in the optical local oscillator arm to lock the phases of the two arms. This step is necessary as the phase difference between the optical local oscillator and the mode modulation beam couples into the mode matching error signal readout and hence needs to be kept fixed.

The photodiode PD_{HOM} measures a mode matching error signal between q_{NPRO} and q_{BSM} as described in section 6.3.2. This error signal must be zeroed by adjusting liquid lens telescope 1 in figure 6.5 to mode match the optical local oscillator to the mode modulation beam before the combined beam can accurately measure the mode matching error signal to the triangular mode cleaner cavity on PD_{refl2}. For subsequent mode matching calculations the Eigenmode of the generating cavity is used as the

reference when the Mach-Zehnder arms are mode matched.

The combined optical local oscillator and the beam modulation sideband are then incident onto a triangular cavity that corresponds to the OMC cavity in a GW detector, which we want to mode match to. This triangular cavity was a monolithic aluminum shell with three mirrors glued at fixed points to form a triangular path inside the shell. This cavity was originally built for a different experiment at the UofA and was used here as a time and cost saving measure. The reflected beam off of a triangular cavity is not collinear with the incident beam and hence there is no need for or a Faraday isolator between the Mach-Zehnder output and the triangular mode cleaner cavity.

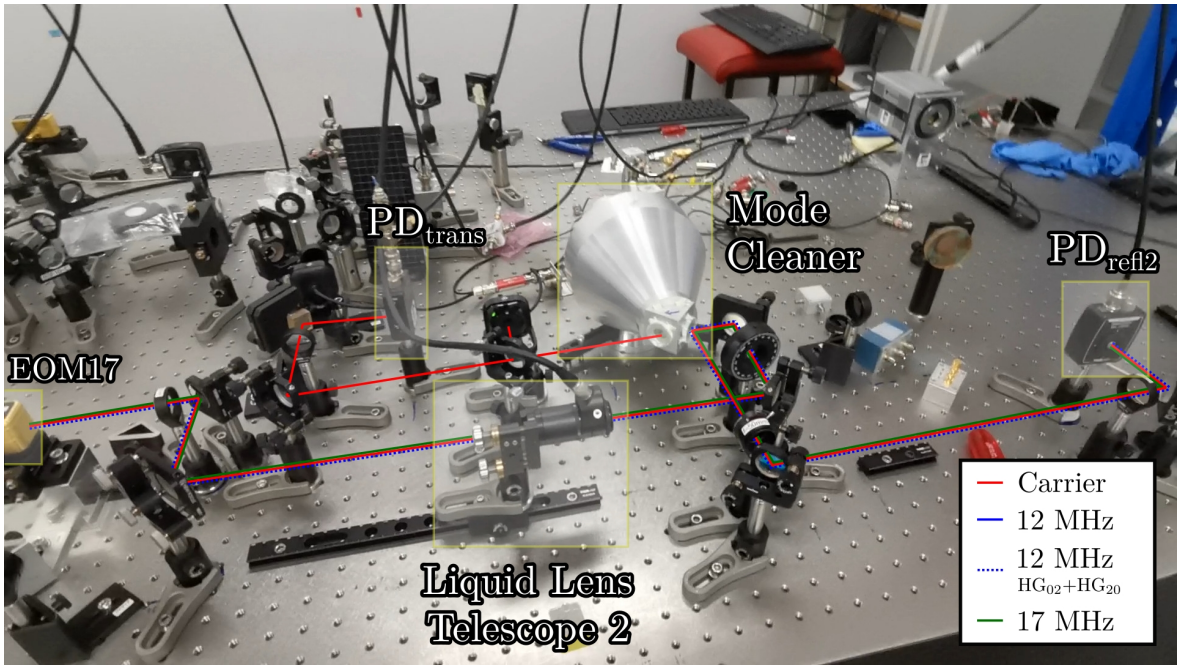

Figure 6.8: Annotated photo of the output mode cleaner side of the tabletop mode matching error signal experiment.

The beam incident on the triangular mode cleaner is phase modulated at 17 MHz with another New Focus 4005 EOM [126] to generate the PDH error signal, which is measured by demodulating PD_{refl2}. On reflection the mode modulation beam produces a 12 MHz amplitude modulation that is proportional to the mode mismatch between the incident beam and the triangular mode cleaner cavity as described in section 6.3.2. The demodulated 12 MHz signal is then fed back to LLT2 to match to q_{NPRO} to q_{cav}. The transmission through the mode cleaner is monitored by the photodiode PD_{trans}. A good mode-matching error signal will ensure the transmission is at a maximum when the mode matching error signal is zeroed.

6.4.2 Electronic path

Phase modulation sidebands

The 12 and 17 MHz signals were generated using two Red Pitaya STEMlab 125-14 [191] FPGAs separately. The Red Pitayas have 14-bit DACs, which allow for high quality RF signal generation. To minimize digitization artifacts we ran the signals at the highest possible output voltage, which was 2 V peak-to-peak. This was not sufficient to drive the EOMs at a suitable modulation depth and so the RF signals had to be amplified. For this we used two ZHL-1A wideband RF amplifiers by Mini-Circuits [161], one for each RF signal frequency. The gain of the ZHL-1A is quoted as 17 dB between 2–500 MHz. To bring the RF signal level down to desirable levels RF attenuators were used.

The amplified RF signals were used to drive the EOMs — a pair New Focus 4005 phase modulators [126] — which contain an electro-optic crystal that changes its refractive index with the voltage applied to a pair of electrodes. The voltages needed to produce a sufficient refractive index change can be large, and so it is common to combine the crystal with an inductor to form a resonant tank circuit. The resonant tank circuit has a large gain when compared to a broadband EOM, but only for the resonant frequency of that tank circuit [126]. The two EOMs used were originally procured for a different experiment, but the coatings and resonance frequencies — 12 and 17 MHz — proved suitable for this experiment. With the modulation frequencies it was important to consider the cavity lengths in this experiment. The length of an optical cavity determines the frequency shift from one longitudinal mode to the next, which is also known the free spectral range of the cavity. If a cavity is too short the phase modulation sidebands become partially resonant with the carrier, which can cause issues. In this experiment it was found that the partially co-resonant sideband and carrier introduced an offset into the mode matching error signal, which is discussed in more depth in section 6.5.1. Thankfully this offset can be measured and subtracted, though the need for the offset subtraction can be removed in the first place by designing the cavities and picking the phase modulation frequencies so that the sidebands do not partially resonate with the carrier.

Photodetector bandwidths

When measuring RF optical beats it is important to ensure that the bandwidth of the photodetectors includes the modulation frequencies The RF sensing photodetectors were all Thorlabs DET10C2 [166] with the exception of PD_{refl}, which was an in-house photodetector, built at the UofA for a different experiment. Its specifications are similar to the DET10C2 and was only used as a cost saving measure.

The Red Pitaya has input impedance of 1 MOhm, similar to most oscilloscopes. Because of this each photodetector was connected to the Red Pitaya input in parallel with a 50 Ohm terminator to minimize RF reflections and to maximize the photodetector bandwidth. The DET10C2 photodetectors are specified to have a 80 pF junction capacitance, which gives them a 35 MHz bandwidth when terminated with 50 Ohm load [166]. This bandwidth is inversely proportional to the resistive load and so in principle the detectors could have been terminated with a 100 Ohm load for more signal gain at a 17.5 MHz bandwidth, which would have been sufficient for the RF frequencies in this experiment.

The photodetector PD_{trans} was only used as a DC power meter, terminated at the Red Pitaya with a 50 KOhm trimpot — a variable resistor that was used to set the signal level to make the most of the 14-bit ADC on the Red Pitaya. Despite the optical signal not having any RF components the resistive load cannot be too large since that introduced visibly noticeable distortions to the resonance peaks of a cavity scan. The distortions could be reduced by lowering the resistive load, thereby increasing detector bandwidth, or reducing the cavity scan rate, which would decrease the frequency content of the signal, allowing it to fit within the limited detector bandwidth. The range of cavity scan rates and load resistance was not tightly constrained and so an appropriate combination of the two was chosen without much consideration. A scan rate of about a tenth of a second per cavity FSR was used in this experiment.

Electronic noise sources

It was found that a non-negligible amount of noise was coupling into the experiment via ground loops, particularly at the mains frequency and the harmonics. A number of measures were taken that appeared to significantly reduce this type of noise. The

optical table used in this experiment, like most was grounded with an explicit connection between the tabletop and the earth of the lab power outlet as a safety measure. The Red Pitaya, unlike some ADCs does not use the lab earth as the ground and is instead grounded through its SMA connectors [191]. This allows the Red Pitaya to have a completely independent electronic ground from the lab earth, greatly reducing ground loop noise. However, this ground loop separation can be easily undone if any of the components connected to the Red Pitaya are grounded to the lab earth ground. This can easily happen for example if any of the photodetectors make electrical contact with optical table, since the photodetectors are typically grounded through their case. The electrical contact usually comes from the optical post, which is typically screwed to the case and then held in place by post mount. The contact can be broken by using a post mount with a base made of a non-conductive material, such as acrylic, thereby insulating the photodetector from the ground.

Additionally it was found that the DC power supplies can induce noise in the sensing loops through capacitive coupling. This noise was reduced by moving the DC power supplies as far away from the Red Pitayas and sensing photodetectors as possible inside the lab. Another known source of noise was attributed to the switch mode power supplies used to power the Red Pitayas. This noise could be removed by replacing the power source for the Red Pitaya with a battery. This switch mode power supply noise had a negligible contribution to the overall signal to noise of the mode matching error signal, which was ultimately limited by the noise of the Mach-Zehnder phase lock loop. For convenience the experiment was performed with the Red Pitaya's bundled switch mode power supplies.

PZT operation

This experiment used 3 PZTs, each of which was handled differently. The PZT controlling the length of the generating cavity was a Thorlabs PK25LA2P2 [167] driven by PiezoDrive PD200 amplifier [178] which has a gain of 20 V/V. The driving signal for the generating cavity PZT came from the PD_{refl} photodetector that was demodulated by the Red Pitaya at 12 MHz. The Red Pitaya can output anywhere between ± 1 V and so the PD200 was operated with 25 V offset to ensure that the voltage at the PZT never drops below 0 V, which is harmful for the PZT.

The 12 MHz demodulation for PD_{refl} can be performed onboard the Red Pitaya without an external 12 MHz reference because the original 12 MHz modulation was referenced to the Red Pitaya clock. Better yet, the Red Pitaya can demodulate at any demodulation phase since any phase shifted 12 MHz it generates is also referenced to the same clock. The demodulated signal is then digitally low passed onboard the Red Pitaya with a 3 KHz bandwidth and fed into an onboard PID controller. This PID controller outputs a sum of the demodulated signal and the same signal filtered through simple IIR digital integrator with an adjustable gain. This makes the Red Pitaya a nearly ideal optical lockbox that can function as a signal generator, ADC, RF mixer, and PID controller all at the same time.

Suitable proportional and integrator gains were found by experimentation. The procedure used to find the gains was to increase the integrator gain until the system began feeding back high frequency noise. The integrator gain was backed off by about 10% from that point, after which the proportional gain was increased until the loop fed back high frequency noise. The proportional gain was then reduced by about 10% from that point. No derivative gain was used for any PID loops in this experiment.

The largest PZT was mounted to the monolithic triangular cavity. This triangular cavity together with its PZT was originally made for a different experiment at the UofA and was used here as a cost saving measure. This PZT was driven by a Thorlabs BPC301 [180] piezo controller with the internal voltage gain set to 7.5 V/V. The BPC301 has an onboard voltage offset, which is set digitally. Unfortunately this digital voltage offset is reset every single time the BPC301 is turned off. In lieu of this an in-house amplifier was made to sit between the Red Pitaya and the BPC301, which added about 5 V to the Red Pitaya output to ensure that the signal fed to the BPC301 is always positive. A separate amplifier is not strictly necessary since the Red Pitaya output signal can be offset onboard the Red Pitaya to always lie between 0 and 1 V to ensure it is always positive. Though this decreases the available bins the signal can occupy by half, which is not ideal. The driving signal for the triangular cavity PZT came from the PD_{refl} photodetector that was demodulated by a Red Pitaya at 17 MHz using the same methods as was for the 12 MHz signal.

The last PZT was another Thorlabs PK25LA2P2 [167] which was mounted to the back

of a mirror inside the optical local oscillator path in the Mach-Zehnder. The driving signal for it was the 12 MHz optical beat as sensed by PD_{phase}, which sat behind an iris that clipped all but a tiny fraction of the center of the beam to break the orthogonality between the HG_{02} sideband and HG_{00} carrier. This 12 MHz signal was demodulated on an analog Mini-Circuits RF mixer because the 12 MHz Red Pitaya had no more available ports and another Red Pitaya could not be used since it would have a different clock. The 12 MHz local oscillator for the demodulation was picked off from the signal going to 12 MHz EOM using an RF splitter. The output of the RF mixer was connected to a third Red Pitaya, which was used only as a PID controller for the Mach-Zehnder length signal. The demodulated signal was amplified prior to the Red Pitaya by a AMP220 voltage amplifier from Thorlabs to avoid digitization artifacts from the Red Pitaya ADC. The output signal from this Red Pitaya was amplified by PDu100B piezo driver from PiezoDrive which has a gain of 27.5 V/V, which was connected directly to the Mach-Zehnder PZT.

The Mach-Zehnder signal was noticeably more noisy than the generating cavity and triangular mode cleaner PDH signals. This is likely due to the increased shot noise from physically obstructing most of the light on PD_{phase}, though this was not investigated in detail. In this experiment all noise from the Mach-Zehnder length is imprinted directly onto the mode matching error signal. Despite this the experimental setup as described in this section proved sufficient to achieve 99% mode matching to the triangular mode cleaner.

6.5 Experimental Results

Varying one of the mode matching degrees of freedom provides a one dimensional slice of the mode matching error signal as shown in Fig. 6.9. The I and Q phase of the mode-matching error signal are each an error signal for a set of two orthogonal mode matching degrees of freedom. The demodulation phase was chosen such that the Q phase was most sensitive to the liquid lens current. The I phase shows less response to changing the liquid lens current, especially around the zero of the Q phase error signal.

A more complete picture of the mode matching error signal can be obtained by independently scanning both mode matching actuator degrees of freedom in figures 6.10

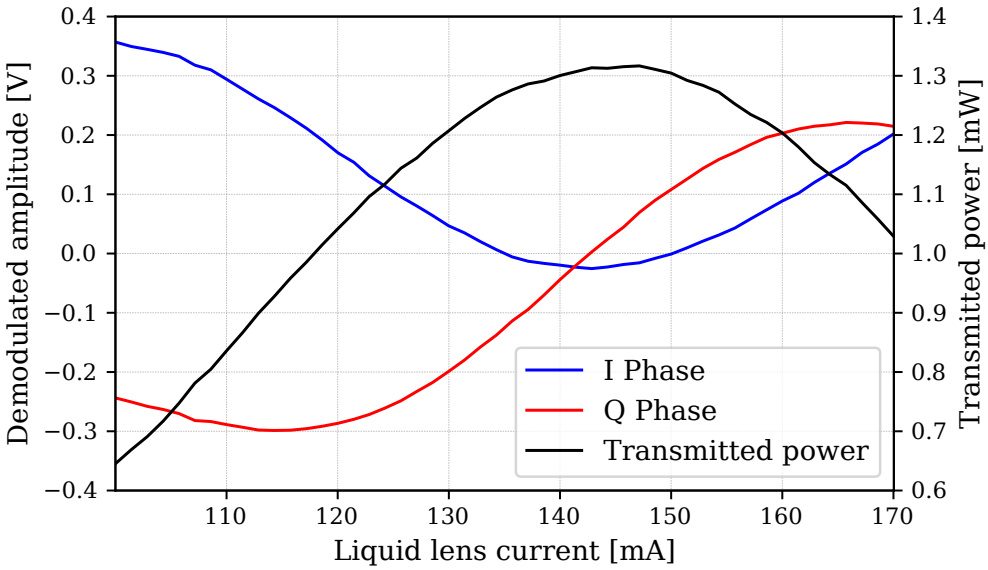

Figure 6.9: A 1D slice of the mode matching error signal measured at PD_{refl2} while varying the current on LLT2 in figure 6.5. The demodulation phase was chosen such that the Q phase was most sensitive to the liquid lens current.

and 6.11. Here the zero crossings of both I and Q phase form straight lines of different slopes, and hence intersect at a single unique point; the point that the mode matching actuators will be led to. As with Fig. 6.9 the demodulation phase has been chosen such that Q phase error signal is insensitive to liquid lens position. This leads to the I phase error signal to sense a linear combination of liquid lens current and position from the 45 degree contours it makes in the 2D error signal plots in figure 6.10. This is due to the fact that liquid lens position and current are not orthogonal mode matching actuators. When the I and Q phase zero crossings are overlaid onto the power transmitted from the cavity in figure 6.12 it can be seen that the zero of the mode matching error signal is offset from the peak of the transmitted power.

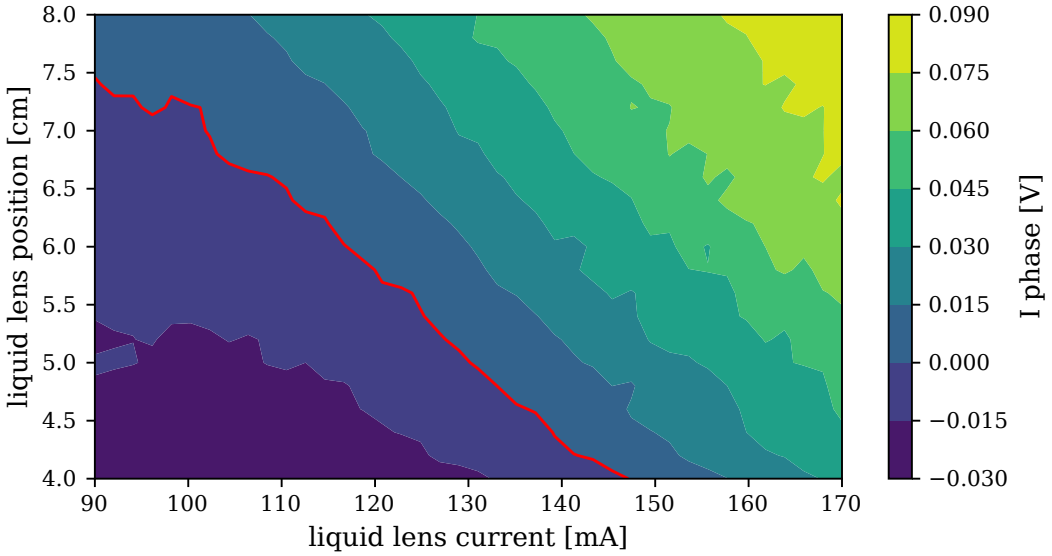

Figure 6.10: Measured I phase of the mode matching error signal. The zero crossing is highlighted in red.

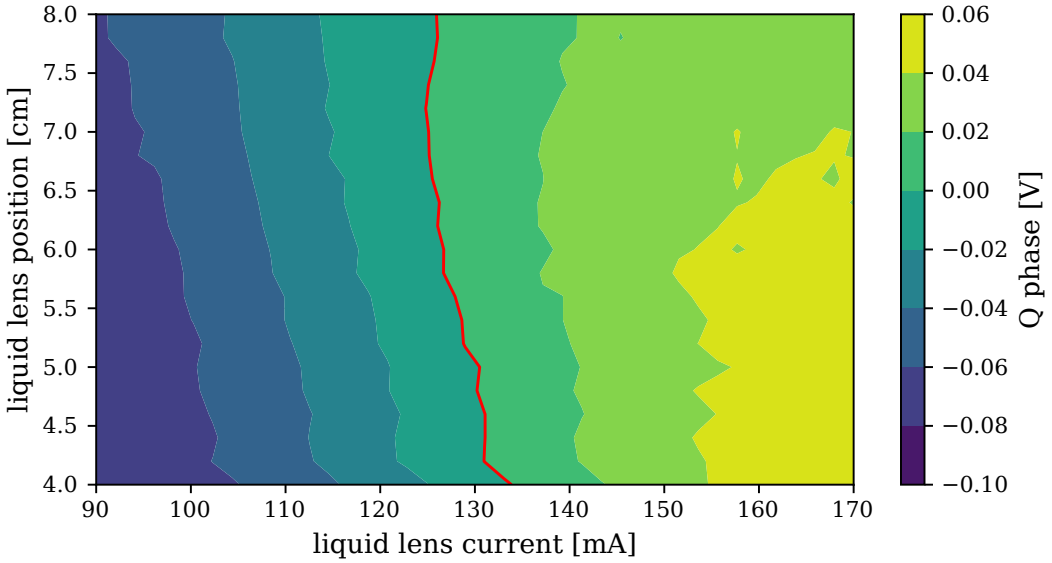

Figure 6.11: Measured Q phase of the mode matching error signal with the zero crossing highlighted in red.

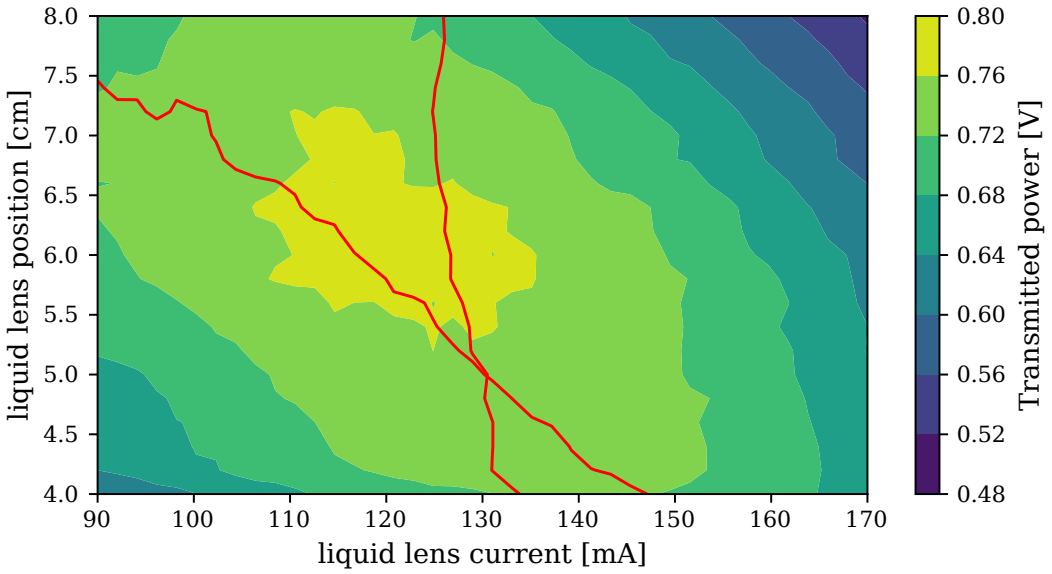

Figure 6.12: The power transmitted through the cavity with both the I and Q crossings overlaid. The offset between the zero crossing and the peak of the transmitted power is a known error signal offset described in section 6.5.1, and results of its subtraction illustrated in figures 6.13 and 6.15.

6.5.1 Error signal offset

Leaked carrier HG_{02} from generating cavity

The main contributor to the offset shown in figure figure 6.12 is the residual carrier HG_{02} leaking through the generating cavity. With a design finesse of 300, and free spectral range (FSR) of 600 MHz a non-negligible amount of carrier HG_{02} would leak through the generating cavity on resonance in addition to the 12 MHz HG_{02}. It was estimated that the ratio of leaked carrier HG_{02} power to 12 MHz HG_{02} in this experiment was about 2%. The leaked carrier HG_{02} and the 12 MHz HG_{02} would produce a beat at 12 MHz which offsets the 12 MHz beat that comes from mode matching error signal.

The offset can be easily measured by demodulating PD_{refl2} at 12 MHz while blocking the optical local oscillator. This beat should read zero if the beam modulation sideband is a pure 12 MHz offset HG_{02}. Any other value read is then the offset for the mode matching error signal. This offset calibration procedure was applied to the mode matching error signals measured in the validating measurement described in section 6.5.2.

The amount of leaked carrier HG_{02} in this experiment could be greatly reduced by either increasing the modulation frequency or increasing the generating cavity finesse, but was found to not be necessary after the offset calibration was performed.

Misalignment

It was found that small misalignment have a quadratic coupling into the proposed mode matching error signal by studying the k_{0200} coupling coefficient described in appendix D.3. Both numerical integration and Taylor expansions of k_{0200} show quadratic dependence on misalignment and linear dependence to mode mismatch.

An experimental verification of alignment sensitivity was not investigated, as manual alignment by hand produced negligible offsets when compared to the larger sources of offset, such as leaked carrier from the generating cavity. Due to imperfect alignment through the liquid lens, they induce misalignments whenever their current or position are changed. An auto-alignment system could be used to actively compensate for this and reduce misalignment further if required.

Astigmatism

It is also possible for astigmatism to present itself as an offset in the mode matching error signal if the cavity being mode matched to is astigmatic compared to the incoming beam or vice versa. The error signal will then have a zero between the individual zeroes of the horizontal and vertical planes. It is possible to extend this mode matching error signal to be able to sense astigmatism by making the cavity that generates the beam modulation sideband to be astigmatic or purely resonate the HG_{20} or HG_{02}. Then this cavity can be locked to the vertical or horizontal second order modes to provide independent mode matching error signals for either plane. An astigmatic actuator is then needed to be able to simultaneously drive the error signals in both planes to zero.

6.5.2 Validating measurement

To validate the mode matching error signal it is necessary to compare it to an external measure of mode mismatch such as a cavity length scan by applying a ramp voltage to a cavity mirror PZT. The ratio of the peak heights of the HG_{02+20} to the HG_{00} resonance provides a measure of mode mismatch. Performing a cavity scan for each point in actuator space is a time intensive task without an automatic cavity lock acquisition system, as the cavity needs to be relocked to the HG_{00} mode after each scan to read off the mode matching error signal. It is therefore desirable to obtain a validating measurement of the mode matching error signal with the fewest possible number of points to prevent ambient low frequency fluctuations to influence the results.

From figures 6.9 to 6.11 we can see that the error signal remains linear over a broad range in actuator space around the perfect mode matching point. One could then envisage a measurement where a small number of sparsely separated points are measured in actuator space. Covering the rest of actuator space can be done by fitting a polynomial surface or using an unstructured interpolation method such as thin plate spline interpolation [210]. We chose the latter due to its simplicity and lack of any external parameters that required optimizing.

With the error signal interpolated across the actuator space the zero of the error signal can be found by brute force evaluation. It is likely that the interpolated zero point would not zero the error signal, but its measurement can be fed back in to the

interpolation to yield an improved estimate of the true zero point of the error signal.

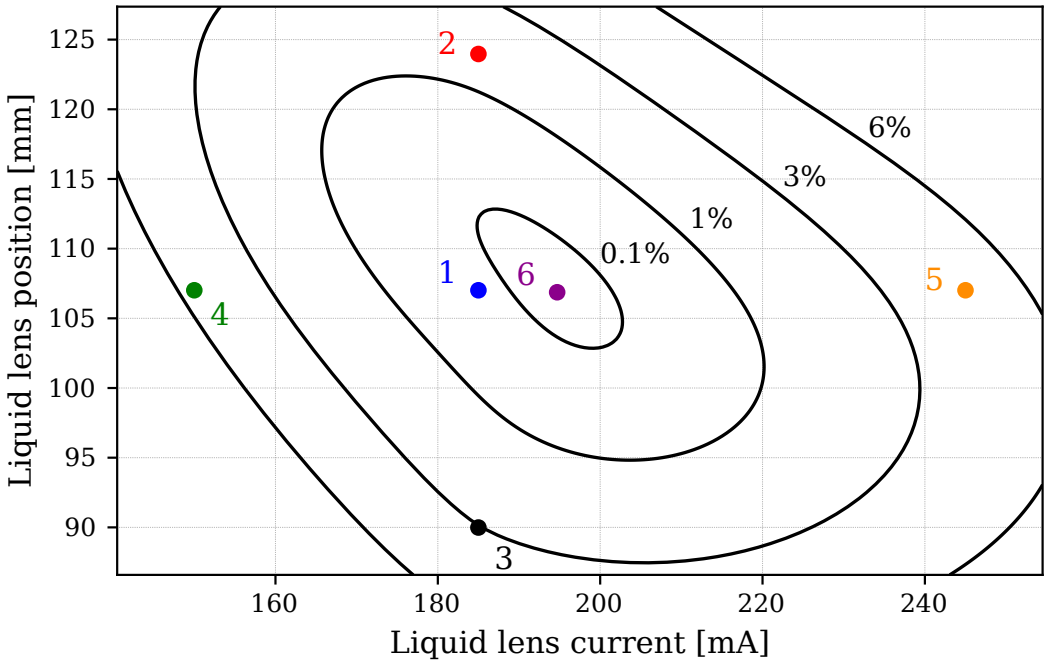

Figure 6.13: The six chosen points in actuator space for the validating measurement of the mode matching error signal. The contours are the corresponding mode mismatch as predicted by the mode matching error signal.

The results of following this procedure are illustrated in figures 6.13 to 6.15. The first 5 points were chosen from prior assumptions of the location of the zero point of the error signal. The 6^{th} point was the zero of the interpolated error signal, which coincided with the true zero of the error signal such that including it in the interpolation did not change the location of the interpolated zero point. The difference between optimal mode matching points in figures 6.12 and 6.13 was due to changes in the optical setup, specifically the positions of the liquid lens telescopes.

Additional measurements were taken near the zero point (not shown in figure 6.13), all yielding higher mode mismatch and non zero error signal values. This confirms that the offset subtraction in section 6.5.1 works as intended and the resulting error signal has no offset down to measurement uncertainty. We quote our best mode matching achieved with the mode matching error signal is $99.9^{+0.01}_{-0.1}\%$. The largest source of noise for the mode matching error signal in this experiment was found to be the Mach-Zehnder phase lock loop measured on PD_{phase} in figure 6.5. An analysis of shot noise was performed in appendix D.4 and was found to be negligible compared to the noise from the Mach-Zehnder phase and PDH loops.

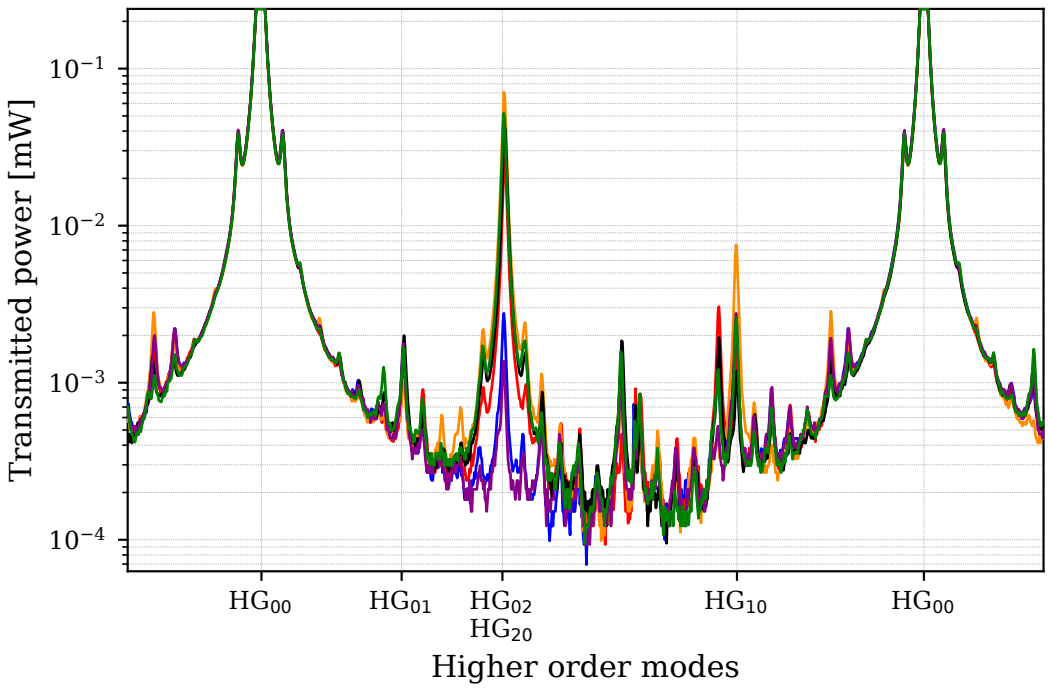

Figure 6.14: Cavity scans at each point in actuator space. The colour of each curve corresponds to the points in actuator space from figure 6.13

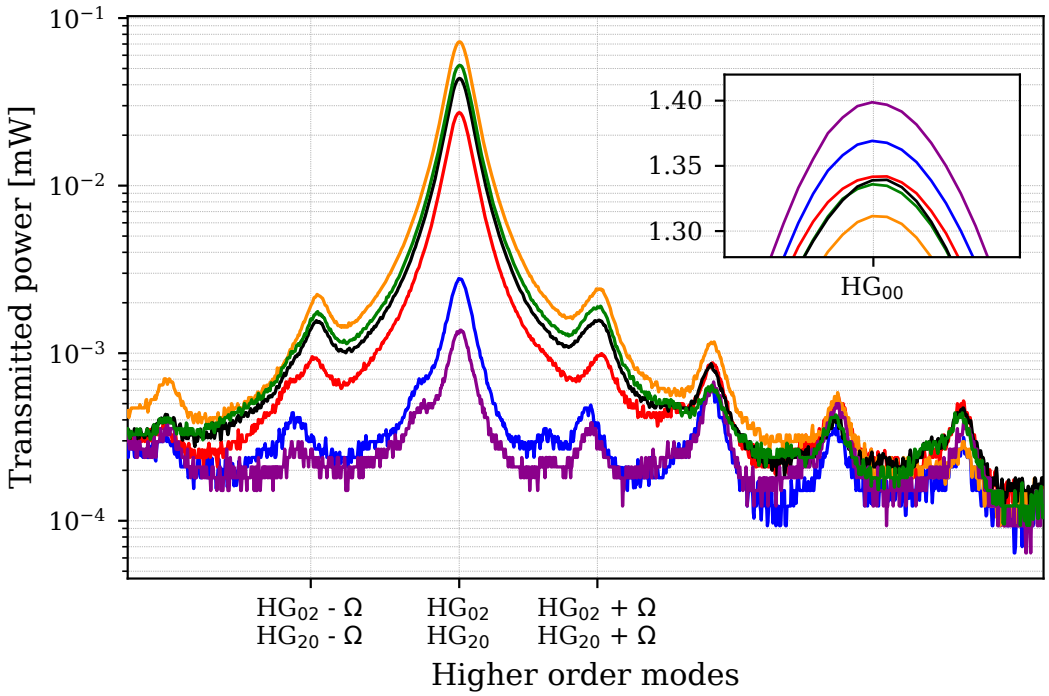

Figure 6.15: A close up of the HG_{02} resonance of the cavity scans from figure 6.14. Inset are the peaks of the HG_{00} resonances. The true mode mismatch is estimated by the ratio of the heights of the HG_{02+20} and HG_{00} resonances.

We hypothesize that our residual mode mismatch is a result of the difference in astigmatism between the incoming beam and mode cleaner. Varying the input alignment

did not strongly affect the height of the HG_{02+20} resonance compared to the $HG_{01,10}$ resonance.

6.6 Application in a gravitational wave detector

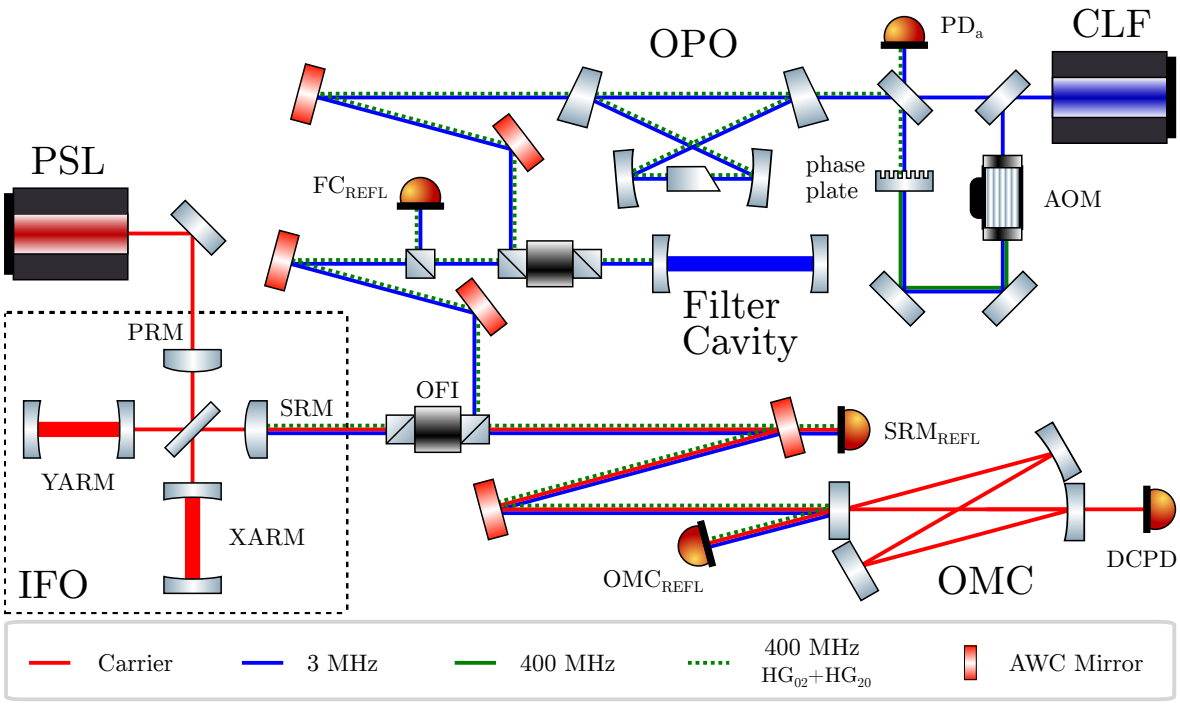

Figure 6.16: Shown is an optical layout of the output side of the a gravitational wave detector with the key photodiodes and cavities that our scheme would interact with. The frequencies listed in the legend are specific to Advanced LIGO. The only optical components that are new to aLIGO are the AOM and phase-plate, along with the extra optics to form the Mach-Zehnder in the CLF path. These extra components could be replaced with a single 400 MHz EOM to make the setup more similar to figure 6.5 at the cost of reducing the $HG_{02,20}$ sideband generation efficiency.

The proposed mode matching error signal can be applied in a gravitational wave detector to sense the mode mismatch between the cavities in the squeezer path and the interferometer beam, in addition to sensing the mode mismatch between the interferometer beam and the output mode cleaner. In this section we will consider how this could be implemented in a detector like Advanced LIGO (aLIGO).

A diagram of showing a possible implementation of the proposed mode matching error signal in aLIGO is shown in figure 6.16. The key idea is that the single reference HG_{20+02} sideband can be generated by exciting the higher order mode resonance in the optical parametric oscillator (OPO) that generates the squeezing simultaneously while

exciting the HG_{00} that would be the squeezed light mode. As described in section 6.3.2 this field can then be matched sequentially to the filter cavity, interferometer, and finally the OMC.

To implement the proposed mode matching error signal in aLIGO would require the addition of an AOM to produce a frequency shifted field at δf_2 , where δf_2 is the frequency offset of the second order transverse modes in the OPO cavity relative to the HG_{00} resonance. In the absence of a $HG_{20,02}$ phase plate, the control light field (CLF) beam must be mismatched to enable some coupling into the $HG_{20,02}$. The $HG_{02,20}$ mode of the frequency shifted field would then resonate inside the OPO. From an analysis of the OPO cavity geometry δf_2 is on the order of 400 MHz in aLIGO.

6.6.1 Online mode matching

To begin considering the mode matching error signal in a gravitational wave detector we start by working from the CLF beam in figure 6.16 towards the OMC. The CLF is frequency offset locked to the pre-stabilised laser (PSL) and is used for locking the OPO cavity [207]. It is purposefully frequency offset from the PSL to prevent it from resonating in the interferometer; in LIGO the CLF offset frequency is set at 3 MHz.

The 400 MHz HG_{02} sideband is then incident onto the filter cavity, which is resonant for the 3 MHz CLF HG_{00}. Demodulating the reflection of the filter cavity on the FC_{REFL} photodiode at 400 MHz would produce a mode matching error signal between the OPO and the filter cavity as described in section 6.3.2. If the filter cavity is not resonant for the CLF but instead some other control field as is in McCuller et.al.[207], the mode matching error signal can still be obtained by demodulating at the frequency difference of the filter cavity resonant field and the 400 MHz sideband.

The generated error signal can be used to drive a pair of orthogonal mode matching actuators located between the OPO and filter cavity, labelled as Active Wavefront Control (AWC) mirrors in figure 6.16. A number of potential actuator designs have been proposed by the [202, 131, 124]. The proposed error signal is independent of this design and is hence compatible with any of the proposed actuators.

The 400 MHz sideband is combined with the interferometer beam on reflection from the SRM. The combined beam will produce a intensity modulation proportional to the

mode mismatch between the OPO and the IFO mode as described in section 6.3. This can be demodulated on the photodiode $\mathrm{SRM}_{\mathrm{REFL}}$ to be used to drive the pair of AWC mirrors between the filter cavity and the output faraday isolator (OFI). The final stage of the mode matching error signal is to then match the interferometer to the OMC mode using the $\mathrm{OMC}_{\mathrm{REFL}}$ photodiode feeding back to the final two AWC actuators.

With all of the previously described mode matching error signals held at their operating point, the entire output chain of the gravitational wave detector should be mode matched to the OMC. The appeal of this mode matching error signal for gravitational wave detectors is its relative simplicity when compared to segmented photodiodes, and a straightforward implementation that requires minimal modification to the existing interferometer.

6.6.2 Offline mode matching

Even without installing the AOM and 400 MHz photodiode electronics an alternative implementation of this mode matching error signal is possible by just locking the OPO cavity to the second order modes and demodulating the same diodes at 3 MHz instead. The main caveat is that the 3 MHz implementation cannot be run concurrently with squeezing, however this does not pose much of a problem in practice as the squeezer is one of the last subsystems to be turned on in LIGO and the mode matching error signal and optimisations could be run during this initial locking phase. A bigger issue is that the phase between the CLF and the PSL is locked by demodulating DCPD at 3 MHz [192, 206], which poses a problem as the HG_{02} CLF will not beat with the IFO beam without mode mismatch. This means that the offline mode matching error signal can only be operated above a certain level of mode mismatch, and could only be used for coarse corrections.

6.6.3 Beacon mode-matching

For LIGO it is known that the carrier mode differs in shape to the gravitational wave signal mode by some amount due to mode mismatches between the coupled cavities in the Dual-Recycled Fabry-Perot Michelson Interferometer (DRFPMI) [113, 135]. The proposed mode matching signals do not sense any mode mismatch inside DRFPMI and instead sense mode mismatch between the squeezer and the DC carrier field of the

interferometer used for the DC readout [115]. Therefore it is desirable to achieve as high mode matching as possible for the signal mode and not necessarily the mode that has most of the power.

In order to do this it is necessary to mimic what the gravitational wave does by modulating the arm cavity length to produce a pair of signal sidebands. The mechanical resonances of the test masses or their suspensions are able to provide a suitable modulation inside the arm cavities that resembles the gravitational wave signal mode. Mode matching or alignment error signals are then able to lock onto this arm cavity modulation by offsetting the demodulation frequency by the frequency of the arm modulation. This technique has been used at LIGO under the name of *beacon sensing* [113], where the arm cavity modulation is being used as an alignment reference instead of the carrier at the anti-symmetric port. A similar beacon scheme can be employed for the proposed mode matching error signal, which should provide a more accurate mode matching error signal, although at the cost of reduced signal to noise.

It is worth mentioning that some future GW detector designs employ balanced homodyne detection (BHD) for their GW readout, such as A+ [176]. For their implementation of our proposed mode matching error signal beacon sensing provides the only available mode matching reference for the interferometer beam as there is no DC carrier field due to the lack of a DC offset.

6.7 Related Work

A portion of this experimental setup was used for testing a separate but related sensing scheme utilizing optical demodulation with a Pockels cell as a radio-frequency switch, which is imaged on a pair of high resolution CMOS cameras to derive alignment, mode matching, and even higher order error signals. This research was published in Optics Express by my supervisors, for which I was a coauthor.

Daniel Brown, Huy Tuong Cao, Alexei Ciobanu, Peter Veitch, and David Ottaway. “Differential wavefront sensing and control using radio-frequency optical demodulation”. In: *Optics Express* 29.11 (May 24, 2021), p. 15995. ISSN: 1094-4087. DOI: 10.1364/OE.425590

This experiment was performed after the mode matching error signal using the same liquid lens telescope, 17 MHz EOM, and triangular mode cleaner cavity as shown in figure 6.5. It successfully demonstrated that the mode matching error signals from the two CMOS cameras can improve mode matching to the same triangular mode cleaner cavity to 99.9%, the same as the mode matching error signal using beam shape modulation.

There are a number of differences between the two methods most of which are technical, but the fundamental one is the potential bandwidth of the mode matching error signal in each case. With beam shape modulation the error signal bandwidth is determined by a photodiode and so can be on the order of MHz, while the optical demodulation method is limited to the bandwidth of the CMOS camera used which is typically on the order of 100 Hz. The choice of one method over the other is thus determined by the use case. The beam shape modulation method is specialized to measure mode mismatch at a high bandwidth with minimal offsets and nothing else. Whereas the optical demodulation method is more general and is potentially very well suited for diagnosing and troubleshooting optical beat signals measured on segmented photodetectors.

6.8 Conclusion

We have proposed and demonstrated a mode matching error signal based on adding a frequency offset HG_{02+20} single sideband to a main carrier HG_{00} field. We have identified and accounted for the main sources of offset in the error signal known to us to as well as how one would go about trying to remove them. With everything presented here we were able to achieve 99.9% mode matching of an unfiltered NPRO beam to an optical cavity by following the generated mode matching error signal. For an aLIGO mode matching error signal it is preferable to be able to mode match the squeezer beam to the gravitational wave detector at LIGO to better than 98% [185], which seems to be possible using this mode matching error signal given what we have found.

Chapter 7

Conclusion

Improvements to the sensitivity of the Advanced LIGO detectors will require more impact from the injected squeezing. This imposes tighter constraints on the allowed mode mismatches inside the interferometer. In this thesis we have explored and demonstrated new modelling and mode matching sensing schemes that can help aLIGO+ reach design sensitivity. This thesis can be summarised as follows:

Chapter 1 presented an introduction to the field of ground-based gravitational wave interferometry.

In chapter 2 we reviewed the application of Hermite-Gauss (HG) modes to paraxial optics and how they form the basis of a geometrically stable cavity with infinite mirrors. This naturally led to a definition of a HG basis, which we used extensively to analyze our mode matching signal presented in chapter 6. We additionally reviewed the ABCD matrix formalism for modelling beam propagation in paraxial optical systems, which is necessary for understanding the new optical modelling methods presented in chapters 3 and 4.

Chapter 3 demonstrated the use of the Linear Canonical Transform (LCT) to study the circulating field in the aLIGO arm cavity with high spatial resolution in the presence of point absorbers and a finite aperture. The model is similar but distinct to existing Fast Fourier Transform (FFT) based optical models. The advantage of the LCT is that a sequence of paraxial optical elements can be efficiently compressed into a single linear operator, which improves computational performance and reduces spatial aliasing from

multiple FFT operations. We demonstrated a further improvement to model runtime by using Krylov subspace iterative solvers in our LCT model. The Krylov solvers are model agnostic and can in principle be used to speed up existing FFT based and possibly HG based models.

In chapter 4 we presented a framework for extending LCT models to coupled cavities by treating an optical model as a directed network graph. By applying a graph reduction procedure a generalization of the round trip operator is produced that describes how the circulating fields in each cavity interact with each other. The circulating fields in the coupled cavity can then be solved using the same methods as a single cavity by replacing the round trip operator with the generalized round trip operator. As a sanity check we demonstrated that the graph based solver produces numerically identical results to a standard sparse matrix solver in an HG based model like Finesse. Future work will demonstrate a graph based coupled cavity solver using LCTs with the aim to create a high spatial resolution model of the circulating field in the dual recycled Fabry-Perot Michelson interferometer used in LIGO with finite apertures and realistic mirror surfaces.

In chapter 5 we presented the commissioning tasks I undertook at the LIGO Hanford observatory. I measured the transverse mode spacing (TMS) in the Hanford (LHO) and Livingston (LLO) output mode cleaners (OMCs) from existing OMC cavity scans and found that the LHO OMC had a TMS that was more than double of the LLO OMC. The LHO OMC astigmatism was found to cause the mode mismatch measured from resonant peak heights to be underestimated by a factor of up to 1.6. I measured the ability of the SR3 rear heater to correct for mode mismatches at LHO and found a small improvement, which could be explained by the beam being in a Gouy phase that was orthogonal to the SR3 heater, where a second actuator on the SRM was needed to correct for it.

Chapter 6 demonstrated a new type of mode matching error signal based on inducing radio-frequency beam shape modulation via the addition of a second order HG mode sideband. This method only uses single element photodetectors and no Gouy phase telescopes to sense the two orthogonal mode matching degrees of freedom. In our tabletop experiment this mode matching error signal was used to increase the mode

matching to a cavity to 99.9%, which is well above the aLIGO+ target of 98%. A potential approach for implementing it in aLIGO+ was presented, serving as the error signal for the planned aLIGO+ mode matching actuators to match the filter cavity, output mode cleaner, and interferometer beam to the same reference.

7.1 Outlook

Personally, I am excited about the future direction of gravitational wave detection. As our understanding of these complex optical systems increases we are able to extract more and more sensitivity from these detectors, going beyond what I had initially believed would be possible. With the improved squeezing in aLIGO+ it seems all but inevitable to me that there will need to be a closed loop mode matching sensing and actuation system. The sensing problem is challenging to solve completely for a coupled cavity interferometer, but this thesis has made progress towards that goal. The remaining challenges on that front I believe are as much conceptual as they are practical. This was one of the main motivating factors for me to pursue alternative theories of optical modelling, which culminated in the LCT research presented in this thesis. The LCT modelling framework elegantly ties the theory of paraxial diffraction with quantum mechanics and signal processing in a way that is both satisfying and insightful. After publishing my LCT paper a number of people have expressed interest in using those techniques in their own work. Beyond this PhD I aim to integrate the LCT methods with a major open source modelling tool such as FINESSE3, hopefully making it more useful to a wider group of people.

Appendix A

Wave Theory

A.1 The wave equation

To derive the wave equation we first start from Maxwell's equations

$$\text{(Gauss's law)} \qquad \nabla \cdot \boldsymbol{E} = \frac{\rho}{\epsilon_0} \tag{A.1}$$

$$\text{(No monopoles)} \qquad \nabla \cdot \boldsymbol{B} = 0 \tag{A.2}$$

$$\text{(Faraday's law)} \qquad \nabla \times \boldsymbol{E} = -\frac{\partial \boldsymbol{B}}{\partial t} \tag{A.3}$$

$$\text{(Ampere's law)} \qquad \nabla \times \boldsymbol{B} = \mu_0 \left(\boldsymbol{J} + \epsilon_0 \frac{\partial \boldsymbol{E}}{\partial t} \right) \tag{A.4}$$

Taking the curl of both sides of Faraday's law equation (A.3) gives us the following

$$\nabla \times \nabla \times \boldsymbol{E} = -\nabla \times \frac{\partial \boldsymbol{B}}{\partial t} \tag{A.5}$$

We can move the curl on the right hand side (RHS) into the time derivative since spatial derivatives commute with time derivatives, this yields

$$\nabla \times \nabla \times \boldsymbol{E} = -\frac{\partial \left(\nabla \times \boldsymbol{B} \right)}{\partial t} \tag{A.6}$$

We can substitute Ampere's law equation (A.4) into the RHS to yield

$$\nabla \times \nabla \times \boldsymbol{E} = -\mu_0 \left(\frac{\partial \boldsymbol{J}}{\partial t} + \epsilon_0 \frac{\partial^2 \boldsymbol{E}}{\partial t^2} \right) \tag{A.7}$$

Here we assume that there is no current density, i.e. $\boldsymbol{J} = 0$. This simplifies us to

$$\nabla \times \nabla \times \boldsymbol{E} = -\mu_0 \epsilon_0 \frac{\partial^2 \boldsymbol{E}}{\partial t^2} \tag{A.8}$$

here we define $\mu_0 \epsilon_0 = \frac{1}{c^2}$

$$\nabla \times \nabla \times \boldsymbol{E} = -\frac{1}{c^2} \frac{\partial^2 \boldsymbol{E}}{\partial t^2} \tag{A.9}$$

Now for the left hand side (LHS) we can simplify using the *curl of curl* identity

(curl of curl) $$\nabla \times (\nabla \times \boldsymbol{A}) = \nabla (\nabla \cdot \boldsymbol{A}) - \nabla^2 \boldsymbol{A} \tag{A.10}$$

which gives us

$$\nabla (\nabla \cdot \boldsymbol{E}) - \nabla^2 \boldsymbol{E} = -\frac{1}{c^2} \frac{\partial^2 \boldsymbol{E}}{\partial t^2} \tag{A.11}$$

here we can substitute Gauss's law equation (A.1) into the LHS, which gives us

$$\nabla \left(\frac{\rho}{\epsilon_0} \right) - \nabla^2 \boldsymbol{E} = -\frac{1}{c^2} \frac{\partial^2 \boldsymbol{E}}{\partial t^2} \tag{A.12}$$

here we assume that the charge density ρ is constant across space which means that its gradient is zero $\nabla \rho = 0$. This yields

$$\nabla^2 \boldsymbol{E} = \frac{1}{c^2} \frac{\partial^2 \boldsymbol{E}}{\partial t^2} \tag{A.13}$$

We can perform the exact same procedure when taking the curl of Ampere's law equation (A.4) to obtain a wave equation for the magnetic field

$$\nabla^2 \boldsymbol{B} = \frac{1}{c^2} \frac{\partial^2 \boldsymbol{B}}{\partial t^2} \tag{A.14}$$

A.2 Helmholtz equation

To derive the Helmholtz wave equation we take our previous vector wave equation equation (A.13)

$$\nabla^2 \left[\boldsymbol{E}(\boldsymbol{x}, t)\right] = \frac{1}{c^2}\frac{\partial^2}{\partial t^2}\left[\boldsymbol{E}(\boldsymbol{x}, t)\right] \tag{A.15}$$

where we explicitly denote the electric field $\boldsymbol{E}$ as a vector function of two inputs, a position vector $\boldsymbol{x}$, and a scalar time t, with the derivatives as operators acting on the function. Next we assume that the electric field $\boldsymbol{E}$ is separable between space and time, that is the electric field takes the following form

$$\boldsymbol{E}(\boldsymbol{x}, t) = \boldsymbol{E}(\boldsymbol{x})E(t) \tag{A.16}$$

where we assume that the time dependent part of the electric field is scalar. The wave equation then becomes

$$E(t)\nabla^2 \left[\boldsymbol{E}(\boldsymbol{x})\right] = \boldsymbol{E}(\boldsymbol{x})\frac{1}{c^2}\frac{\partial^2}{\partial t^2}\left[E(t)\right] \tag{A.17}$$

For this equation to hold the spatial and temporal parts can be solved independently. In separation of variables we can do a sneaky trick to make the equations simpler, which won't make much sense now without foresight. We can multiply both left hand and right hand side of equation (A.17) by an arbitrary constant. We choose to multiply both sides by $-k^2$, which will cancel nicely later on. The rescaled wave equation is now

$$-k^2 E(t)\nabla^2 \left[\boldsymbol{E}(\boldsymbol{x})\right] = -k^2\boldsymbol{E}(\boldsymbol{x})\frac{1}{c^2}\frac{\partial^2}{\partial t^2}\left[E(t)\right] \tag{A.18}$$

When we consider the spatial part of equation (A.18) equation we keep only the right hand side $-k^2$ and when we consider the temporal part we only keep the left hand side $-k^2$. It doesn't make much sense to do this now but it will pay off later. The spatial part is then the Helmholtz equation

$$\nabla^2 \left[\boldsymbol{E}(\boldsymbol{x})\right] = -k^2\boldsymbol{E}(\boldsymbol{x}) \tag{A.19}$$

and the temporal part is

$$-k^2 E(t) = \frac{1}{c^2}\frac{\partial^2}{\partial t^2}\left[E(t)\right] \tag{A.20}$$

The temporal part is a well known second order ordinary differential equation (ODE), which has the following solution.

$$E(t) = ae^{\mathrm{i}wt} \tag{A.21}$$

we identify that the ODE has an oscillatory solution with angular frequency $\omega = kc$, where a is a constant complex scalar that comes from the initial condition of the ODE.

The Helmholtz equation is more complicated but has been solved with the general solution being given in terms of spherical harmonics [74], for which the lowest order is a spherical wave. In polar coordinates a spherical wave is given by

$$\boldsymbol{E}(\boldsymbol{r}) = \frac{\boldsymbol{r} - \boldsymbol{r}_0}{|\boldsymbol{r} - \boldsymbol{r}_0|^2}\, e^{-\mathrm{i}k|\boldsymbol{r}-\boldsymbol{r}_0|} \tag{A.22}$$

where $\boldsymbol{r}_0$ is the point source origin of the spherical wave.

A.3 Paraxial scalar wave equation

The standard method of solving the scalar Helmholtz equation is to assume that the solution is of the following form

$$E(x, y, z) = A(x, y, z)e^{-ikz} \tag{A.23}$$

where we assume that the envelope function $A(x, y, z)$ is slowly varying with z. For brevity we may not write the spatial coordinates to A but will assume that the spatial

dependence is still there. Taking the Laplacian of this trial solution gives us

$$\nabla^2 E(x,y,z) = \left(\partial_x^2 + \partial_y^2 + \partial_z^2\right) A e^{-ikz} \tag{A.24}$$

$$= \left(\partial_x^2 + \partial_y^2\right) A e^{-ikz} + \partial_z \left(\partial_z A e^{-ikz}\right) \tag{A.25}$$

$$= \left(\partial_x^2 + \partial_y^2\right) A e^{-ikz} + \partial_z \left(e^{-ikz}\left[\partial_z A - ikA\right]\right) \tag{A.26}$$

$$= \left(\partial_x^2 + \partial_y^2\right) A e^{-ikz} + e^{-ikz}\left(\partial_z^2 A - 2ik\partial_z A - k^2 A\right) \tag{A.27}$$

The slowly varying envelope approximation assures us that the $\partial_z^2 A$ is much much smaller than every other term in the equation so we can safely neglect it. Substituting the reduced expression for the Laplacian into the Helmholtz equation we get

$$\nabla^2 E(x,y,z) = -k^2 E(x,y,z) \tag{A.28}$$

$$\left(\partial_x^2 + \partial_y^2\right) A e^{-ikz} + e^{-ikz}\left(-2ik\partial_z A - k^2 A\right) = -k^2 A e^{-ikz} \tag{A.29}$$

Eliminating the common term e^{-ikz} and rearranging we get

$$\left(\partial_x^2 + \partial_y^2\right) A - 2ik\partial_z A = 0 \tag{A.30}$$

which is the paraxial wave equation for the envelope field $A(x,y,z)$. The paraxial wave equation is solved by any Hermite-Gauss mode, with the simplest being the fundamental Gaussian beam. We won't derive the functional form of the Gaussian beam here. Instead we choose the less conventional, but simpler complex source point method to do so, which we discuss later.

A.3.1 Fresnel diffraction integral

The Green's function of the paraxial wave equation (A.30) is given by

$$G(x,y,z) = \frac{1}{4\pi z} \exp\left[-ik\frac{\left(x^2+y^2\right)}{2z}\right] \tag{A.31}$$

which serves as the kernel of the Fresnel diffraction integral. Equation (A.31) can be verified by noting that it is a valid solution to equation (A.30). The Fresnel diffraction

integral is given by

$$E(x', y', z) = -2ike^{-ikz} \iint_{-\infty}^{\infty} G(x - x', y - y', z)E(x, y, 0)dydx \tag{A.32}$$

A.3.2 Exponential paraxial wave propagation operator

We can obtain an expression for wave propagation directly from the paraxial wave equation by noting the similarity to the Schrodinger equation. Take the paraxial wave equation (A.30) and relabel the envelope of the field A to be ψ

$$\left(\partial_x^2 + \partial_y^2\right)\psi - 2ik\partial_z\psi = 0 \tag{A.33}$$

$$\left(\partial_x^2 + \partial_y^2\right)\psi = 2ik\partial_z\psi \tag{A.34}$$

where the Schrodinger equation is given by

$$\hat{H}\psi = i\hbar\frac{d}{dt}\psi \tag{A.35}$$

Here we identify that equation (A.34) is just the Schrodinger equation in 2D for a free particle with z acting as the time coordinate, $2k$ acting as $\hbar$, and the Hamiltonian being given by

$$\hat{H} = \partial_x^2 + \partial_y^2 \tag{A.36}$$

The time evolution of the wavefunction ψ, now being the spatial evolution of the electric field is given by the exponential of the Hamiltonian.

$$\psi(z) = e^{-i\hat{H}z/2k}\psi(0) \tag{A.37}$$

which is valid for any given envelope field ψ since the choice of origin $z = 0$ is arbitrary.

It is not completely obvious how equation (A.37) can be used in numerical models. The exponential of a derivative operator at first seems like an abuse of notation. However

taking the Taylor series of the exponential shows something interesting

$$e^X = 1 + X + \frac{XX}{2!} + \frac{XXX}{3!} + \frac{XXXX}{4!} + \dots \tag{A.38}$$

$$= \sum_{n=0}^{\infty} \frac{X^n}{n!} \tag{A.39}$$

The Taylor series of e^X is perfectly computable even if X is a matrix or an operator where an n'th power of X is taken to mean n applications of the operator X. Taking $\hat{H}$ to be a second order finite difference operator equation (A.39) gives a way of computing the propagation by summing even order finite differences of some discrete sampled wave field ψ.

Alternatively we can take a Pade series of e^X which converges faster than the Taylor series for any given order but requires us to compute the inverse of powers of X, this is difficult to implement for an arbitrary operator but straightforward if X is an invertible matrix. Fortunately the finite difference operator can be written in a matrix form.

However, both Taylor and Pade series pale in comparison in terms of computational speed to the next approach, which will ultimately lead us to the FFT model for propagation. We begin by taking note of the following Fourier transform pair

$$\mathcal{F}[xf] = \mathrm{i}\partial_x \mathcal{F}[f] \tag{A.40}$$

$$\mathcal{F}[\partial_x f] = \mathrm{i}x\mathcal{F}[f] \tag{A.41}$$

where $\mathcal{F}$ is a Fourier transform operator. The second identity is particularly useful as it allows us to replace the derivative of a function with a coordinate multiplication and a pair of Fourier transforms in the following way

$$\partial_x f = \mathcal{F}^{-1}[\mathrm{i}x\mathcal{F}[f]] \tag{A.42}$$

This generalizes to higher order derivatives in a rather natural way

$$(\partial_x)^n f = \mathcal{F}^{-1}[(\mathrm{i}x)^n \mathcal{F}[f]] \tag{A.43}$$

an interesting aside is that the RHS of this equation is valid for noninteger n, which

leads to a definition of fractional order derivatives.

Going back to our Hamiltonian, the following Fourier identity applies

$$\hat{H} = \partial_x^2 + \partial_y^2 \tag{A.44}$$
$$= \mathcal{F}^{-1}\left[(ix)^2 + (iy)^2\right]\mathcal{F} \tag{A.45}$$
$$= \mathcal{F}^{-1}\left[-(x^2 + y^2)\right]\mathcal{F} \tag{A.46}$$

and similarly for powers of $\hat{H}$

$$\hat{H}^n = (\partial_x^2 + \partial_y^2)^n \tag{A.47}$$
$$= \mathcal{F}^{-1}\left[\left(-(x^2 + y^2)\right)^n\right]\mathcal{F} \tag{A.48}$$

we can then write the exponential of $\hat{H}$ as

$$e^{\hat{H}} = \sum_{n=0}^{\infty} \frac{\hat{H}^n}{n!} \tag{A.49}$$
$$= \sum_{n=0}^{\infty} \mathcal{F}^{-1}\left[\frac{\left(-(x^2 + y^2)\right)^n}{n!}\right]\mathcal{F} \tag{A.50}$$
$$= \mathcal{F}^{-1}\left[\sum_{n=0}^{\infty} \frac{\left(-(x^2 + y^2)\right)^n}{n!}\right]\mathcal{F} \tag{A.51}$$
$$= \mathcal{F}^{-1}\left[e^{-(x^2+y^2)}\right]\mathcal{F} \tag{A.52}$$

and so we can finally write the Fourier dual of the exponential propagator as

$$\psi(z) = \mathcal{F}^{-1}\left[e^{-\mathrm{i}z(x^2+y^2)/2k}\right]\mathcal{F}\psi(0) \tag{A.53}$$

This expression for paraxial wave propagation is highly efficient when the Fourier transforms are implemented with FFTs. The exponential in the middle is just a regular complex exponential function and doesn't require any fancy tricks to evaluate. Overall the majority of the computational burden is now placed onto the FFT which is orders of magnitude faster than summing a convergent infinite series of finite difference operators. It is for this reason that optical models that use equation (A.53) are referred to as FFT models.

A.4 Complex source point (CSP) method

An alternative and perhaps more elegant derivation of the Gaussian beam comes from placing the point source of a spherical wave $\boldsymbol{r}_0$ a complex distance away, which creates an exact solution to the Helmholtz equation that is also beam-like, reducing to the standard Gaussian beam in the paraxial approximation. This trick of moving the point source of a spherical wave into the complex domain was found independently in 1971 by Deschamps [21] and Keller [23].

To show how the complex source point (CSP) method produces a Gaussian beam we begin with the scalar spherical wave

$$E(r) = \frac{1}{r} e^{-\mathrm{i}kr} \tag{A.54}$$

where

$$r = \sqrt{(x - x_0)^2 + (y - y_0)^2 + (z - z_0)^2} \tag{A.55}$$

is the distance from the point source located at $r_0 = \{x_0, y_0, z_0\}$. This can be verified by noting that equation (A.54) solves equation (A.19) with the the 3D Laplacian ∇^2 in spherical coordinates being

$$\nabla^2 = \frac{1}{r^2}\frac{\partial}{\partial r}\left(r^2 \frac{\partial}{\partial r}\right) + \frac{1}{r^2 \sin(\theta)}\frac{\partial}{\partial \theta}\left(\sin(\theta)\frac{\partial}{\partial \theta}\right) + \frac{1}{r^2 \sin(\theta)^2}\frac{\partial^2}{\partial \varphi^2} \tag{A.56}$$

where we can set $\dfrac{\partial E}{\partial \theta} = \dfrac{\partial E}{\partial \varphi} = 0$ since we want a uniform spherical wave.

Placing the point source at $r_0 = \{0, 0, -\mathrm{i}z_R\}$ we find the radial distance is

$$r = \sqrt{x^2 + y^2 + (z + \mathrm{i}z_R)^2} \tag{A.57}$$

Here we make the paraxial approximation $x^2 + y^2 \ll |z + \mathrm{i}z_R|^2$, the Taylor expansion of r around $x = 0$ and $y = 0$ is then

$$r = (z + \mathrm{i}z_R) + \frac{x^2 + y^2}{2(z + \mathrm{i}z_R)} + \mathcal{O}(x^4) + \mathcal{O}(y^4) \tag{A.58}$$

substituting it back into the scalar spherical wave and neglecting higher order terms

$$E(x,y,z) = \frac{1}{z+\mathrm{i}z_R}\exp\left[-\mathrm{i}k\left((z+\mathrm{i}z_R)+\frac{x^2+y^2}{2(z+\mathrm{i}z_R)}\right)\right] \tag{A.59}$$

where we drop the $\frac{x^2+y^2}{2(z+\mathrm{i}z_R)}$ term in $1/r$ since $x^2+y^2 \ll |z+\mathrm{i}z_R|^2$. Rewriting in a more familiar form

$$E(x,y,z) = \frac{e^{-\mathrm{i}k(z+\mathrm{i}z_R)}}{z+\mathrm{i}z_R}\exp\left[-\mathrm{i}k\frac{x^2+y^2}{2(z+\mathrm{i}z_R)}\right] \tag{A.60}$$

which is identical to the paraxial HG_{00} beam, barring an overall normalization factor. Equation (A.60) contains the plane wave phase term $e^{-\mathrm{i}kz}$, the same transverse beam size and radius of curvature. The $1/(z+\mathrm{i}z_R)$ term performs serves two purposes, the first is to keep the power of the beam constant as it expands, and the second is to compute the Gouy phase. The overall constant term given by e^{kz_R} can be discarded as it does not normalize the beam to unit power and is too numerically large to have a floating point representation, making it of limited use in computer calculations. The correct normalization for equation (A.60) therefore has to be derived separately.

Higher order Gaussian modes can be derived by using the complex source point method on higher order spherical harmonic functions, which also solve the scalar Helmholtz equation and correspond to radiation emitted by a multipole source. This was first demonstrated by Shin and Felsen in 1977 [33].

Even though we invoked the paraxial approximation in equation (A.58) the complex source point method itself makes no paraxial approximation. Therefore the full non-paraxial complex source point radius in equation (A.57) can be used to obtain a non-parxial analogue of the Gaussian beam and its higher order modes that are an exact solution of the scalar Helmholtz equation.

The derivation we present here can also be performed in reverse; starting with the paraxial Gaussian beam higher order parxial corrections can be derived by using the methods described by Lax et al. (1975) [32], or Agrawal et al. (1979) [34]. Summing all orders of the paraxial corrections reproduces the complex source point spherical wave as was shown by Couture and Belanger in 1981 [37].

The complex source point method also works for the vector Helmholtz equation, which can produce vector beam-like solutions that exactly satisfy Maxwell's equations in homogeneous free space. In 1979 Cullen and Yu [35] published closed form expressions for the six vector components of the electric and magnetic field that satisfy Maxwell's equations based on the radiation emitted by crossed electric and magnetic dipole whose origin lies in the complex plane. They found that this beam reduces to the standard Gaussian beam in the paraxial approximation but also had other desirable properties, such as a symmetric electric and magnetic field magnitude, which makes it suitable for calculations where vector polarization is needed.

The solution by Cullen and Yu had one major flaw in that it produced a ring of amplitude singularities around the focus of the beam where the complex radius in equation (A.57) goes to zero. This singularity was addressed by Sheppard and Saghafi in 1998 for the scalar spherical wave by introducing a complex sink in addition to the complex source [72]. The next year in 1999 they extended their results to vector beams [76] and multipole radiation [77, 78], completing their theory of complex source/sink pairs to generate closed form beam-like solutions to Maxwell's equations that are singularity-free and reduce to standard Gaussian beams in the paraxial limit. In removing the singularity their solutions introduce a backwards travelling wave, which the authors acknowledge violates Sommerfeld's radiation condition [77]. Though the authors claim that it does not mean that their solution is unphysical.

The complex source and sink pair solutions by Sheppard and Saghafi have seen subsequent use in modelling nonparaxial beams [119, 125], though some authors had an issue that their solution contains a backwards travelling wave, calling it non-causal [177].

A.5 Bayer-Helms scattering coefficients

The Bayer-Helms solution [43] is given in closed-form as a complex exponential scaling factor multiplied by a rational function of the basis parameters.

$$k_{n_1 n_2}[q_1, q_2, \delta, \gamma] = C_1[n_1, n_2]\, C_2[n_1, n_2, q_1, q_2]\, C_3[q_1, q_2, \delta, \gamma] \\ \big(S_g[n_1, n_2, q_1, q_2, \delta, \gamma] - S_u[n_1, n_2, q_1, q_2, \delta, \gamma]\big) \tag{A.61}$$

where

$$C_1[n_1, n_2] = (-1)^{n_2}\sqrt{n_1!\, n_2!} \tag{A.62}$$

$$C_2[n_1, n_2, q_1, q_2] = (1 + K_0)^{\left(\frac{n_1}{2}+\frac{1}{4}\right)} (1 + K^*)^{\left(\frac{-n_1-n_2-1}{2}\right)} \tag{A.63}$$

$$C_3[q_1, q_2, \delta, \gamma] = \exp\left[\frac{-X\bar{X}}{2} - \frac{\mathrm{i}\delta\,\mathrm{Im}[q_2]\sin[\gamma]}{{w_0}^2}\right] \tag{A.64}$$

where the terms are

$$w_0[q_2] = \sqrt{\frac{\lambda\,\mathrm{Im}[q_2]}{\pi}} \tag{A.65}$$

$$K_0[q_1, q_2] = \frac{\mathrm{Im}[q_1] - \mathrm{Im}[q_2]}{\mathrm{Im}[q_2]} \tag{A.66}$$

$$K_2[q_1, q_2] = \frac{\mathrm{Re}[q_1] - \mathrm{Re}[q_2]}{\mathrm{Im}[q_2]} \tag{A.67}$$

$$K[q_1, q_2] = \frac{K_0 + \mathrm{i}K_2}{2} \tag{A.68}$$

$$X[q_1, q_2, \delta, \gamma] = \left(\frac{\delta}{w_0} - \left(\frac{\mathrm{Re}[q_2]}{\mathrm{Im}[q_2]} + \mathrm{i}\,(1 + 2K^*)\right)\frac{\mathrm{Im}[q_2]\ \sin[\gamma]}{w_0}\right)\left(\frac{1}{\sqrt{1 + K^*}}\right) \tag{A.69}$$

$$\bar{X}[q_1, q_2, \delta, \gamma] = \left(\frac{\delta}{w_0} - \left(\frac{\mathrm{Re}[q_2]}{\mathrm{Im}[q_2]} - \mathrm{i}\right)\frac{\mathrm{Im}[q_2]\ \sin[\gamma]}{w_0}\right)\left(\frac{1}{\sqrt{1 + K^*}}\right) \tag{A.70}$$

The two sum terms S_g and S_u are

$$S_g[n_1, n_2, q_1, q_2, \delta, \gamma] = \sum_{\mu_1=0}^{\lfloor n_1/2\rfloor}\sum_{\mu_2=0}^{\lfloor n_2/2\rfloor}\frac{(-1)^{\mu_1}\bar{X}^{(n_1-2\mu_1)}X^{(n_2-2\mu_2)}}{(n_1-2\mu_1)!\,(n_2-2\mu_2)!}\sum_{\sigma=0}^{\min[\mu_1,\mu_2]}\frac{(-1)^{\sigma}\bar{F}^{(\mu_1-\sigma)}F^{(\mu_2-\sigma)}}{(2\sigma)!\,(\mu_1-\sigma)!\,(\mu_2-\sigma)!} \tag{A.71}$$

$$S_u[n_1, n_2, q_1, q_2, \delta, \gamma] = \sum_{\mu_1=0}^{\lfloor (n_1-1)/2\rfloor}\sum_{\mu_2=0}^{\lfloor (n_2-1)/2\rfloor}\frac{(-1)^{\mu_1}\bar{X}^{(n_1-2\mu_1-1)}X^{(n_2-2\mu_2-1)}}{(n_1-2\mu_1-1)!\,(n_2-2\mu_2-1)!}\sum_{\sigma=0}^{\min[\mu_1,\mu_2]}\frac{(-1)^{\sigma}\bar{F}^{(\mu_1-\sigma)}F^{(\mu_2-\sigma)}}{(2\sigma+1)!\,(\mu_1-\sigma)!\,(\mu_2-\sigma)!} \tag{A.72}$$

where $\lfloor x \rfloor$ is the integer floor function, and $\min[x_1, x_2]$ is the minimum function, which returns x_1 if $x_1 < x_2$ and otherwise returns x_2. The new terms used in the sums are

$$F[q_1, q_2] = \frac{K^*}{2} \tag{A.73}$$

$$\bar{F}[q_1, q_2] = \frac{K}{2\,(1 + K_0)} \tag{A.74}$$

where K^* is the complex conjugate of K.

Appendix B

Linear Canonical Transform

B.1 Metaplectic sign ambiguity

The LCT has some implications when calculating the accumulated Gouy phase through an optical system—which is due to the LCT being a faithful representation of the metaplectic group. Here we find a new formula for the 1D accumulated Gouy phase, which can also be used to compute the accumulated Gouy phase in a simple astigmatic 2D optical system.

The ABCD matrices discussed here form a group known as the symplectic group $\mathrm{Sp}_2(\mathbb{R})$ [95], which are all 2×2 matrices with unit determinant. There are 2 distinct LCTs for every ABCD matrix because the metaplectic group $\mathrm{Mp}_2(\mathbb{R})$ is a double cover of the symplectic group $\mathrm{Sp}_2(\mathbb{R})$. The additional parameter that allows us to uniquely specify an LCT is called the metaplectic sign [95].

The metaplectic sign manifests in optics as a sign ambiguity in the Gouy phase accumulated by a beam propagating through an ABCD optical system. This sign ambiguity disappears in 2D optical systems exhibiting cylindrical symmetry due to both vertical and horizontal having the same metaplectic sign, which end up cancelling yielding an overall expression for accumulated Gouy phase that has no sign ambiguity [65, 48].

The accumulated Gouy phase for a Gaussian beam with beam parameter q through an

ABCD system in two dimensions with cylindrical symmetry is

$$\exp(\mathrm{i}\Psi) = \exp(\mathrm{i}2\psi) = \frac{A + B/q^*}{|A + B/q^*|} \tag{B.1}$$

and in one dimension

$$\exp(\mathrm{i}\psi) = \pm\sqrt{\frac{A + B/q^*}{|A + B/q^*|}} \tag{B.2}$$

where the $\pm$ sign, which we identify as the *metaplectic sign* is a real sign ambiguity that is present in the 1D accumulated Gouy phase for an arbitrary ABCD matrix.

An algorithm to determine the metaplectic sign for LCTs to the best of our knowledge was first presented by Littlejohn (appendix A of [44], and [51]) and has been subsequently used by Lopez [189]. Their algorithm computes and tracks a winding number from the multiplication of ABCD matrices, which is then used to determine the metaplectic sign. We propose a modification to this algorithm that bypasses the need to track the winding number and instead tracks the metaplectic sign directly. We use this algorithm to define a group action, which is an extension of regular matrix multiplication between ABCD matrices paired with a metaplectic sign, which we call a *metaplectic matrix*.

B.1.1 Metaplectic Matrices

A metaplectic matrix $\mathfrak{M} \in \mathrm{Mp}_2(\mathbb{R})$ is a composite object that can be represented as a tuple/ordered set containing a symplectic matrix $\mathbf{M} \in \mathrm{Sp}_2(\mathbb{R})$ and a binary sign $\sigma \in \{-1, 1\}$, which is the metaplectic sign.

$$\mathfrak{M} = \{\mathbf{M}, \sigma\}. \tag{B.3}$$

The multiplication law between two metaplectic matrices is then defined as

$$\mathfrak{M}_3 = \mathfrak{M}_2\mathfrak{M}_1 = \{\mathbf{M}_2\mathbf{M}_1, \sigma_3\}, \tag{B.4}$$

where the new sign σ_3 is given by

$$\sigma_3 = (\sigma_2 \times \sigma_1) \times (-1)^{\rho(\mathbf{M}_2, \mathbf{M}_1)} \tag{B.5}$$

where $\rho(\mathbf{M}_2, \mathbf{M}_1) \in \{0, 1\}$ is given by

$$\rho(\mathbf{M}_2, \mathbf{M}_1) = [\theta(\mathbf{M}_2) < 0] \oplus [\theta(\mathbf{M}_2\mathbf{M}_1) < \theta(\mathbf{M}_1)] \tag{B.6}$$

where $\oplus$ is a logical exclusive or (XOR), and $-\pi < \theta(\mathbf{M}) \leq \pi$ is a metaplectic phase associated with an ABCD matrix given by

$$\theta(\mathbf{M}) = \arg(A + \mathrm{i}B). \tag{B.7}$$

We adopt the convention of the boolean True and False being represented by 1 and 0 respectively.

(B.6) was derived from logical expressions of the following kind: if the metaplectic phase is decreasing $[\theta(\mathbf{M}_2) < 0]$, and if the output metaplectic phase is less than the input metaplectic phase $[\theta(\mathbf{M}_2\mathbf{M}_1) < \theta(\mathbf{M}_1)]$, then the metaplectic sign hasn't flipped $[\rho(\mathbf{M}_2, \mathbf{M}_1) = 0]$. Enumerating all possible combinations of True and False for the conditions in (B.6) reveals that the truth table for determining if a metaplectic sign flip has occurred is equivalent to an XOR of the two conditions.

The 1D Gouy phase of a Gaussian beam with beam parameter q through a metaplectic ABCD matrix $\mathfrak{M} = (\mathbf{M}, \sigma)$ is then

$$\exp(\mathrm{i}\psi) = \sigma\sqrt{\frac{A + B/q^*}{|A + B/q^*|}}. \tag{B.8}$$

With this we can define the Gouy phase of a Gaussian beam through a 2D optical system with simple astigmatism described with two metaplectic matrices $\mathfrak{M}_x$ and $\mathfrak{M}_y$ for the x and y axes respectively as

$$\exp(\mathrm{i}\Psi) = \sigma_x\sigma_y \exp\big[\mathrm{i}(\psi_x + \psi_y)\big] \tag{B.9}$$

which reduces to (B.1) to in the case of cylindrical symmetry, where $\mathfrak{M}_x = \mathfrak{M}_y$.

It should be noted that the expressions for Gouy phase in (B.8) and (B.9) are not analytic (i.e. they don't have Taylor series) due to the discrete nature of the metaplectic sign $\sigma \in \{-1, 1\}$. We believe that it is likely impossible to derive an analytical ex-

pression for 1D Gouy phase that uses a single ABCD matrix to represent an arbitrary optical system. A similar statement has been made by other authors for 2D Gouy phase in general astigmatic optical systems [110].

B.2 Structured Matrices

Structured matrix is a generic term for any matrix that has a fast matrix-vector multiplication algorithm [86]. For example all sparse matrices are structured, and their fast matrix-vector multiplication is performed by ignoring the matrix zeroes in the calculation. Other forms of structured matrices exist, each with their own specialized fast matrix-vector multiplication. An example of a dense structured matrix is the DFT matrix, with the fast matrix-vector multiplication being the FFT algorithm.

For this paper the structured matrix in question is the $N^2 \times N^2$ separable 2D DLCT kernel $\mathbf{L}_{\mathbf{M}}$, which we find can be written as a Kronecker product of two $N \times N$ 1D DLCT kernels $\mathbf{L}_{\mathbf{M}_x}$ and $\mathbf{L}_{\mathbf{M}_y}$ respectively.

$$\mathbf{L}_{\mathbf{M}} = \mathbf{L}_{\mathbf{M}_x} \otimes \mathbf{L}_{\mathbf{M}_y} \tag{B.10}$$

The fast matrix-vector multiplication algorithm for a Kronecker product of two matrices is given by Roth's relation [6, 96].

$$(\mathbf{A} \otimes \mathbf{B}) \operatorname{vec}[\mathbf{X}] = \operatorname{vec}\left[\mathbf{B}\mathbf{X}\mathbf{A}^T\right] \tag{B.11}$$

where $\operatorname{vec}[\mathbf{X}]$ is an operation that unravels any matrix $\mathbf{X}$ into a vector by stacking its columns underneath each other [96]. This identity was used in discretizing the separable 2D LCT in equation (3.15). The fast round trip procedure used in equation (3.28) is

$$\mathbf{X}_{\text{out}} = \mathbf{R}_1 \circ \left(\mathbf{L}_{\mathbf{M}_d} \left(\mathbf{R}_2 \circ \left(\mathbf{L}_{\mathbf{M}_d} \mathbf{X}_{\text{in}} \left(\mathbf{L}_{\mathbf{M}_d} \right)^T \right) \right) \left(\mathbf{L}_{\mathbf{M}_d} \right)^T \right) \tag{B.12}$$

where the order of parentheses has to be respected since matrix and Hadamard multiplication are neither commutative or associative with each other. (B.12) can be thought of as the fast matrix-vector multiplication algorithm for a 2D cavity round trip with mirror maps and a separable free-space propagation kernel.

B.3 Apertured LCT model

Using the formalism described in chapter 3 the circulating field $\boldsymbol{X}_1$ in the arm cavity is given by

$$\boldsymbol{X}_1 = \boldsymbol{X}_5 + \mathrm{i}t_1 \boldsymbol{A}_1 \circ \boldsymbol{X}_{inc} \tag{B.13}$$

where $\boldsymbol{X}_{inc}$ is the incident field and $\boldsymbol{X}_5$ is the round trip propagation in with the LCT and can be expanded to linear operations on the circulating field $\boldsymbol{X}_1$.

$$\boldsymbol{X}_2 = \boldsymbol{D}_{y1} \boldsymbol{X}_1 \boldsymbol{D}_{x1}^T \tag{B.14}$$

$$\boldsymbol{X}_3 = \boldsymbol{A}_2 \circ \boldsymbol{R}_{c,2} \circ (r_2 \boldsymbol{X}_2) \tag{B.15}$$

$$\boldsymbol{X}_4 = \boldsymbol{D}_{y2} \boldsymbol{X}_3 \boldsymbol{D}_{x2}^T \tag{B.16}$$

$$\boldsymbol{X}_5 = \boldsymbol{A}_1 \circ \boldsymbol{R}_{c,1} \circ (r_1 \boldsymbol{X}_4) \tag{B.17}$$

B.3.1 LCT model parameters

Table B.1: Physical parameters describing the LIGO arm cavity.

r_1	ITM amplitude reflection	$\sqrt{1-0.014}$
t_1	ITM amplitude transmission	$\sqrt{0.014}$
r_2	ETM amplitude reflection	$\sqrt{1-5\times10^{-6}}$
t_2	ETM amplitude transmission	$\sqrt{5\times10^{-6}}$
L_{arm}	arm length	3994.5 m
A_{diam}	test mass diameter	32.6 cm
$R_{c,1}$	ITM radius of curvature	1934 m
$R_{c,2}$	ETM radius of curvature	2245 m

Table B.2: LCT model parameters

P_{in}	incident power	1 W
q_1	incident beam parameter	$-1834.2 + 427.8\mathrm{i}$ m
w_1	beam size at ITM	5.3 cm
w_2	beam size at ETM	6.2 cm

`N`	number of points per grid axis	801
`x1`	x-axis at ITM	$5w_1\times$ `linspace(-1,1,N)`
`y1`	y-axis at ITM	$5w_1\times$ `linspace(-1,1,N)`
`x2`	x-axis at ETM	$5w_2\times$ `linspace(-1,1,N)`
`y2`	y-axis at ETM	$5w_2\times$ `linspace(-1,1,N)`
$\boldsymbol{X}_{in}$	incident field	$\sqrt{P_{in}}\times$ `U00(x1, y1,` q_1`)`
`Md`	cavity length ABCD matrix	$\begin{bmatrix} 1 & L_{arm} \\ 0 & 1 \end{bmatrix}$

Table B.3: Mirror maps and LCT operators.

$\boldsymbol{D}_{x1}$	x-axis LCT from ITM to ETM	`DLCT(x1, x2, Md)`
$\boldsymbol{D}_{y1}$	y-axis LCT from ITM to ETM	`DLCT(y1, y2, Md)`
$\boldsymbol{D}_{x2}$	x-axis LCT from ETM to ITM	`DLCT(x2, x1, Md)`
$\boldsymbol{D}_{y2}$	y-axis LCT from ETM to ITM	`DLCT(y2, y1, Md)`
$\boldsymbol{R}_{c,1}$	ITM curvature phase map	`RoC_phase_map(x1, y1,` $R_{c,1}$`)`
$\boldsymbol{R}_{c,2}$	ETM curvature phase map	`RoC_phase_map(x1, y1,` $R_{c,2}$`)`
$\boldsymbol{A}_1$	ITM aperture map	`circ_ap(x1, y1,` A_{diam}`)`
$\boldsymbol{A}_2$	ETM aperture map	`circ_ap(x1, y1,` A_{diam}`)`

B.3.2 LCT model outputs

Here we show visual representations of various operators used in the LCT model with the aim of making it easier to understand the inner workings of the model.

The mirror maps for the ITM and ETM shown in figures B.1 and B.2 highlight an interesting application of the LCT — that it can work with dynamic grid sizes. This can be seen by noting that the apparent size of the test mass aperture is slightly different between figures B.1 and B.2. The aperture for the ITM appears occupies a larger area of the grid than the ETM aperture because the ITM grid uses a smaller step size. The grid extent is chosen to be scaled to 10 times the beam size at that plane as shown in table B.2, which naturally leads to a dynamic grid size.

The ring structure seen figures B.1 and B.2 corresponds to a phase shift associated with

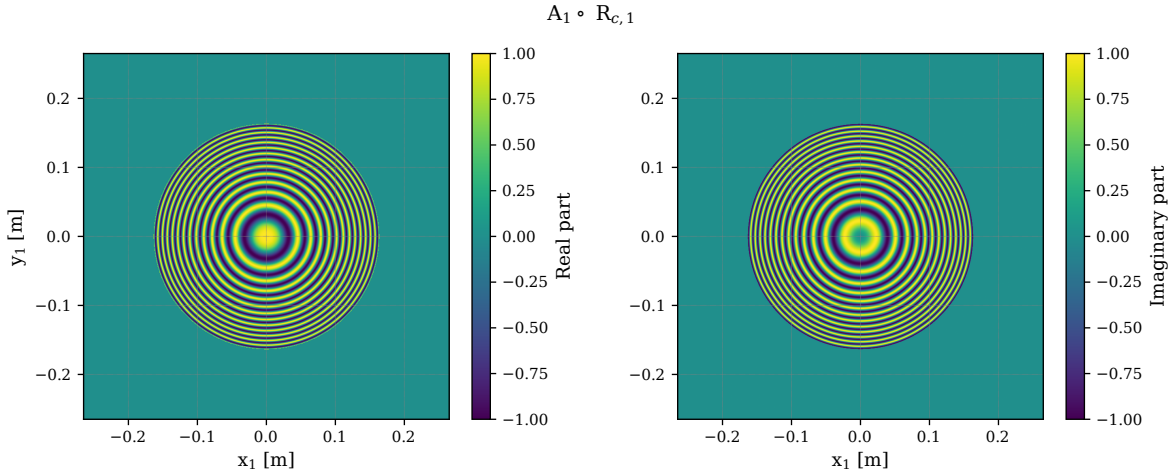

Figure B.1: ITM aperture and curvature phase map.

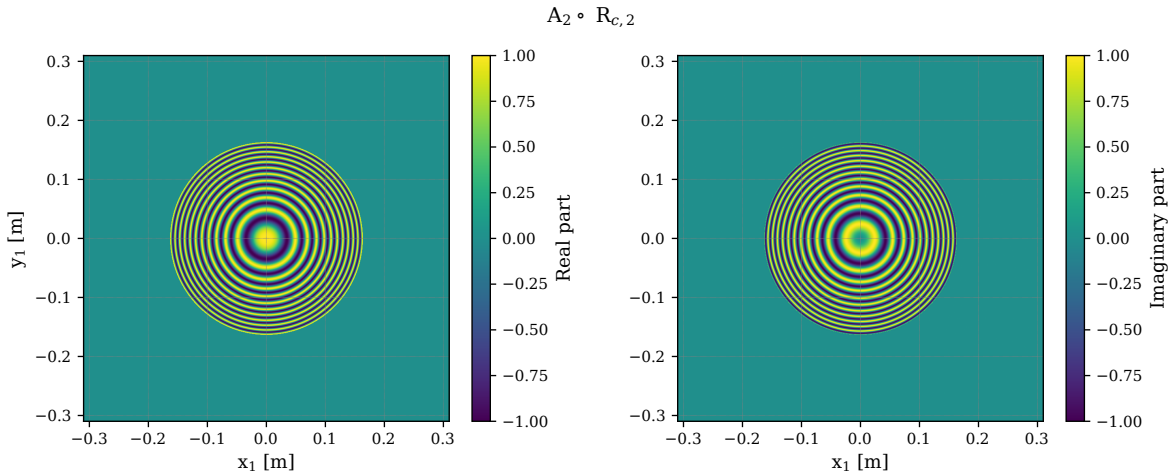

Figure B.2: ETM aperture and curvature phase map.

the radius of curvature at the mirrors. The ETM and ITM have a similar enough radius of curvature that there isn't an appreciable difference in the periodicity of the rings, despite the ITM having a smaller radius of curvature. This method of implementing a mirror reflection operator can potentially lead to issues if the radius of curvature is small and the oscillation frequency of the rings exceeds the Nyquist frequency of the grid. This can often happen with fast telescopes, such as the one in the aLIGO power recycling cavity. In those cases the sampling frequency of the grid has to be carefully chosen with those telescopes in mind.

Figure B.3 is the LCT operator for the arm cavity length free space propagation. The operator shown in figure B.3 is explicitly $\boldsymbol{D}_{y1}$, but since there is no difference between the x-axis and y-axis in this model it follows that there is no difference between the

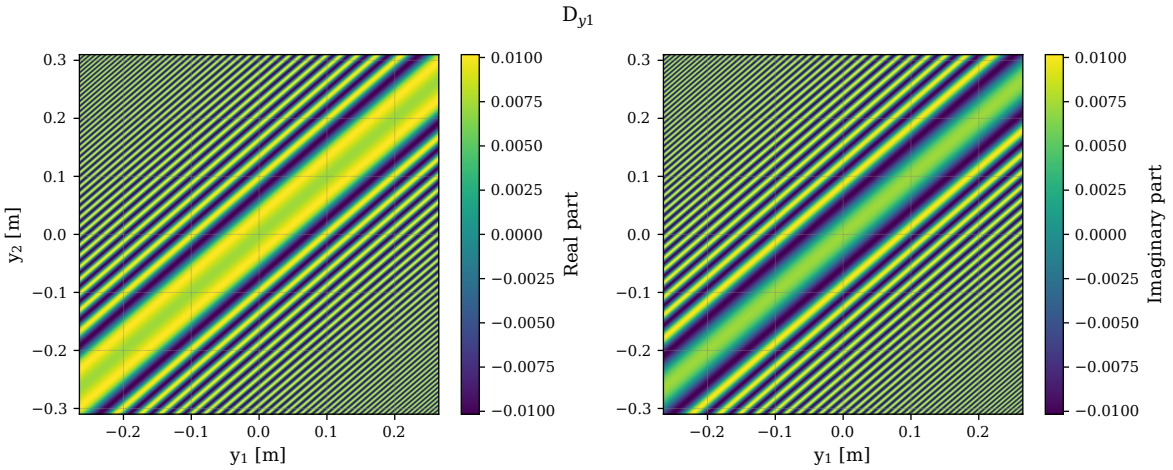

Figure B.3: Space propagation LCT operator for the y-axis arm cavity length free space propagation.

operators for the two axes, that is $\boldsymbol{D}_{y1} = \boldsymbol{D}_{x1}$. The dynamic grid scaling mentioned earlier is also present here. In fact the $\boldsymbol{D}_{y1}$ operator is the one that implements the grid scaling operation — expanding the grid as the beam propagates from the ITM plane to the ETM plane. The operator $\boldsymbol{D}_{y2}$ for propagating from the ETM back to the ITM has to perform the same free space propagation, but the inverse scaling operation — shrinking the grid as the beam propagates from the ETM to the ITM. In this model the inverse scaling operation is given by the transpose of the original scaling operator, and so the propagation operators between the ITM and ETM plane are related by a transpose $\boldsymbol{D}_{y2} = \boldsymbol{D}_{x2} = \boldsymbol{D}_{y1}^T = \boldsymbol{D}_{x1}^T$. It follows that a free space propagation operator that doesn't scale the grid is transpose symmetric.

Appendix C

LIGO commissioning

C.1 aLIGO design Finesse3 model

```
# modulators for core interferometer sensing - Advanced LIGO, CQG, 2015
# http://iopscience.iop.org/article/10.1088/0264-
9381/32/7/074001/meta#cqg507871s4-8
# 9MHz (CARM, PRC, SRC loops)
variable f1 9099471
variable f2 5*&f1
variable nsilica 1.45
variable Mloss 30u
###############################################################################
###   length definitions
###############################################################################
variable Larm 3994
variable LPR23 16.164  # distance between PR2 and PR3
variable LSR23 15.443  # distance between SR2 and SR3
variable LPR3BS 19.538 # distance between PR3 and BS
variable LSR3BS 19.366 # distance between SR3 and BS
variable lmich 5.342   # average length of MICH
variable lschnupp 0.08
variable lPRC (3+0.5)*c0/(2*&f1) # T1000298 Eq2.1, N=3
```

```
variable lSRC (17)*c0/(2*&f2) # T1000298 Eq2.2, M=3
################################################################################
###   laser
################################################################################
laser L0 P=125
mod mod1 f=&f1 midx=0.18 order=1 mod_type=pm
mod mod2 f=&f2 midx=0.18 order=1 mod_type=pm
link(L0, mod1, mod2)
################################################################################
###   PRC
################################################################################
s sPRCin mod2.p2 PRMAR.p1
m PRMAR R=0 L=40u xbeta=&PRM.xbeta ybeta=&PRM.ybeta phi=&PRM.phi
s sPRMsub1 PRMAR.p2 PRM.p1 L=0.0737 nr=&nsilica
m PRM T=0.03 L=8.5u Rc=11.009
s lp1 PRM.p2 PR2.p1 L=&lPRC-&LPR3BS-&LPR23-&lmich
bs PR2 T=250u L=&Mloss alpha=-0.79 Rc=-4.545
s lp2 PR2.p2 PR3.p1 L=&LPR23
bs PR3 T=0 L=&Mloss alpha=0.615 Rc=36.027
s lp3 PR3.p2 BS.p1 L=&LPR3BS
################################################################################
###   BS
################################################################################
bs BS R=0.5 L=&Mloss alpha=45
s BSsub1 BS.p3 BSAR1.p1 L=0.0687 nr=&nsilica
s BSsub2 BS.p4 BSAR2.p2 L=0.0687 nr=&nsilica
bs BSAR1 L=50u R=0 alpha=-29.195
bs BSAR2 L=50u R=0 alpha=29.195
################################################################################
###   Yarm
################################################################################
# Distance from beam splitter to Y arm input mirror
```

```
s ly1 BS.p2 ITMYlens.p1 L=&lmich-&lschnupp/2-&ITMYsub.L*&ITMXsub.nr
lens ITMYlens f=34500
s ly2 ITMYlens.p2 ITMYAR.p1
m ITMYAR R=0 L=20u xbeta=&ITMY.xbeta ybeta=&ITMY.ybeta phi=&ITMY.phi
s ITMYsub ITMYAR.p2 ITMY.p1 L=0.2 nr=&nsilica
m ITMY T=0.014 L=&Mloss Rc=-1934
s LY ITMY.p2 ETMY.p1 L=&Larm
m ETMY T=5u L=&Mloss Rc=2245
s ETMYsub ETMY.p2 ETMYAR.p1 L=0.2 nr=&nsilica
m ETMYAR 0 500u xbeta=&ETMY.xbeta ybeta=&ETMY.ybeta phi=&ETMY.phi
cav cavYARM ETMY.p1.o
################################################################################
###   Xarm
################################################################################
# Distance from beam splitter to X arm input mirror
s lx1 BSAR1.p3 ITMXlens.p1 L=&lmich+&lschnupp/2-&ITMXsub.L*&ITMXsub.nr-
&BSsub1.L*&BSsub1.nr
lens ITMXlens f=34500
s lx2 ITMXlens.p2 ITMXAR.p1
m ITMXAR R=0 L=20u xbeta=&ITMX.xbeta ybeta=&ITMX.ybeta phi=&ITMX.phi
s ITMXsub ITMXAR.p2 ITMX.p1 L=0.2 nr=&nsilica
m ITMX T=0.014 L=&Mloss Rc=-1934
s LX ITMX.p2 ETMX.p1 L=&Larm
m ETMX T=5u L=&Mloss Rc=2245
s ETMXsub ETMX.p2 ETMXAR.p1 L=0.2 nr=&nsilica
m ETMXAR 0 500u xbeta=&ETMX.xbeta ybeta=&ETMX.ybeta phi=&ETMX.phi
cav cavXARM ETMX.p1.o
################################################################################
###   SRC
################################################################################
s ls3 BSAR2.p4 SR3.p1 L=&LSR3BS
bs SR3 T=0 L=&Mloss alpha=0.785 Rc=35.972841
```

```
s ls2 SR3.p2 SR2.p1 L=&LSR23
bs SR2 T=0 L=&Mloss alpha=-0.87 Rc=-6.406
s ls1 SR2.p2 SRM.p1 L=&lSRC-&LSR3BS-&LSR23-&BSsub2.L*&BSsub2.nr-&lmich
m SRM T=0.2 L=8.7u Rc=-5.6938
s SRMsub SRM.p2 SRMAR.p1 L=0.0749 nr=&nsilica
m SRMAR R=0 L=50n
################################################################################
###   Output path
################################################################################
dbs OFI
sq sqz db=6 angle=90.0
link(sqz, OFI.p2)

# (as built parameters: D1300507-v1)
s sSRM_OFI SRMAR.p2 OFI.p1 L=0.7278
s sOFI_OM1 OFI.p3 OM1.p1 L=2.9339

bs OM1 T=800u L=0 alpha=2.251 Rc=[4.6, 4.6]
s sOM1_OM2 OM1.p2 OM2.p1 L=1.395
bs OM2 T=0 L=0 alpha=4.399 Rc=[1.7058, 1.7058]
s sOM2_OM3 OM2.p2 OM3.p1 L=0.631
bs OM3 T=0 L=0 alpha=30.037
s sOM3_OMC OM3.p2 OMC_IC.p1 L=0.2034
################################################################################
###   OMC
################################################################################
cav cavOMC OMC_IC.p3.o
bs OMC_IC T=0.0076 L=10u alpha=2.7609
s lIC_OC OMC_IC.p3 OMC_OC.p1 L=0.2815
bs OMC_OC T=0.0075 L=10u alpha=4.004
s lOC_CM1 OMC_OC.p2 OMC_CM1.p1 L=0.2842
bs OMC_CM1 T=36u L=10u alpha=4.004 Rc=[2.57321, 2.57321]
```

```
s lCM1_CM2 OMC_CM1.p2 OMC_CM2.p1 L=0.2815
bs OMC_CM2 T=35.9u L=10u alpha=4.004 Rc=[2.57369, 2.57369]
s lCM2_IC OMC_CM2.p2 OMC_IC.p4 L=0.2842
################################################################################
### DC power measurements
################################################################################
pd Px ETMX.p1.i
pd Py ETMX.p1.i
pd Pprc PRM.p2.o
pd Psrc SRM.p1.i
pd Prefl ETMX.p1.i
pd Pas OMC_OC.p3.o
```

Appendix D

Mode matching error signal

D.1 Gaussian beams

The 1D complex amplitude of a Gaussian beam centered at $x = \delta$ travelling at angle γ to the z-axis with a waist size of w_0 located at $z = 0$ is given by [50]

$$u_n(x, q, \delta, \gamma) = \left(\frac{2}{\pi}\right)^{1/4} \left(\frac{1}{2^n n! w_0}\right)^{1/2} \left(\frac{\mathrm{i} z_R}{q}\right)^{1/2} \left(\frac{-q^*}{q}\right)^{n/2} H_n\left(\frac{(x-\delta)\sqrt{2}}{w(z)}\right) \exp\left[\frac{-\mathrm{i}\pi}{\lambda}\left(\frac{(x-\delta)^2}{q} + x\gamma\right)\right] \quad \text{(D.1)}$$

where q is the complex beam parameter [50], which encodes all of the necessary information of a beam's shape as

$$q = z + \mathrm{i} z_R \quad \text{(D.2)}$$

where z is the location of the beam waist, and $z_R = \pi w_0^2/\lambda$ is the Rayleigh range of a beam with waist size w_0 and wavelength λ. The beam size $w(z)$ is given by

$$w(z) = w_0 \sqrt{1 + \left(\frac{z}{z_R}\right)^2}. \quad \text{(D.3)}$$

The complex amplitude of a 2D Hermite-Gaussian HG_{nm} beam with beam shape (q_x, q_y) can be given as a product of two 1D HG beams due to the separability

of HG modes in Cartesian coordinates

$$U_{nm}(x, y, q_x, q_y, \delta_x, \delta_y, \gamma_x, \gamma_y) = u_n(x, q_x, \delta_x, \gamma_x)\, u_m(y, q_y, \delta_y, \gamma_y). \tag{D.4}$$

For brevity we will assume cylindrical symmetry ($q = q_x = q_y$) and no misalignments ($\delta_x = \delta_y = \gamma_x = \gamma_y = 0$) unless otherwise stated. To compute the magnitude of coupling of mode mismatch to higher order HG modes in section 6.3.2 and table D.1 it is convenient to rescale the degrees of freedom to the following relative quantities

$$\varepsilon_\delta = \frac{\delta}{w_0} \qquad \varepsilon_\gamma = \frac{\pi w(z)\gamma}{\lambda} \tag{D.5}$$

$$\varepsilon_{w_0} = \frac{\Delta w_0}{w_0} \qquad \varepsilon_z = \frac{\Delta z}{z_R}. \tag{D.6}$$

For the mode matching degrees of freedom it is also convenient to define a relative change in the q parameter from equation D.2 as

$$\varepsilon_q = \varepsilon_z + \mathrm{i}\varepsilon_{z_R} \tag{D.7}$$

where ε_{z_R} is the relative change in Rayleigh range, which is given by

$$\varepsilon_{z_R} = \frac{\Delta z_R}{z_{R,1}} = \varepsilon_{w_0}^2. \tag{D.8}$$

D.2 Basis change and projections

To describe an incident beam with electric field given by $E(x, y)$ in terms of cavity eigenmodes it is necessary to find the amplitude coefficients $a_{n,m}$ of those modes that describe the incident beam by computing the following integral

$$a_{n,m;q} = \iint_{-\infty}^{\infty} E(x, y) U^*_{n,m}(x, y, q) dy dx \tag{D.9}$$

for all possible combinations of n and m. However for models with a predominantly HG_{00} field and mismatches less than 10% it is typically sufficient to compute all $a_{n,m}$ with $n + m \leq 6$.

This lets us write an arbitrary electric field given by $E(x, y)$ as a sum of HG modes

$$E(x, y) = \sum_{n,m} a_{n,m;q} U_{n,m}(x, y, q). \tag{D.10}$$

To translate the set of $a_{n,m}$ coefficients from one basis q_1 to another we can substitute (D.10) into (D.9) to obtain

$$a_{n_2,m_2;q_2} = \sum_{n_1,m_1} a_{n_1,m_1;q_1} \iint_{-\infty}^{\infty} U_{n_1,m_1}(x, y, q_1) U^*_{n_2,m_2}(x, y, q_2) dy. \tag{D.11}$$

The integral in (D.11) is an overlap between two normalized HG modes from different bases

$$k_{n_1,m_1,n_2,m_2;q_1,q_2} = \iint_{-\infty}^{\infty} U_{n_1,m_1}(x, y, q_1) U^*_{n_2,m_2}(x, y, q_2) dy dx. \tag{D.12}$$

Due to the fact that HG modes are separable in Cartesian coordinates we can rewrite the (D.12) as a product of two 1D integrals in the following way

$$k_{n_1,m_1,n_2,m_2;q_1,q_2} = k_{n_1,n_2;q_1,q_2} \times k_{m_1,m_2;q_1,q_2} \tag{D.13}$$

where the two 1D integrals are given by

$$k_{n_1,n_2;q_1,q_2} = \int_{-\infty}^{\infty} u_{n_1}(x, q_1) u^*_{n_2}(x, q_2) dx \tag{D.14}$$

$$k_{m_1,m_2;q_1,q_2} = \int_{-\infty}^{\infty} u_{m_1}(y, q_1) u^*_{m_2}(y, q_2) dy \tag{D.15}$$

where if $q_1 = q_2$ both integrals reduce to

$$k_{n_1,n_2;q_1,q_1} = \delta_{n_1,n_2} \tag{D.16}$$

where δ_{n_1,n_2} is the Kronecker delta. For brevity we will omit the q parameters from k_{n_1,n_2} unless multiple projections are being considered. For $q_1 \neq q_2$ this integral can be computed either numerically or from an analytic solution [43, 128]. In principle this integral needs to be computed for every possible combination of n_1 and n_2, but in practice for small mismatches one only needs to consider the integrals where $|n_1 - n_2| = 2$. A table of the coupling coefficients to first order in mismatch and misalignment is included in table D.1.

Coupling Coefficient	Expression	Notes
k_{n_1,m_1,n_2,m_2}	$k_{n_1,n_2} \times k_{m_1,m_2}$	2D $\rightarrow$ 1D
$k_{n,n}$	$1 - \frac{\mathrm{i}}{4}(2n+1)\,\varepsilon_z + \mathcal{O}(\varepsilon^2)$	phase shift
$k_{n,n+1}$	$\left(\varepsilon_\delta - \frac{q}{\lvert q\rvert}\varepsilon_\gamma\right)\sqrt{(n+1)} + \mathcal{O}(\varepsilon^2)$	misalignment
$k_{n,n+2}$	$\frac{\mathrm{i}}{4}\varepsilon_q\sqrt{(n+1)\,(n+2)} + \mathcal{O}(\varepsilon^2)$	mismatch
k_{n_1,n_2}	$-k^*_{n_2,n_1} + \mathcal{O}(\varepsilon^2)$	$n \neq m$

Table D.1: **First Order Coupling Coefficients**

In general the integral in (D.12) appears whenever one wishes to convert the amplitudes of one set of eigenmodes to another set of eigenmodes. We refer to this operation as a *change of basis*, or a *projection* onto a basis, where the basis is parameterised by the complex beam parameter q.

D.3 Mode matching error signals

D.3.1 Mode matching error signal between two beams

The proposed mode matching error signal between two beams can be obtained considering a HG_{00} carrier and a beam modulation sideband with powers P_{00} and P_{02} respectively.

$$E = \left[\sqrt{P_{00}}U_{00}(q_1) + \sqrt{P_{02}}(U_{20}(q_2) + U_{02}(q_2))e^{\mathrm{i}\Omega t}\right] e^{\mathrm{i}\omega_0 t}. \tag{D.17}$$

To compute the interference between the two we choose to project the beam modulation sideband into the carrier basis, which results in an RF HG_{00} component in the carrier basis given by the k_{0200} scattering coefficient from (D.12) to first order in mismatch.

$$\begin{aligned} E = \Big\{ &\sqrt{P_{00}}U_{00}(q_1) + \sqrt{P_{02}}\Big[2k_{0200}(U_{00}(q_1)) \\ &+ k_{0202}(U_{20}(q_1) + U_{02}(q_1))\Big]e^{\mathrm{i}\Omega t}\Big\}e^{\mathrm{i}\omega_0 t} + \mathcal{O}(\varepsilon^2)\,. \end{aligned} \tag{D.18}$$

The mode matching error signal $\mathcal{Z}$ is then obtained by demodulating the intensity of the combined beams at the offset frequency Ω, which gives

$$\mathcal{Z}_{\mathrm{beam}} = 2\sqrt{P_{00}P_{02}}\,(k^*_{0200}) + \mathcal{O}(\varepsilon^2) \tag{D.19}$$

where we dropped the k_{0202} terms because they do not beat with the HG_{00} carrier as they are now in the same q_1 basis, and hence orthogonal. We can break up the k_{0200} 2D coupling coefficient into a product of two 1D scattering coefficients due to the fact that HG modes are separable in Cartesian coordinates

$$\mathcal{Z}_{\text{beam}} = 2\sqrt{P_{00}P_{02}}\,(k_{20}^{*}k_{00}^{*}) + \mathcal{O}\big(\varepsilon^2\big)\,. \tag{D.20}$$

Here we can substitute the 1D coupling coefficients with their first order approximation from table D.1

$$\mathcal{Z}_{\text{beam}} = -\mathrm{i}\sqrt{P_{00}P_{02}}\frac{\sqrt{2}}{2}\left(\varepsilon_q + \frac{\mathrm{i}}{4}\varepsilon_q\varepsilon_z\right) + \mathcal{O}\big(\varepsilon^2\big)\,. \tag{D.21}$$

We can drop the $\varepsilon_q\varepsilon_z$ term as it is quadratic in ε. The overall factor of i can be ignored if the absolute demodulation phase is not relevant. This leaves us with the final form of the mode matching error signal between two beams that was stated in (6.6)

$$\mathcal{Z}_{\text{beam}} = -\mathrm{i}\sqrt{P_{00}P_{02}}\frac{\sqrt{2}}{2}\varepsilon_q + \mathcal{O}\big(\varepsilon^2\big)\,. \tag{D.22}$$

D.3.2 Mode matching error signal for resonant cavity

Consider a beam consisting of a carrier HG_{00} and sideband HG_{02} both in basis q_1 incident on a cavity with eigenmode basis q_{cav}. In order to compute the cavity reflected field it is necessary to project the incident beam into the q_{cav} basis. The incident electric field of the incident beam in the q_{cav} basis is

$$\begin{aligned} E_{\text{inc}} = \Big\{ & U_{00}(q_{\text{cav}})\left[\sqrt{P_{00}}k_{0000} + \sqrt{P_{02}}e^{\mathrm{i}\Omega t}\big(k_{0200} + k_{2000}\big)\right] \\ & + U_{02}(q_{\text{cav}})\left[\sqrt{P_{00}}k_{0002} + \sqrt{P_{02}}k_{0202}e^{\mathrm{i}\Omega t}\right] \\ & + U_{20}(q_{\text{cav}})\left[\sqrt{P_{00}}k_{0020} + \sqrt{P_{02}}k_{2020}e^{\mathrm{i}\Omega t}\right]\Big\}e^{\mathrm{i}\omega_0 t} \\ & + \mathcal{O}\big(\varepsilon^2\big) \end{aligned} \tag{D.23}$$

On reflection all components are promptly reflected with the exception of the resonant mode and frequency, that being the HG_{00} mode at the carrier frequency ω_0, which picks up a cavity reflection R_{cav} defined in equation 6.8. The reflected electric field is

then

$$\begin{aligned} E_{\text{refl}} = \Big\{ & U_{00}(q_{\text{cav}}) \left[R_{\text{cav}} \sqrt{P_{00}} k_{0000} + \sqrt{P_{02}} e^{\mathrm{i}\Omega t} \left(k_{0200} + k_{2000} \right) \right] \\ & + U_{02}(q_{\text{cav}}) \left[\sqrt{P_{00}} k_{0002} + \sqrt{P_{02}} k_{0202} e^{\mathrm{i}\Omega t} \right] \\ & + U_{20}(q_{\text{cav}}) \left[\sqrt{P_{00}} k_{0020} + \sqrt{P_{02}} k_{2020} e^{\mathrm{i}\Omega t} \right] \Big\} e^{\mathrm{i}\omega_0 t} \\ & + \mathcal{O}\left(\varepsilon^2\right) \end{aligned} \tag{D.24}$$

To compute the error signal amplitude we now demodulate at the sideband frequency. The complex demodulated amplitude is then

$$\begin{aligned} \mathcal{Z}_{\text{cav}} = \sqrt{P_{00} P_{02}} \Big[& R_{\text{cav}} \left(k_{0000} k_{0200}^* + k_{0000} k_{2000}^* \right) \\ & + k_{0002} k_{0202}^* + k_{0020} k_{2020}^* \Big] + \mathcal{O}\left(\varepsilon^2\right). \end{aligned} \tag{D.25}$$

Here we can use the $k_{n,n}$ entry in table D.1 to note that to first order in ε the following equalities hold: $k_{0000} = k_{2020} = k_{0202} = 1$, $k_{0002} = k_{0020} = k_{02}$, and $k_{0200} = k_{2000} = k_{20}$. Applying those simplifications leaves us with

$$\mathcal{Z}_{\text{cav}} = \sqrt{P_{00} P_{02}} \left[2 R_{\text{cav}} k_{20}^* + 2 k_{02} \right] + \mathcal{O}\left(\varepsilon^2\right). \tag{D.26}$$

We can simplify further by using the last entry of table D.1 to note that $k_{02} = -k_{20}^*$, leaving us with

$$\mathcal{Z}_{\text{cav}} = -2\sqrt{P_{00} P_{02}} \left[R_{\text{cav}} k_{02} - k_{02} \right] + \mathcal{O}\left(\varepsilon^2\right) \tag{D.27}$$

$$= -2\sqrt{P_{00} P_{02}} \left(R_{\text{cav}} - 1 \right) k_{02} + \mathcal{O}\left(\varepsilon^2\right). \tag{D.28}$$

We can substitute the k_{02} with its first order approximation from table D.1 to obtain the result quoted in (6.7)

$$\mathcal{Z}_{\text{cav}} = -\mathrm{i}\sqrt{P_{00} P_{02}} \left(R_{\text{cav}} - 1 \right) \frac{\sqrt{2}}{2} \varepsilon_q + \mathcal{O}\left(\varepsilon^2\right). \tag{D.29}$$

D.4 Shot Noise

For a single demodulation of a single optical sideband, the single sided shot noise PSD is given by [103]

$$S(f) = 2\hbar ckP \tag{D.30}$$

where P is the average incident DC optical power. The root mean square (RMS) noise is then given by

$$\text{RMS}^2 = \int_0^{\Delta f} S(f)df \tag{D.31}$$

$$\text{RMS} = \sqrt{2\hbar ckP\Delta f} \tag{D.32}$$

$$= \sqrt{\frac{2\hbar ckP}{T}} \tag{D.33}$$

where $\Delta f = 1/T$ is the integration bandwidth and T is the integration time in seconds. The signal to noise ratio is then given by

$$\text{SNR} = \frac{|\mathcal{Z}|}{\text{RMS}} \tag{D.34}$$

$$= \frac{|\mathcal{Z}|}{\sqrt{2\hbar ck\left(P_{00} + P_{02}\right)}}\sqrt{T} \tag{D.35}$$

$$= \frac{\sqrt{P_{00}P_{02}}}{\sqrt{2\hbar ck\left(P_{00} + P_{02}\right)}}\left|(R_{\text{cav}} - 1)\frac{\sqrt{2}}{4}\varepsilon_q\right|\sqrt{T} \tag{D.36}$$

Evaluating the constants and assuming an impedance matched cavity ($R_{\text{cav}} = 0$) results in

$$\text{SNR} = 5.8 \times 10^8 \ |\varepsilon_q| \left(\frac{\sqrt{P_{00}P_{02}}}{\sqrt{P_{00} + P_{02}}}\right)\sqrt{T}. \tag{D.37}$$

Substituting in the measured powers in the tabletop experiment $P_{00} = 2mW$, $P_{02} = 20\mu W$ gives us

$$\text{SNR} = 2.6 \times 10^6 \ |\varepsilon_q|\sqrt{T}. \tag{D.38}$$

We can convert the SNR into units of mode mismatch by substituting (6.3)

$$\mathrm{SNR} = 1.7 \times 10^{12}\ \mathrm{M} \times T. \tag{D.39}$$

This translates to sub-ppm of mode mismatch even with a 1 μs integration time. We conclude that in practice technical noise sources and not shot noise will be relevant to the SNR of the mode matching error signal.

List of Publications

A. A. Ciobanu, D. D. Brown, P. J. Veitch, and D. J. Ottaway. "Mode matching error signals using radio-frequency beam shape modulation". In: *Applied Optics* 59.31 (Nov. 1, 2020). Number: 31, p. 9884. ISSN: 1559-128X, 2155-3165. DOI: 10.1364/AO.404646

Daniel Brown, Huy Tuong Cao, Alexei Ciobanu, Peter Veitch, and David Ottaway. "Differential wavefront sensing and control using radio-frequency optical demodulation". In: *Optics Express* 29.11 (May 24, 2021), p. 15995. ISSN: 1094-4087. DOI: 10.1364/OE.425590

A. A. Ciobanu, D. D. Brown, P. J. Veitch, and D. J. Ottaway. "Modeling circulating cavity fields using the discrete linear canonical transform". In: *Journal of the Optical Society of America A* 38.9 (Sept. 1, 2021). Number: 9, p. 1293. ISSN: 1084-7529, 1520-8532. DOI: 10.1364/JOSAA.433575

Technical Reports, Presentations, and Posters

Alexei Ciobanu, Daniel Brown, Peter Veitch, and David Ottaway. *Modeling circulating cavity fields using the discrete linear canonical transform.* G2101163. LIGO DCC, June 26, 2021

Alexei Ciobanu, Daniel Brown, Peter Veitch, and David Ottaway. *Introducing information theoretic beam basis optimization.* T2000605. LIGO DCC, Oct. 21, 2020

Alexei Ciobanu. *Optical modelling with Linear Canonical Transforms (LCT).* G2001508. LIGO DCC, Sept. 11, 2020

Alexei Ciobanu, Daniel Brown, Peter Veitch, and David Ottaway. *(LAWG presen-*

tation) Mode matching error signals using radio-frequency beam shape modulation. G2001257. LIGO DCC, June 4, 2020

Alexei Ciobanu, Daniel Brown, and David Ottaway. *A practical guide to Linear Canonical Transforms.* G2000254. LIGO DCC, Feb. 19, 2020

Alexei Ciobanu, Daniel Brown, Peter Veitch, and David Ottaway. *OzGrav retreat 2019 poster.* G1902197. LIGO DCC, Nov. 14, 2019

Alexei Ciobanu, Daniel Brown, and David Ottaway. *Finesse Workshop - Linear Canonical Transform and Graph Reduction.* G1901692. LIGO DCC, Sept. 2, 2019

Alexei Ciobanu, Daniel Brown, and David Ottaway. *jupyter notebook: tutorial on computing OMC astigmatism from OMC scans.* T1900180. LIGO DCC, Apr. 8, 2019

Alexei Ciobanu, Daniel Brown, and David Ottaway. *Measurement of LLO and LHO OMC astigmatism.* T1900084. LIGO DCC, Apr. 3, 2019

Alexei Ciobanu, Daniel Brown, David Ottaway, and Peter Veitch. *Mode matching error signals from cavity eigenmode modulation (poster).* G1802332. LIGO DCC, Dec. 16, 2018

Alexei Ciobanu, Daniel Brown, David Ottaway, and Peter Veitch. *LAWG mode mismatch presentation.* G1802180. LIGO DCC, Nov. 13, 2018

Alexei Ciobanu. *Parametrization of mismatch contours.* T1800193. LIGO DCC, Apr. 29, 2018

Alexei Ciobanu and Daniel Brown. *Effects of OMC astigmatism on mismatch calculations from OMC scans.* T1800191. LIGO DCC, Apr. 26, 2018

Alexei Ciobanu, Daniel Brown, Thomas Vo, and Terra Hardwick. *Mode mismatch of astigmatic gaussian beams from a cavity scan.* T1800165. LIGO DCC, Apr. 16, 2018

Alexei Ciobanu, Daniel Brown, and David Ottaway. *Modelling Beam Shape Noise in Gravitational Wave Interferometers.* G1702312. LIGO DCC, Nov. 22, 2017

Bibliography

[1] Urbain J. Le Verrier. “Theorie du mouvement de Mercure”. In: *Annales de l’Observatoire de Paris* 5 (Jan. 1, 1859). ADS Bibcode: 1859AnPar...5....1L, p. 1.

[2] Albert Einstein. “Die Feldgleichungen der Gravitation”. In: *Sitzungsberichte der Königlich Preußischen Akademie der Wissenschaften (Berlin* (Jan. 1915), pp. 844–847.

[3] Albert Einstein. “Erklärung der Perihelbewegung des Merkur aus der allgemeinen Relativitätstheorie”. In: *Sitzungsberichte der Königlich Preußischen Akademie der Wissenschaften (Berlin* (Jan. 1915), pp. 831–839.

[4] Albert Einstein. “Näherungsweise Integration der Feldgleichungen der Gravitation”. In: *Sitzungsberichte der Königlich Preußischen Akademie der Wissenschaften (Berlin), Seite 688-696.* (1916).

[5] Albert Einstein. “Über Gravitationswellen”. In: *Sitzungsberichte der Königlich Preußischen Akademie der Wissenschaften (Berlin* (Jan. 1918), pp. 154–167.

[6] W. E. Roth. “On direct product matrices”. In: *Bulletin of the American Mathematical Society* 40.6 (1934). Number: 6 Publisher: American Mathematical Society, pp. 461–468.

[7] Olin J. Eggen. “Vulcan”. In: *Leaflet of the Astronomical Society of the Pacific* 6 (Jan. 1, 1953). ADS Bibcode: 1953ASPL....6..291E, p. 291. ISSN: 0004-6272.

[8] Samuel Mason. “Feedback Theory-Some Properties of Signal Flow Graphs”. In: *Proceedings of the IRE* 41.9 (Sept. 1953). Number: 9, pp. 1144–1156. ISSN: 0096-8390. DOI: 10.1109/JRPROC.1953.274449.

[9] Samuel Mason. “Feedback Theory-Further Properties of Signal Flow Graphs”. In: *Proceedings of the IRE* 44.7 (July 1956). Number: 7, pp. 920–926. ISSN: 0096-8390. DOI: 10.1109/JRPROC.1956.275147.

[10] S. Mason. “About Such Things as Unistors, Flow Graphs, Probability, Partial Factoring, and Matrices”. In: *IRE Transactions on Circuit Theory* 4.3 (1957), pp. 90–97. ISSN: 0096-2007. DOI: 10.1109/TCT.1957.1086386.

[11] A. G. Fox and Tingye Li. “Resonant Modes in a Maser Interferometer”. In: *Bell System Technical Journal* 40.2 (Mar. 1961). Number: 2, pp. 453–488. ISSN: 00058580. DOI: 10.1002/j.1538-7305.1961.tb01625.x.

[12] Louis P. A Robichaud, Maurice Boisvert, and Jean Robert. *Signal Flow Graphs and Applications*. Prentice Hall, 1962.

[13] Willem Brouwer. *Matrix Methods in Optical Instrument Design*. W. A. Benjamin, Inc., 1964.

[14] Stuart A. Collins. “Analysis of Optical Resonators Involving Focusing Elements”. In: *Applied Optics* 3.11 (Nov. 1, 1964). Number: 11, p. 1263. ISSN: 0003-6935, 1539-4522. DOI: 10.1364/AO.3.001263.

[15] Stuart A. Collins and Daniel T. M. Davis. “Modes in a Triangular Ring Optical Resonator”. In: *Applied Optics* 3.11 (Nov. 1, 1964). Number: 11, p. 1314. ISSN: 0003-6935, 1539-4522. DOI: 10.1364/AO.3.001314.

[16] H. Kogelnik. “Imaging of optical modes — resonators with internal lenses”. In: *The Bell System Technical Journal* 44.3 (Mar. 1965). Number: 3, pp. 455–494. ISSN: 0005-8580. DOI: 10.1002/j.1538-7305.1965.tb01672.x.

[17] Herwig Kogelnik. “On the Propagation of Gaussian Beams of Light Through Lenslike Media Including those with a Loss or Gain Variation”. In: *Applied Optics* 4.12 (Dec. 1, 1965), p. 1562. ISSN: 0003-6935, 1539-4522. DOI: 10.1364/AO.4.001562.

[18] H. Kogelnik and T. Li. “Laser Beams and Resonators”. In: *Applied Optics* 5.10 (Oct. 1, 1966). Number: 10, pp. 1550–1567. ISSN: 1539-4522. DOI: 10.1364/AO.5.001550.

[19] J. A. Arnaud and H. Kogelnik. “Gaussian Light Beams with General Astigmatism”. In: *Applied Optics* 8.8 (Aug. 1, 1969). Number: 8, p. 1687. ISSN: 0003-6935, 1539-4522. DOI: 10.1364/AO.8.001687.

[20] Stuart A. Collins. "Lens-System Diffraction Integral Written in Terms of Matrix Optics*". In: *Journal of the Optical Society of America* 60.9 (Sept. 1, 1970). Number: 9, p. 1168. ISSN: 0030-3941. DOI: 10.1364/JOSA.60.001168.

[21] G.A. Deschamps. "Gaussian beam as a bundle of complex rays". In: *Electronics Letters* 7.23 (1971). Number: 23, p. 684. ISSN: 00135194. DOI: 10.1049/el:19710467.

[22] M. H. Dunn. "Use of Flow Graphs in the Analysis of Optical Cavities". In: *Applied Optics* 10.6 (June 1, 1971), p. 1393. ISSN: 0003-6935, 1539-4522. DOI: 10.1364/AO.10.001393.

[23] Joseph B. Keller and William Streifer. "Complex Rays with an Application to Gaussian Beams". In: *Journal of the Optical Society of America* 61.1 (Jan. 1, 1971). Number: 1, p. 40. ISSN: 0030-3941. DOI: 10.1364/JOSA.61.000040.

[24] M. Moshinsky and C. Quesne. "Linear Canonical Transformations and Their Unitary Representations". In: *Journal of Mathematical Physics* 12.8 (Aug. 1971). Number: 8, pp. 1772–1780. ISSN: 0022-2488, 1089-7658. DOI: 10.1063/1.1665805.

[25] Daryle E. Riegle. "Topological Properties Of Matrix Signal Flow Graphs". ISBN: 9798658667416 Publication Title: ProQuest Dissertations and Theses. PhD thesis. 1971. 169 pp.

[26] R. H. Bartels and G. W. Stewart. "Solution of the matrix equation AX + XB = C [F4]". In: *Communications of the ACM* 15.9 (Sept. 1972). Number: 9, pp. 820–826. ISSN: 0001-0782, 1557-7317. DOI: 10.1145/361573.361582.

[27] D. Riegle and P. Lin. "Matrix signal flow graphs and an optimum topological method for evaluating their gains". In: *IEEE Transactions on Circuit Theory* 19.5 (1972). Number: 5, pp. 427–435. ISSN: 0018-9324. DOI: 10.1109/TCT.1972.1083542.

[28] Rainer Weiss. *Electromagnetically Coupled Broadband Gravitational Antenna*. Quarterly Progress Report 105. Research Laboratory of Electronics: Massachusetts Institute of Technology, 1972.

[29] Charles W. Misner, Kip S. Thorne, and John Archibald Wheeler. *Gravitation*. San Francisco: W. H. Freeman, 1973. 1279 pp. ISBN: 978-0-7167-0334-1 978-0-7167-0344-0.

[30] R. A. Hulse and J. H. Taylor. "Discovery of a pulsar in a binary system". In: *The Astrophysical Journal* 195 (Jan. 1975), p. L51. ISSN: 0004-637X, 1538-4357. DOI: 10.1086/181708.

[31] D. B. Kushev. "Signal flow graphs in the analysis of the transmission and reflection of plane-parallel layers". In: *Journal of Applied Spectroscopy* 22.4 (Apr. 1975), pp. 567–573. ISSN: 0021-9037, 1573-8647. DOI: 10.1007/BF00614718.

[32] Melvin Lax, William H. Louisell, and William B. McKnight. "From Maxwell to paraxial wave optics". In: *Physical Review A* 11.4 (Apr. 1, 1975). Number: 4, pp. 1365–1370. ISSN: 0556-2791. DOI: 10.1103/PhysRevA.11.1365.

[33] S. Y. Shin and L. B. Felsen. "Gaussian beam modes by multipoles with complex source points*". In: *Journal of the Optical Society of America* 67.5 (May 1, 1977). Number: 5, p. 699. ISSN: 0030-3941. DOI: 10.1364/JOSA.67.000699.

[34] G. P. Agrawal and D. N. Pattanayak. "Gaussian beam propagation beyond the paraxial approximation". In: *Journal of the Optical Society of America* 69.4 (Apr. 1, 1979). Number: 4, p. 575. ISSN: 0030-3941. DOI: 10.1364/JOSA.69.000575.

[35] Alexander Lamb Cullen and P. K. Yu. "Complex source-point theory of the electromagnetic open resonator". In: *Proceedings of the Royal Society of London. A. Mathematical and Physical Sciences* 366.1725 (June 12, 1979). Number: 1725, pp. 155–171. ISSN: 0080-4630. DOI: 10.1098/rspa.1979.0045.

[36] H. Bacry and M. Cadilhac. "Metaplectic group and Fourier optics". In: *Physical Review A* 23.5 (May 1, 1981). Number: 5, pp. 2533–2536. ISSN: 0556-2791. DOI: 10.1103/PhysRevA.23.2533.

[37] Marc Couture and Pierre-A. Belanger. "From Gaussian beam to complex-source-point spherical wave". In: *Physical Review A* 24.1 (July 1, 1981). Number: 1, pp. 355–359. ISSN: 0556-2791. DOI: 10.1103/PhysRevA.24.355.

[38] R. W. P. Drever et al. "Optical Cavity Laser Interferometers for Gravitational Wave Detection". In: *Laser Spectroscopy V*. Springer, Berlin, Heidelberg, 1981, pp. 33–40.

[39] J. H. Taylor and J. M. Weisberg. "A new test of general relativity - Gravitational radiation and the binary pulsar PSR 1913+16". In: *The Astrophysical Journal* 253 (Feb. 1982), p. 908. ISSN: 0004-637X, 1538-4357. DOI: 10.1086/159690.

[40] R. W. P. Drever et al. "Gravitational Wave Detectors Using Laser Interferometers and Optical Cavities: Ideas, Principles and Prospects". In: *Quantum Optics, Experimental Gravity, and Measurement Theory*. Ed. by Pierre Meystre and Marlan O. Scully. Springer US, 1983, pp. 503–514. ISBN: 978-1-4613-3714-0.

[41] R. W. P. Drever et al. "Laser phase and frequency stabilization using an optical resonator". In: *Applied Physics B* 31.2 (1983). Number: 2, pp. 97–105.

[42] Dana Z. Anderson. "Alignment of resonant optical cavities". In: *Applied Optics* 23.17 (1984). Number: 17, pp. 2944–2949. DOI: https://doi.org/10.1364/AO.23.002944.

[43] F. Bayer-Helms. "Coupling coefficients of an incident wave and the modes of a spherical optical resonator in the case of mismatching and misalignment". In: *Applied Optics* 23.9 (May 1, 1984). Number: 9, p. 1369. ISSN: 0003-6935, 1539-4522. DOI: 10.1364/AO.23.001369.

[44] R Littlejohn. "The semiclassical evolution of wave packets". In: *Physics Reports* 138.4 (May 1986). Number: 4-5, pp. 193–291. ISSN: 03701573. DOI: 10.1016/0370-1573(86)90103-1.

[45] Youcef Saad and Martin H. Schultz. "GMRES: A Generalized Minimal Residual Algorithm for Solving Nonsymmetric Linear Systems". In: *SIAM Journal on Scientific and Statistical Computing* 7.3 (July 1986). Number: 3, pp. 856–869. ISSN: 0196-5204, 2168-3417. DOI: 10.1137/0907058.

[46] Anthony E. Siegman. "11: Laser Mirrors and Regenerative Feedback". In: *Lasers*. Mill Valley, Calif: Univ. Science Books, 1986, pp. 398–456. ISBN: 978-0-935702-11-8.

[47] Anthony E. Siegman. "15: Ray Optics and Ray Matrices". In: *Lasers*. Mill Valley, Calif: Univ. Science Books, 1986, pp. 581–625. ISBN: 978-0-935702-11-8.

[48] Anthony E. Siegman. "20: Complex Paraxial Wave Optics". In: *Lasers*. Mill Valley, Calif: Univ. Science Books, 1986, pp. 777–814. ISBN: 978-0-935702-11-8.

[49] Anthony E. Siegman. "21: Generalized Paraxial Resonator Theory". In: *Lasers*. Mill Valley, Calif: Univ. Science Books, 1986, pp. 815–857. ISBN: 978-0-935702-11-8.

[50] Anthony E. Siegman. *Lasers*. OCLC: 14525287. Mill Valley, California: University Science Books, 1986. 1283 pp. ISBN: 978-0-935702-11-8.

[51] Robert G. Littlejohn and Jonathan M. Robbins. “New way to compute Maslov indices”. In: *Physical Review A* 36.6 (Sept. 1, 1987). Number: 6, pp. 2953–2961. ISSN: 0556-2791. DOI: 10.1103/PhysRevA.36.2953.

[52] Brian J. Meers. “Recycling in laser-interferometric gravitational-wave detectors”. In: *Physical Review D* 38.8 (1988). Number: 8, p. 2317.

[53] D. Shoemaker et al. “Noise behavior of the Garching 30-meter prototype gravitational-wave detector”. In: *Physical Review D* 38.2 (July 15, 1988), pp. 423–432. ISSN: 0556-2821. DOI: 10.1103/PhysRevD.38.423.

[54] J. Demmel. “LAPACK: a portable linear algebra library for supercomputers”. In: *IEEE Control Systems Society Workshop on Computer-Aided Control System Design*. IEEE Control Systems Society Workshop on Computer-Aided Control System Design. Tampa, FL, USA: IEEE, 1989, pp. 1–7. DOI: 10.1109/CACSD.1989.69824.

[55] Tomihisa Kamada and Satoru Kawai. “An algorithm for drawing general undirected graphs”. In: *Information Processing Letters* 31.1 (Apr. 1989), pp. 7–15. ISSN: 00200190. DOI: 10.1016/0020-0190(89)90102-6.

[56] B.J. Meers. “The frequency response of interferometric gravitational wave detectors”. In: *Physics Letters A* 142.8 (Dec. 1989). Number: 8-9, pp. 465–470. ISSN: 03759601. DOI: 10.1016/0375-9601(89)90515-X.

[57] B F Schutz. “Gravitational wave sources and their detectability”. In: *Classical and Quantum Gravity* 6.12 (Dec. 1, 1989), pp. 1761–1780. ISSN: 0264-9381, 1361-6382. DOI: 10.1088/0264-9381/6/12/006.

[58] Alex Abramovici et al. “LIGO: The Laser Interferometer Gravitational-Wave Observatory”. In: *Science* 256.5055 (Apr. 17, 1992), pp. 325–333. ISSN: 0036-8075, 1095-9203. DOI: 10.1126/science.256.5055.325.

[59] Jean-Yves Vinet et al. “A high accuracy method for the simulation of non-ideal optical cavities”. In: *Journal de Physique I* 2.7 (July 1992). Number: 7, pp. 1287–1303. ISSN: 1155-4304, 1286-4862. DOI: 10.1051/jp1:1992211.

[60] H. A. van der Vorst. “Bi-CGSTAB: A Fast and Smoothly Converging Variant of Bi-CG for the Solution of Nonsymmetric Linear Systems”. In: *SIAM Journal on Scientific and Statistical Computing* 13.2 (Mar. 1992). Number: 2, pp. 631–644. ISSN: 0196-5204, 2168-3417. DOI: 10.1137/0913035.

[61] J. Mizuno et al. "Resonant sideband extraction: a new configuration for interferometric gravitational wave detectors". In: *Physics Letters A* 175.5 (Apr. 1993), pp. 273–276. ISSN: 03759601. DOI: 10.1016/0375-9601(93)90620-F.

[62] Sumiyoshi Abe and John T. Sheridan. "Optical operations on wave functions as the Abelian subgroups of the special affine Fourier transformation". In: *Optics Letters* 19.22 (Nov. 15, 1994). Number: 22, p. 1801. ISSN: 0146-9592, 1539-4794. DOI: 10.1364/OL.19.001801.

[63] D. Minkov. "Flow-graph approach for optical analysis of planar structures". In: *Applied Optics* 33.33 (Nov. 20, 1994), p. 7698. ISSN: 0003-6935, 1539-4522. DOI: 10.1364/AO.33.007698.

[64] Karsten Danzmann. "LISA: laser interferometer space antenna for gravitational wave measurements". In: (1996), p. 5.

[65] M. Fatih Erden and Haldun M. Ozaktas. "Accumulated Gouy phase shift in Gaussian beam propagation through first-order optical systems". In: *Journal of the Optical Society of America A* 14.9 (Sept. 1, 1997). Number: 9, pp. 2190–2194. ISSN: 1520-8532. DOI: 10.1364/JOSAA.14.002190.

[66] Christian Pedersen and Torben Skettrup. "Signal-flow graphs in coupled laser resonator analysis". In: *Journal of the Optical Society of America A* 14.8 (Aug. 1, 1997), p. 1791. ISSN: 1084-7529, 1520-8532. DOI: 10.1364/JOSAA.14.001791.

[67] Partha Saha. "Fast estimation of transverse fields in high-finesse optical cavities". In: *Journal of the Optical Society of America A* 14.9 (Sept. 1, 1997). Number: 9, p. 2195. ISSN: 1084-7529, 1520-8532. DOI: 10.1364/JOSAA.14.002195.

[68] R. B. Lehoucq, D. C. Sorensen, and C. Yang. *ARPACK Users' Guide: Solution of Large-Scale Eigenvalue Problems with Implicitly Restarted Arnoldi Methods*. Society for Industrial and Applied Mathematics, Jan. 1998. ISBN: 978-0-89871-407-4. DOI: 10.1137/1.9780898719628.

[69] Yu. Levin. "Internal thermal noise in the LIGO test masses: A direct approach". In: *Physical Review D* 57.2 (Jan. 15, 1998), pp. 659–663. ISSN: 0556-2821, 1089-4918. DOI: 10.1103/PhysRevD.57.659.

[70] Nergis Mavalvala, Daniel Sigg, and David Shoemaker. "Experimental test of an alignment-sensing scheme for a gravitational-wave interferometer". In: *Applied*

Optics 37.33 (Nov. 20, 1998). Number: 33, pp. 7743–7746. ISSN: 1539-4522. DOI: 10.1364/AO.37.007743.

[71] M. Möller et al. "Fabry-Pérot and ring cavity configurations and transverse optical patterns". In: *Journal of Modern Optics* 45.9 (Sept. 1998). Number: 9, pp. 1913–1926. ISSN: 0950-0340, 1362-3044. DOI: 10.1080/09500349808231710.

[72] C. J. R. Sheppard and S. Saghafi. "Beam modes beyond the paraxial approximation: A scalar treatment". In: *Physical Review A* 57.4 (Apr. 1, 1998). Number: 4, pp. 2971–2979. ISSN: 1050-2947, 1094-1622. DOI: 10.1103/PhysRevA.57.2971.

[73] R. G. Beausoleil and D. Sigg. "Spatiotemporal model of the LIGO interferometer". In: *Journal of the Optical Society of America A* 16.12 (Dec. 1, 1999). Number: 12, p. 2990. ISSN: 1084-7529, 1520-8532. DOI: 10.1364/JOSAA.16.002990.

[74] John David Jackson. *Classical electrodynamics*. 3rd ed. New York: Wiley, 1999. 808 pp. ISBN: 978-0-471-30932-1.

[75] D. A. Shaddock, M. B. Gray, and D. E. McClelland. "Frequency locking a laser to an optical cavity by use of spatial mode interference". In: *Optics Letters* 24.21 (Nov. 1, 1999). Number: 21, p. 1499. ISSN: 0146-9592, 1539-4794. DOI: 10.1364/OL.24.001499.

[76] C. J. R. Sheppard and S. Saghafi. "Electromagnetic Gaussian beams beyond the paraxial approximation". In: *Journal of the Optical Society of America A* 16.6 (June 1, 1999). Number: 6, p. 1381. ISSN: 1084-7529, 1520-8532. DOI: 10.1364/JOSAA.16.001381.

[77] C. J. R. Sheppard and S. Saghafi. "Transverse-electric and transverse-magnetic beam modes beyond the paraxial approximation". In: *Optics Letters* 24.22 (Nov. 15, 1999). Number: 22, p. 1543. ISSN: 0146-9592, 1539-4794. DOI: 10.1364/OL.24.001543.

[78] R Sheppard and S Saghafi. "Electric and magnetic dipole beam modes beyond the paraxial approximation". In: *Optik* 110.10 (1999). Number: 10, p. 6.

[79] Thibault Damour and Alexander Vilenkin. "Gravitational Wave Bursts from Cosmic Strings". In: *Physical Review Letters* 85.18 (Oct. 30, 2000), pp. 3761–3764. ISSN: 0031-9007, 1079-7114. DOI: 10.1103/PhysRevLett.85.3761.

[80] Guido Mueller et al. "Determination and optimization of mode matching into optical cavities by heterodyne detection". In: *Optics Letters* 25.4 (Feb. 15, 2000). Number: 4, pp. 266–268. ISSN: 1539-4794. DOI: 10.1364/OL.25.000266.

[81] A. E. Siegman. "Laser beams and resonators: Beyond the 1960s". In: *IEEE Journal of Selected Topics in Quantum Electronics* 6.6 (Nov. 2000). Number: 6, pp. 1389–1399. ISSN: 1077-260X. DOI: 10.1109/2944.902193.

[82] A.E. Siegman. "Laser beams and resonators: the 1960s". In: *IEEE Journal of Selected Topics in Quantum Electronics* 6.6 (Nov. 2000). Number: 6, pp. 1380–1388. ISSN: 1077-260X, 1558-4542. DOI: 10.1109/2944.902192.

[83] Soo-Chang Pei and Jian-Jiun Ding. "Closed-form discrete fractional and affine Fourier transforms". In: *IEEE Transactions on Signal Processing* 48.5 (May 2000). Number: 5, pp. 1338–1353. ISSN: 1053587X. DOI: 10.1109/78.839981.

[84] Eric D. Black. "An introduction to Pound–Drever–Hall laser frequency stabilization". In: *American Journal of Physics* 69.1 (Jan. 2001). Number: 1, pp. 79–87. ISSN: 0002-9505, 1943-2909. DOI: 10.1119/1.1286663.

[85] Haldun M. Ozaktas, M. Alper Kutay, and Zeev Zalevsky. *The fractional Fourier transform with applications in optics and signal processing*. Wiley series in pure and applied optics. Chichester ; New York: Wiley, 2001. 513 pp. ISBN: 978-0-471-96346-2.

[86] Victor Y. Pan. *Structured Matrices and Polynomials*. Boston, MA: Birkhäuser Boston, 2001. ISBN: 978-1-4612-6625-9. DOI: 10.1007/978-1-4612-0129-8.

[87] The Virgo Collaboration. *The Virgo Book of Physics: Optics and Related Topics*. Virgo, 2001.

[88] Gregory M Harry et al. "Thermal noise in interferometric gravitational wave detectors due to dielectric optical coatings". In: *Classical and Quantum Gravity* 19.5 (Mar. 7, 2002), pp. 897–917. ISSN: 0264-9381, 1361-6382. DOI: 10.1088/0264-9381/19/5/305.

[89] Ryan Lawrence et al. "Adaptive thermal compensation of test masses in advanced LIGO". In: *Classical and Quantum Gravity* 19.7 (Apr. 7, 2002). Number: 7, pp. 1803–1812. ISSN: 0264-9381, 1361-6382. DOI: 10.1088/0264-9381/19/7/377.

[90] Raymond G. Beausoleil et al. “Model of thermal wave-front distortion in interferometric gravitational-wave detectors I Thermal focusing”. In: *Journal of the Optical Society of America B* 20.6 (June 1, 2003). Number: 6, p. 1247. ISSN: 0740-3224, 1520-8540. DOI: 10.1364/JOSAB.20.001247.

[91] Brett Bochner and Yaron Hefetz. “Grid-based simulation program for gravitational wave interferometers with realistically imperfect optics”. In: *Physical Review D* 68.8 (Oct. 30, 2003). Number: 8, p. 082001. DOI: 10.1103/PhysRevD.68.082001.

[92] John Ellson et al. “Graphviz and Dynagraph — Static and Dynamic Graph Drawing Tools”. In: *Graph Drawing Software*. Ed. by Michael Jünger and Petra Mutzel. Red. by Gerald Farin et al. Series Title: Mathematics and Visualization. Berlin, Heidelberg: Springer Berlin Heidelberg, 2004, pp. 127–148. ISBN: 978-3-642-62214-4. DOI: 10.1007/978-3-642-18638-7_6.

[93] A. Freise et al. “Frequency-domain interferometer simulation with higher-order spatial modes”. In: *Classical and Quantum Gravity* 21.5 (2004). Number: 5, S1067. ISSN: 0264-9381. DOI: 10.1088/0264-9381/21/5/102.

[94] J. M. Weisberg and J. H. Taylor. “Relativistic Binary Pulsar B1913+16: Thirty Years of Observations and Analysis”. In: *arXiv:astro-ph/0407149* (July 7, 2004). arXiv: astro-ph/0407149.

[95] Kurt Bernardo Wolf. *Geometric optics on phase space*. Texts and monographs in physics. Berlin ; New York, NY: Springer, 2004. 373 pp. ISBN: 978-3-540-22039-8.

[96] Karim M. Abadir and Jan R. Magnus. “Kronecker product, vec-operator, and Moore-Penrose inverse”. In: *Matrix Algebra*. 1st ed. Cambridge University Press, Aug. 22, 2005, pp. 273–297. ISBN: 978-0-521-53746-9. DOI: 10.1017/CBO9780511810800.

[97] Norman Hodgson and Horst Weber. “1: Geometrical Optics”. In: *Laser resonators and beam propagation: fundamentals, advanced concepts and applications*. 2nd ed. Springer series in optical sciences v. 108. OCLC: ocm60564637. New York: Springer, 2005, pp. 7–55. ISBN: 978-0-387-40078-5.

[98] Norman Hodgson and Horst Weber. “2: Wave Optics”. In: *Laser resonators and beam propagation: fundamentals, advanced concepts and applications*. 2nd

ed. Springer series in optical sciences v. 108. OCLC: ocm60564637. New York: Springer, 2005, pp. 56–152. ISBN: 978-0-387-40078-5.

[99] ISO-11146-2:2005(E). *Lasers and laser-related equipment - Test methods for laser beam widths, divergence angles and beam propagation ratios - Part 2: General astigmatic beams*. Standard. International Organization for Standardization, 2005.

[100] Ekanathan Palamadai Natarajan. "KLU - A High Performance Sparse Linear Solver For Circuit Simulation Problems". PhD thesis. University of Florida, 2005.

[101] Gregory M. Harry et al. "Thermal noise from optical coatings in gravitational wave detectors". In: *Applied Optics* 45.7 (Mar. 1, 2006), p. 1569. ISSN: 0003-6935, 1539-4522. DOI: 10.1364/AO.45.001569.

[102] Rana Adhikari, Peter Fritschel, and Sam Waldman. *Enhanced LIGO*. Technical Notes T060156. LIGO, 2006.

[103] Jan Harms, Paul Cochrane, and Andreas Freise. "Quantum-noise power spectrum of fields with discrete classical components". In: *Physical Review A* 76.2 (Aug. 7, 2007). Number: 2, p. 023803. ISSN: 1050-2947, 1094-1622. DOI: 10.1103/PhysRevA.76.023803.

[104] Muzammil A. Arain and Guido Mueller. "Design of the Advanced LIGO recycling cavities". In: *Optics Express* 16.14 (July 7, 2008). Number: 14, pp. 10018–10032. ISSN: 1094-4087. DOI: 10.1364/OE.16.010018.

[105] D A Shaddock. "Space-based gravitational wave detection with LISA". In: *Classical and Quantum Gravity* 25.11 (June 7, 2008), p. 114012. ISSN: 0264-9381, 1361-6382. DOI: 10.1088/0264-9381/25/11/114012.

[106] Hiro Yamamoto. *SIS (Stationary Interferometer Simulation) manual*. T070039. Issue: T070039. LIGO, Dec. 12, 2008.

[107] B P Abbott et al. "LIGO: the Laser Interferometer Gravitational-Wave Observatory". In: *Reports on Progress in Physics* 72.7 (July 1, 2009). Number: 7, p. 076901. ISSN: 0034-4885, 1361-6633. DOI: 10.1088/0034-4885/72/7/076901.

[108] B. S. Sathyaprakash and Bernard F. Schutz. "Physics, Astrophysics and Cosmology with Gravitational Waves". In: *Living Reviews in Relativity* 12.1 (Dec. 2009), p. 2. ISSN: 2367-3613, 1433-8351. DOI: 10.12942/lrr-2009-2.

[109] Timothy A. Davis and Ekanathan Palamadai Natarajan. "Algorithm 907: KLU, A Direct Sparse Solver for Circuit Simulation Problems". In: *ACM Transactions on Mathematical Software* 37.3 (Sept. 1, 2010). Number: 3, pp. 1–17. ISSN: 00983500. DOI: 10.1145/1824801.1824814.

[110] Steven J. M. Habraken and Gerard Nienhuis. "Geometric phases in astigmatic optical modes of arbitrary order". In: *Journal of Mathematical Physics* 51.8 (Aug. 2010). Number: 8, p. 082702. ISSN: 0022-2488, 1089-7658. DOI: 10.1063/1.3456078.

[111] M Punturo et al. "The Einstein Telescope: a third-generation gravitational wave observatory". In: *Classical and Quantum Gravity* 27.19 (Oct. 7, 2010), p. 194002. ISSN: 0264-9381, 1361-6382. DOI: 10.1088/0264-9381/27/19/194002.

[112] S Hild et al. "Sensitivity studies for third-generation gravitational wave observatories". In: *Classical and Quantum Gravity* 28.9 (May 7, 2011), p. 094013. ISSN: 0264-9381, 1361-6382. DOI: 10.1088/0264-9381/28/9/094013.

[113] N. Smith-Lefebvre et al. "Optimal alignment sensing of a readout mode cleaner cavity". In: *Optics Letters* 36.22 (Nov. 15, 2011). Number: 22, p. 4365. ISSN: 0146-9592, 1539-4794. DOI: 10.1364/OL.36.004365.

[114] Thomas Estruch et al. "Mason's rule and Signal Flow Graphs applied to sub-wavelength resonant structures". In: *Optics Express* 20.24 (Nov. 19, 2012), p. 27155. ISSN: 1094-4087. DOI: 10.1364/OE.20.027155.

[115] Tobin T. Fricke et al. "DC readout experiment in Enhanced LIGO". In: *Classical and Quantum Gravity* 29.6 (Mar. 21, 2012). Number: 6, p. 065005. ISSN: 0264-9381, 1361-6382. DOI: 10.1088/0264-9381/29/6/065005. arXiv: 1110.2815.

[116] NASA Goddard Space Flight Center. *The Gravitational Wave Spectrum*. Gravitational Astrophysics Laboratory. Jan. 9, 2012. URL: https://science.gsfc.nasa.gov/663/images/gravity/GWspec.jpg.

[117] Nicholas Smith-Lefebvre and Negris Mavalvala. *Modematching feedback control for interferometers with an output mode cleaner*. P1200034-v3. Issue: P1200034-v3. LIGO, 2012.

[118] A Rocchi et al. "Thermal effects and their compensation in Advanced Virgo". In: *Journal of Physics: Conference Series* 363 (June 1, 2012), p. 012016. ISSN: 1742-6596. DOI: 10.1088/1742-6596/363/1/012016.

[119] O. A. Sapozhnikov. "An exact solution to the Helmholtz equation for a quasi-Gaussian beam in the form of a superposition of two sources and sinks with complex coordinates". In: *Acoustical Physics* 58.1 (Jan. 2012). Number: 1, pp. 41–47. ISSN: 1063-7710, 1562-6865. DOI: 10.1134/S1063771012010216.

[120] Du Wang et al. "Eigenvector method for unstable resonator simulations". In: *Optics Communications* 285.10 (May 2012). Number: 10-11, pp. 2682–2687. ISSN: 00304018. DOI: 10.1016/j.optcom.2011.12.005.

[121] Koji Arai. *On the accumulated round-trip Gouy phase shift for a general optical cavity*. T1300189-v1. Issue: T1300189-v1. LIGO, Mar. 10, 2013.

[122] Mahdi Bahadoran, Jalil Ali, and Preecha P. Yupapin. "Ultrafast all-optical switching using signal flow graph for PANDA resonator". In: *Applied Optics* 52.12 (Apr. 20, 2013), p. 2866. ISSN: 1559-128X, 2155-3165. DOI: 10.1364/AO.52.002866.

[123] Andreas Freise, Daniel Brown, and Charlotte Bond. "Finesse, Frequency domain INterferomEter Simulation SoftwarE". In: *arXiv:1306.2973 [physics]* (June 12, 2013). arXiv: 1306.2973.

[124] Marie Kasprzack et al. "Performance of a thermally deformable mirror for correction of low-order aberrations in laser beams". In: *Applied Optics* 52.12 (Apr. 20, 2013). Number: 12, p. 2909. ISSN: 1559-128X, 2155-3165. DOI: 10.1364/AO.52.002909.

[125] F. G. Mitri. "Quasi-Gaussian electromagnetic beams". In: *Physical Review A* 87.3 (Mar. 11, 2013). Number: 3, p. 035804. ISSN: 1050-2947, 1094-1622. DOI: 10.1103/PhysRevA.87.035804.

[126] New Focus. *DC-250MHz Electro-Optic Phase Modulators Models 400X, 406X*. 400412 Rev J. Newport, 2013.

[127] Daniel David Brown and Andreas Freise. *Finesse*. Programmers: _:n15750. May 19, 2014. DOI: 10.5281/ZENODO.821363.

[128] Daniel David Brown and Andreas Freise. *Finesse*. May 2014. DOI: 10.5281/zenodo.821363.

[129] R. A. Day, G. Vajente, and M. Pichot du Mezeray. "Accelerated convergence method for fast Fourier transform simulation of coupled cavities". In: *Journal of*

the Optical Society of America A 31.3 (Mar. 1, 2014). Number: 3, p. 652. ISSN: 1084-7529, 1520-8532. DOI: 10.1364/JOSAA.31.000652.

[130] John Miller and Matthew Evans. "Length control of an optical resonator using second-order transverse modes". In: *Optics Letters* 39.8 (Apr. 15, 2014). Number: 8, p. 2495. ISSN: 0146-9592, 1539-4794. DOI: 10.1364/OL.39.002495.

[131] Aidan Brooks et al. *Active wavefront control in and beyond Advanced LIGO*. Technical notes T1500188-v5. Issue: T1500188-v5. LIGO, Apr. 21, 2015.

[132] Aidan Brooks. *SR3 heater actuator update*. G1501373. LIGO, 2015.

[133] Koji Arai. *aLIGO OMC optical testing procedure*. T1500060-v1. Issue: T1500060-v1. LIGO, 2015.

[134] John Miller et al. "Prospects for doubling the range of Advanced LIGO". In: *Physical Review D* 91.6 (Mar. 16, 2015). Number: 6, p. 062005. ISSN: 1550-7998, 1550-2368. DOI: 10.1103/PhysRevD.91.062005.

[135] The LIGO Scientific Collaboration. "Advanced LIGO". In: *Classical and Quantum Gravity* 32.7 (2015). Number: 7, p. 074001. ISSN: 0264-9381. DOI: 10.1088/0264-9381/32/7/074001.

[136] The Virgo Collaboration. "Advanced Virgo: a second-generation interferometric gravitational wave detector". In: *Classical and Quantum Gravity* 32.2 (2015). Number: 2. ISSN: 0264-9381. DOI: 10.1088/0264-9381/32/2/024001.

[137] Liang Zhao, John J. Healy, and John T. Sheridan. "Constraints on additivity of the 1D discrete linear canonical transform". In: *Applied Optics* 54.33 (Nov. 20, 2015). Number: 33, p. 9960. ISSN: 0003-6935, 1539-4522. DOI: 10.1364/AO.54.009960.

[138] B. P. Abbott et al. "GW150914: First results from the search for binary black hole coalescence with Advanced LIGO". In: *Physical Review D* 93.12 (June 7, 2016), p. 122003. ISSN: 2470-0010, 2470-0029. DOI: 10.1103/PhysRevD.93.122003.

[139] B. P. Abbott et al. "Properties of the Binary Black Hole Merger GW150914". In: *Physical Review Letters* 116.24 (June 14, 2016), p. 241102. ISSN: 0031-9007, 1079-7114. DOI: 10.1103/PhysRevLett.116.241102.

[140] Charlotte Bond et al. "Interferometer techniques for gravitational-wave detection". In: *Living Reviews in Relativity* 19.1 (Dec. 2016). Number: 1. ISSN: 2367-3613, 1433-8351. DOI: 10.1007/s41114-016-0002-8.

[141] Aidan F. Brooks et al. "Overview of Advanced LIGO adaptive optics". In: *Applied Optics* 55.29 (Oct. 10, 2016). Number: 29, p. 8256. ISSN: 0003-6935, 1539-4522. DOI: 10.1364/AO.55.008256.

[142] Matthew Evans. *Optickle2*. 2016.

[143] Matthew Evans and Yuta Michimura. *Optickle 2*. T1600129-v1, Apr. 29, 2016.

[144] John J. Healy et al., eds. *Linear canonical transforms: theory and applications*. Springer series in optical sciences 198. OCLC: ocn910411981. New York: Springer, 2016. 453 pp. ISBN: 978-1-4939-3027-2.

[145] Kiwamu Izumi and Daniel Sigg. "Advanced LIGO: length sensing and control in a dual recycled interferometric gravitational wave antenna". In: *Classical and Quantum Gravity* 34.1 (2016). Number: 1, p. 015001. ISSN: 0264-9381. DOI: 10.1088/0264-9381/34/1/015001.

[146] LIGO Scientific Collaboration and Virgo Collaboration et al. "Observation of Gravitational Waves from a Binary Black Hole Merger". In: *Physical Review Letters* 116.6 (Feb. 11, 2016). Number: 6, p. 061102. DOI: 10.1103/PhysRevLett.116.061102.

[147] Soo-Chang Pei and Shih-Gu Huang. "Fast Discrete Linear Canonical Transform Based on CM-CC-CM Decomposition and FFT". In: *IEEE Transactions on Signal Processing* 64.4 (Feb. 2016). Number: 4, pp. 855–866. ISSN: 1053-587X, 1941-0476. DOI: 10.1109/TSP.2015.2491891. arXiv: 1709.06222.

[148] Soo-Chang Pei and Shih-Gu Huang. "Two-dimensional nonseparable discrete linear canonical transform based on CM-CC-CM-CC decomposition". In: *Journal of the Optical Society of America A* 33.2 (Feb. 1, 2016). Number: 2, p. 214. ISSN: 1084-7529, 1520-8532. DOI: 10.1364/JOSAA.33.000214. arXiv: 1707.03688.

[149] Joel M. Weisberg and Yuping Huang. "Relativistic Measurements from Timing the Binary Pulsar PSR B1913+16". In: *The Astrophysical Journal* 829.1 (Sept. 21, 2016), p. 55. ISSN: 1538-4357. DOI: 10.3847/0004-637X/829/1/55. arXiv: 1606.02744.

[150] Kurt Bernardo Wolf. "Development of Linear Canonical Transforms: A Historical Sketch". In: *Linear Canonical Transforms*. Ed. by John J. Healy et al. Vol. 198. Series Title: Springer Series in Optical Sciences. New York, NY: Springer New York, 2016, pp. 3–28. ISBN: 978-1-4939-3027-2. DOI: 10.1007/978-1-4939-3028-9_1.

[151] B. P. Abbott et al. "Exploring the Sensitivity of Next Generation Gravitational Wave Detectors". In: *Classical and Quantum Gravity* 34.4 (Feb. 23, 2017), p. 044001. ISSN: 0264-9381, 1361-6382. DOI: 10.1088/1361-6382/aa51f4. arXiv: 1607.08697.

[152] Alexei Ciobanu, Daniel Brown, and David Ottaway. *Modelling Beam Shape Noise in Gravitational Wave Interferometers*. G1702312. LIGO DCC, Nov. 22, 2017.

[153] Coherent. *Mephisto Laser Operator's Manual*. 1307511. 2017.

[154] Dar Dahlen, Russell Wilcox, and Wim Leemans. "Modeling Herriott cells using the linear canonical transform". In: *Applied Optics* 56.2 (Jan. 10, 2017). Number: 2, p. 267. ISSN: 0003-6935, 1539-4522. DOI: 10.1364/AO.56.000267.

[155] Karsten Danzmann. *LISA - Laser Interferometer Space Antenna*. 2017.

[156] ESO/E. Pian et al./S. Smartt & ePESSTO. *X-shooter spectra montage of kilonova in NGC 4993*. Oct. 16, 2017. URL: https://commons.wikimedia.org/wiki/File:Eso1733j_X-shooter_spectra_montage_of_kilonova_in_NGC4993.png.

[157] P. Fulda et al. "Alignment sensing for optical cavities using radio-frequency jitter modulation". In: *Applied Optics* 56.13 (May 1, 2017). Number: 13, pp. 3879–3888. ISSN: 2155-3165. DOI: 10.1364/AO.56.003879.

[158] Daniel Kasen et al. "Origin of the heavy elements in binary neutron-star mergers from a gravitational-wave event". In: *Nature* 551.7678 (Nov. 2, 2017), pp. 80–84. ISSN: 0028-0836, 1476-4687. DOI: 10.1038/nature24453.

[159] Sofía Liberman and Kurt Bernardo Wolf. "The structural development of linear canonical transforms". In: *Physics of Atomic Nuclei* 80.4 (July 2017). Number: 4, pp. 814–821. ISSN: 1063-7788, 1562-692X. DOI: 10.1134/S1063778817040160.

[160] LIGO Scientific Collaboration and Virgo Collaboration. "GW170817: Observation of Gravitational Waves from a Binary Neutron Star Inspiral". In: *Physical*

Review Letters 119.16 (Oct. 16, 2017), p. 161101. ISSN: 0031-9007, 1079-7114. DOI: 10.1103/PhysRevLett.119.161101.

[161] Mini-Circuits. *ZHL-1A+ Datasheet*. Rev E. 2017.

[162] L. Neuhaus et al. "PyRPL (Python Red Pitaya Lockbox) — An open-source software package for FPGA-controlled quantum optics experiments". In: *2017 Conference on Lasers and Electro-Optics Europe & European Quantum Electronics Conference (CLEO/Europe-EQEC)*. 2017 Conference on Lasers and Electro-Optics Europe & European Quantum Electronics Conference (CLEO/Europe-EQEC). Munich, Germany: IEEE, June 2017, pp. 1–1. ISBN: 978-1-5090-6736-7. DOI: 10.1109/CLEOE-EQEC.2017.8087380.

[163] G. H. C. New. "Computing unstable resonator modes". In: *Journal of Modern Optics* 64.20 (Nov. 13, 2017). Number: 20, pp. 2185–2194. ISSN: 0950-0340, 1362-3044. DOI: 10.1080/09500340.2017.1346152.

[164] E. Pian et al. "Spectroscopic identification of r-process nucleosynthesis in a double neutron-star merger". In: *Nature* 551.7678 (Nov. 2, 2017), pp. 67–70. ISSN: 0028-0836, 1476-4687. DOI: 10.1038/nature24298.

[165] Keith Riles. "Recent searches for continuous gravitational waves". In: *Modern Physics Letters A* 32.39 (Dec. 21, 2017), p. 1730035. ISSN: 0217-7323, 1793-6632. DOI: 10.1142/S021773231730035X.

[166] Thorlabs. *DET10C2 InGaAs Biased Detector User Guide*. Rev A. 2017.

[167] Thorlabs. *Round Piezoelectric Stack with Two End Plates, 200 V, 12.0 m Travel*. CTN010616-S01. 2017.

[168] Alexei Ciobanu. *Parametrization of mismatch contours*. T1800193. LIGO DCC, Apr. 29, 2018.

[169] Alexei Ciobanu and Daniel Brown. *Effects of OMC astigmatism on mismatch calculations from OMC scans*. T1800191. LIGO DCC, Apr. 26, 2018.

[170] Alexei Ciobanu et al. *LAWG mode mismatch presentation*. G1802180. LIGO DCC, Nov. 13, 2018.

[171] Alexei Ciobanu et al. *Mode matching error signals from cavity eigenmode modulation (poster)*. G1802332. LIGO DCC, Dec. 16, 2018.

[172] Alexei Ciobanu et al. *Mode mismatch of astigmatic gaussian beams from a cavity scan*. T1800165. LIGO DCC, Apr. 16, 2018.

[173] Chiara Caprini and Daniel G Figueroa. "Cosmological backgrounds of gravitational waves". In: *Classical and Quantum Gravity* 35.16 (Aug. 23, 2018), p. 163001. ISSN: 0264-9381, 1361-6382. DOI: 10.1088/1361-6382/aac608.

[174] Daniel Brown. *OPO to OMC beam profiling with new lenses*. aLIGO LHO Logbook 41683. LIGO, Apr. 26, 2018.

[175] John J Healy. "Simulating first order optical systems—algorithms for and composition of discrete linear canonical transforms". In: *Journal of Optics* 20.1 (Jan. 1, 2018). Number: 1, p. 014008. ISSN: 2040-8978, 2040-8986. DOI: 10.1088/2040-8986/aa9e20.

[176] Lee McCuller and Lisa Barsotti. *Design Requirement Document of the A+ filter cavity and relay optics for frequency dependent squeezing*. T1800447. Issue: T1800447. LIGO, 2018, p. 63.

[177] John Lekner and Petar Andrejic. "Nonexistence of exact solutions agreeing with the Gaussian beam on the beam axis or in the focal plane". In: *Optics Communications* 407 (Jan. 2018), pp. 22–26. ISSN: 00304018. DOI: 10.1016/j.optcom.2017.08.071.

[178] PiezoDrive. *PD200 V6 Manual*. 2018.

[179] I. Tews, J. Margueron, and S. Reddy. "Critical examination of constraints on the equation of state of dense matter obtained from GW170817". In: *Physical Review C* 98.4 (Oct. 22, 2018), p. 045804. ISSN: 2469-9985, 2469-9993. DOI: 10.1103/PhysRevC.98.045804.

[180] Thorlabs. *BPC301 Benchtop Piezo Controller User Guide*. HA0248T Rev F. 2018.

[181] Alexei Ciobanu, Daniel Brown, and David Ottaway. *Finesse Workshop - Linear Canonical Transform and Graph Reduction*. G1901692. LIGO DCC, Sept. 2, 2019.

[182] Alexei Ciobanu, Daniel Brown, and David Ottaway. *jupyter notebook: tutorial on computing OMC astigmatism from OMC scans*. T1900180. LIGO DCC, Apr. 8, 2019.

[183] Alexei Ciobanu, Daniel Brown, and David Ottaway. *Measurement of LLO and LHO OMC astigmatism*. T1900084. LIGO DCC, Apr. 3, 2019.

[184] Alexei Ciobanu et al. *OzGrav retreat 2019 poster*. G1902197. LIGO DCC, Nov. 14, 2019.

[185] Lisa Barsotti, Jan Harms, and Roman Schnabel. "Squeezed vacuum states of light for gravitational wave detectors". In: *Reports on Progress in Physics* 82.1 (Jan. 1, 2019). Number: 1, p. 016905. ISSN: 0034-4885, 1361-6633. DOI: 10.1088/1361-6633/aab906.

[186] Huy Tuong Cao, Peter Veitch, and David Ottaway. "Development of Technologies for Active Wavefront Control of Advanced Gravitational Wave Detectors". PhD thesis. University of Adelaide, 2019.

[187] Nelson Christensen. "Stochastic gravitational wave backgrounds". In: *Reports on Progress in Physics* 82.1 (Jan. 1, 2019), p. 016903. ISSN: 0034-4885, 1361-6633. DOI: 10.1088/1361-6633/aae6b5.

[188] Aykut Koç, Burak Bartan, and Haldun M. Ozaktas. "Discrete Linear Canonical Transform Based on Hyperdifferential Operators". In: *IEEE Transactions on Signal Processing* 67.9 (May 1, 2019). Number: 9, pp. 2237–2248. ISSN: 1053-587X, 1941-0476. DOI: 10.1109/TSP.2019.2903031. arXiv: 1805.11416.

[189] N. A. Lopez and I. Y. Dodin. "Pseudo-differential representation of the metaplectic transform and its application to fast algorithms". In: *Journal of the Optical Society of America A* 36.11 (Nov. 1, 2019). Number: 11, p. 1846. ISSN: 1084-7529, 1520-8532. DOI: 10.1364/JOSAA.36.001846.

[190] Fabian Magaña-Sandoval et al. "Sensing optical cavity mismatch with a mode-converter and quadrant photodiode". In: *Physical Review D* 100.10 (Nov. 18, 2019). Number: 10, p. 102001. ISSN: 2470-0010, 2470-0029. DOI: 10.1103/PhysRevD.100.102001.

[191] Red Pitaya. *Red Pitaya STEMlab Documentation*. 0.97. 2019.

[192] M. Tse et al. "Quantum-Enhanced Advanced LIGO Detectors in the Era of Gravitational-Wave Astronomy". In: *Physical Review Letters* 123.23 (Dec. 5, 2019). Number: 23, p. 231107. ISSN: 0031-9007, 1079-7114. DOI: 10.1103/PhysRevLett.123.231107.

[193] Liang Zhao et al. "A fast numerical algorithm for the 2D non-separable linear canonical transform based on a decomposition of the ABCD matrix". In: *Holography: Advances and Modern Trends VI*. Holography: Advances and Mod-

ern Trends. Ed. by Antonio Fimia, Miroslav Hrabovský, and John T. Sheridan. Prague, Czech Republic: SPIE, Apr. 23, 2019, p. 54. ISBN: 978-1-5106-2726-0. DOI: 10.1117/12.2522839.

[194] K. Ackley et al. "Neutron Star Extreme Matter Observatory: A kilohertz-band gravitational-wave detector in the global network". In: *Publications of the Astronomical Society of Australia* 37 (2020), e047. ISSN: 1323-3580, 1448-6083. DOI: 10.1017/pasa.2020.39.

[195] R X Adhikari et al. "A cryogenic silicon interferometer for gravitational-wave detection". In: *Classical and Quantum Gravity* 37.16 (Aug. 20, 2020), p. 165003. ISSN: 0264-9381, 1361-6382. DOI: 10.1088/1361-6382/ab9143.

[196] Alexei Ciobanu. *Optical modelling with Linear Canonical Transforms (LCT)*. G2001508. LIGO DCC, Sept. 11, 2020.

[197] Alexei Ciobanu, Daniel Brown, and David Ottaway. *A practical guide to Linear Canonical Transforms*. G2000254. LIGO DCC, Feb. 19, 2020.

[198] Alexei Ciobanu et al. *(LAWG presentation) Mode matching error signals using radio-frequency beam shape modulation*. G2001257. LIGO DCC, June 4, 2020.

[199] Alexei Ciobanu et al. *Introducing information theoretic beam basis optimization*. T2000605. LIGO DCC, Oct. 21, 2020.

[200] Daniel D. Brown et al. "Pykat: Python package for modelling precision optical interferometers". In: *SoftwareX* 12 (July 2020), p. 100613. ISSN: 23527110. DOI: 10.1016/j.softx.2020.100613.

[201] A. Buikema et al. "Sensitivity and performance of the Advanced LIGO detectors in the third observing run". In: *Physical Review D* 102.6 (Sept. 11, 2020). Number: 6, p. 062003. ISSN: 2470-0010, 2470-0029. DOI: 10.1103/PhysRevD.102.062003.

[202] Huy Tuong Cao et al. "High dynamic range thermally actuated bimorph mirror for gravitational wave detectors". In: *Applied Optics* 59.9 (Mar. 20, 2020). Number: 9, p. 2784. ISSN: 1559-128X, 2155-3165. DOI: 10.1364/AO.376764.

[203] Collin D. Capano et al. "Stringent constraints on neutron-star radii from multimessenger observations and nuclear theory". In: *Nature Astronomy* 4.6 (June 2020), pp. 625–632. ISSN: 2397-3366. DOI: 10.1038/s41550-020-1014-6.

[204] A. A. Ciobanu et al. "Mode matching error signals using radio-frequency beam shape modulation". In: *Applied Optics* 59.31 (Nov. 1, 2020). Number: 31, p. 9884. ISSN: 1559-128X, 2155-3165. DOI: 10.1364/AO.404646.

[205] Charles R. Harris et al. "Array programming with NumPy". In: *Nature* 585.7825 (Sept. 17, 2020). Number: 7825, pp. 357–362. ISSN: 0028-0836, 1476-4687. DOI: 10.1038/s41586-020-2649-2.

[206] Nutsinee Kijbunchoo et al. "Low phase noise squeezed vacuum for future generation gravitational wave detectors". In: *Classical and Quantum Gravity* (July 10, 2020). ISSN: 0264-9381, 1361-6382. DOI: 10.1088/1361-6382/aba4bb.

[207] L. McCuller et al. "Frequency-Dependent Squeezing for Advanced LIGO". In: *Physical Review Letters* 124.17 (Apr. 28, 2020). Number: 17, p. 171102. ISSN: 0031-9007, 1079-7114. DOI: 10.1103/PhysRevLett.124.171102.

[208] David Reitze et al. *Cosmic Explorer: The U.S. Contribution to Gravitational-Wave Astronomy beyond LIGO*. White paper. LIGO Laboratory, 2020, p. 13.

[209] Jameson Graef Rollins et al. *pygwinc: Gravitational Wave Interferometer Noise Calculator*. Pages: ascl:2007.020 _eprint: 2007.020. July 2020.

[210] SciPy 1.0 Contributors et al. "SciPy 1.0: fundamental algorithms for scientific computing in Python". In: *Nature Methods* 17.3 (Mar. 2020). Number: 3, pp. 261–272. ISSN: 1548-7091, 1548-7105. DOI: 10.1038/s41592-019-0686-2.

[211] Alexander Weaver, Paul Fulda, and Guido Mueller. "Analytic HG-mode propagation through circular apertures with Zernike phase offset". In: *OSA Continuum* 3.7 (July 15, 2020). Number: 7, p. 1891. ISSN: 2578-7519. DOI: 10.1364/OSAC.394476.

[212] Hiro Yamamoto. *SIS*. Version 20. 2020.

[213] Alexei Ciobanu et al. *Modeling circulating cavity fields using the discrete linear canonical transform*. G2101163. LIGO DCC, June 26, 2021.

[214] Abedalgany Athamneh and Shadi A. Alboon. "Analysis of Liquid Crystal Tunable Thin-Film Optical Filters Using Signal Flow Graph Technique". In: *International Journal of Optics* 2021 (July 13, 2021). Ed. by Mustapha Tlidi, pp. 1–4. ISSN: 1687-9392, 1687-9384. DOI: 10.1155/2021/5513995.

[215] M. Bailes et al. “Gravitational-wave physics and astronomy in the 2020s and 2030s”. In: *Nature Reviews Physics* 3.5 (May 2021), pp. 344–366. ISSN: 2522-5820. DOI: 10.1038/s42254-021-00303-8.

[216] Aidan Brooks et al. “Point Absorbers in Advanced LIGO”. In: *Applied Optics* (Apr. 7, 2021). ISSN: 1559-128X, 2155-3165. DOI: 10.1364/AO.419689.

[217] Daniel Brown et al. “Differential wavefront sensing and control using radio-frequency optical demodulation”. In: *Optics Express* 29.11 (May 24, 2021), p. 15995. ISSN: 1094-4087. DOI: 10.1364/OE.425590.

[218] Craig Cahillane. “Controlling and Calibrating Interferometric Gravitational Wave Detectors”. PhD thesis. California Institute of Technology Pasadena, 2021.

[219] A. A. Ciobanu et al. “Modeling circulating cavity fields using the discrete linear canonical transform”. In: *Journal of the Optical Society of America A* 38.9 (Sept. 1, 2021). Number: 9, p. 1293. ISSN: 1084-7529, 1520-8532. DOI: 10.1364/JOSAA.433575.

[220] Alexei Ciobanu. *LCT tutorials*. Version 0.0.1. Programmers: _:n16038 Language: en. July 20, 2021. DOI: 10.5281/ZENODO.5115421.

[221] The LIGO Scientific Collaboration et al. “GWTC-3: Compact Binary Coalescences Observed by LIGO and Virgo During the Second Part of the Third Observing Run”. In: *arXiv:2111.03606 [astro-ph, physics:gr-qc]* (Nov. 17, 2021). arXiv: 2111.03606.

[222] Matthew Evans et al. “A Horizon Study for Cosmic Explorer: Science, Observatories, and Community”. In: (2021). Publisher: arXiv Version Number: 2. DOI: 10.48550/ARXIV.2109.09882.

[223] Michele Maiorano, Francesco De Paolis, and Achille A. Nucita. “Principles of Gravitational-Wave Detection with Pulsar Timing Arrays”. In: *Symmetry* 13.12 (Dec. 14, 2021), p. 2418. ISSN: 2073-8994. DOI: 10.3390/sym13122418. arXiv: 2112.08064.

[224] optotune. *Datasheet: EL-10-30-Series*. 2021.

[225] Mark Stone et al. “Optical mode conversion in coupled Fabry–Perot resonators”. In: *Optics Letters* 46.1 (Jan. 1, 2021). Number: 1, p. 21. ISSN: 0146-9592, 1539-4794. DOI: 10.1364/OL.400998.

[226] J. P. W. Verbiest, S. Oslowski, and S. Burke-Spolaor. "Pulsar Timing Array Experiments". In: *arXiv:2101.10081 [astro-ph]* (2021), pp. 1–42. DOI: 10.1007/978-981-15-4702-7_4-1. arXiv: 2101.10081.

[227] LIGO Scientific Collaboration. *Timeline*. LIGO Caltech. 2022. URL: https://www.ligo.caltech.edu/page/timeline (visited on 02/03/2022).